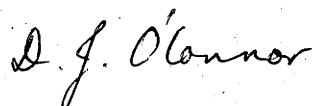# ELASTIC AND INELASTIC SCATTERING OF LOW ENERGY IONS OFF CRYSTAL SURFACES

D.J. O'CONNOR

A thesis submitted for the

Degree of Doctor of Philosophy

at the Australian National University

August 1978

I hereby declare that the work reported in
this thesis has not been submitted before for a
higher degree or award at any other institution or
university. All measurements associated with ion
surface scattering experiments and the associated
computer simulations and data analysis are the
results of my own efforts. When the material and
ideas of others are used, the appropriate
acknowledgements are made.

D.J. O'Connor

ACKNOWLEDGEMENTS

The members of the Physics Department who have provided a congenial environment in which to work.

CONTENTS

ABSTRACT

A study has been made of the basic physical processes associated with the scattering of low energy inert gas ions from crystalline surfaces.

The analysis of published gas scattering results has revealed that the Moliere potential best describes the interaction at these energies. Detailed analysis has shown that improved agreement is obtained if a correction factor is applied to the Firsov screening length. This conclusion is supported by the measurements reported in this thesis as well as published results of other ion surface scattering experiments.

The identification of a component of the scattering yield from the second atomic layer has allowed low energy measurements of the inelastic energy loss for He^+, Ne^+, Ar^+ and Kr^+ off a W(110) surface. The energy dependence of the inelastic loss for Ne^+ and Ar^+ is in general agreement with the theories which predict that the loss is proportional to velocity, but it is typically 0.25 to 0.40 of the expected value.

The comparison of experimental results to computer simulations has allowed the determination of the inelastic loss for ions scattered off the surface atomic layer. It has been shown that the inelastic loss for Ar^+ scattered off a W(110) surface atomic layer is also proportional to velocity.

The investigation of the charge exchange mechanism has raised serious doubts about experimental methods which can involve scattering from subsurface atomic layers. The possibility is also raised that the neutralization mechanism for ions after a collision may be different to that before the collision.

The determination of the surface crystallography of the W(110) face reveals that there is no measurable relaxation in the plane of the surface atomic layer, but at this stage no statements on the relaxation perpendicular to the surface can be made.

The application of low energy ion scattering to the surface structure analysis of a Si(100) face is described and preliminary results presented. From these results, one model of the Si(100) relaxed surface is selected as the most probable structure to exist under these experimental conditions. More conclusive results can be obtained if simultaneous Auger and LEED analyses, to monitor surface purity and structure, are included.

During Ar^+ bombardment of Si, a strong recoil Si^+ component was detected in the energy spectra. By monitoring the yield at different angles of incidence of the ion beam to the surface, the characteristic velocity for neutralization can be determined. The measured velocity is characteristic of an Auger process and a mechanism is proposed to explain this observation.

CHAPTER ONE

INTRODUCTION

The surface of a solid presents a problem in a number of disciplines because it is a departure from the regular structure of the solid and hence has different physical and chemical properties to that of the bulk. It is a discontinuity which can introduce localized strain to the crystal lattice structure causing a rearrangement of the surface atoms (known as "relaxation") and modification of electronic properties. These effects are important factors in the processes of adsorption, catalysis, corrosion and the emission of ions and electrons.

The appreciation of the importance of the physical, chemical and electronic properties of the surface of a solid to a large number of fields of scientific research has encouraged the development of a range of surface analysis techniques.[1] A measure of the importance of this field can be gauged from the number of techniques so far developed to analyse various properties of the surface region. A recent review by Trietz[2] lists 23 techniques even though techniques like Rutherford backscattering were not included. The effects produced by techniques which involve ion bombardment are collectively referred to as Ion-Surface Interactions. Here the term "surface" typically describes the sampling depth for the individual technique and can vary from a few Ångstrøms up to 10^3 Ångstrøms or more. Most of these techniques are still being developed but information is already available to indicate that some are sufficiently selective to allow the analysis of the top one or two atomic layers.

Studies of the interaction between an ion and a surface yield important clues to plasma-wall processes and radiation damage in

solids, which are important factors in nuclear fission and fusion reactor technology. The inelastic components of the interaction in the form of electrons, photons and sputtered target atoms have been used extensively in compositional analysis of solids. Elastic scattering of ions is also an important tool for surface and near surface studies. Rutherford backscattering utilizing high energy light ions has been used extensively to monitor radiation damage in solids, diffusion, and thin film growth. More recently interest has developed in the scattering of low energy ions from surfaces as the analysis depth is limited to the surface atomic layers. Some of the applications of low energy ion scattering include surface compositional analysis, measurement of the surface Debye temperature, identification of surface defects, the measurement of the interatomic potential and investigation of ion neutralization processes near surfaces.

The technique, called Ion Scattering Spectroscopy (ISS), involves the scattering of low energy inert gas ions from solid surfaces to determine its structure and composition. The surface sensitivity of ISS relies on the rapid neutralization of inert gas ions entering the solid. As analysers at these energies (0-10 keV) have been mainly developed for detecting charged particles, projectiles, mainly neutrals, scattered from subsurface atomic layers will escape detection.

As the ions in this work are described as "low energy", it is necessary to define the meaning of that term. In all atomic collision studies, particle energies are categorized as low, medium or high energy. The purpose of this division is to assist in identifying the characteristic properties of the interaction. Low energy describes the energy range for which information is obtained relating to the top one or two atomic layers, while high energy interactions reveal the composition and features of the bulk. Interactions involving medium energy particles are a compromise between these two and can simultaneously reveal the properties of the bulk and the surface. To allocate energies to these classes is a difficult exercise as there is considerable overlap between the types of interaction. In the

following chapters, the energies assigned to the low energy category is 0-10 keV, while for medium energy it is 10-100 keV and the high energy category describes interactions for energies greater than 100 keV.

The various aspects of ISS are reviewed in chapter two and some of the physical processes associated with the scattering studies have been investigated experimentally. A description of the equipment used in this investigation is detailed in chapter three and the experimental results are presented in chapter six. As analytical methods are either unsuccessful or too complex at these energies, it has been necessary to use computer simulations to assist in relating physical parameters of the surface and the ion-atom interaction to the experimental observations. Chapter five is devoted to a description of these computer simulations and the results obtained from them.

The information obtained relating to the interatomic potential is compared to the results of other studies described in chapter four and agreement is found for the Thomas-Fermi-Moliere potential. Evidence is also found for the need for a correction factor to be applied to the Firsov screening length in some applications. The conclusions drawn from this work and suggestions for future studies are presented in chapter seven.

REFERENCES

(1) *Proceedings of the Seventh International Vacuum Conference and the Third International Conference on Solid Surfaces*, eds. R. Dobrozemsky, F. Rüdenauer, F.P. Biehbäck and A. Breth (F. Berger and Söhne, 1977).

(2) N. Trietz, *Journal of Physics E: Scientific Instruments* 10 (1977) 573.

CHAPTER TWO

ION SCATTERING SPECTROSCOPY

2.1 HISTORY

The earliest experiments which are regarded as involving surface analysis by the application of ion bombardment are credited to Rubin[1] who used 1.5-2.0 MeV protons to analyse metal surfaces. This technique was extended by Davies *et al.*[2] and Bogh[3] by incorporating ion channelling at energies of 0.4-2.0 MeV to improve the sensitivity by reducing the yield from the bulk. Further refinements[4] have improved the depth resolution of this technique but it still has not reached the stage where it can isolate the surface atomic layer component of a depth profile.

Brunnée[5] in 1957 found that 0.4-4.0 keV alkali ions scattered off a molybdenum surface had a maximum energy equivalent to that predicted by classical binary collision theory. Similar results were obtained by Panin[6] for 10-100 keV ion scattering and by Datz and Snoek[7] for 40-80 keV Ar^+ scattering off metals. In some of the medium energy experiments, charged recoil target atoms have been detected. These are target atoms which, during a binary collision with an energetic incident ion, receive an energy in excess of the surface binding energy and escape the solid in a charged state.

In 1967 Smith[8] investigated 0.5-3.0 keV ion scattering (He^+, Ne^+, Ar^+) off Mo and Ni surfaces and confirmed the validity of the binary collision assumption. It was also shown that approximately a monolayer of adsorbed gas was sufficient to prevent the detection of ion scattering from the metal surface, thus emphasizing the surface sensitivity of this technique as well as the need to maintain clean surfaces in similar experimental studies.

There is no single review available which adequately covers all aspects of Ion Scattering Spectroscopy (ISS). There do exist a number of commendable accounts of the various aspects. The early work has been reviewed by Kaminsky,[9] Smith[8] and Arifov[10] while two reviews by Suurmeijer *et al.*[11,12] cover the background as well as the basic requirements for experimental conditions. Reviews by Boers,[13] Baun,[14] Heiland and Taglauer[15,17] as well as a book edited by Tolk *et al.*[16] cover the more recent advances. As medium energy ion-surface interaction is similar to low energy ion scattering, the comprehensive reviews by Mashkova and Molchanov[18-20] on medium energy ion scattering are useful for a description of the history and the variety of possible scattering processes. To view the purpose and scope of ISS in a wider context, the general reviews of ion bombardment of solids[21-23] are recommended.

2.2 GAS PHASE COLLISIONS

The scattering of energetic ions from solid surfaces has much in common with gas phase collision studies. Where the binary collision assumption is valid in ISS studies, the target atom is treated as an unbound atom for the duration of the collision event, which is identical to scattering off a gas atom. Gas phase studies are important as they provide information concerning the collision process without the complications of multiple collisions and interface electronic structure encountered in ISS. Gas phase collision studies have investigated the importance of collisional inelastic energy losses and the mechanisms of collisional charge exchange. The oscillatory charge exchange cross section, only recently discovered for ISS, has been known to exist in gas phase collisions for a long time. Differential scattering cross section measurements have been used to determine the interatomic potential for a range of elements (see Chapter Four).

2.3 THE BINARY COLLISION EVENT

The collision sequence for an energetic particle of mass M_1,

energy E_0 and initial velocity v_0 scattered off a target atom of mass M_2, initially at rest, is illustrated in figure 2.1. The conservation of energy and momentum yield the following equations:

$$\frac{E_1}{E_0} = \left(\frac{\cos\theta + \sqrt{\mu^2 - \sin^2\theta}}{1 + \mu} \right)^2 , \qquad \mu = \frac{M_2}{M_1} > 1 \qquad\qquad 2.1$$

or

$$\frac{E_1}{E_0} = \left(\frac{\cos\theta \pm \sqrt{\mu^2 - \sin^2\theta}}{1 + \mu} \right)^2 , \qquad \mu < 1 \qquad\qquad 2.2$$

and

$$\frac{E_2}{E_0} = \frac{4\mu\,\cos^2\phi}{(1 + \mu)^2} . \qquad\qquad 2.3$$

In equation 2.2 there are two possible final energies for an incident particle scattered through an angle θ, but this angle is limited by the condition:

$$\theta_l < \sin^{-1}\mu . \qquad\qquad 2.4$$

Experimental observation of a peak corresponding to the lower energy has not been reported because it has a lower cross section.

The recoil angle is limited by the condition:

$$\phi \leqslant 90° . \qquad\qquad 2.5$$

From these equations the mass of the target atoms can be deduced from the initial and final energies of the incident particle, the scattering angle and the incident particle mass. This is the basis of surface compositional analysis in ISS. Deviations from the predicted values of E_1 and E_2 are attributed to inelastic collisional processes[24-27] (e.g. electron excitation, etc.). Inclusion of this loss, Q, in equations 2.1 and 2.3 yield the following expressions:

$$\frac{E_1}{E_0} = \left(\frac{\cos\theta + \sqrt{\mu^2 - \sin^2\theta - \mu(1 + \mu)\frac{Q}{E_0}}}{1 + \mu} \right)^2 , \qquad\qquad 2.6$$

and

$$\frac{E_2}{E_0} = \mu\left(\frac{\cos\phi + \sqrt{\cos^2\phi - \frac{1 + \mu}{\mu}\frac{Q}{E_0}}}{1 + \mu} \right)^2 . \qquad\qquad 2.7$$
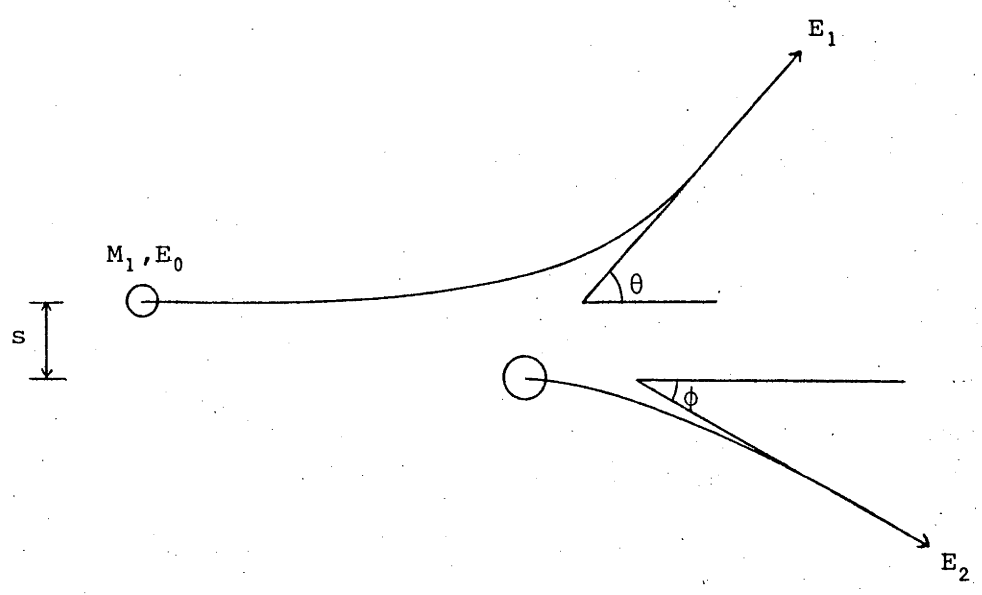
Fig. 2.1: Scattering sequence for an energetic particle off a target, initially stationary, in the laboratory frame of reference.
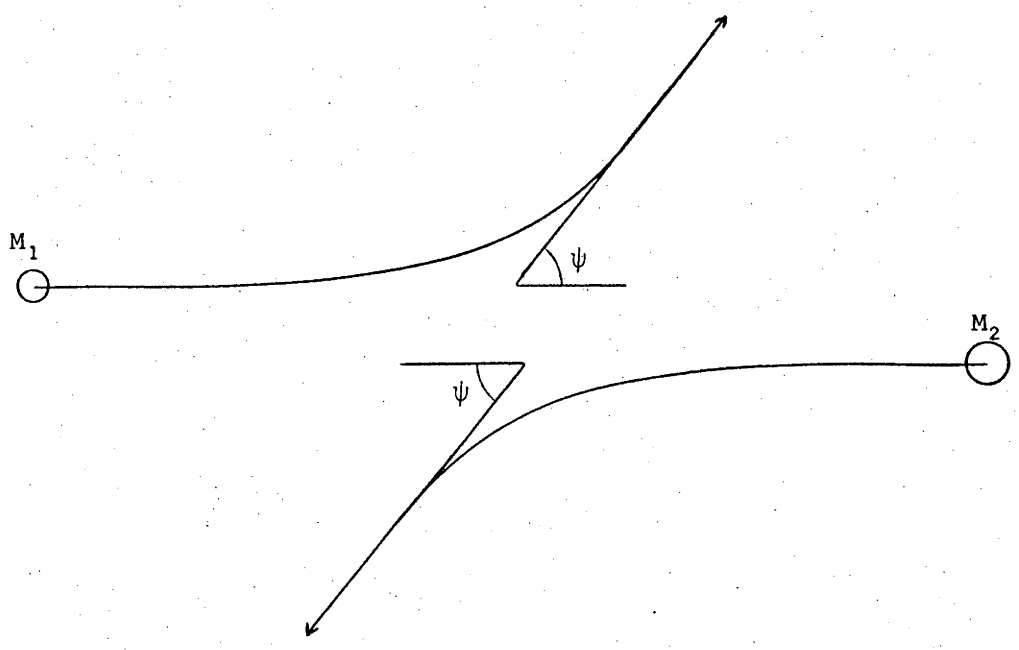
Fig. 2.2: Scattering sequence in the centre of mass frame of reference.

The probability that the incident particle will be scattered through an angle θ is proportional to the cross section for scattering. This is a function of the masses of the two particles, their initial energies and the magnitude and form of the interatomic force. For all energies discussed in this work, the incident energy is sufficiently large ($\gg 1 \, eV$) to allow the attractive component of the interatomic force to be ignored. The algebraic representation of this force is still largely in doubt but for the following equations it is only necessary to assume that it is a function of the interatomic separation, r.

The force, $F(r)$, can be obtained by derivation of the more commonly used quantity; the interatomic potential, $V(r)$,

$$F(r) = - \frac{dV(r)}{dr} .$$
2.8

The collision sequence in the centre of mass frame of reference is illustrated in figure 2.2. For an elastic collision the scattering angle ψ is given by[28]

$$\psi = \pi - 2s \int_{R_0}^{\infty} \frac{dr}{r^2 \sqrt{1 - \frac{s^2}{r^2} - \frac{V(r)}{E_R}}} ,$$
2.9

where

$$E_R = \frac{\mu \, E_0}{1 + \mu} .$$
2.10

s is the impact parameter (see figure 2.2), and the distance of closest approach, R_0, satisfies the condition:

$$1 - \frac{s^2}{R_0^2} - \frac{V(R_0)}{E_R} = 0 ,$$
2.11

The scattering angles can be transformed to the laboratory frame of reference by the expressions:

$$\theta = \tan^{-1}\left(\frac{\mu \, \sin\psi}{1 + \mu \, \cos\psi}\right) ,$$
2.12

and

$$\phi = \frac{\pi}{2} - \frac{\psi}{2} .$$
2.13

The number of particles scattered through an angle between θ and $\theta + d\theta$, $N(\theta)$, is given by:

$$N(\theta) = n.N_0.\sigma(\theta) ,$$ 2.14

where n is the number of incident particles per unit area. N_0 is the number of scattering centres, and $\sigma(\theta)$ is the scattering cross section which, from figure 2.3, is given by:

$$\sigma(\theta) = 2\pi\,s\,ds .$$ 2.15
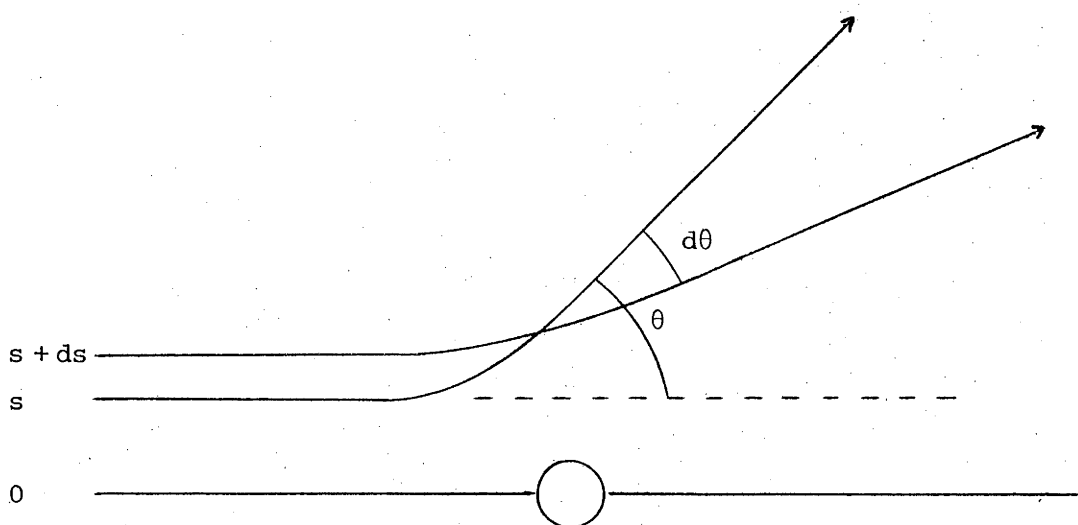
Fig. 2.3: Illustration of the definition of the scattering cross section for angles between θ and $\theta - d\theta$.

As θ is related to the impact parameter, s, by equations 2.9 and 2.12, the cross section is also a function of the initial energy.

2.4 ION SCATTERING SPECTROSCOPY

The early studies of ion scattering from solid surfaces[7,8] led to the simple gas model to describe the collision event. This model treats the target atom as a free particle, unaffected by bonds with neighbouring atoms for the duration of the collision event, analogous to the freedom experienced by gas atoms. The justification for this model relies on the time for the collision ($\sim 10^{-15}$ secs) being much less than the lattice vibration period ($\sim 10^{-13}$ secs). This ensures that the coupling between the target atom and its neighbours does not

affect the collision kinetics and therefore the scattering can be treated as a simple two-body collision.

If the energy of the incident particle is reduced sufficiently so that these assumptions are no longer valid then it is expected that the coupling between the target atom and its neighbours will become significant and that the incident particle will be effectively colliding with more than one atom. The energy it retains will be greater than for a simple binary collision, which is analogous to colliding with a single atom of greater mass than the target atom. This greater apparent mass is called the "effective mass". As it is important to know the limit of validity for the binary collision effect, a number of experimental and theoretical studies have attempted to measure the lower energy limit for simple elastic scattering.

The calculations of 30 eV Cu atoms scattering off a one-dimensional Cu lattice by Langberg[29] using the Morse potential suggested that the effective mass was not required at these energies. However, the calculations of Gay and Harrison[30] of 25 eV to 10 keV Cu scattering off a Cu lattice using a Born-Mayer potential revealed that an effective mass was important at 25 eV. They also claimed that the binary collision approximation was not valid below several hundred eV.

The experimental investigations involved measuring E_1/E_0 as E_0 is decreased to detect an increase in this quantity above that predicted by equation 2.1. The results of Matsevich and Zyryanov[31] indicated that the limit was less than 100 eV for He off LiF, but the results presented in a review by Arifov[10] revealed that for energies below 400 eV, the effective mass was important for Li^+, Na^+ and K^+ scattering off W and Mo, and that for Cs^+ the limit was 300 eV. This is in agreement with Veksler's[31] conclusion that the effective mass for 50 eV K^+ onto Mo was twice the target atom mass, although Smith[32] suggests that this particular result may be explained by the lack of well-defined target surface conditions and that recoil K atoms which had adsorbed onto the surface were responsible for the observed peak. This criticism cannot apply to Arifov's results as the scattering

angle used was 135° which is outside the angular limit for recoils (i.e. 90°).

Smith and Goff[33] found no evidence for the effective mass phenomena for He and Ar onto Cu down to 100 eV and similarly Tongson and Cooper[34] found no deviation from the predicted value down to 40 eV for He^+ onto Cu and 20 eV for Ne^+ onto Cu.

The results of Heiland and Taglauer[35] have in general revealed excellent agreement with the predicted values of E_1/E_0 down to 200 eV but below that a range of deviations were observed. These deviations were usually small but systematic, and generally show a slight decrease in the E_1/E_0 value which is the opposite of that expected if the effective mass was increasing. For Ne^+ scattered through 95° off Ni[36] agreement with the predicted value extended down to 50 eV, but marked deviations were observed for Ar^+ off Ni below 1 keV.[37]

The limit of validity for the binary collision approximation is therefore in doubt, but this uncertainty can be partially reconciled by noting two important variables in the work mentioned so far. The results of computer simulations and theoretical calculations are strongly dependent on the form of the interatomic potential used. As there has not been general agreement on which potential is accurate, the numerical results can be expected to disagree when different potentials are used.

Care must also be taken in the interpretation of the experimental results as it has been assumed that the deviations from the predicted value of E_1/E_0 are only caused by the influence of neighbouring atoms. There is another effect which warrants consideration. This is the inelastic energy loss due to electron excitation which is believed to be proportional to velocity[38,39] for low energy ions. There is still uncertainty about the absolute value of the proportionality constant, in particular for surface scattering, but nevertheless it can be shown that the relative importance of this loss will increase with decreasing energy.

Assume that the inelastic loss rate of energy is given by the

following equation:

$$\frac{dE}{dx} = -k E^{\frac{1}{2}},$$
2.16

thus on the approach to the surface the energy loss will be:

$$\Delta E = -\beta E_0^{\frac{1}{2}},$$
2.17

where β incorporates k plus geometric factors (pathlength, etc.) and E_0 is the incident ion energy. It has been assumed that the inelastic loss has been sufficiently small to allow the particle energy to be regarded as constant over the path.

After the collision with the target atom, the energy of the ion, E_4, is given by:

$$E_4 = \gamma E_3,$$
2.18

where E_3 is the energy of the ion before the collision and γ is given by equation 2.1. On the departure from the surface, the inelastic loss will be given by:

$$\Delta E = -\beta E_4^{\frac{1}{2}}.$$
2.19

If the effective mass becomes important, then γ will increase by an amount which will be called $d\gamma$. Thus the final energy of a scattered ion will be given by:

$$E_1' = (\gamma + d\gamma) \cdot (E_0 - \beta E_0^{\frac{1}{2}}) - \beta[(\gamma + d\gamma) \cdot (E_0 - \beta E_0^{\frac{1}{2}})]^{\frac{1}{2}}$$

$$= \gamma E_0 + \{d\gamma \cdot E_0 - \beta(\gamma + d\gamma) E_0^{\frac{1}{2}} - \beta[(\gamma + d\gamma) \cdot (E_0 - \beta E_0^{\frac{1}{2}})]^{\frac{1}{2}}\}$$

$$= \gamma E_0 + dE.$$
2.20

If dE does not exceed the resolution of the energy analyser then it is possible that an effective mass can become important without it being detected experimentally. The divergence from the predicted value of E_1/E_0 will occur at an energy which depends on the relative importance of $d\gamma$ and β. These parameters will be determined by experimental conditions and the ion target combination.

It is perhaps significant that the effective mass has been observed for the scattering of alkali ions, but not for inert gas ions. As there are many effects of unknown importance involved in such experiments, no firm conclusions can be reached.

From the available information, keeping in mind the effects mentioned above, it would seem that the binary collision model is valid for incident energies certainly greater than a few hundred eV.

2.5 SURFACE COMPOSITIONAL ANALYSIS

The energy spectra of scattered inert gas ions (He^+, Ne^+, Ar^+, Kr^+) generally consist of sharp binary collision related peaks but this is not necessarily the case when reactive gas ions are used.[32] As the ionization potential of inert gas atoms is large, there is a strong probability that an inert gas ion entering a solid will be neutralized.[40] Thus, particles scattered from the bulk will be atoms and thereby escape detection by the low energy charged particle analysers. As the ionization potential for reactive gases is less than for inert gas atoms, scattering from the bulk may be observed.

The particles which are reflected from the bulk emerge from the solid with a lower energy than surface particles by virtue of elastic and inelastic losses on the path into and out of the solid. The processes of neutralization and inelastic energy loss will be described in greater detail in a later section.

The surface sensitivity of low energy ion scattering prompted a continuing interest in the application to surface compositional analysis.[8,32,41-46] Consider in the simplest case, a multicomponent surface. The yield of scattered ions from the "i"th component can be expressed as:[44]

$$I_i = I_0 \ N_i \ \frac{d\sigma_i}{d\Omega} \ (1 - P_N) \ T \ d\Omega \ , \qquad\qquad 2.21$$

where I_0 is the incident beam intensity,

N_i the surface atomic concentration of the "i"th component,

$\frac{d\sigma}{d\Omega}$ is the scattering cross section,

P_N is the neutralization probability,

T the transmission of the detector system, and

$d\Omega$ is the solid angle subtended by the detector system.

If some the surface atoms are "shadowed" by other elements then $N_i \, d\sigma_i/d\Omega$ in the above equation should be replaced by:

$$\left(N_i \frac{d\sigma_i}{d\Omega} - \alpha_j \, N_j \frac{d\sigma_j}{d\Omega} \right) , \quad (42,47)$$

where α_j is the shadowing factor specific for this species due to other species of surface density N_j. Using this, the ratio of yields from two components is given by:[48]

$$\frac{I_i}{I_j} = \frac{P_i}{P_j} \cdot \frac{d\sigma_i}{d\sigma_j} \cdot \frac{N_i}{N_j} \frac{1}{1 - \alpha_{ij} \cdot \frac{N_i}{N_j}} , \qquad 2.22$$

where

$$\alpha_{ij} = \alpha_i \frac{d\sigma_i}{d\sigma_j} .$$

If there is no shadowing then α_i is zero and the yield is proportional to coverage if P_i and $d\sigma_i$ are independent of coverage. Where shadowing does occur, then the proportionality only applies for low levels of coverage ($\alpha_{ij} \ll 1$).

The linear relationship between coverage and ISS yield has been observed for Au on Ni by Smith[32] and for O and S on Ni by Taglauer and Heiland.[42,48] The non-linear relationship for O and Be on W[44] was attributed to the change in neutralization probability caused by a change in the work function at the surface.

The absolute determination of surface atomic concentration is further hampered by surface microtopography which can shadow significant portions of the surface. Estimates of the importance of this effect are rarely made, however to give an idea of its significance an example by Begemann[49] taken from an electron micrograph of a Cu(110) surface bombarded with a 4 keV Ar^{+} (total dose

2×10^{15} ions/cm^2) shows that 14-17% of the surface was shadowed by microrelief.

2.6 MULTIPLE SCATTERING

Multiple scattering is the term used to describe the scattering of the incident ion by two or more target atoms and it is found to be an excellent measure of the structure of a surface. This scattering (see figure 2.4) was first reported by Mashkova *et al.*[50] in 1965. They interpreted the peak at a higher energy than the single scattering peak as due to ions suffering two "softer" (i.e. smaller angle) collisions. The energy retained by an ion which is scattered through the angles θ_1 and θ_2 in separate collisions is given by the following equation and in most cases is greater than that retained by an ion scattered through the same total angle by a single collision:

$$\frac{E_1}{E_0} = [\cos\theta_1 + (\mu^2 - \sin^2\theta_1)^{\frac{1}{2}}]^2 \cdot [\cos\theta_2 + (\mu^2 - \sin^2\theta_2)^{\frac{1}{2}}]^2 \cdot (1+\mu)^{-4} . \quad 2.23$$

Considerable effort has been devoted to the experimental examination of the double scattering phenomena to assess its possible applications.[10,13,19,42,49,51,52] Much of the early work concentrated on verifying the relationship proposed for the ratio of the intensities of the single scattering to the double scattering peak:[53]

$$\frac{I_2}{I_1} \propto \frac{Z_1 Z_2}{d^2 \, E_0 \, \theta^{5/2}} , \quad 2.24$$

where Z_1 and Z_2 are the atomic numbers of the ion and atom respectively, d is the interatomic spacing, θ is the total scattering angle and E_0 is the incident ion energy. Most of the investigations confirmed the dependencies given by equation 2.24[54-59] but under some experimental conditions, the ratio of intensities was found to be roughly proportional to energy.[60-62] The discrepancies may evolve from the use of the two atom model instead of considering an infinite atomic row (called the chain model) and also by disregarding charge exchange processes. Equation 2.24 was derived using the inverse square potential which probably best describes the interatomic
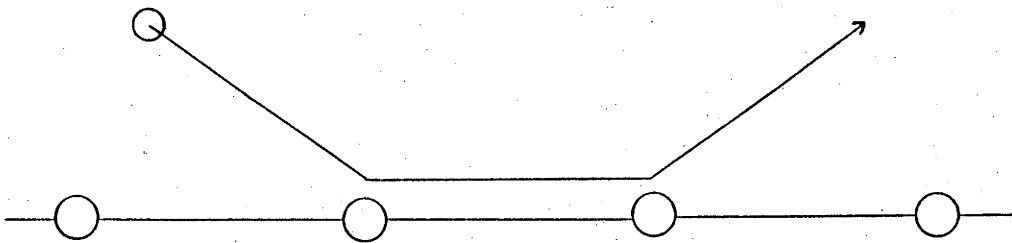
Fig. 2.4: The low angle double collision event.
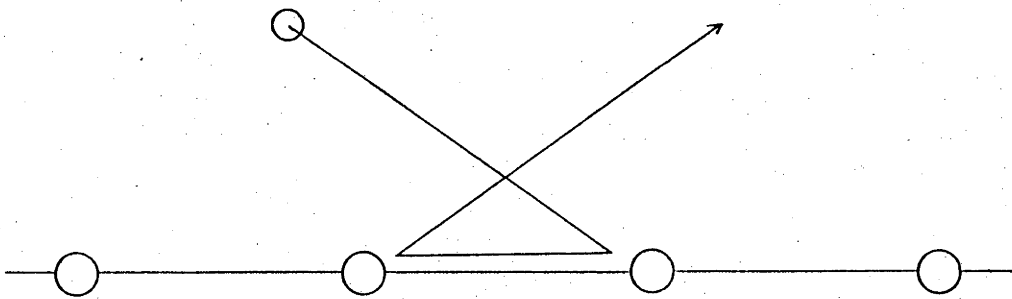
Fig. 2.5: The large angle double collision event.

potential in the medium energy region, but it is not applicable for low energy scattering. For this reason the above expression must be used with care for low energy scattering where it is most useful as a guide to predicting general trends only.

Another double collision process with the two atom model, involving two large angle collisions (see fig. 2.5), was predicted by computer simulations reported by Pryde et al.[63] As the cross section for a process involving two large angle scattering events is small, it has not yet been experimentally verified. The two large angle collisions reduce the final energy of the ion to well below that for single scattering.

Mashkova et al.[64] have shown that the double scattering peak may have a number of contributions from double collisions out of the plane defined by the incident beam and the analyser direction, i.e. scattering to an adjacent row or a lattice site below the surface. At lower energies this process is not usually considered as it is assumed that the longer time spent near the target surface will increase the neutralization probability of low energy ions. It will be shown in the presentation of the results of this investigation (Chapter Six) that this assumption is not strictly correct, and that under some experimental conditions, significant yields are believed to be attributable to these scattering events.

For a more complete description of the scattering of ions from a surface, the "chain model", proposed by Kivrilis et al.[65] has been adopted (see figure 2.6) and although the energy spectra predicted by this model are similar to those predicted by the two atom model, differences occur when the angle of incidence is reduced relative to the crystal surface.

In the chain model the process of single scattering no longer strictly applies. The projectile which is regarded as the singly scattered particle is the one which is strongly scattered by one atom, and it is weakly deflected by its neighbours (sometimes referred to as "quasi-single scattering"). Similarly the projectile which suffers roughly equal deflections by two atoms, although also weakly scattered
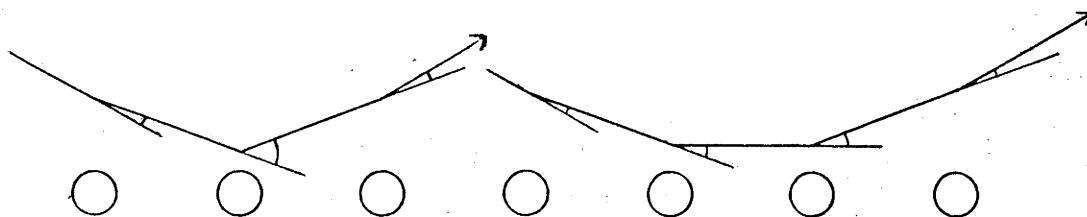
Fig. 2.6: "Quasi-Single" (left) and "Quasi-Double" (right) scattering from an atomic chain.

by their neighbours, is referred to as the doubly scattered particle ("quasi-double scattering"). These two scattering sequences are illustrated in figure 2.6.

These definitions become less precise as the angle of incidence is reduced. Take for example the case for single and double scattering of ions through a constant total scattering angle so that it is appropriate for the experimental conditions used in this investigation.

As the angle of incidence is reduced the single scattering particle passes closer to the atom preceding the one from which it is strongly scattered. The particle will be weakly deflected by the preceding atom and as it has suffered two collisions instead of one through the same total scattering angle, its final energy will be greater. As the angle of incidence decreases further, the scattering off the preceding atoms becomes stronger, until the particle is deflected past, instead of at, the second atom, indicating that the second atom is shielded by the first. When this occurs the projectile cannot be deflected sufficiently by the second atom to be scattered through the required total scattering angle.

For double scattering, the deflection angle for the first collision must be such that it ensures that the scattered ion is directed along the surface to collide with the second atom. Therefore, as the angle of incidence is reduced, the deflection angle for the first collision is reduced and the final energy of the doubly scattered particle is reduced. A small angle and a large angle

scattering sequence results in a lower final energy than two equal angle collisions through the same total scattering angle. As the angle of incidence is reduced further, the same limit as for single scattering is reached. After the first collision, the scattered particle is directed past, and not at the second atom which means that no scattering is possible through the fixed total scattering angle. The angle at which this limit is reached is the critical angle of incidence (not directly related to the critical angle for channelling). As the angle of incidence is reduced towards the critical angle the final energy of the doubly scattered particles decreases and for the singly scattered particles it increases. At the critical angle the two scattering sequences are identical, so that the final energies for the two are equal.

For angles of incidence below the critical angle the chain model predicts that no scattering can occur through the fixed total scattering angle because neighbouring atoms in the chain shield the ion from having a hard enough collision with a chain atom to scatter it through a large angle. Measurement of the scattering yields at angles of incidence below the critical angle is attributed to surface defects and the influence of thermal vibrations in producing an imperfect chain. The yield at angles below the critical angle can be as high as 50% of that measured under specular conditions. [66]

The critical angle is dependent on the atomic species used (Z_1, Z_2), the energy of the incident ion, the interatomic spacing in the chain, the total scattering angle and the target temperature. The critical angle, measured to the target surface, decreases with decreasing atomic number, or an increase in any one of the other parameters. The thermal vibrations affect the critical angle by creating a range of angles of incidence on an atomic scale for a parallel ion beam (fig. 2.7).

The critical angle of incidence predicted by computer simulation has been found to be dependent on the form of the interatomic potential used [51,52,67] and if all the other factors mentioned above are adequately incorporated in the simulation then the comparison of experimentally measured critical angles to simulation results will
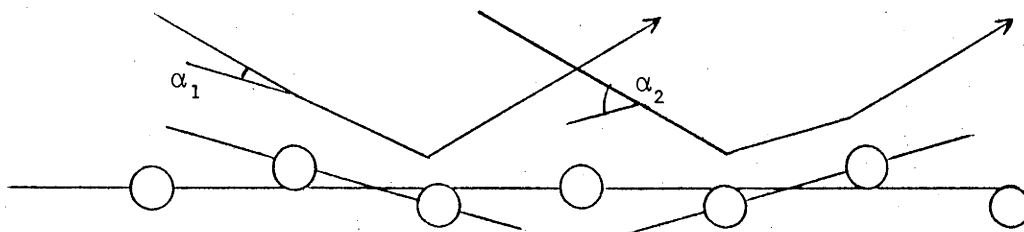
Fig. 2.7: The effect of thermal vibrations of chain atoms on the effective angle of incidence.

allow estimates of the interatomic potential to be made. Reports of such measurements have been made by Heiland *et al.*[52] and Poelsema *et al.*[68] The former report must be treated with caution because although the effects of thermal vibrations are emphasized, these effects do not seem to have been taken into account in the simulations which predict the critical angle.

The effect of surface defects has been investigated by Begemann and Boers,[49] and steps and vacancies in atomic chains were identified. The study of defects, although a complex problem, is necessary before an understanding of the effect they have on quantitative analysis is possible. The greatest experimental difficulty is the maintenance of a clean, damage free surface for the duration of the experiments. Begemann and Boers used vacuum deposition of Cu on a Cu substrate and vacuum cleaving of NaCl to achieve clean surfaces of these targets, and a low current density to minimize bombardment induced damage. Further investigations would prove useful if measurements could be made of the defect density as this would then indicate whether the chain model is justified on a real surface suffering ion bombardment.

Although the chain model can successfully explain most of the effects observed for the scattering of ions in aligned directions, additional chains must be included to explain the zig-zag collisions observed by Begemann and Boers[49] and the wedge focusing effect reported by Skripka.[69]

The observation of zig-zag collisions (i.e. a double collision

where the second atom involved is in an adjacent atomic chain) is important as it means that the popular assumption that the neutralization probability is sufficiently high for the longer path length in the surface region is invalid and ions experiencing zig-zag collisions may affect measurements of critical angles and single to double scattering yield ratios.

To model zig-zag collisions, parallel chains of surface atoms are used. Where the chains of the second layer lie between the surface chains, they too must be included as they are responsible for wedge focusing or "surface semi-channelling".[69,70] In this case, ions passing between surface atomic chains are "focused"[71,72] onto the underlying chains and after scattering they are focused again on the way out. The yield in a wedge focusing direction should be more than double that obtained in any other direction, however the greater time spent in the surface will increase the neutralization probability so that the measured yield may be greatly reduced from that expected.

It is possible to use the surface wedge to determine the importance of the inelastic energy loss in the surface region.[128] As mentioned previously the inelastic stopping power is believed to be velocity dependent:[38,39]

$$\frac{d\varepsilon}{d\rho} = k \, \varepsilon^{\frac{1}{2}} ,$$ 2.25

where

$$\varepsilon = \frac{a \, M_2 \, E}{Z_1 Z_2 \, e^2 (M_1 + M_2)} ,$$ 2.26

$$\rho = \frac{4\pi \, a^2 \, M_1 M_2 \, Nx}{(M_1 + M_2)^2} ,$$ 2.27

$$a = 0.88534 \cdot a_0 \cdot (Z_1^{\frac{1}{2}} + Z_2^{\frac{1}{2}})^{-2/3} ,$$ 2.28

and where E is the projectile energy, x is the distance, a_0 the Bohr radius and N is the target atomic density.

The ions scattered from the second layer will have travelled an additional distance, $d\ell$, inside the surface (see fig. 2.8):
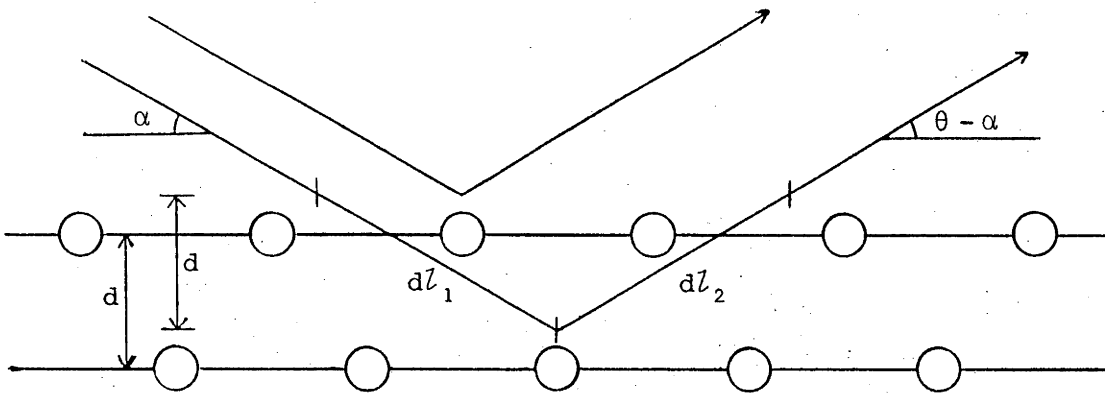
Fig. 2.8: Illustration of the added path length $(dl_1 + dl_2)$ traversed by an ion scattered off the second layer.

$$dl = \frac{d}{\sin\alpha} + \frac{d}{\sin(\theta - \alpha)} , \qquad 2.29$$

where α is the angle of incidence, d is the depth of the wedge and θ is the total scattering angle.

For the incoming path, the additional energy loss suffered by the ion scattered off the second layer is given by:

$$d\varepsilon_1 = \int_0^{\frac{d}{\sin\alpha}} k \, \varepsilon^{\frac{1}{2}} \, d\rho . \qquad 2.30$$

Assuming that $d\varepsilon_1$ is small compared to ε_0, the initial energy, then $\varepsilon^{\frac{1}{2}}$ may be treated as a constant which simplifies the expression shown above to:

$$d\varepsilon_1 = \frac{k \, \varepsilon_0^{\frac{1}{2}} \, d}{\sin\alpha} . \qquad 2.31$$

After the collision (from equation 2.1), the energy is given by:

$$\varepsilon_1 = \gamma \, \varepsilon_0 . \qquad 2.32$$

Making the same assumption as before, the energy loss is given by:

$$d\varepsilon_2 = \frac{k \, \gamma^{\frac{1}{2}} \, \varepsilon_0^{\frac{1}{2}} \, d}{\sin(\theta - \alpha)} . \qquad 2.33$$

Thus the total additional inelastic energy loss is given by:

$$d\varepsilon = k \; \varepsilon_0^{\frac{1}{2}} \; d\left(\frac{1}{\sin\alpha} + \frac{\gamma^{\frac{1}{2}}}{\sin(\theta - \alpha)}\right) .$$ 2.34

Comparison of the energy spectra in the wedge focusing direction to that in any other direction then allows the coefficient, k, to be evaluated. The results of these measurements will be reported in Chapter Six.

The ions scattered from the surface layer also lose energy by inelastic processes but the analysis of this process is much more complex as the electron density in the surface region is not uniform and there is insufficient information available on its distribution.

In addition to losses from simple collisions with electrons, inelastic losses may result from charge exchange processes or the excitation of bound electrons in the incident particle or the target atom. One such process has been proposed to explain the decreasing E_1/E_0 ratio as a function of decreasing E_0 for Ne scattered off Ag. The inelastic component was attributed to the excitation of Ne to an autoionizing state: [15]

$Ne^+ + Surface \rightarrow Ne^0 + e^-$ (Auger neutralization into ground state)

$Ne^0 + Ag \rightarrow Ne^{**} + Ag - Q$ (excitation)

$Ne^{**} \rightarrow Ne^+ + e^-$ (autoionization) .
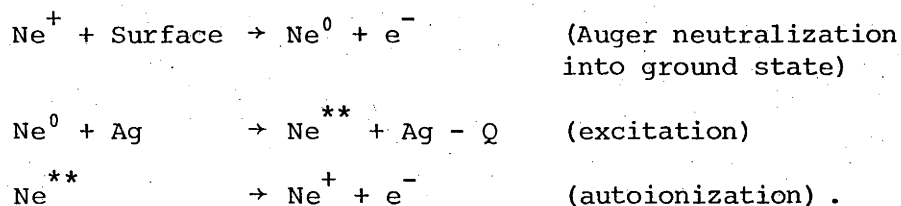
The measured energy deficit, Q, was 45 ± 5 eV, and was found to be independent of incident ion energy and scattering angle.

It is believed that collisional excitation is more important in double scattering than for single scattering, as the ion, if excited in the first collision, is unlikely to de-excite before the second collision ($\sim 10^{-15}$ secs), in which it may be excited to an even higher energy level. Thus the probability for ionization or radiative decay could be greater for multiply scattered particles, however there is no experimental evidence to substantiate such a process to date.

2.7 CHARGE EXCHANGE

As most energy analysers in the low energy range are charge particle detectors, it is important to know what effect the neutralization processes have on quantitative and qualitative analysis of experimental results. Measurements of the charge fraction of particles scattered off solid surfaces reveal that it is a strong function of energy. Some of the experimental charge fraction results are listed in table 2.1.

Table 2.1

Projectile	Target	Energy (keV)	Charge Fraction	Reference
H	Cu, Si	25	0.40	Buck *et al.* [73]
H	Cu, Si	160	0.90	"
He	Cu, Si	30	0.10	"
He	Cu, Si	150	0.58	"
Ar	Au	4	0.0	Buck *et al.* [74]
Ar	Au	26	0.20	"
He	Cu	2	0.007	Verhey *et al.* [75]
He	Cu	10	0.024	"

This neutralization must be accounted for in any measurement of surface atomic concentration, but also important is the effect of surface contaminants or submonolayer coatings and the variation of the surface electron band structure on the neutralization processes and rates.

The qualitative analysis of energy spectra also relies on a knowledge of the neutralization process as is illustrated by the comparison of ion and neutral spectra obtained by Chicherov. [76] A charge exchange cell was used to ionize the neutral component of 16 keV Ar scattered off polycrystalline Cu and 9 keV Ar scattered off the Cu(100) face. Although the energy spectra of the neutral atoms were similar to those of the ions, the peak positions were shifted and the relative intensity of the single to double scattering was reduced.

Similar experiments by Eckstein and Verbeek[77] using 2 keV He scattered off Ni reveal that the energy spectra of the ions consist of a single peak. However the energy spectrum of the neutrals consists of a single peak plus a considerable yield at lower energies which is considered to be from scattering off subsurface atomic layers.

Hagstrum[78] has identified four basic electronic transitions involving ions and atoms near a surface but only the first three have a major influence on ISS studies as they affect the charge state.

Electron Exchange Processes

(1) Resonance Neutralization of an Ion

(2) Resonance Ionization of an Atom

(3) Auger Neutralization of an Ion

(4) Auger De-excitation of an Excited Atom

This list could be expanded to include two and three electron processes[79] but these are believed to be far less probable to occur in the short time the particle spends in the surface region.

More recent studies[80] have drawn attention to the quasi-resonant transition which, together with the first three processes listed above, is illustrated in figure 2.9.

The theoretical analysis of these processes is complex and comparison to experiment is difficult, but in general it is believed that the resonance process will dominate where it is energetically possible as its transition rate is much higher. Shekhter,[81] and Cobas and Lamb[82] derived similar expressions for the transition rate, $R(s)$, for a process between a particle and a surface separated by a distance s:

$$R(s) = A \exp(-as) , \qquad 2.35$$

where A and a are characteristic constants for the process; examples of which are given in table 2.2.

The Auger process has been used to explain the neutralization of ions with an energy of less than 100 eV[83] but the validity of this
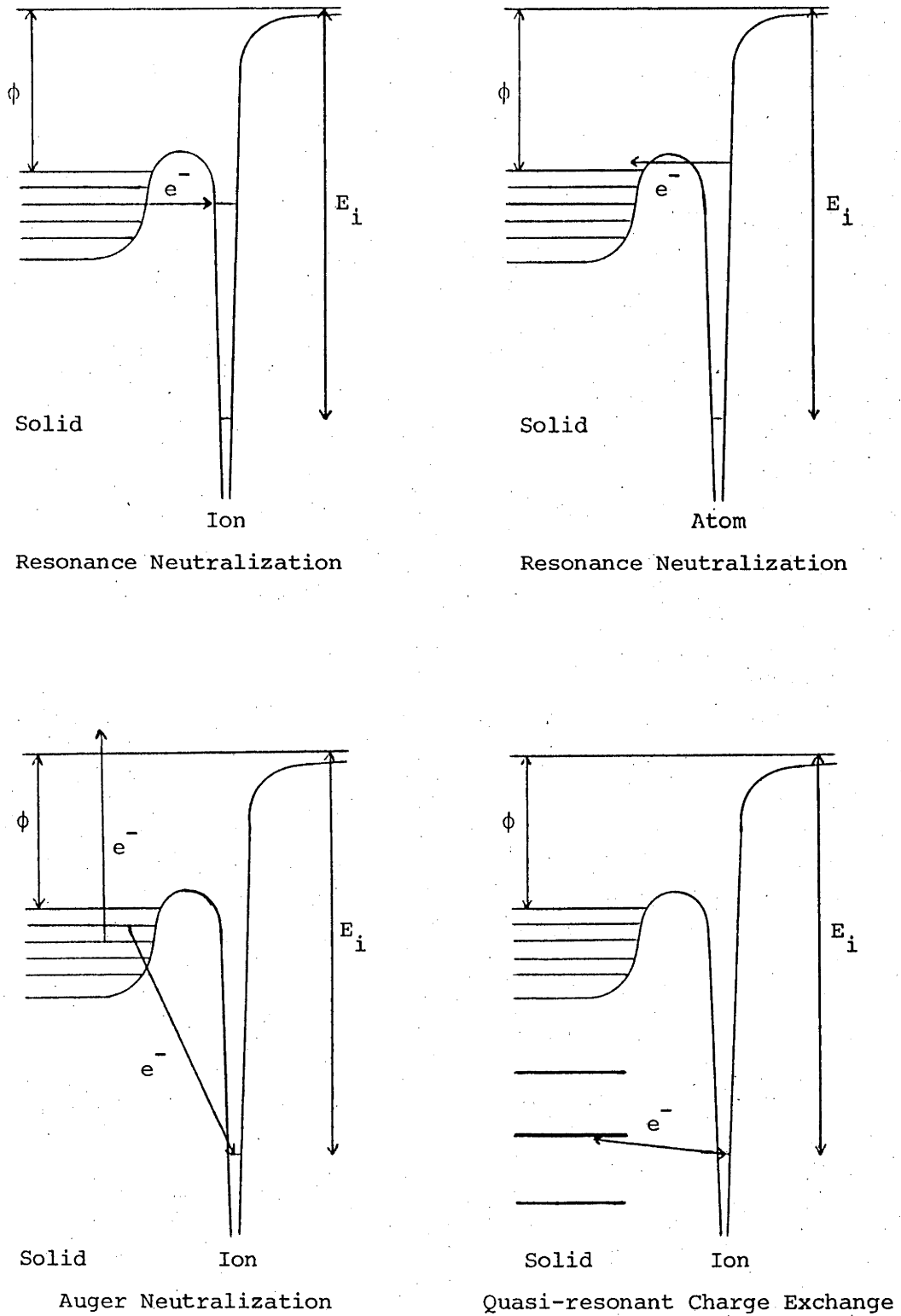
Fig. 2.9: The principal charge exchange processes for inert gas atoms and ions. The work function of the solid is ϕ and the ionization energy of the inert gas atom is E_i.

Table 2.2

Theoretical Transition Rate Parameters

Reference	Auger Neutralization		Auger De-excitation		Resonance Processes	
	A (sec^{-1})	a (cm^{-1})	A (sec^{-1})	a (cm^{-1})	A (sec^{-1})	a (cm^{-1})
Shekhter (81)	6.35×10^{14}	3.9×10^{10}			5.74×10^{19}	3.2×10^{10}
Cobas & Lamb (82)			9.6×10^{16}	7.3×10^{10}	9.1×10^{18}	1.9×10^{10}

model is in doubt at higher energies as many of the assumptions upon which the model is based no longer hold. Nevertheless, a number of authors[51,67,75,84-86] have shown that "Auger-like" transitions can adequately explain the neutralization of keV ions near solid surfaces.

The probability that an ion will escape the solid without being neutralized is given by:[87]

$$P^+ = \exp\left(-\frac{v_c}{v_\perp}\right) ,$$ 2.36

where v_c is characteristic of the ion-atom combination and $v_\perp$ is the component of the velocity of the ion perpendicular to the surface.

The different transition rates, A, and characteristic distances, a, for Auger and resonance processes will give different characteristic velocities. These are believed to be about 10^5 m/sec for Auger transitions and 10^7 m/sec or more for resonance transitions. To illustrate the effect this difference would have on an ion yield, consider an 8 keV Ar^+ ion leaving the surface at an angle of 30° (measured to the surface) where $v_\perp$ is approximately 10^5 m/sec:

$$P^+(\text{Auger}) \doteq \exp(-1)$$
$$\doteq 0.368 ,$$ 2.37

and

$$P^+(\text{Resonance}) \doteq \exp(-100)$$
$$\doteq 10^{-43} .$$ 2.38

It is clear from this example that if the resonance process does occur then it competes with another ionization process, otherwise no charged particles would be observed.

The quasi-resonant charge exchange process has been used to explain the oscillatory ion yield as a function of energy. Although similar oscillations have been observed in gas collision studies for some time,[88-90] it was only recently observed for ISS.[80] These oscillations in yield have been observed for He^+ scattering off solids which have energy levels (3d, 4d, 5d) within about 10 eV of the He

ground state, as well as for Ne$^+$ off Au and Ga.[91,92] Brongersma and Buck[84] report that the existence of this energy difference is not a sufficient condition for oscillatory yields.

Details of the quasi-resonance model have been presented by a number of authors[90,93,94] and it is from these that the following explanation is derived.

During a collision the incident ion (typically He$^+$) and the target atom, denoted here by X, form a quasimolecule which modifies the atomic electron energy levels. The model assumes that there is a mixing of the He$^+$ - X states and the He - X$^+$ states at some distance R_m (see fig. 2.10) and that during the collision a differential phase, $d\phi$ (given by the following equations 2.41 and 2.42), develops between the two electronic energy levels on the incoming and outgoing stages. The intensities of the scattered ions, I_+, and neutral atoms, I_0, are determined by the total accumulation of differential phase:

$$I_+ = \alpha_+ + \beta \cos^2\left(\frac{d\phi}{2}\right) , \qquad 2.39$$

and

$$I_0 = \alpha_0 + \beta \sin^2\left(\frac{d\phi}{2}\right) , \qquad 2.40$$

where α_+, α_0 and β are slowly varying functions of ion energy which include damping effects due to other neutralization processes and the finite width of the surface d level[93] involved in this transition. The ion intensity will be a maximum when $d\phi$ is an integral multiple of 2π, and $d\phi$ is given by the following expressions:

$$d\phi = \frac{2}{\hbar} \int_{R_m}^{R_0} \Delta E(t) \, dt , \qquad 2.41$$

or

$$d\phi = \frac{2}{\hbar} \int_{R_m}^{R_0} \frac{\Delta E(r)}{v(r)} \, dr , \qquad 2.42$$

where R_0 is the distance of closest approach, $v(r)$ is the velocity of approach of the two nuclei and $\Delta E(r)$ is the energy difference between
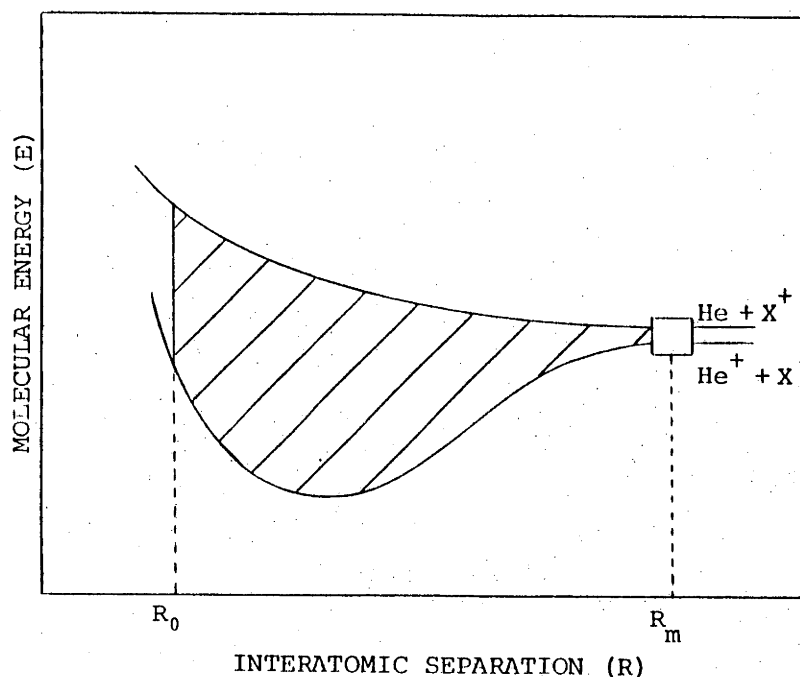
Fig. 2.10: Energy levels of two quasi-molecular states which mixed at a separation R_m (from ref. 94).

the two levels at separation r.

For high energies and small scattering angles where v(r) is nearly constant, equation 2.42 can be simplified to give:

$$d\phi = \frac{2}{\hbar v} \int_{R_0}^{R_m} \Delta E(r) \; dr$$

$$= \frac{2}{\hbar v} \cdot \langle Er \rangle .$$ 2.43

Thus the peaks in the oscillations should be equally spaced when plotted as a function of v^{-1} and this has been experimentally verified.[93]

For a more accurate estimation of the accumulated differential phase, the velocity change must be included and this then gives the following expression:

$$d\phi = \frac{2m}{\hbar} \int_{R_m}^{R_0} \frac{\Delta E(r) \; dr}{\left[2m(E - V(r)) - \frac{L^2}{r^2} \right]^{\frac{1}{2}}} ,$$ 2.44

where V(r) is the interatomic potential, E the initial energy, L is the angular momentum and m is given by:

$$m = \frac{m_1 \cdot m_2}{m_1 + m_2} .$$

2.45

To properly calculate the differential phase this way, the magnitude of the level splitting, $\Delta E(r)$, must be known, as well as the mixing separation R_m. These can only be determined by the calculation of quasi-molecular energy levels which is a complex numerical problem.

Rush and Erickson[91] have identified the four different classes of energy dependent ion yield shown in figure 2.11.
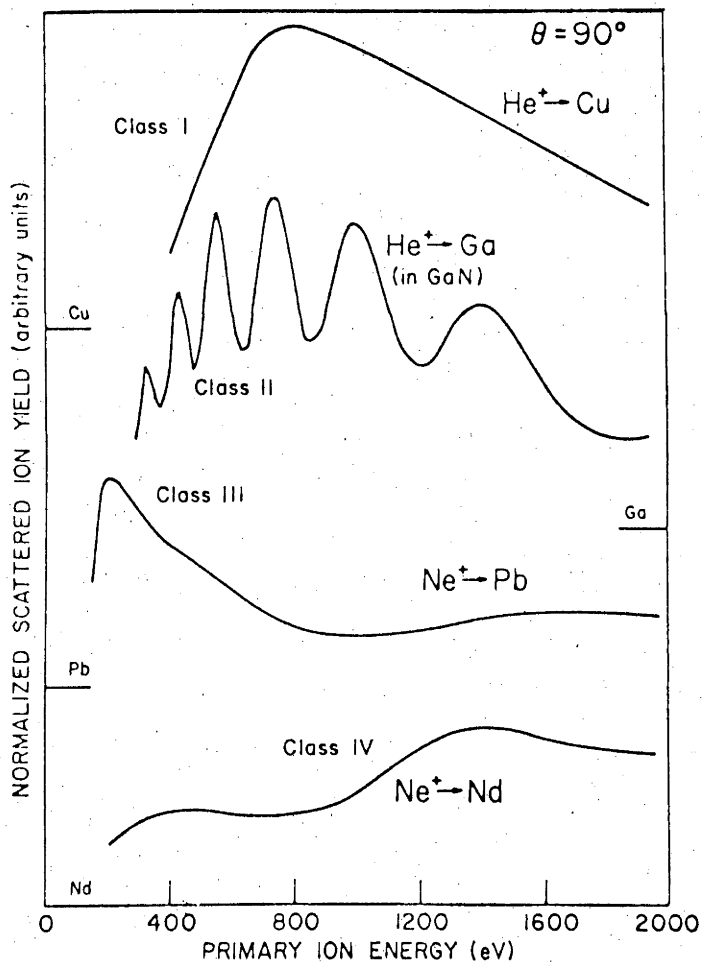
Fig. 2.11: Examples of the four classes of energy dependent ion yields (from ref. 92).

Class I is the result of an Auger-like neutralization process, class II is the quasiresonant charge exchange process, but classes III and IV have not yet been identified with known physical processes. The classes to which different ion-atom combinations belong are given in table 2.3.[93]

Table 2.3

Energy Dependent Ion Yield Classification[93]

Class	Incident Ion		
	He^+	Ne^+	Ar^+
I	Al, Si, Ni, Cu, Zn, Zr, Nb, Pd, Ag, Cd, Ta, Au	Zn, Sb, Te, W	
II	Ga, Ge, As, In, Sn, Sb, Tl, Pb, Bi	Ga	
III		Si, S, Ni, Cu, Ge, Pd, Ag, In, Sn, Hf, Pt, Au, Pb	In, Tl, Pb
IV	S, Te, Sc, La, Ce, Nd, Sm, Gd, Dy, Er, Yb, Hf	Cd, La, Ce, Nd, Sm, Gd, Dy, Er, Yb, Tl	Cu, Ge, Pd, Ag, Cd, Sn, Sb, Te, La, Ce, Nd, Sm, Gd, Dy, Er, Yb, Hf, Pt, Au

The existence of two classes of energy dependent ion yields which cannot be fitted into existing theories of charge exchange is proof of the need for more research to be undertaken in this field.

2.8 EXPERIMENTAL TECHNIQUES FOR THE MEASUREMENT OF THE CHARACTERISTIC VELOCITY FOR NEUTRALIZATION

In the cases where an Auger-like transition occurs it is possible to measure the characteristic velocity in the neutralization expression (from equation 2.36) as well as the collisional neutralization and ionization probabilities.[75,84-86,95,96] There are a number of techniques available, but essentially they involve

measurement of the ion yield as a function of some other parameter
(e.g. angle of incidence, total scattering angle, incident energy)
which effectively alters the perpendicular component of the velocity
to the surface, $v_\perp$.

The technique used by Brongersma and Buck[84] was to measure the
ion yield as a function of incident ion energy assuming that the cross
section for the scattering of ions, σ^+, is given by:

$$\sigma^+ = \sigma \, P^+ , \qquad\qquad\qquad 2.46$$

where σ is the cross section for scattering of incident particles, and
P^+ is the ion fraction of the scattered particles. To determine P^+,
the scattering cross section, σ, which is a strong function of energy
and interatomic potential, must be evaluated. In general the Moliere
approximation to the Thomas-Fermi potential is used, but lack of a
complete knowledge of the interatomic potential increases the degree
of uncertainty in the results. The major error in this analysis
however comes from the collisional charge exchange process (ionization
and neutralization) which have been shown to be strongly energy
dependent.[75,85,92] The importance of these uncertainties in cross
section and collisional charge exchange is indeterminate, however it
may explain the deviations from the expected linear relationship
between $\log(\text{Yield}/\sigma)$ and v^{-1}.

Table 2.4

Measured Values of v_c

Collision Partners	Energy (keV)	v_c (m/sec)	Reference
He – Ni	0.5 – 2.5	3.7×10^5	Brongersma & Buck[84]
He – Cu	0.4 – 1.25	$(5.0 – 6.0) \times 10^4$	Bertrand *et al.*[86]
He – Cu	2.0 – 10.0	2.5×10^5	Verhey *et al.*[75]
Ne – Au	1.0 – 2.0	$(4.0 – 7.0) \times 10^5$	Brongersma & Buck[97]
Ne – Au	2.0	3.7×10^5	Brongersma *et al.*[95]

A different technique used by Brongersma *et al.* [95] and by Bertrand *et al.* [86] is to measure the ion yield as the total scattering angle is increased, but this also relies on a knowledge of the angular scattering cross section as well as analysing particles at different scattering angles which have had different distances of closest approach to the target atom. This introduces the possibility of different excitation and exchange processes. Another error may arise from the assumption of a constant number of scattering centres which may not be valid when looking at ions scattered over a range of angles from 20° to 130°, where the effects of shadowing and penetration may become important.

Bertrand *et al.* [86] also varied the angle of incidence and although the results were in better agreement with the predicted behaviour, it was found that the v_c value decreased with angle of incidence.

Brongersma *et al.* [95] initially fitted the results to the expression:

$$P^+ = \exp\left(-\frac{v_c}{v_{f\perp}}\right) , \qquad 2.47$$

where $v_{f\perp}$ is the perpendicular component of the velocity of the particle leaving the surface. As poor agreement was obtained, the expression was modified to incorporate collisional neutralization yielding the equation:

$$P^+ = \exp\left(-\left(\frac{b}{v} + a\left(\frac{1}{v_{i\perp}} + \frac{1}{v_{f\perp}}\right)\right)\right) , \qquad 2.48$$

where v is the centre of mass velocity which is used to account for collisional neutralization and $v_{i\perp}$ is added to account for neutralization before scattering. It was not explained why $v_{i\perp}$ was not incorporated in equation 2.47 for comparison with other similar studies.

The technique reported by Verhey *et al.* [85] overcomes most of these problems by only varying the angle of incidence and by

incorporating both Auger and collisional processes.

The neutralization is broken up into three separate stages involving the incoming trajectory, the collision event and the outgoing trajectory. The Auger neutralization is applied to the incoming and outgoing paths while during the collision, neutralization is considered as well as collisional ionization of those particles neutralized before the collision. A simplification of this technique uses atomic beams, but first a comment should be made about the scattering cross section.

In these experiments the total scattering angle remains constant so that to a first order approximation the scattering cross section is constant, but as a chain of atoms is involved the "quasi-single" scattering must be considered. Verhey[85] has verified by computer simulation that for small angles about the specular reflection angle, the cross section for scattering is symmetric so that it can be cancelled out by the ratio of yields either side of the specular direction. For larger total scattering angles where "single scattering" from the chain is possible, then for small angles around the specular direction, the cross section is constant.

For the scattering of N_0 incident ions, the following table (2.5) lists the charge fraction after each stage of the collision.[85]

For N_0 incident atoms the interaction is simpler, as can be gauged from table 2.6.

Thus the ion yield for an incident ion beam is given by:

$$N(\alpha) = N_0 \cdot \frac{d\sigma}{d\Omega} \cdot n \cdot \Delta\Omega \; f_2 \left[f_1 (1 - P_N) + (1 - f_1) \; P_I \right] , \qquad 2.49$$

and for an incident atomic beam:

$$N(\alpha) = N_0 \cdot \frac{d\sigma}{d\Omega} \cdot n \cdot \Delta\Omega \; f_2 \; P_I , \qquad 2.50$$

where n is the target atom density, $d\sigma/d\Omega$ is the differential cross section and $\Delta\Omega$ is the acceptance angle of the detector.

Table 2.5

Charge Fraction for Incident Ions

Stage	Ions	Atoms
Initially	N_0	0
Pre collision	$N_0 f_1$	$N_0(1-f_1)$
Post collision	$N_0[f_1(1-P_N) + (1-f_1)\,P_I]$	$N_0[f_1 P_N + (1-f_1)(1-P_I)]$
Finally	$N_0 f_2[f_1(1-P_N) + (1-f_1)\,P_I]$	$N_0(1-f_2\{f_1(1-P_N) + (1-f_1)\,P_I\})$

where $f_1 = \exp\left(-\dfrac{v_c}{v_0 \sin\alpha}\right)$,

$f_2 = \exp\left(-\dfrac{v_c}{v_1 \sin(\theta-\alpha)}\right)$,

and α is the angle of incidence measured to the surface,

θ is the total scattering angle,

P_I is the collisional ionization probability,

P_N is the collisional neutralization probability,

and v_1 is given by equation 2.1.

Table 2.6

Charge Fraction for Incident Atoms

Stage	Ions	Atoms
Initially	0	N_0
Pre collision	0	N_0
Post collision	$N_0 P_I$	$N_0(1 - P_I)$
Finally	$N_0 P_I f_2$	$N_0(1 - P_I f_2)$

The results of the atomic bombardment are relatively simple to analyse by applying the cross section assumptions made previously and by changing the variables to those given below:

$$\beta = \frac{\theta}{2},$$

and

$$\delta = |\beta - \alpha|.$$

2.51

2.52

Substituting β and δ into equation 2.50 and comparing yields at equal angles either side of the specular direction, the following expression is obtained:

$$ln\left(\frac{N(\beta - \delta)}{N(\beta + \delta)}\right) = \frac{v_c}{v_0} \frac{2 \cos\alpha \sin\delta}{\sin^2\beta - \sin^2\delta}.$$

2.53

Thus v_c can be determined from the gradient of a graph of

$$ln\left(\frac{N(\beta - \delta)}{N(\beta + \delta)}\right) \quad \text{against} \quad \frac{\sin\delta}{\sin^2\beta - \sin^2\delta}.$$

As the use of atomic beams introduces a number of technical difficulties, ion beams are more frequently used. However the method of analysis of the ion scattering results is not as straight forward as for the atomic scattering. Unless P_I and/or P_N are assumed to be negligible, the analysis of the ion yield of a scattered ion beam can only be achieved by a least squares fitting process of the results to equation 2.49 using v_c, P_I and P_N as the fitting parameters. The fitting procedure is not very sensitive to these parameters, but the

resulting values are in accord with comparable available results. The collisional ionization probability for He onto Cu increases from 0.02 at 3 keV to 0.30 at 10 keV and v_c was found to be a weak function of primary energy and is approximately 2×10^5 m/sec.[85]

This parameter fitting technique was the one used to analyse the experimental results obtained in this investigation, and the v_c, P_I and P_N values will be reported in Chapter Six.

2.9 INELASTIC ENERGY LOSS

As mentioned previously, the inelastic energy loss is that which is lost to electron excitation or collisions with electrons of the solid. The electron excitation process usually occurs during a collision with a target atom and arises because electrons can be promoted to higher energy states when energy levels cross in the quasimolecules formed during the collision event. It is believed that this form of energy loss is responsible for the 45 ± 5 eV deficit observed for 0.2-2.0 keV Ne^+ onto Ag.[35] Similar losses have been observed for gas scattering experiments and it has been shown that such losses increase in steps as a function of distance of closest approach.[98-100] Unfortunately very little is known about corresponding processes in solids as the accurate coincidence detection of scattered particle and recoil particle is not possible.

The inelastic loss has been investigated by a number of researchers since the theories of Lindhard and Scharff[101] and of Firsov et $al.$[102-104] predicted a velocity dependent loss, and most measurements have involved the channelling of medium to high energy particles. It has been found necessary to modify these theories[105,106] to take into account the different electronic structures of various ions and atoms. This structure is responsible for the oscillatory dependence of the loss rate on the incident ion atomic number.[107-110] The modified Firsov theories[105,106] have been successful in determining the loss rate by numerical methods to a reasonable degree of accuracy.

In general the loss rate is believed to be adequately described by equation 2.25 but this expression assumes a uniform electron distribution over the distance travelled by the projectile or a sufficiently long enough path to smooth out any non-uniformities which may exist. This is not applicable for an ion or atom scattered off the surface of a solid, where the electron density changes with distance from the surface. In general the process of inelastic energy loss of ions and atoms scattered off surface atomic layers is unknown and so far very little research has been directed to resolving this uncertainty. The information obtained from such research may assist in determining the electron density distribution at or near the surface.

2.10 THERMAL EFFECTS

The fact that the target atoms of a solid have a randomly directed thermal velocity at the time of collision will result in a broadening of the scattered atoms energy distribution by a quantity given by:

$$\Delta E = (E_0 \cdot E_{Th})^{\frac{1}{2}} , \qquad 2.54$$

where E_{Th} is the thermal energy and E_0 is the incident ion energy. To give an estimate of the magnitude of this broadening, a beam of 1 keV particles scattered off target atoms with a thermal energy of 0.025 eV would have an energy spectrum with a 5 eV width. Clearly, this effect must be considered when planning experiments involving high energy resolution, high temperatures or low incident energies.

As mentioned previously in this chapter, the collision time for keV ions is sufficiently short that the atomic chain may be regarded as "frozen", however due to the thermal vibrations, the "frozen" state is not necessarily a straight regularly spaced chain of atoms but one in which the atoms are displaced in the surface plane and perpendicular to it. In general, this will have the effect of "smearing out" any fine structure in energy spectra or angular distributions predicted by the chain model. This has been

demonstrated by the results of computer simulations,[52,111-114] and is especially important when it has a direct effect on other measurements, e.g. the critical angle determination as a measure of the interatomic potential (see section 2.6).

The modelling of the thermal vibrations of surface atoms is hampered by the fact that the nature and magnitude of such vibrations is different from that of the bulk, which can be regarded as a variation in the Debye temperature. The Debye temperature, θ_D, is a characteristic temperature for solids which is related to the temperature, T, and the mean square thermal vibration of lattice atoms, $\langle u^2 \rangle$, by the expression:[115,116]

$$\theta_D = \left(\frac{h^2 T}{Mk \langle u^2 \rangle} \right)^{\frac{1}{2}} , \qquad\qquad 2.55$$

where h is Planck's constant divided by 2π, k is Boltzmann's constant and M is the mass of the atom.

Calculations have shown[117,118] that the surface Debye temperature is markedly different to that of the bulk. The calculations of Jackson[118] reveal that the Debye temperature has different values along different crystallographic directions in the surface and perpendicular to it.

A technique has been developed to measure the surface Debye temperature from the results of ion scattering studies.[119-121] It has been shown that the intensity of "quasi-triple" scattering is a function of the target temperature. "Quasi-triple" scattering involves the scattering through approximately equal angles from three surface atoms which form a "pit" (see fig. 2.12). The results of computer simulations were found to be insensitive to model parameters, in particular the interatomic potential. The surface Debye temperature for Cu(100), for vibrations perpendicular to the surface, was measured to be 147 °K ± 6%. This technique has the advantage that it is sensitive to only the surface layer, the lower layers which have Debye temperatures approaching that of the bulk will not contribute to the result.
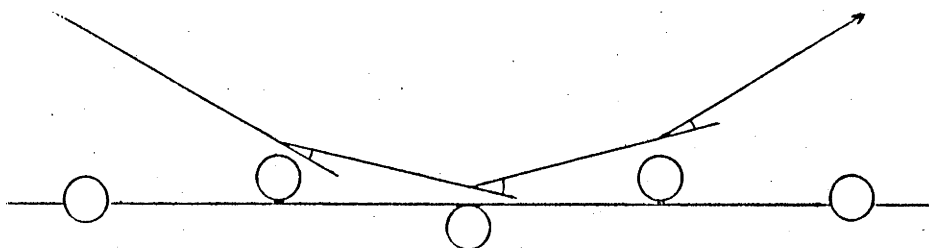
Fig. 2.12: Quasi-triple scattering from a "thermal pit" in the atomic chain.

2.11 ADSORPTION

One of the important applications of low energy ion scattering is the determination of the initial adsorption sites on single crystal surfaces. This information is important to chemists and solid state physicists who need it to determine the method of bonding, the surface electronic structure and reaction mechanisms for the processes of catalysis, electroplating and corrosion.

The sensitivity of low energy ion scattering to the determination of adsorption sites is enhanced by the "shadowing" process previously mentioned. If an adsorbed atom shadows surface atoms then a rise in the adsorbate ISS yield will be accompanied by a fall in the substrate yield. However, if there is no shadowing, the substrate yield should remain constant till the initial sites are saturated. Smith[8] first drew attention to this application when he found that for CO adsorbed on Ni, the ISS signal for O was much greater than that for C (after cross section corrections were made). It was concluded that the C bonded to the surface and was therefore shadowed by the oxygen. This interpretation was in agreement with the results of infra-red techniques and electron diffraction studies.

A recent review by Heiland and Taglauer[122] describes the application of ISS to surface structure studies and lists a number of references to the studies of O adsorption on Ni, W and Ag.[37,44,123-127] To take two examples of this work, the study of O on Ni(001) by Brongersma and Theeton[127] found that the oxygen atom was located above the surface layer of Ni atoms (0.9 ± 0.2 Å) and

between four surface Ni atoms. The studies of oxygen adsorption on Ag(110)[124] found that the ISS signal from oxygen nearly disappeared along the ⟨100⟩ direction but was detected in the ⟨110⟩ direction indicating that the oxygen atoms were adsorbed between the top ⟨110⟩ rows of Ag and slightly below the surface.

2.12 CONCLUSION

The major applications of ISS to surface analysis have been discussed but these are by no means the limit of this technique. In many of the applications mentioned the results are from preliminary investigations and are not completely proven techniques. Before these techniques can be properly researched some of the basic properties relating to charge exchange, scattering cross section, surface structure and inelastic energy loss must also be more thoroughly investigated. While these uncertainties exist, this field of science will continue to attract the interest of theoretical and experimental physicists.

REFERENCES

(1) S. Rubin, *Nucl. Inst. Methods* 5 (1959) 177.

(2) J.A. Davies, J. Denhartog, L. Eriksson and J.W. Mayer, *Can. J. Physics* 45 (1967) 4053.

(3) E. Bogh, *Can. J. Physics* 46 (1968) 653.

(4) J.S. Williams, *Ion Beam Surface Layer Analysis*, Vol. 1, p.223, eds. O. Meyer, G. Linker and F. Köppler (Plenum Press, 1976).

(5) C. Brunnée, *Z. Physik* 147 (1957) 161.

(6) B.V. Panin, *Sovt. Physics JETP* 15 (1962) 215.

(7) S. Datz and C. Snoek, *Phys. Rev.* 134 (1964) A347.

(8) D.P. Smith, *Journal of Applied Physics* 38 (1967) 340.

(9) M. Kaminsky, *Atomic and Ionic Impact Phenomena on Metal Surfaces* (Springer-Verlag, 1965).

(10) V.A. Arifov, *Interaction of Atomic Particles with a Solid Surface* (Consultants Bureau, 1969).

(11) E.P.Th.M. Suurmeijer, A.L. Boers and S.H.A. Begemann, *Surface Science* 20 (1970) 424.

(12) E.P.Th.M. Suurmeijer and A.L. Boers, *Surface Science* 43 (1974) 309.

(13) A.L. Boers, *Surface Science* 63 (1977) 475.

(14) W.L. Baun, *Applications of Surface Science* 1 (1977) 81.

(15) W. Heiland and E. Taglauer, *Nucl. Inst. Methods* 132 (1976) 535.

(16) N.H. Tolk, J.C. Tully, W. Heiland and C.W. White, *Inelastic Ion Surface Collisions* (Academic Press, 1977).

(17) W. Heiland and E. Taglauer, *Surface Science* 68 (1977) 96.

(18) E.S. Mashkova and V.A. Molchanov, *Radiation Effects* 16 (1972) 143.

(19) E.S. Mashkova and V.A. Molchanov, *Radiation Effects* 23 (1974) 215.

(20) E.S. Mashkova and V.A. Molchanov, *Radiation Effects* 19 (1973) 29.

(21) G. Carter and J.S. Colligon, *Ion Bombardment of Solids* (Heineman, 1968).

(22) R.J. MacDonald, *Advances in Physics* 19 (1970) 457.

(23) G.M. McCracken, *Rep. Prog. Phys.* 38 (1975) 241.

(24) G.H. Morgan and E. Everhart, *Phys. Rev.* 128 (1962) 667.

(25) D. Coffey, D.C. Lorents and F.T. Smith, *Phys. Rev.* 187 (1969) 201.

(26) B. Fastrup, G. Hermann and K.J. Smith, *Phys. Rev.* A3 (1971) 1591.

(27) B. Fastrup and G. Hermann, *Phys. Rev.* A3 (1971) 1955.

(28) H. Goldstein, *Classical Mechanics*, chapter 3 (Addison-Wesley, 1950).

(29) E. Langberg, *Phys. Rev.* 111 (1958) 91.

(30) W.L. Gay and D.E. Harrison, *Phys. Rev.* A135 (1964) 1780.

(31) D.I. Veksler, *Sov. Phys. — Solid State* 6 (1965) 1767.

(32) D.P. Smith, *Surface Science* 25 (1971) 171.

(33) D.P. Smith and R.F. Goff, *Bull. Am. Phys. Soc.* 14 (1969) 788.

(34) L.L. Tongson and C.B. Cooper, *Surface Science* 52 (1975) 263.

(35) W. Heiland and E. Taglauer, *Nucl. Instr. Methods* 132 (1976) 535.

(36) E. Taglauer and W. Heiland, *Surface Science* 33 (1972) 27.

(37) W. Heiland, H.G. Schäffler and E. Taglauer, *Surface Science* 35 (1973) 381.

(38) O.B. Firsov, *Sov. Phys. — JETP* 9 (1959) 1076.

(39) J. Lindhard and M. Scharff, *Phys. Rev.* 124 (1961) 128.

(40) E. Taglauer and W. Heiland, p.2495, *Proceedings of the Seventh International Vacuum Congress and the Third International Conference on Solid Surfaces*, eds. R. Dobrozemsky, F. Rudenauer, F.P. Viehbock and A. Breth (F. Berger and Söhne, 1977).

(41) H.H. Brongersma, M.J. Sparnaay and T.M. Buck, *Surface Science* 71 (1978) 657.

(42) E. Taglauer and W. Heiland, *Surface Science* 47 (1975) 234.

(43) W. Heiland and E. Taglauer, *Surface Science* 68 (1977) 96.

(44) H. Niehus and E. Bauer, *Surface Science* 47 (1975) 222.

(45) D.J. Ball, T.M. Buck, D. MacNair and G.H. Wheatley, *Surface Science* 30 (1972) 69.

(46) H.H. Brongersma and P.M. Mul, *Surface Science* 35 (1973) 393.

(47) R.E. Honig and W.L. Harrington, *Thin Solid Films* 19 (1973) 43.

(48) E. Taglauer and W. Heiland, *App. Phys. Letts.* 24 (1974) 437.

(49) S.H.A. Begemann and A.L. Boers, *Surface Science* 30 (1972) 134.

(50) E.S. Mashkova, V.A. Malchanov, E.S. Parilis and N.Yu. Turaev, *Phys. Letters* 18 (1965) 7.

(51) A.G.J. De Wit, G.A. Van der Schootbrugge and J.M. Fluit, *Surface Science* 47 (1975) 258.

(52) W. Heiland, E. Taglauer and M.T. Robinson, *Nucl. Instr. Methods* 132 (1976) 655.

(53) E.S. Mashkova and V.A. Molchanov, *Sov. Phys. — Solid State* 8 (1966) 1206.

(54)   E.S. Mashkova and V.A. Molchanov, *Sov. Phys. – Doklady* <u>12</u> (1967) 133.

(55)   E.S. Mashkova, V.A. Molchanov and V. Soshka, *Phys. Stat. Sol.* <u>19</u> (1967) 425.

(56)   V.A. Arifov and A.A. Aliev, *Proc. X International Conf. Phen. in Ionised Gases*, p.76 (Oxford, 1971).

(57)   V.A. Arifov and A.A. Aliev, *Sov. Physics – JETP* <u>30</u> (1970) 1015.

(58)   V.A. Arifov and A.A. Aliev, *Sov. Physics – Doklady* <u>14</u> (1970) 1166.

(59)   W.F. Van der Weg and D.J. Bierman, *Physica* <u>35</u> (1968) 406.

(60)   V.A. Molchanov, V.A. Snisar and V.M. CHicherov, *Sov. Physics – Doklady* <u>14</u> (1969) 43.

(61)   V.M. Chicherov, *Proc. VIII Internat. Conf. Phen. in Ionised Gases, Wien*, p.49 (1967).

(62)   V.M. Chicherov, *Sov. Physics – JETP* <u>28</u> (1969) 13.

(63)   M. Pryde, A.G. Smith and G. Carter, *Atomic Collision Phenomena in Solids*, p.573, eds. D.W. Palmer, M.W. Thompson and P.D. Townsend (North-Holland, 1970).

(64)   E.S. Mashkova, V.A. Molchanov, E.S. Parilis and N.Yu. Turaev, *Sov. Physics – Doklady* <u>11</u> (1966) 52.

(65)   V.M. Kivrilis, E.S. Parilis and N.Yu. Turaev, *Dokl. Akad. Nauk. SSSR* <u>173</u> (1967) 805.

(66)   W. Heiland, H.G. Schaffler and E. Taglauer, *Atomic Collisions in Solids*, Vol. 2, p.599, eds. S. Datz, B.H. Appleton and C.D. Moak (Plenum Press, 1975).

(67)   A. Van Veen and J. Haak, *Physics Letters* <u>40A</u> (1972) 378.

(68)   B. Poelsema, L.K. Verhey and A.L. Boers, *Surface Science* <u>64</u> (1977) 554.

(69)   Yu.G. Skripka, *Radiation Effects* <u>19</u> (1973) 211.

(70)   H.H.W. Feijen, Thesis, Groningen, 1975.

(71)   V.I. Shulga, *Radiation Effects* <u>26</u> (1975) 61.

(72)   M.W. Thompson and H.J. Pabst, to be published in *Radiation Effects*.

(73)   T.M. Buck, G.H. Wheatley and L.C. Feldman, *Surface Science* <u>35</u> (1973) 345.

(74) T.M. Buck, Y.S. Chen, G.H. Wheatley and W.F. Van der Weg,
      Surface Science 47 (1975) 244.

(75) L.K. Verhey, B. Poelsema and A.L. Boers, *Radiation Effects* 27
      (1975) 47.

(76) V.M. Chicherov, *Zh. Eksp. i. Teor. Fiz. Pis. Red.* 16 (1972) 328.

(77) W. Eckstein and H. Verbeek, to be published, see ref. 40.

(78) H.D. Hagstrum, *Phys. Rev.* 96 (1953) 325.

(79) H.D. Hagstrum and G.E. Becker, *Phys. Rev.* B8 (1973) 107.

(80) R.L. Erickson and D.P. Smith, *Phys. Rev. Letts.* 34 (1975) 297.

(81) S.S. Shekhter, *Zh. Eksp. i. Teor. Fiz.* 7 (1937) 750.

(82) A. Cobas and W.E. Lamb, *Phys. Rev.* 65 (1944) 327.

(83) H.D. Hagstrum, *Phys. Rev.* 122 (1961) 83.

(84) H.H. Brongersma and T.M. Buck, *Nucl. Inst. Methods* 132 (1976)
      559.

(85) L.K. Verhey, B. Poelsema and A.L. Boers, *Nucl. Inst. Methods* 132
      (1976) 559.

(86) P. Bertrand, F. Delannay, C. Bulers and J.M. Steydio, *Surface
      Science* 68 (1977) 108.

(87) H.D. Hagstrum, *Phys. Rev.* 96 (1954) 336.

(88) F.P. Ziemba and E. Everhart, *Phys. Rev. Letts.* 2 (1959) 297.

(89) W.C. Keever and E. Everhart, *Phys. Rev.* 150 (1966) 43.

(90) W. Lichten, *Phys. Rev.* 139 (1965) A27.

(91) T.W. Rusch and R.L. Erickson, *J. Vac. Sci. Technol.* 13 (1976)
      374.

(92) T.W. Rusch and R.L. Erickson, *Inelastic Ion-Surface Collisions*,
      p.73, eds. N.H. Tolk, J.C. Tully, W. Heiland and C.W. White
      (Academic Press, 1977).

(93) N.H. Tolk, J.C. Tully, J. Kraus, C.W. White and S.H. Neff, *Phys.
      Rev. Letts.* 36 (1976) 747.

(94) J.C. Tully and N.H. Tolk, *Inelastic Ion-Surface Collisions*,
      p.105, eds. N.H. Tolk, J.C. Tully, W. Heiland and C.W. White
      (Academic Press, 1977).

(95) H.H. Brongersma, N. Hazewindus, J.M. van Nieuwland, A.M.M. Otten
      and A.J. Smets, *J. Vac. Sci. Technol.* 13 (1976) 670.

(96)   L.K. Verhey, B. Poelsema and A.L. Boers, *Radiation Effects* <u>34</u> (1977) 163.

(97)   H.H. Brongersma and T.M. Buck, *Surface Science* <u>53</u> (1975) 649.

(98)   F.J. Eriksen, S.M. Fernandez, A.B. Bray and E. Pollack, *Phys. Rev.* <u>A11</u> (1975) 1239.

(99)   G.H. Morgan and E. Everhart, *Phys. Rev.* <u>128</u> (1962) 667.

(100) V.V. Afrosimov and N.V. Fedorenko, *Sov. Physics Tech. Phys.* <u>2</u> (1957) 2391.

(101) J. Lindhard and M. Scharff, *Phys. Rev.* <u>124</u> (1961) 128.

(102) O.B. Firsov, *Zh. Eksp. i. Teor. Fiz.* <u>9</u> (1959) 1076.

(103) Ya.A. Teplova, V.S. Nikolaev, I.S. Dimitriev and L.N. Fateeva, *Zh. Eksp. i. Teor. Fiz.* <u>42</u> (1962) 44.

(104) Ya.A. Teplova, V.S. Nikolaev, I.S. Dimitriev and L.N. Fateeva, *Sov. Phys. — JETP* <u>15</u> (1962) 31.

(105) I.M. Cheshire and J.M. Poate, *Atomic Collision Phenomena in Solids*, p.351, eds. D.W. Palmer, M.W. Thompson and P.D. Townsend (North-Holland, 1970).

(106) C.P. Bhalla, J.N. Bradford and G. Reese, *Atomic Collision Phenomena in Solids*, p.361, eds. D.W. Palmer, M.W. Thompson and P.D. Townsend (North-Holland, 1970).

(107) P. Hvelplund and B. Fastrup, *Phys. Rev.* <u>165</u> (1968) 408.

(108) J.H. Ormond and H.E. Duckworth, *Can. J. Phys.* <u>41</u> (1963) 1424.

(109) J.H. Ormond, J.R. MacDonald and H.E. Duckworth, *Z. Naturforsch.* <u>21a</u> (1966) 130.

(110) B. Fastrup, P. Hvelplund and C.A. Sautter, *Dan. Vid. Selsk. Mat. Fys. Medd.* <u>35</u> (1966) No. 10.

(111) D.S. Karpuzov, *Surface Science* <u>45</u> (1974) 342.

(112) V.E. Yurasova, *Prov. VII Symposium and Summer School on the Physics of Ionised Gases*, p.427, Rovinj (1974).

(113) B. Poelsema, L.K. Verhey and A.L. Boers, *Surface Science* <u>64</u> (1977) 537.

(114) B. Poelsema, L.K. Verhey and A.L. Boers, *Surface Science* <u>56</u> (1976) 445.

(115) B.T.M. Willis and A.W. Pryer, *Thermal Vibrations in Crystallography* (Cambridge Univ. Press, 1975).

(116)   C.B. Duke, *Electron Emission Spectroscopy*, p.51, eds.
        W. Dekeyser, L. Fiermans, G. Vanderkelen and J. Vennik
        (D. Reidel Pub. Coy, 1973).

(117)   F.O. Goodman, *Surface Science* 30 (1972) 1.

(118)   D.P. Jackson, *Surface Science* 43 (1974) 431.

(119)   L.K. Verhey, B. Poelsema and A.L. Boers, *Physics Letters* 53A
        (1975) 381.

(120)   B. Poelsema, L.K. Verhey and A.L. Boers, *Surface Science* 47
        (1975) 256.

(121)   B. Poelsema, L.K. Verhey and A.L. Boers, *Nucl. Instr. Methods*
        132 (1976) 623.

(122)   W. Heiland and E. Taglauer, *Surface Science* 68 (1977) 96.

(123)   W. Heiland and E. Taglauer, *J. Vac. Sci. Technol.* 9 (1972) 620.

(124)   W. Heiland, F. Iberl, E. Taglauer and D. Menzel, *Surface
        Science* 53 (1975) 383.

(125)   H. Niehus, S. Prigge and E. Bauer, *Verh. Deut. Physik. Ges.* 9
        (1975) 383.

(126)   S. Prigge, H. Niehus and E. Bauer, *Surface Science* 65 (1977)
        141.

(127)   H.H. Brongersma and J.B. Theeton, *Surface Science* 54 (1976)
        519.

(128)   H.H.W. Feijen, Thesis, Ch. 3, Groningen (1975).

CHAPTER THREE

EXPERIMENTAL METHOD

3.1 INTRODUCTION

It is desirable in a study of low energy ion scattering to direct a parallel, mass analysed, mono-energetic beam of ions onto a clean flat crystal surface.[1] The reflected ions should be energy analysed and efficiently detected. The equipment required can be divided into three main units:

(1) Ion Source, incorporating ion optics,

(2) Target Chamber, including target manipulator,

(3) Energy Analyser and detector.

These three units are shown in figure 3.1. After a discussion of the reasons for the above conditions each of the units will be described in detail.

A component of the energy spread of the analysed ions is the resolution of the energy analyser. The resolution can usually be improved by varying design parameters but often at the expense of a reduced measured yield. Another contribution to the energy spread of the scattered ions comes from the energy spread of the ion source and the angular spread of the incident beam. A minimum spread in these is necessary for optimum resolution. The ion beam must be mass analysed to ensure that the ion beam consists of one type of ion.

3.2 TARGET CLEANLINESS

As low energy ion scattering is a surface analysis technique it is essential that the target be flat. It is impossible to get a surface free of defects even without the continual damage induced by
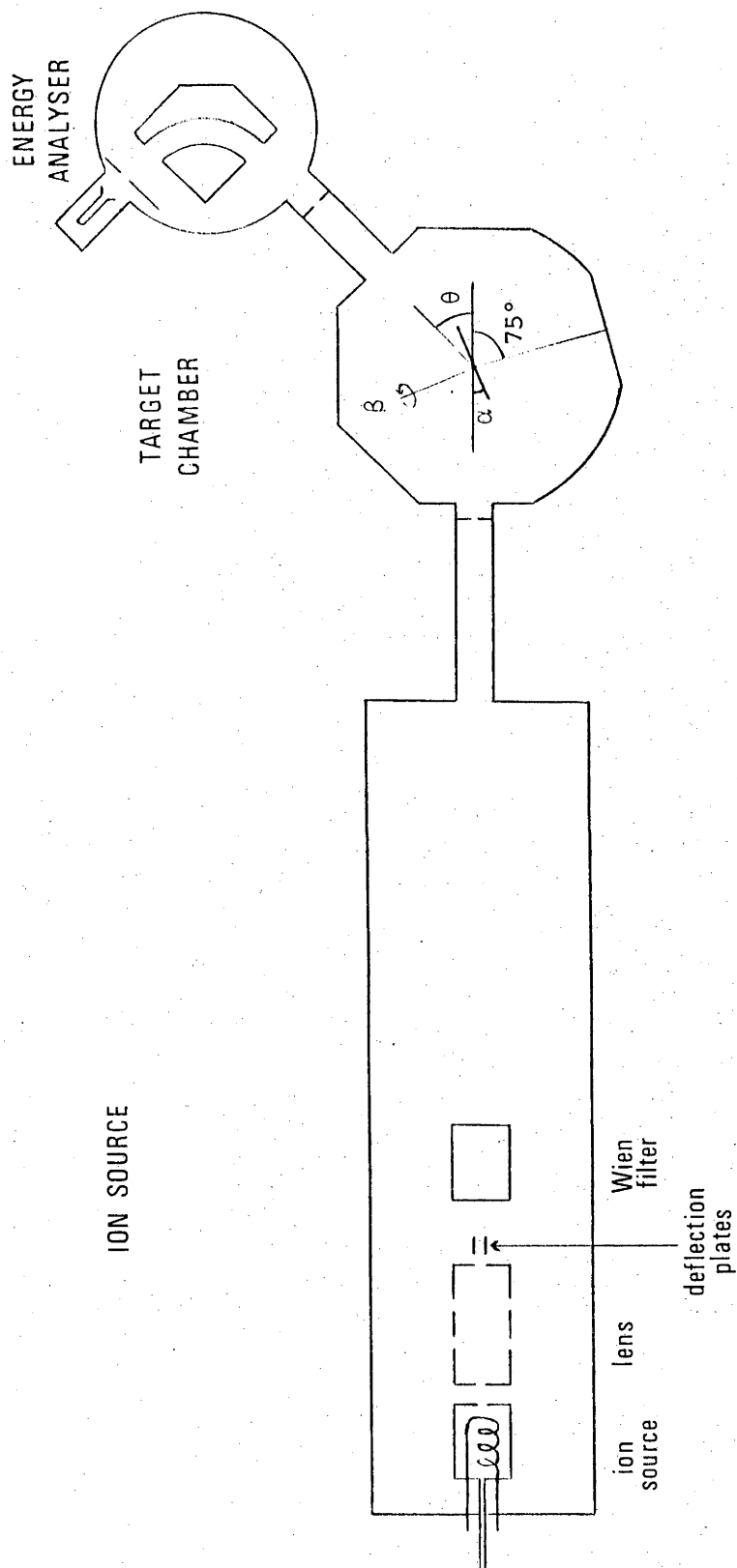
Fig. 3.1: Schematic diagram of the experimental equipment.

the ion bombardment, but the macroscopic surface roughness should be a minimum (< 1 micron).

The surface should also be free from contaminants. As the atoms and molecules of the residual gas in the vacuum system impinge on the surface and have a probability of "sticking" or adsorbing to the surface, it is necessary to continually remove them or to minimize their effect. The two most popular techniques for obtaining a clean surface are:

(1) Vacuum deposition of a film of the desired element onto a substrate in ultra high vacuum.

(2) Cleaning by ion bombardment to sputter off the contaminants, followed by annealing.

As the second technique was employed in these experiments it is necessary to determine how "clean" the surface was, and an estimate is as follows. The number of atoms and molecules adsorbed on a surface is a fraction of the total number actually impinging on that area. We can consider the worst case by assuming that all the impinging atoms and molecules are adsorbed.

The impinging rate,[2,3] γ, which by the above assumption is the adsorption rate, is given by the expression:

$$\gamma = 3.535 \times 10^{22} \frac{P}{\sqrt{MT}} \text{ atoms/cm}^2\text{/sec ,} \qquad 3.1$$

where P = pressure in torr,

      M = molecular mass in a.m.u.,

and   T = absolute temperature (°K).

For M = 20 amu and T = 300 °K, the adsorption rate is:

$$\gamma = 5 \times 10^{10} \text{ atoms/cm}^2\text{/sec}$$

for $P = 10^{-10}$ torr.

As the surface layer density is roughly 10^{15} atoms/cm^2, a monolayer can be adsorbed after 10^4 seconds. The number of atoms

sputtered from a solid per unit time, N_s, is calculated as:

$$N_s = S \cdot N_0 \quad \text{atoms/sec} , \qquad 3.2$$

where S is the sputtering coefficient which can vary from 0.1 to 10, and N_0 is the number of incident ions/sec. If a 1% coverage of the contaminant is acceptable then the sputtering rate must be 100 times greater than the adsorption rate. Therefore, if the sputtering coefficient is taken as unity, then:

$$N_0 \geqslant 5 \times 10^{12} \text{ ions/cm}^2\text{/sec} \quad \text{at } 10^{-10} \text{ torr} ,$$

so that

$$I \geqslant 1 \text{ } \mu\text{A/cm}^2 ,$$

where I is the incident ion current density.

The current density used in these experiments, typically $1 - 10$ μA/cm^2, always satisfied the cleanliness criterion. In these calculations the contamination caused by diffusion of foreign atoms from the bulk of the target have been ignored. This component is difficult to estimate as it is a function of the bulk concentration of the contaminant, the type of contaminant, its diffusion rate and the effect of the incident ion beam on the diffusion process. As reliable estimates of the diffusion rate of contaminants from the bulk were not possible, it was necessary to experimentally determine the cleanliness of the target surface. Under ion bombardment, no peaks in the energy spectra of scattered ions attributable to scattering off surface contaminants were detected. From this, it is estimated that the surface coverage of contaminants did not exceed 1%.

3.3 ION SOURCE

The ion source must produce a beam with a small energy spread, high efficiency and high purity. The ions were produced by a "Colutron"[4] hot cathode electron bombardment source which delivers an intense beam with an energy spread of 0.11 eV if the arc power is limited to 15 watts.[5] This source is capable of producing ions of

inert gases, some reactive gases and a large number of the solid elements, but in the experiments described here only inert gas ions were used. To maintain a constant beam current for long periods of time the arc conditions had to be stable. This was achieved by maintaining a constant gas pressure in the source with the equipment shown schematically in figure 3.2.

The pressure on the ion source side of the servo-driven leak valve was monitored by a Pirani gauge. The Pirani gauge controller supplied a pressure dependent voltage to the automatic pressure controller (Granville Phillips series 213) through the servo response filter preamplifier. The preamplifier was used to eliminate the instability arising from the mismatch of response times between the Pirani gauge and the automatic pressure controller. The preamplifier controlled the sampling times which were set to allow the gauge time to respond to pressure changes.

The ion beam was extracted and focused by an einzel lens which incorporates vertical deflection plates mounted on the exit side of the third electrode. The accelerating and focusing voltages were supplied by 6 kV Fluke 408B power supplies chosen for their low ripple factors (5 mV at 6 kV). This is important in helping to minimize the beams energy spread.

The ion beam was then velocity filtered by a Wien Filter, consisting of crossed electric and magnetic fields.[6-9] In the case of ions with the selected velocity, the force due to the magnetic field was cancelled by an equal and opposite force due to the electric field. For all other velocities these forces were unequal, causing deflection. The only ionized impurities which could be passed by the Wien Filter were those with the same energy to mass ratio (E/m) as the selected beam. As the probability of encountering such a combination is negligible, the Wien Filter is an effective mass filter.

Neutral atoms, unaffected by the Wien Filter, would follow the path of the selected ion beam and could be a possible source of bombardment by impurity atoms. However, when the ion beam was deflected so that it did not strike the target, no secondary electron
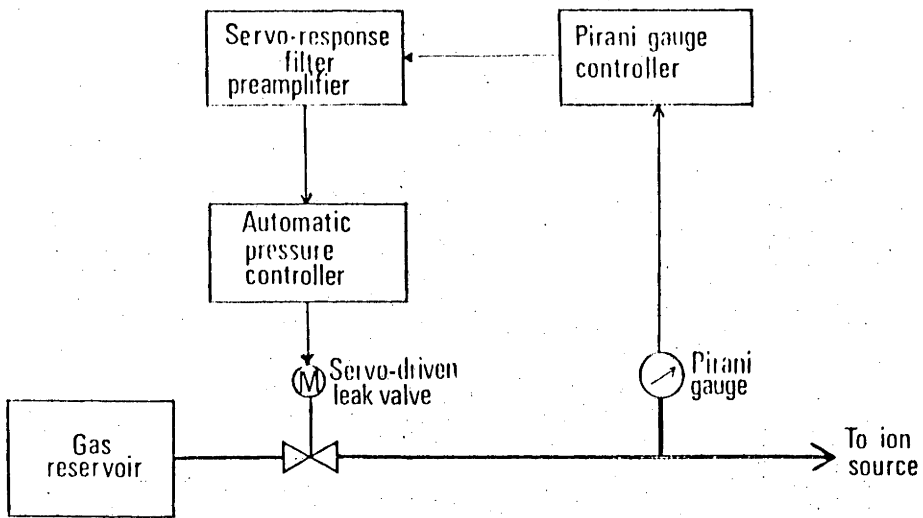
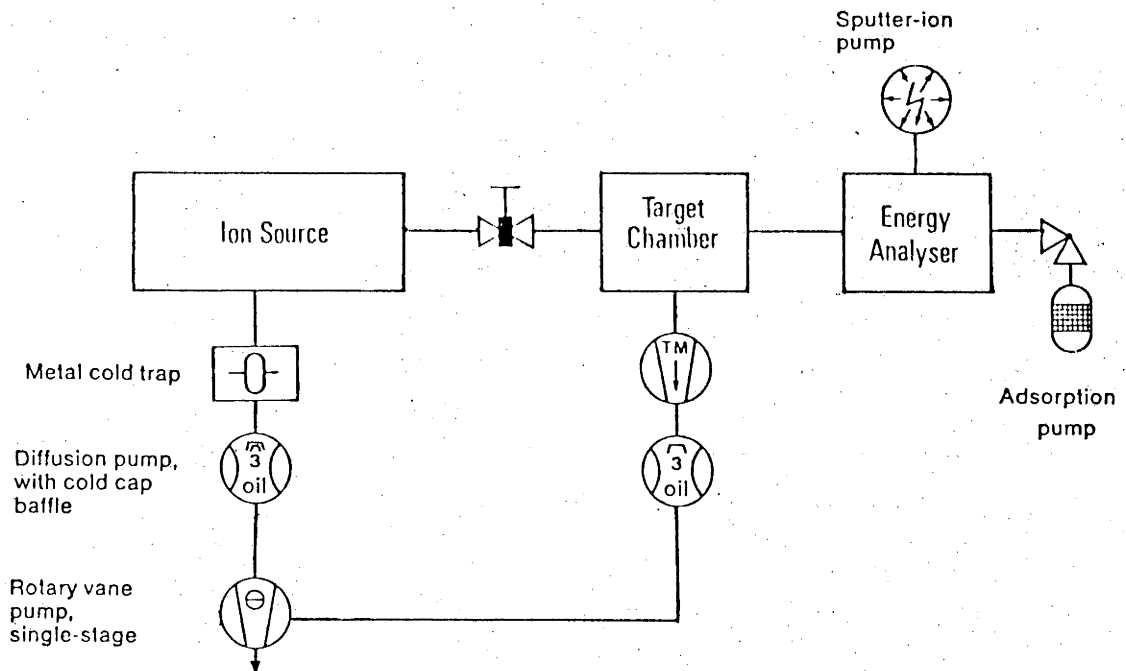Fig. 3.2: Block diagram of the ion source automatic pressure control.

Fig. 3.3: Block diagram of the vacuum system.

current was measured from the target (i.e. $I_{s.e.} < 10^{-10}$ Amp), and no scattered particles were detected by the energy analyser. This indicated that if a neutral beam existed, then its intensity was less than 0.1% of the intensity of the ion beam, and it made no measurable contribution to the scattered ion yield.

To correct the defocusing effect of the crossed fields on the ion beam, the Wien Filter incorporated a set of electrostatic shims which modified the electric field distribution and focused the beam without affecting the selectivity.

The ion beam, after leaving the Wien Filter then passed through the insulated entrance aperture to the target chamber. The current striking the aperture could be monitored to allow normalization to beam current when it was not possible to normalize the results to the current incident on the target.

Steady beam currents in the range $0.2 - 20$ $\mu A/cm^2$ were obtained with short term (< 10 mins) current fluctuations of less than 0.3% and long term (~ 1 hour) fluctuations less than 2%. The ion beam divergence measured at the target was 0.25°.

3.4   ION SOURCE VACUUM SYSTEM

To minimize the gas load on the target chamber it was necessary to maintain a low operating pressure in the source region. The ion source was evacuated by a 1500 l/sec diffusion pump backed by a single stage rotary pump (Edwards ES150) (see fig. 3.3). A chemically activated copper mesh foreline trap was installed between the rotary pump and the diffusion pump to minimize the back streaming of rotary pump oil. To guard against problems arising from power failures, a solenoid controlled valve was installed between the rotary pump and the foreline trap. The diffusion pump was charged with Santovac 5 oil, chosen principally for its low backstreaming properties and its high thermal and oxidative stability.[13] The use of Santovac 5 also avoids the build-up of conducting films associated with silicone-based oils, which can cause problems with an ion source.

The liquid nitrogen cooled reservoir above the diffusion pump was automatically filled from a pressurized dewar, thereby allowing continuous pumping of this region. The base pressure was 5×10^{-8} torr. However the operating pressure of $(0.4 - 1.5) \times 10^{-6}$ torr depended on the source gas in use.

3.5 TARGET CHAMBER

The target chamber, which stands 32 cm high, was milled from a forged billet of 308 stainless steel. The entrance and exit flanges on the 20 cm diameter collar were oriented as shown in fig. 3.1 and allowed scattering angles at every multiple of 15° from 0° to 135°, excluding 120°. These flanges, which have a maximum angular location error of 0.1°, are flat faced and sealed with 0.13 cm diameter gold wire.

The target was mounted on a Vacuum Generators HPT-SM2 target manipulator which has facilities for rotation about two axes as well as three translational motions and a heater capable of raising the target temperature to 1000 °C (see fig. 3.4).

The manipulator was mounted so that one of the rotations was about the target chamber axis (perpendicular to the ion beam), thus altering the angle of incidence of the ion beam to the target surface. This rotation had a range of 360° and an accuracy of 0.1°. The second rotation was about the normal to the target surface (called the azimuthal angle), thus altering the crystallographic direction along which the ion beam was directed without altering the angle of incidence. This rotation had a range of ±90° and an accuracy of 0.3°.

The three translational movements were mutually perpendicular and independent. They were driven by micrometer movements with a range of 2.5 cm (5.0 cm along axis of target chamber) and an accuracy of 0.01 mm. Both of the rotational movements were fitted with a 12 position stepper motor (Calderon Limited) and a 1000:1 gearbox (Weyer Bros) to allow controlled rotation of the target. This allowed a step size on the angle of incidence of 0.03° and 0.00125° on the azimuthal angle.
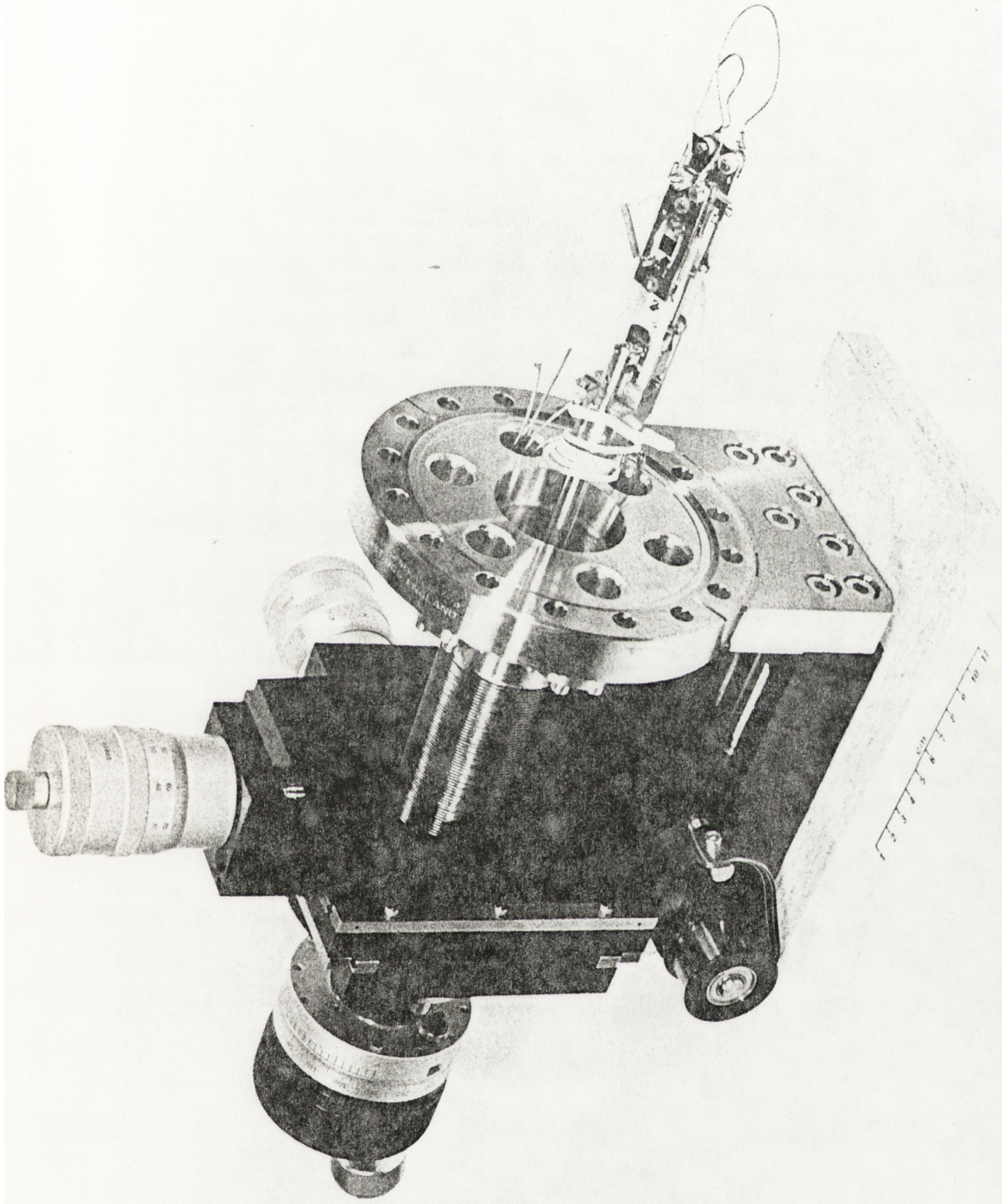
Fig. 3.4: The two axis target manipulator with 3 translational movements (Vacuum Generators HPT1).

The target was insulated to allow the incident beam current to be measured, and thus the normalization of results to integrated incident charge. Where the measured current could be affected by changing secondary electron emission efficiency, the results were normalized to the incident charge on the entrance aperture to the target chamber.

3.6 TARGET CHAMBER VACUUM SYSTEM

The target chamber was pumped by a 450 l/sec turbomolecular pump (Leybold-Hereaus) which was backed by a 50 l/sec oil diffusion pump (see figure 3.3). This diffusion pump was backed by the rotary pump shared with the diffusion pump on the source. As the diffusion pump was more efficient in removing the low mass background gas, for which the turbomolecular pump had a low pumping speed, the target chamber background pressure decreased by an order of magnitude below that obtained when only the rotary pump was used.

The pressure in the target chamber was measured by a Kreisman Cold Cathode Gauge which had been calibrated with a glass encapsulated Bayard-Alpert ionization gauge down to 1×10^{-9} torr. With the Bayard-Alpert gauge the minimum pressure measured was 5×10^{-10} torr which was believed to be due largely to the X-ray limit. With the cold cathode gauge, the pressure could be monitored down to 5×10^{-11} torr. For all experiments described in this investigation the pressure in the target chamber was less than 10^{-10} torr as measured with the cold cathode gauge.

3.7 ENERGY ANALYSER

The analyser was a 90° hemispherical electrostatic energy analyser designed to have a resolution of better than 1%[10,11] (i.e. $\Delta E/E < 0.01$). A diagram of the analyser can be seen in figure 3.5.

The 0.5 mm entrance aperture defined the analysing direction, the angular resolution (0.15°) and in association with the 0.5 mm exit aperture, the analyser energy resolution.

ELECTROSTATIC ENERGY ANALYSER

CEM

+ve

−ve

44mm

55mm

36.5mm

−3kV

output

CEM

exit
aperture
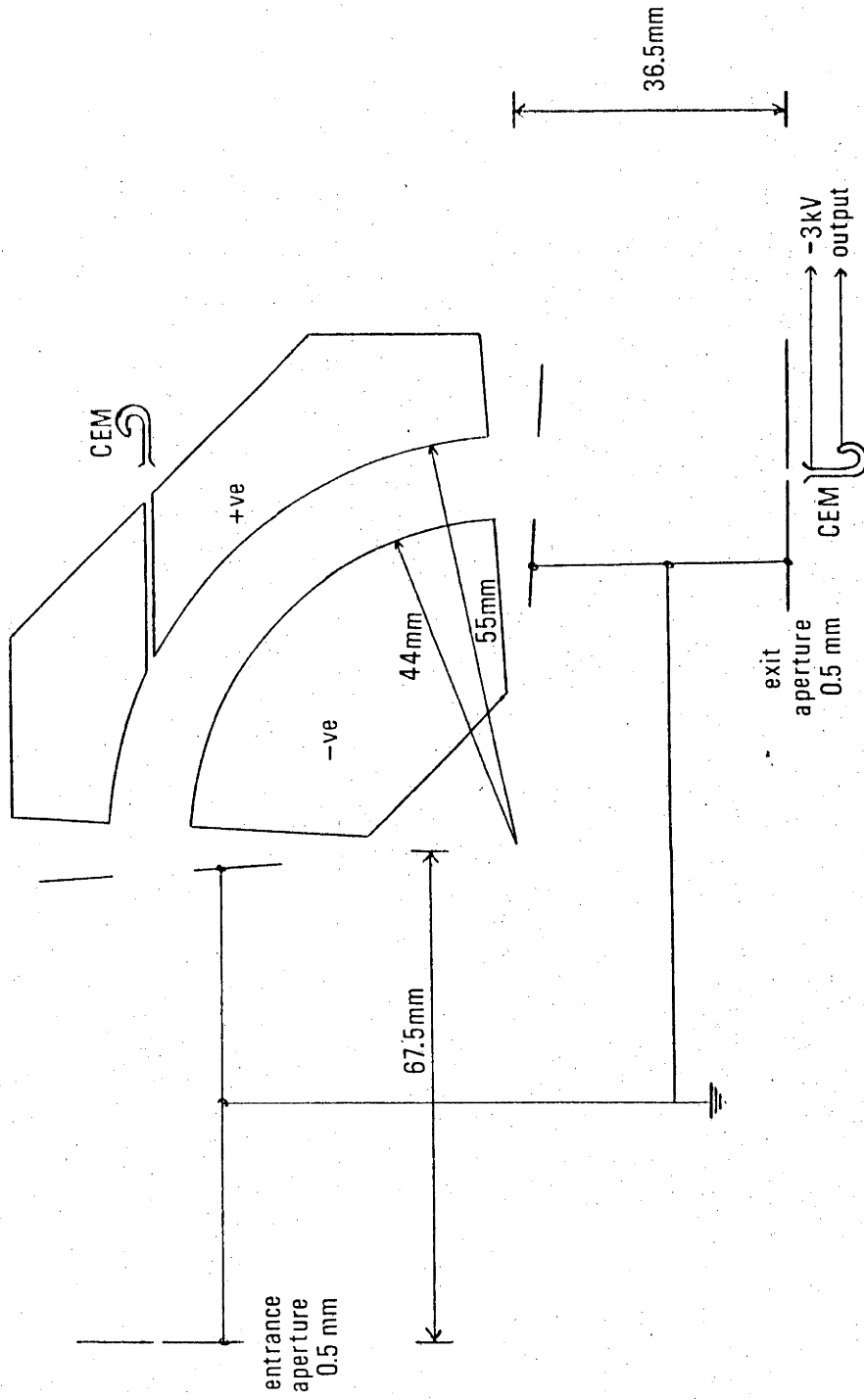0.5 mm

67.5mm

entrance
aperture
0.5 mm

Fig. 3.5: Scale drawing of the electrostatic energy analyser (scale 1:1).

The inner and outer plates of the hemispherical analyser were machined from aluminium to radii of 4.40 cm and 5.50 cm respectively. The outer plate had a 0.1 cm hole in the straight through direction to allow the transmission of the neutral particles, thereby reducing the background noise produced by the reflection of the neutrals off the outer plate. The separation of the plates was set with accurate 1.100 cm ruby spheres. The analyser was mounted on a support stand which had two translation motions to assist in alignment. The extent of the fringing field of the hemispherical plates was reduced by including shielding diaphragms designed from published information by Wollnick.[10]

The detector was a bakeable channel electron multiplier (CEM) operated in the pulse counting mode. To overcome the energy dependent efficiency of the CEM, the operating potential of -3 kV was applied to the entrance (see fig. 3.5), so that after passing through the exit aperture, the ions were given an added energy of 3 keV.

A second CEM was mounted on the back of the outer plate to detect the neutrals passing through the 0.1 cm hole, and thus obtain a comparison of the ion to neutral ratio. This CEM suffered continual bombardment from all the neutrals scattered into the analyser. The high flux fatigued the straight through CEM to the point where it was unserviceable and thus satisfactory measurements of the ion to neutral ratio could not be made. The exit aperture CEM did not suffer noticeable fatigue as it was bombarded by a lower flux only when the deflection voltages were favourable.

3.8   ENERGY ANALYSER VACUUM SYSTEM

To minimize CEM noise due to background gas and to avoid the deposition of molecular films on the analyser components, it was necessary to have a clean UHV pump. The only available pump which fitted these criteria was a 150 l/sec triode type cold cathode, getter ion pump. As this pump included a large magnet, it was necessary to ensure that the magnetic field did not affect the energy spectra obtained.

The residual field at the energy analyser is approximately 0.003 Tesla. The pump and magnet were aligned in the direction of the average velocity of the analysed ions so that any effect introduced by the ion entering the residual field would be counteracted by the opposite effect when leaving the region. The result of these precautions will be discussed in the following section on the energy analyser calibration.

After a 48 hour bakeout at 100 °C, the ion pump would evacuate the energy analyser chamber to the limit of pressure measurable by the pump controller (i.e. less than 10^{-9} torr). As the ions produced by the pump contributed an excessive background to the count rate from the CEM, the ion pump was shut down for the duration of any experiment. The pressure never rose above 1×10^{-8} torr over the periods that the pump was off. The low operating pressures of this chamber contributed to the attainment of the low noise levels from the CEM of 0.01 to 0.1 counts/sec.

3.9 CALIBRATION OF THE ENERGY ANALYSER

To calibrate the energy analyser and to investigate the effect of various operating conditions on the source, the energy analyser was placed at the exit of the ion source chamber in order to analyse the direct beam. The energy spectra of $1.0 - 6.0$ keV ions were measured and it was found that:

$$\frac{E_0}{E_M} = 1.016 \pm 0.001 \qquad\qquad 3.3$$

over the stated range of energies,

where E_0 = energy of the ions from the source,

and E_M = apparent energy of the ions as measured by the analyser.

As the correction factor was energy independent, it indicates that the residual magnetic field did not affect the ions. The difference of 1.6% could be due to one or more errors in the construction of the analyser, including:

(1) Error in the angle of 90° for the sector,

(2)   Error in the plate separation,

(3)   Deviations from ideal spherical plates,

(4)   Field distortion introduced by the 0.1 cm hole in the outer
plate.

It was found that He^+ ions were deflected slightly out of the
analysing plane without affecting the motion in the plane of analysis.
This was caused by the residual magnetic field which was not coplanar
with the plane of analysis, but instead curved across it.   This effect
was removed by raising the magnet 6", and was not observed at all for
the heavier ions.

The widths of the measured energy spectra were assumed to be due
solely to the resolution limit of the energy analyser, and so the
resolution was measured to be:

$$\frac{\Delta E}{E} = 0.009 .$$ 3.4

3.10   ELECTRONICS

The control electronics[12] shown in figure 3.6 were designed
around the Ortec 6240B, 4096 channel multichannel analyser (MCA) used
in a multi-scaling mode.   Although the electronic units were
conventional items, the function of some must be explained before the
operation of the whole can be appreciated.

The current incident upon the target or entrance aperture was
measured by the Digital Current Integrator (Ortec 439) which converted
the current to digital pulses corresponding to integrated charge.   The
digital current integrator could measure currents from $10^{-10} - 10^{-3}$
amps.

The potentials for the inner and outer plates of the energy
analyser were supplied by two 0 - 2000 volt operational power supplies
(Kepco OPS 2000).   For a 0 - 10 volt input, the positive supply had a
range of 0 - 2000 volts and the negative supply had a range of
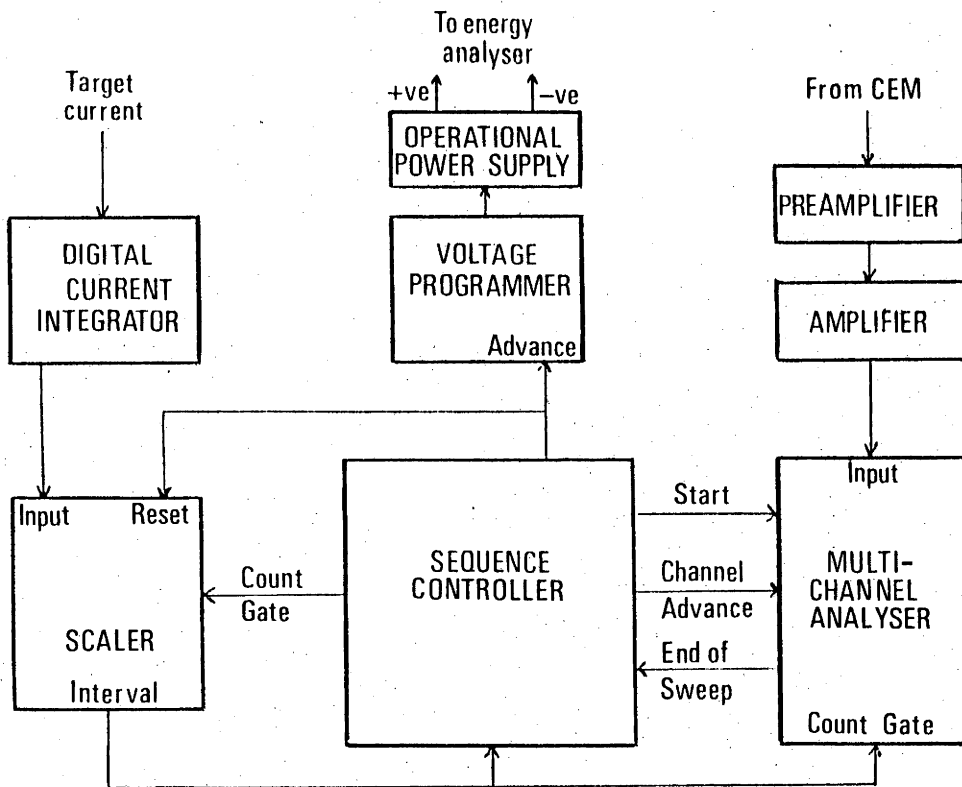0 - -1600 volts.   The 0 - 10 volt reference was supplied by a voltage

Fig. 3.6a: Block diagram of data acquisition system using the voltage programmer and operational power supply.
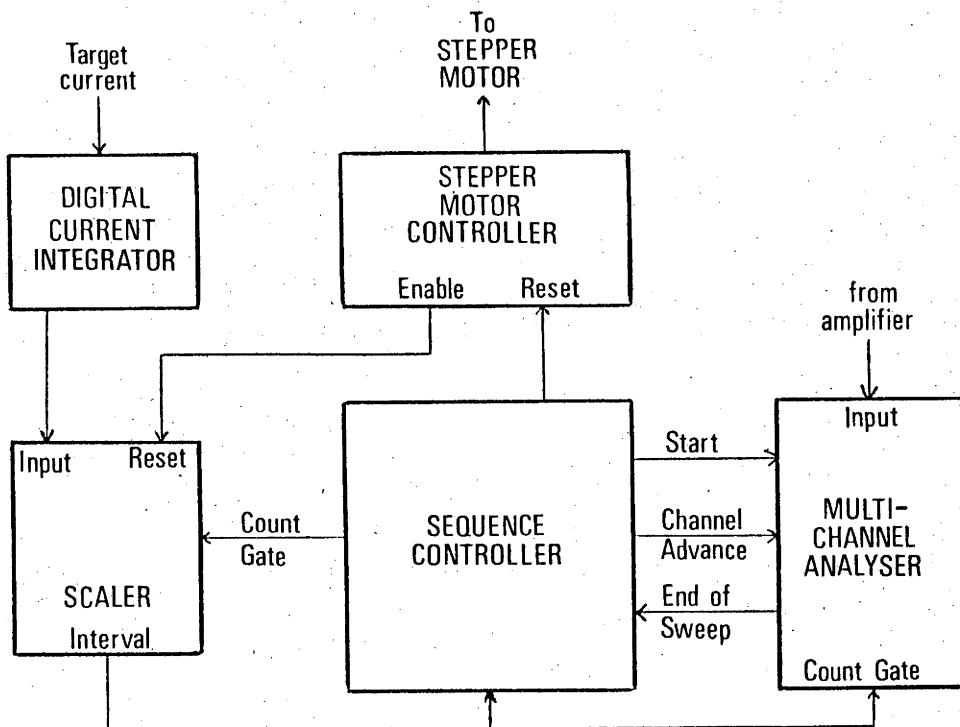

Fig. 3.6b: Block diagram of data acquisition system using the stepper motor controller.

programmer which stepped by equal voltage decrements from a preset upper level to a preset lower level over 16, 32, 64, 128, 256, 512, or 1024 steps. The stepping of the voltage programmer was controlled by a logic pulse from the Sequence Controller.

The output pulses from the CEM were fed into the preamplifier (Canberra 1706) and then to the main amplifier (Ortec 451). The output from the main amplifier was fed into the analogue to digital converter on the MCA to take advantage of the signal discriminator and the count gate which are associated with this input.

When the Scaler (Ortec 431) had collected a preset number of pulses from the digital current integrator, it transmitted a logic pulse to the Sequence Controller which gated the input to the MCA, stepped the MCA channel address, stepped the voltage programmer, then reset the Scaler and removed the gate from the MCA input. This sequence then repeated itself till the limit of the MCA memory was reached, at which time the sequence controller gated all signals.

In this circuit it was possible to replace the voltage programmer with the McLean Stepper Motor Controller as shown in fig. 3.6b. This controller advanced the stepper motors attached to the rotational motions a preset number of steps from 1 to 10^6 at a range of speeds from 1 to 400 steps per second. The sequence controller gated the input to the MCA till the stepping sequence was complete, at which time the stepper motor controller reset the scaler, which removed the gate to the MCA and the sequence recommenced.

These two control circuits were combined (figure 3.7) so that at the end of an energy spectrum, one of the target rotations was incremented by a preset angle and then the sequence recommenced with another energy spectrum. The energy spectra were controlled as explained above by Sequence Controller #1 and Scaler #1 except that the voltage programmer was reset by Sequence Controller #2.

While an energy spectrum was being accumulated, the output pulses from Scaler #1 were fed into Scaler #2 and when the preset limit was reached, the voltage programmer was reset and the stepper motor
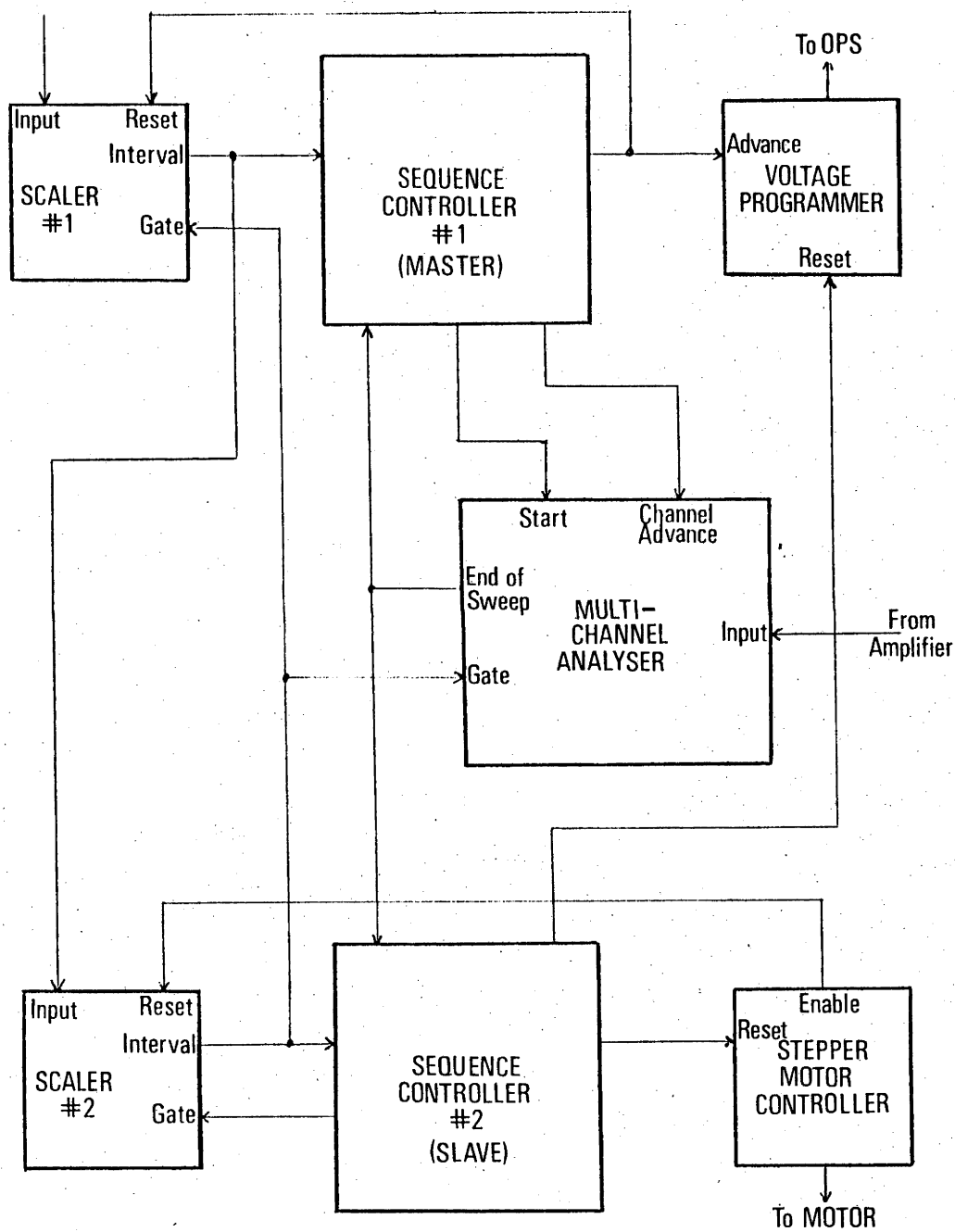
Fig. 3.7: Block diagram of data acquisition system for angular
dependence of energy spectra.

controller enabled to start the stepping sequence. When the stepper motor sequence was completed, Scaler #2 was reset and the next energy spectrum sequence was commenced. With this arrangement it was possible to monitor a region of interest of the energy spectrum as the angle of incidence or azimuthal angle were incremented by controlled amounts.

3.11 TARGET PREPARATION

The W target was prepared from high purity (99.999%) 5.5 mm diameter single crystal rods supplied by Materials Research Corporation. The crystal was aligned to within 1° of the ⟨110⟩ direction using X-ray diffraction techniques.

The crystal was cut with a spark eroder (Servomet, Metals Research Ltd) and polished with diamond pastes. After a final polish with 0.3 micron diamond paste, the crystals were cleaned with acetone, mounted on the target manipulator and placed in the target chamber. The crystal was heated to 700 °C and sputter cleaned by 6 keV Ar bombardment.

The Si target was prepared from a P type single crystal (Monsanto). The Si crystal was aligned to within 1° of the ⟨100⟩ direction and cut on a diamond saw. The target was polished with a range of Al_2O_3 powders, then cleaned with an ultra-sonic cleaner. It was boiled for 5 minutes in alcohol and rinsed in distilled water. It was further cleansed by boiling in nitric acid for 5 minutes and rinsed in distilled water. The sample was etched in a solution of HNO_3 and HF (8:1) at 20 °C for 10 minutes. This etch was quenched and the target rinsed thoroughly in distilled water. The silicon target was annealed at 700 °C and sputter cleaned with 6 keV Ne bombardment.

The results of ion scattering off these targets will be described in chapter six.

REFERENCES

(1)   E.P.Th.M. Suurmeijer, A.L. Boers and S.H.A. Begemann, *Surface Science* 20 (1970) 424.

(2)   N.W. Robinson, *The Physical Principles of Ultra High Vacuum Systems and Equipment* (Chapman and Hall Ltd, 1968).

(3)   S. Dushman, *Scientific Foundations of Vacuum Technique*, 2nd edition, ed. J.M. Lafferty (John Wiley and Sons, 1966).

(4)   L. Wåhlin, *Nucl. Instr. Methods* 27 (1964) 55.

(5)   M. Menzinger and L. Wåhlin, *Rev. Sci. Instr.* 40 (1969) 102.

(6)   R.L. Seliger, *Record of the 11th Symposium on Electron, Ion and Laser Beam Technology*, p.183, ed. R.F.M. Thornley (San Francisco Press).

(7)   R.L. Seliger, *J. Appl. Phys.* 43 (1972) 2352.

(8)   R.G. Wilson, *Nucl. Instr. Methods* 100 (1972) 9.

(9)   K. Jensen and E. Veje, *Nucl. Instr. Methods* 122 (1974) 511.

(10)   H. Wollnick, *Focussing of Charged Particles*, Ch. 4, A. Septier (Academic, 1967).

(11)   E.M. Purcell, *Phys. Rev.* 54 (1938) 818.

(12)   R.E. Auer, *Rev. Sci. Instrum.* 43 (1972) 666.

(13)   L. Holland, *Vacuum* 20 (1970) 175.

CHAPTER FOUR

THE INTERATOMIC POTENTIAL

4.1 INTRODUCTION

An understanding of the interaction between energetic ions and atoms is necessary for the analysis and interpretation of scattering processes. The force between atoms is known to be repulsive at short ranges, decreasing to become a weakly attractive force at larger separations. The collisions in Ion Scattering Spectroscopy involve particles which have sufficient energy to allow the attractive force to be neglected. In most scattering applications, the interaction between the energetic atoms is described with respect to the interatomic potential rather than to the force. The relationship between the force, $F(r)$, and the potential, $V(r)$, is given by:

$$F(r) = - \frac{dV(r)}{dr} .$$
$$4.1$$

The deflection angle for the scattering of a projectile off a target atom is related to the impact parameter and the interatomic potential by the scattering integral, which has an analytical solution for a restricted number of potentials. For high energy collision processes (> 1 MeV), the atomic nuclei completely penetrate the electron clouds of their collision partners. Under these conditions the Coulombic repulsion of the positively charged nuclei dominates the scattering process and for the Coulomb potential the scattering integral has an analytical solution. Unfortunately for most low and medium energy scattering applications, not enough is known about the behaviour of the interatomic potential to allow confident estimates to be made of scattering angles, distances of closest approach and differential scattering cross sections for different impact parameters. This uncertainty is due to the fact that at these

energies there is only partial penetration of the electron clouds of the two atoms. The "screening" of the nuclear charge by the inner shell electrons reduce the repulsive potential below that expected for a Coulomb interaction. The effectiveness of the screening is governed by the density distribution of the electron "cloud" about the nucleus.

Both theoretical and experimental methods have been used to derive the interatomic potential and this has resulted in a wide range of analytical expressions which purport to describe the interaction at different separations and for different atomic species. These potentials are described in many review articles[1-3] and in most cases there is only a limited comparison between them and experimental results. Seldom is there a recommendation on which is the more successful potential for general use.

In the following sections, the general characteristics of the theoretical and empirical potentials will be described and a comparison will be made between the Thomas-Fermi (TF) potentials and the empirical potentials derived from gas scattering experiments. These empirical results are fitted to the Moliere potential by varying the Firsov screening length. A linear relationship is found between the correction factors and a function of the atomic numbers of the collision partners (Z_1, Z_2).

The Thomas-Fermi potential has been chosen for the comparison to experimental results because it has a "universal" form. This means that the potential does not include one or more constants which depend on the collision partners and need to be evaluated from experimental results. The potential can therefore be derived from the separation and the atomic numbers of the collision partners. The choice of the Moliere potential is justified on the basis of its agreement with empirical results, and will be discussed in greater detail later.

4.2   EMPIRICAL RESULTS

As the range of empirical potentials is reviewed by Torrens,[1] only the two more popular potentials for low and medium energy

scattering will be mentioned here. These are the Born-Mayer potential (equation 4.2) and the Born potential (equation 4.3), sometimes known as the inverse power potential:

(1) $$V(r) = A_1 \exp(- b_1 r) ,$$ 4.2

(2) $$V(r) = A_2 r^{-b_2} .$$ 4.3

These have been successful in describing the interatomic potential over limited ranges of validity. Unfortunately the constants, A_i and b_i, depend on the collision partners and must be estimated from theoretical[4] or experimental analysis.[25-55]

4.3   THEORETICAL POTENTIALS

The theoretical analysis involves the determination of the radial electron density distribution from a quantum mechanical model. The interatomic potential can be derived from the density distribution. Although there have been a number of different models[1,5-11] used, the simplicity of the Thomas-Fermi approach has made it the most popular one.

The Thomas[9]-Fermi[10] model treats the electrons of the atom as a free electron gas which obeys Fermi-Dirac statistics. Using this approach a non-linear differential equation involving the electrostatic potential, V, can be obtained:

$$\nabla^2 (V - V_0) = 4\pi \sigma_0 e (V - V_0)^{3/2} ,$$ 4.4

where

$$\sigma_0 = \left(\frac{8\pi}{3h^3}\right) \cdot (2me)^{3/2} ,$$ 4.5

and eV_0 is the Fermi energy.

This equation can be reduced to a dimensionless expression by the use of the following substitutions:

$$V - V_0 = -\left(\frac{Ze}{r}\right) \Phi(x) ,$$ 4.6

$$x = \frac{r}{a} , \qquad\qquad 4.7$$

and

$$a = \left(\frac{9\pi^2}{128}\right)^{1/3} \frac{a_0}{z^{1/3}} , \qquad\qquad 4.8$$

where a_0 is the Bohr radius.

Equation 6.4 then reduces to the following differential equation:

$$\frac{d^2\Phi}{dx^2} = \frac{\Phi^{3/2}}{x^{1/2}} , \qquad\qquad 4.9$$

with the boundary conditions:

$$\Phi(0) = 1 , \qquad\qquad 4.10$$

$$\lim_{x\to\infty} \Phi(x) = 0 , \qquad\qquad 4.11$$

and

$$\lim_{x\to\infty} \frac{d\Phi(x)}{dx} = 0 . \qquad\qquad 4.12$$

There is no analytical solution for this differential equation but it has been solved numerically and fitted to analytical expressions. These solutions and other similar screening functions are listed below:

(1) Latter screening function:[12]

$$\Phi(x) = [1 + 0.02747 \; x^{1/2} + 1.243 \; x - 0.1486 \; x^{3/2}$$

$$+ 0.2302 \; x^2 + 0.007298 \; x^{5/2} + 0.006944 \; x^3]^{-1} . \qquad 4.13$$

This screening function deviates from the accurate solution of equation 4.9 by less than 3%.[1]

(2) Moliere screening function:[13]

$$\Phi(x) = 7\alpha \, \exp(-\beta x) + 11\alpha \, \exp(-4\beta x) + 2\alpha \, \exp(-20\beta x) , \qquad 4.14$$

where $\alpha = 0.05$ and $\beta = 0.3$.

(3) Csavinsky screening function:[14]

$$\Phi(x) = [0.7111 \exp(-0.175\ x) + 0.2889 \exp(-1.6625\ x)]^2 .\qquad 4.15$$

(4) Roberts' screening function:[15]

$$\Phi(x) = (1 + \alpha x^{1/2}) \exp(-\alpha x^{1/2}) ,\qquad 4.16$$

where $\alpha = 1.7822$ (ref. 16).

(5) Bohr screening function:[17]

$$\Phi(x) = \exp(-x) .\qquad 4.17$$

(6) Inverse square potential:

$$\Phi(x) = \exp(-1)/x .\qquad 4.18$$

Although the inverse square potential is not normally regarded as a T.F. potential, its effective screening function is included in this list because it is believed to be applicable for some medium energy applications. It is matched to the Bohr potential at $x = 1$ (hence the factor $\exp(-1)$) and is believed to be applicable over the range:

$$0.5 < x < 5.0 .\qquad 4.19$$

These screening functions are compared in figure 4.1. The more accurate solutions of the Thomas-Fermi model, represented by the Latters potential, evidence a characteristic slow decay for large separations. It is caused in part by ignoring the exchange energy term arising from the Pauli Exclusion principle, which imposes a limit on the occupancy of any state to one electron. Inclusion of this energy term modifies the previous equations (4.6 and 4.9) to give:

$$V(r) + b^2 = -\frac{Ze}{r} \Phi(x) ,\qquad 4.20$$

where

$$b = \frac{(2me^3)^{\frac{1}{2}}}{h} ,\qquad 4.21$$

and

THE ANALYTIC SCREENING FUNCTIONS
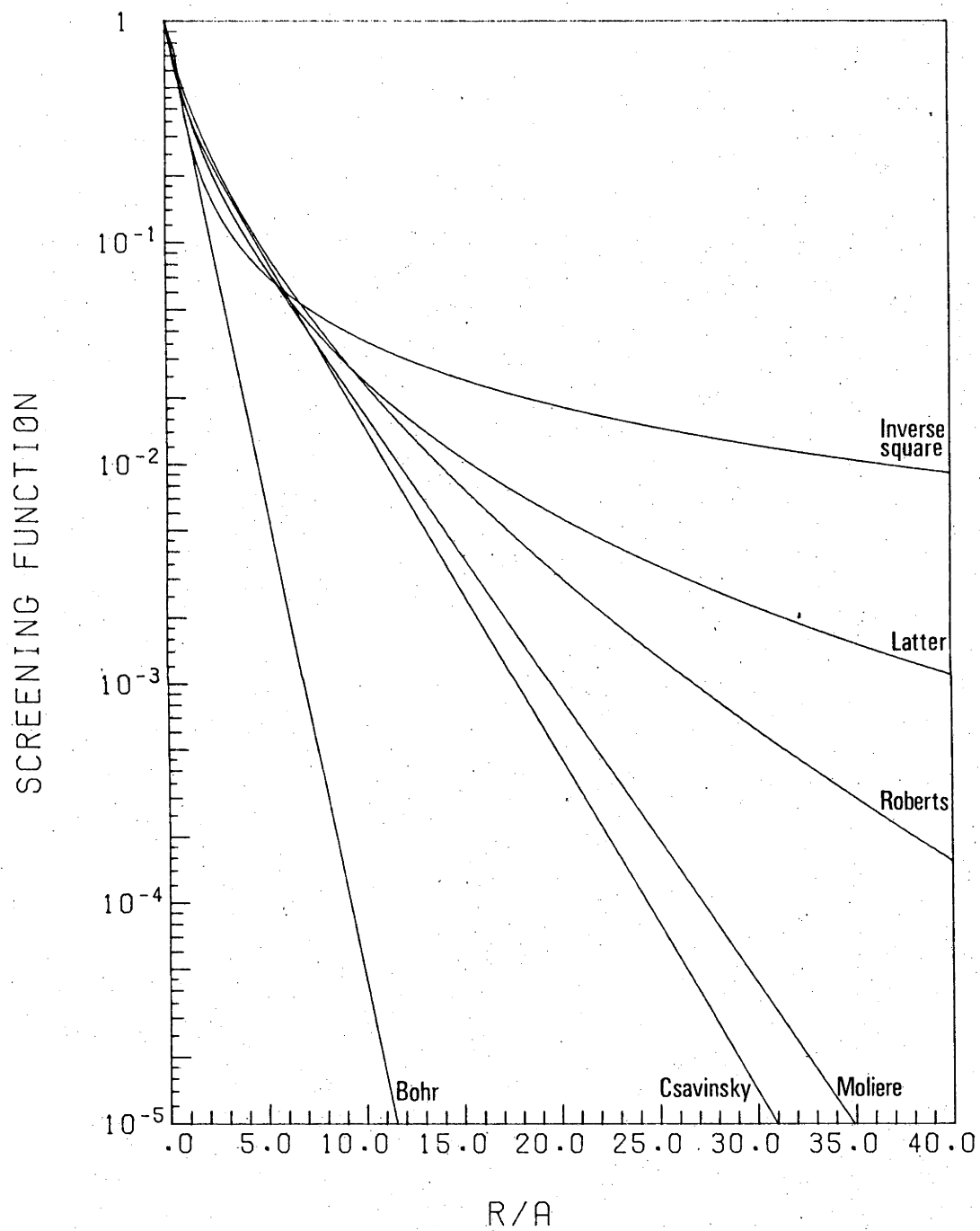
Fig. 4.1:   Comparison of the analytical screening functions described
    in the text.

$$\frac{d^2\Phi}{dx^2} = x\left(\alpha + \left(\frac{\Phi}{x}\right)^{\frac{1}{2}}\right)^2 , \qquad\qquad 4.22$$

where

$$\alpha = \frac{6^{1/3}}{4(\pi Z)^{2/3}} .$$

The existence of the atomic number dependent variable in the differential equation results in the solution not being a "universal" function. It is necessary to solve the differential equation for each element. This has been accomplished by Abrahamson *et al.*,[4,18-20] who found that a Born-Mayer potential could be fitted to the numerical results over a limited range of internuclear separations. There has been some criticism[21,22] of the technique used by Abrahamson *et al.* but as the solution of the differential equation does not yield a universal function, it will not be considered further.

4.4 COMPARISON BETWEEN EMPIRICAL AND THEORETICAL POTENTIALS

To assess the accuracy of the theoretical potentials it is necessary to test them by comparison to some physical observable which is potential dependent. In this work the theoretical potentials will be compared to the interatomic potentials derived from gas scattering experiments. In these experiments, the differential scattering cross section is measured for different atomic pairs over a range of scattering angles. Using the inversion technique[23,24,56] the interatomic potential can be derived from cross section measurements, and it is usually fitted to one of the empirical potentials mentioned previously (equations 4.2 and 4.3). As these results apply to different combinations of atoms it is necessary to reduce them to a common form to allow comparison with other empirical results and with theoretical potentials. The most convenient form for this comparison involves the screening function $\Phi(x)$ and the dimensionless separation x. The effective screening function for the experimental results is determined using the following equation:

$$\Phi_E\left(\frac{r}{a}\right) = \frac{rV(r)}{Z_1 Z_2 e^2} .$$ 4.23

The dimensionless separation is given by equation 4.7, but to determine this the screening length for atoms with atomic number Z_1 and Z_2 must be calculated. The expression for the screening length normally takes the form:

$$a = \left(\frac{9\pi^2}{128}\right)^{1/3} \frac{a_0}{F(Z_1,Z_2)} .$$ 4.24

Some of the suggested expressions for the function $F(Z_1,Z_2)$ are listed below:

$$F_1(Z_1,Z_2) = (Z_1 + Z_2)^{1/3} ,$$ 4.25

$$F_2(Z_1,Z_2) = (Z_1^{2/3} + Z_2^{2/3})^{1/2} ,$$ 4.26

$$F_3(Z_1,Z_2) = (Z_1^{1/2} + Z_2^{1/2})^{2/3} , \quad \text{ref. (64)}$$ 4.27

$$F_4(Z_1,Z_2) = (Z_1 . Z_2)^{1/6} ,$$ 4.28

$$F_5(Z_1,Z_2) = 3[(Z_1 + Z_2)^{7/3} - Z_1^{7/3} - Z_2^{7/3}]/(7 . Z_1 . Z_2) , \quad \text{ref. (64)} .$$
4.29

To determine the accuracy of the screening length functions and of the theoretical potentials the results of a range of gas scattering experiments[25-55] were plotted (see fig. 4.2) using equations 4.23 to 4.29. Some experimental results[57-59] were not included because they have been claimed to be unreliable.[56]

Best agreement exists between the empirical potentials and the theoretical potentials for the Csavinsky and the Moliere screening functions when $F_2(Z_1,Z_2)$ and $F_3(Z_1,Z_2)$ were used to estimate the screening length. In the following sections, the Moliere screening function and $F_3(Z_1,Z_2)$ will be used in preference to other possible combinations because it gives marginally better agreement with the empirical potentials. As well, the use of this combination allows the comparison of the correction factors to the screening length determined from gas scattering potentials with similar correction
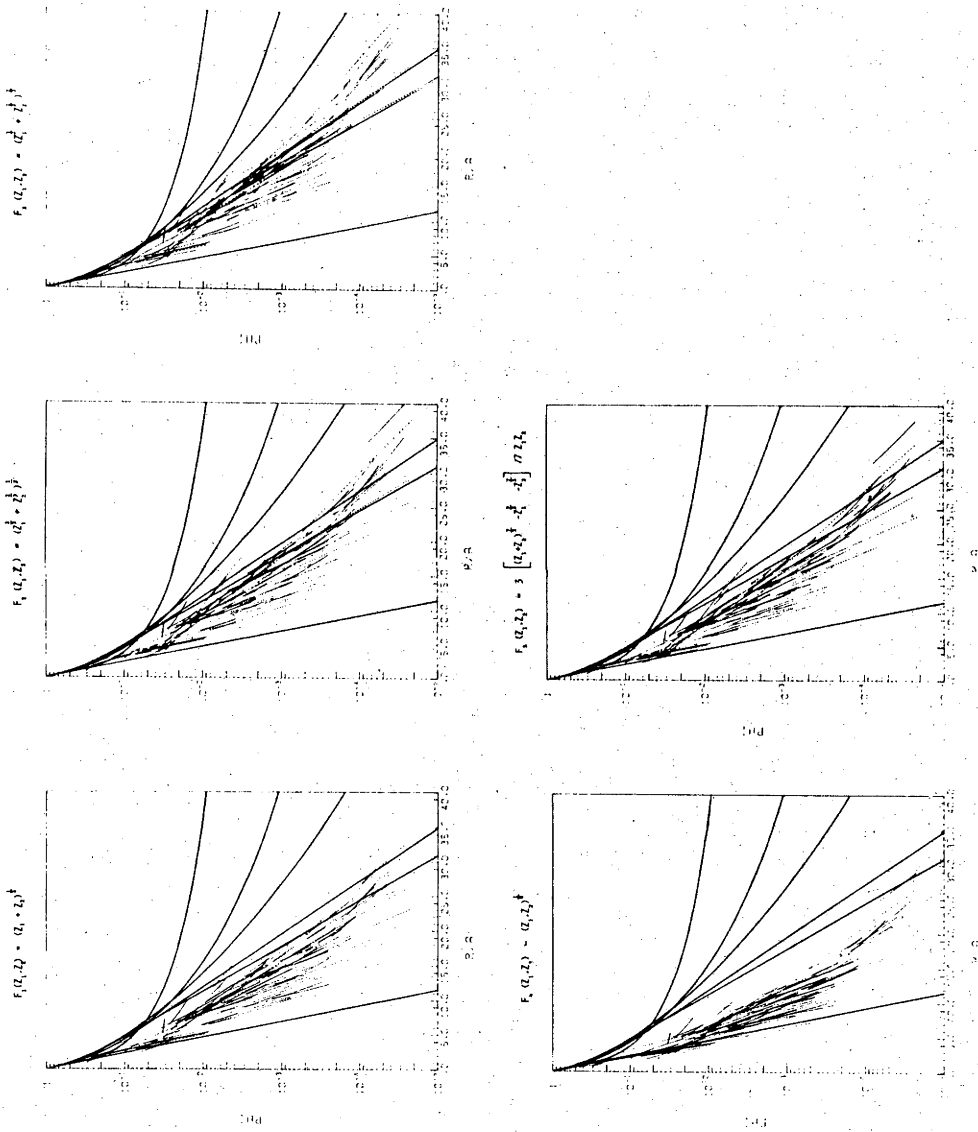
Fig. 4.2: Comparison between empirical and theoretical potentials using the screening lengths evaluated from equations 4.25 - 4.29.

factors measured from Ion Scattering Spectroscopy experiments.

4.5 SCREENING LENGTH CORRECTION FACTORS

The experimental results were fitted to the Moliere screening function by a least squares fitting procedure[60] which involved varying the screening length correction factor, γ (equation 4.30), to minimize the integrated relative standard deviation, σ (equation 4.31):

$$a_1' = \gamma \cdot \left(\frac{9\pi^2}{128}\right)^{1/3} \frac{a_0}{F_3(Z_1, Z_2)} \qquad 4.30$$

and

$$\sigma^2 = \frac{1}{X_B - X_A} \int_{X_A}^{X_B} \left[\frac{\Phi_M(x) - \Phi_E(x)}{\Phi_M(x)}\right]^2 dx . \qquad 4.31$$

where

$$x = \frac{r}{a_1'} , \qquad 4.32$$

X_A and X_B are the non-dimensional limits for the empirical potential,

$\Phi_E(x)$ is the effective screening function for the empirical potential (equation 4.23),

and $\Phi_M(x)$ is the Moliere screening function (equation 4.14).

The results of this fitting procedure can be seen in figure 4.3 where the original empirical potentials (fig. 4.3a) and the fitted potential (fig. 4.3b) are compared to the Moliere screening function. To measure the quality of agreement between all the potentials and the Moliere screening function a new variable, η, is defined:

$$\eta = \left(\sum_{i=1}^{N} \sigma_i^2\right)^{\frac{1}{2}} , \qquad 4.33$$

where σ_i is the integrated relative standard deviation (from equation 4.31) for the "i"th empirical potential and N is the number of available empirical potentials (N = 95). This fitting procedure
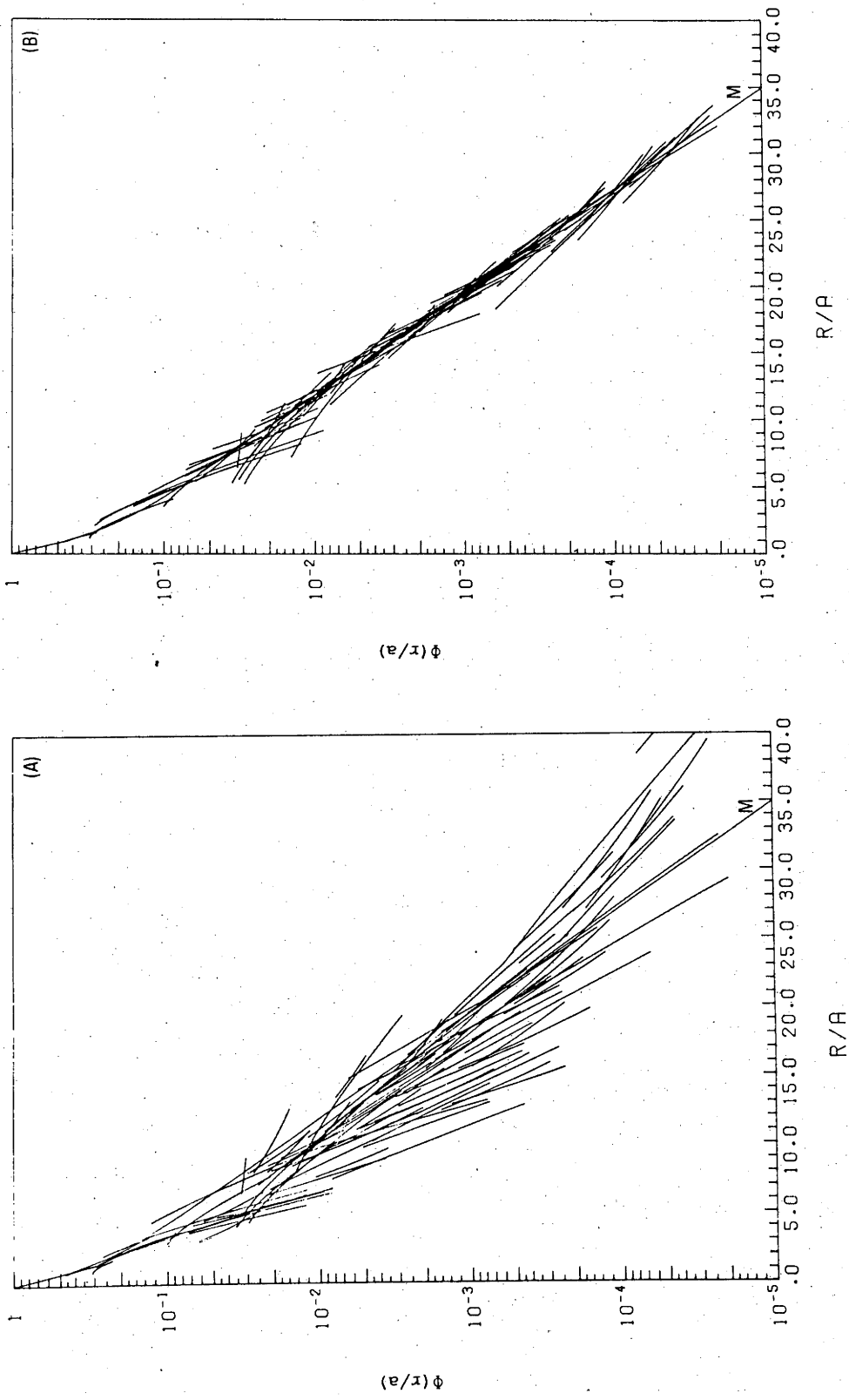
Fig. 4.3: Comparison between the empirical potentials and the Moliere potential before (A) and after (B) the fitting procedure.

reduces η from 42.4 for the unfitted results down to 1.37 for the fitted results. The correction factors obtained from this fitting procedure were plotted as a function of the atomic numbers of the collision partners (figure 4.4) and although there is a large scatter in these results, a general linear trend is evident. The spread in the results could be due to one or more of the factors listed below:

(1) The varied range of experimental techniques used to measure the scattering cross section. Combined with this is the effect of the different data analysis techniques used to determine the potential.

(2) The spread in the correction factors may result from trying to fit the empirical potentials to a screening function which does not adequately describe the "true" interaction.

(3) The scatter in these results may be confirmation of the proposition that it is unlikely that any one potential can properly describe the interaction between atoms with markedly different electronic configurations. The range of collision partners used to obtain the empirical potentials include combinations of inert gases, halogens, alkali metals and transition elements.

(4) Evidence is available to indicate that the electronic stopping power is an oscillatory function of the atomic number. This may also be the case for the interatomic potential as it is also dependent on the electronic structure of the atoms.

Included on the graphs in figure 4.4 are the lines of best fit to the correction factors which were determined by the method of least squares.[61] The equations for these lines as well as the statistical error in the coefficients are given below:

$$\gamma_1 = (0.042 \pm 0.003) \cdot (Z_1^{\frac{1}{2}} + Z_2^{\frac{1}{2}}) + (0.57 \pm 0.03) , \qquad 4.34$$

or

$$\gamma_2 = (0.0049 \pm 0.0004) \cdot (Z_1 + Z_2) + (0.71 \pm 0.02) . \qquad 4.35$$

The use of these equations increases η to 8.0 ± 0.5. The experimental results of Poelsema $et~al.$[62] and of Heiland $et~al.$[63] are also included on fig. 4.4. These are measured from ion scattering spectroscopy experiments and are identified by circles to distinguish
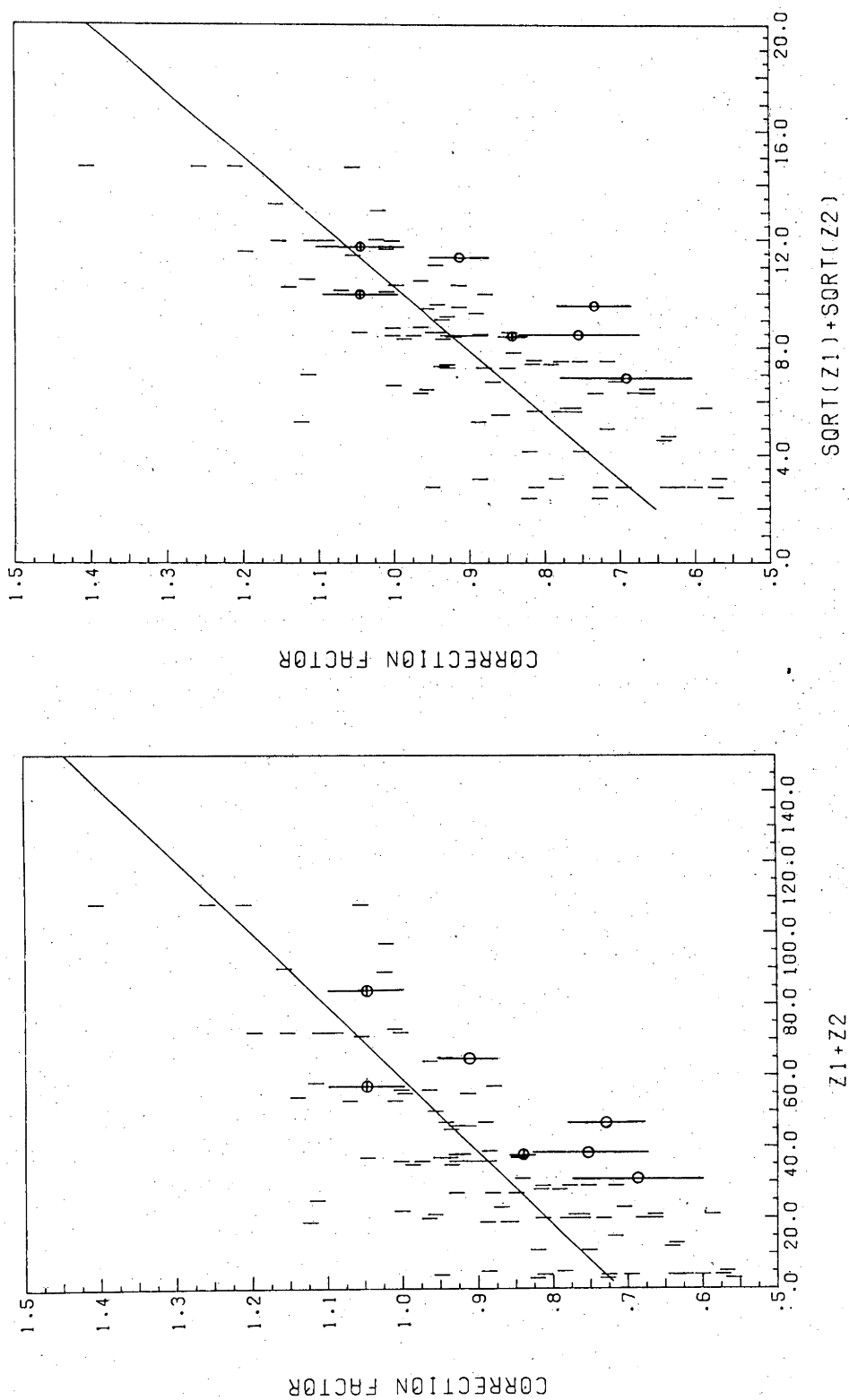
Fig. 4.4: Comparison of the correction factors to the screening length determined from the empirical potentials with the ISS results of Poelsema *et al.* (o) and Heiland *et al.* (⊖). The indicated uncertainty in the correction factors from the empirical potentials are from estimates of the accuracy of the fitting procedure. Also included is the least squares fit to the evaluated correction factors.

them from the gas scattering results.   The results of Heiland *et al.* are measured using the dependence of multiply scattered ions on the interatomic potential, whereas the results of Poelsema *et al.* are from measurements of potential dependent features of the single scattering of ions from surfaces.

The spread in the correction factors in fig. 4.4 suggests that there may be at least one other variable involved in this comparison. The additional variable may be the distance of closest approach, the incident ion energy or some other non-characteristic property of the interaction.   As a crude test of this proposition, the empirical potentials were divided into two groups.   The first group included all the empirical potentials which described the interaction above 10 eV and the second were those which applied for less than 10 eV.   It should be stated before continuing that 10 eV is an arbitrary division, chosen to yield two reasonable size groups of results.   The correction factors for these groups are shown in figure 4.5.   It is evident that the linear relationship is more pronounced for the low energy results and that the dependence for the higher energy results is nearly a constant.

4.6   CONCLUSIONS

There is experimental evidence from both gas scattering and ion scattering spectroscopy to indicate that the Moliere potential is an accurate description of the interatomic potential for low energy atomic collision applications.   It has also been shown that better agreement to this potential can be achieved if a simple correction factor is applied to the Firsov screening length $(F_3(Z_1,Z_2))$.   The increased confidence in scattering cross sections obtained using the Moliere potential and the corrected screening length will assist in investigations of other Ion Scattering Spectroscopy phenomena (e.g. charge exchange, thermal vibrations, surface composition, etc.).

The results presented in fig. 4.4 will be compared with experimental results reported in chapter six from this investigation.
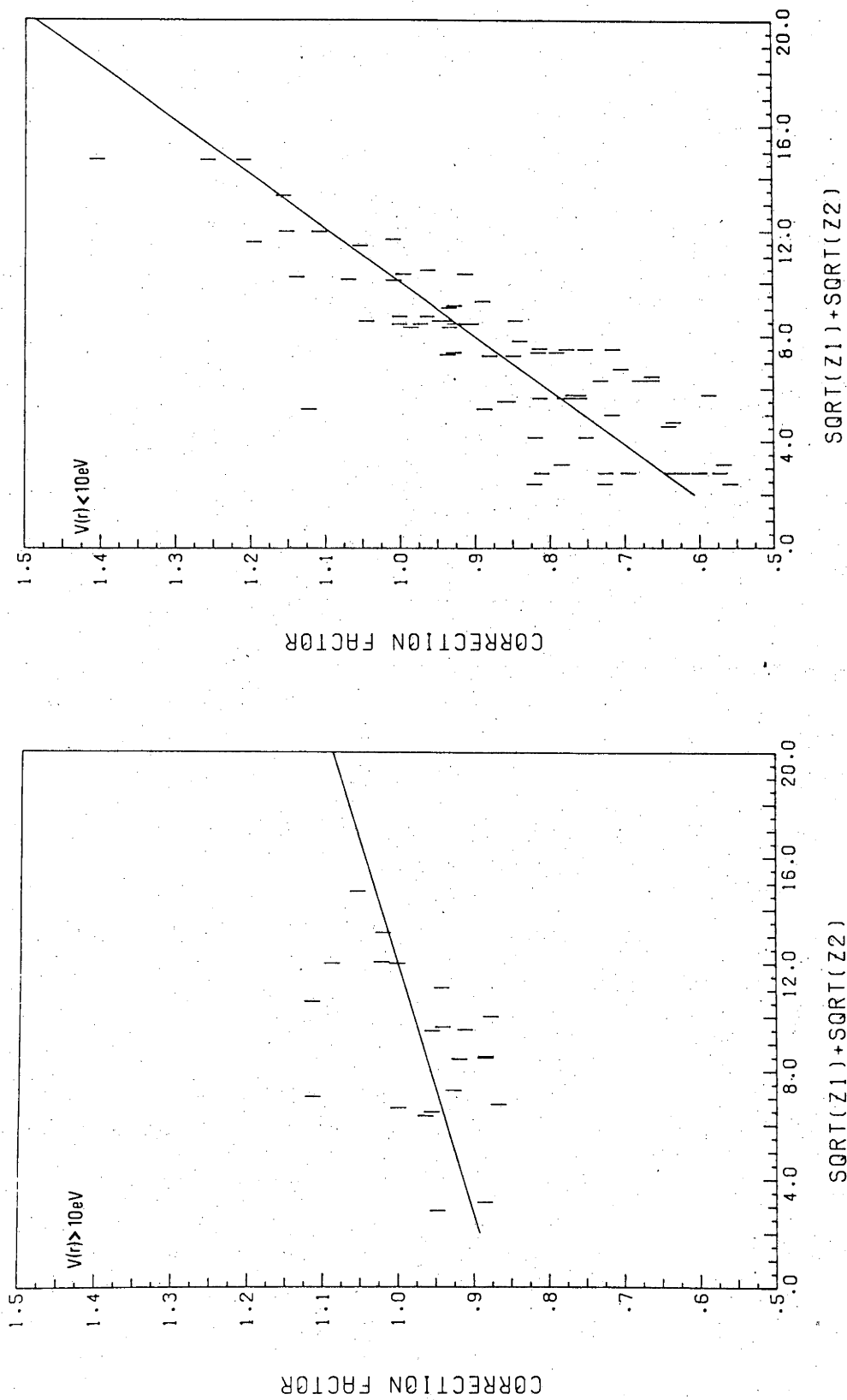
Fig. 4.5: Comparison of the screening length correction factors for empirical potentials which describe the potential above 10 eV with those which describe the potential below 10 ev.

Additional analysis is in progress to determine the nature and importance of other parameters to the screening length correction factor to attempt to improve on the agreement so far obtained.

REFERENCES

(1) I.M. Torrens, *Interatomic Potentials* (Academic Press, 1972).

(2) P. Sigmund, *Rev. Roum. Phys.* 17 (1972) 823.

(3) *Interatomic Potentials and Simulation of Lattice Defects*, eds. P.C. Gehlen, J.R. Beeler Jr. and R.I. Jaffee (Plenum Press, 1972).

(4) A.A. Abrahamson, *Phys. Rev.* A178 (1969) 76.

(5) D.R. Hartree, *Proc. Cambridge Philos. Soc.* 24 (1928) 111.

(6) D.R. Hartree, *The Calculation of Atomic Structures* (Wiley, 1955).

(7) J.C. Slater, *Phys. Rev.* 25 (1950) 210.

(8) V. Fock, *Z. Phys.* 61 (1930) 126.

(9) L.H. Thomas, *Proc. Cambridge Philos. Soc.* 23 (1927) 542.

(10) E. Fermi, *Z. Phys.* 48 (1928) 73.

(11) P.A.M. Dirac, *Proc. Cambridge Philos. Soc.* 26 (1930) 376.

(12) R. Latter, *Phys. Rev.* 99 (1955) 510.

(13) G. Moliere, *Z. Naturforsch.* 2a (1947) 133.

(14) P. Csavinsky, *Phys. Rev.* 166 (1968) 53.

(15) R.E. Roberts, Univ. Wisconsin Theoret. Phys. Inst. Rep. WIS-TCI (1967).

(16) N. Anderson, A.M. Arthurs and P.D. Robinson, *Nuovo Cimento* 57B (1968) 523.

(17) N. Bohr, *Kgl. Dansk. Vid. Selsk. Mat.-Fys. Medd.* 18 (1948) No. 8.

(18) A.A. Abrahamson, R.D. Hatcher and G. Vineyard, *Phys. Rev.* 121 (1961) 159.

(19) A.A. Abrahamson, *Phys. Rev.* 130 (1963) 693.

(20) A.A. Abrahamson, *Phys. Rev.* 133 (1964) A990.

(21) K. Gunther, *Ann. Phys.* <u>14</u> (1964) 296.

(22) O. Gustafsson, *Ark. Fys.* <u>40</u> (1970) 465.

(23) O.B. Firsov, *Zh. Esksperim. Teor. Fiz.* <u>24</u> (1963) 279.

(24) F.T. Smith, R.P. Marchi and K.G. Dedrick, *Phys. Rev.* <u>150</u> (1966) 79.

(25) I. Amdur, *J. Chem. Phys.* <u>17</u> (1949) 844.

(26) I. Amdur, D.E. Davenport and M.C. Kells, *J. Chem. Phys.* <u>18</u> (1950) 525.

(27) I. Amdur and A.L. Harkness, *J. Chem. Phys.* <u>22</u> (1954) 664.

(28) I. Amdur and E.A. Mason, *J. Chem. Phys.* <u>22</u> (1954) 670.

(29) I. Amdur, E.A. Mason and A.L. Harkness, *J. Chem. Phys.* <u>22</u> (1954) 1071.

(30) I. Amdur and E.A. Mason, *J. Chem. Phys.* <u>23</u> (1955) 415.

(31) I. Amdur and E.A. Mason, *J. Chem. Phys.* <u>23</u> (1955) 2268.

(32) I. Amdur and E.A. Mason, *J. Chem. Phys.* <u>25</u> (1956) 624.

(33) I. Amdur and E.A. Mason, *J. Chem. Phys.* <u>25</u> (1956) 630.

(34) I. Amdur and E.A. Mason, *J. Chem. Phys.* <u>25</u> (1956) 632.

(35) S.O. Colgate, J.E. Jordan, I. Amdur and E.A. Mason, *J. Chem. Phys.* <u>51</u> (1969) 968.

(36) Y.U.N. Belgaev and V.B. Leonas, *Sov. Physics — Doklady* <u>12</u> (1967) 233.

(37) A.B. Kamnev and V.B. Leonas, *Sov. Physics — Doklady* <u>10</u> (1965) 529.

(38) A.B. Kamnev and V.B. Leonas, *Sov. Physics — Doklady* <u>10</u> (1965) 1202.

(39) V.B. Leonas and A.B. Sermyagin, *JETP Letters* <u>12</u> (1970) 300.

(40) R.E. Olson, F.T. Smith and C.R. Mueller, *Phys. Rev.* <u>A1</u> (1970) 27.

(41) J.E. Jordan and I. Amdur, *J. Chem. Phys.* <u>46</u> (1967) 165.

(42) A.J.H. Boerboom, H. Van Dop and J. Las, *Physica* <u>46</u> (1970) 458.

(43) I. Amdur and J.E. Jordan, *Advances in Chemical Physics* <u>10</u> (1966) 29.

(44) I. Amdur, J.E. Jordan, K.R. Chien, M. Fung, R.L. Hance, E. Hulpke and S.E. Johnson, *J. Chem. Phys.* 57 (1972) 5.

(45) H. Inouye and S. Kito, *J. Chem. Phys.* 57 (1972) 1301.

(46) H. Inouye and S. Kito, *J. Chem. Phys.* 56 (1972) 4877.

(47) W.J. Savola Jr, F.J. Eriksen and E. Pollack, *Phys. Rev.* A7 (1973) 932.

(48) V.B. Leonas, *Sov. Physics — Uspekhi* 15 (1973) 266.

(49) J. Sielanki, H. Van Dop, J. Las and J. Kistemaker, *Physica* 70 (1973) 591.

(50) P.B. Foreman, P.K. Roland and K.P. Coffin, *J. Chem. Phys.* 61 (1974) 1658.

(51) S. Kito, K. Noda and H. Inouye, *J. Chem. Phys.* 63 (1974) 1658.

(52) I. Amdur, H.J. Engler, J.E. Jordan and E.A. Mason, *J. Chem. Phys.* 63 (1975) 597.

(53) S. Kito, K. Noda and H. Inouye, *J. Chem. Phys.* 64 (1976) 3446.

(54) C. Foster, I.H. Wilson and M.W. Thompson, *Journ. Physics* B5 (1972) 1332.

(55) M.W. Thompson and C. Foster, private communication.

(56) E.A. Mason and J.T. Vanderslice, *Atomic and Molecular Processes*, Ch. 17, ed. D.R. Bates (Academic Press).

(57) I. Amdur and H. Pearlman, *J. Chem. Phys.* 9 (1941) 503.

(58) H.W. Berry, *Phys. Rev.* 75 (1949) 913.

(59) H.W. Berry, *Phys. Rev.* 99 (1955) 553.

(60) D.J. O'Connor and R.J. MacDonald, *Radiation Effects* 34 (1977) 247.

(61) E. Kreyszig, *Advanced Engineering Mathematics*, p.785 (Wiley, 1972).

(62) B. Poelsema, L.K. Verhey and A.L. Boers, *Surface Science* 64 (1977) 554.

(63) W. Heiland, E. Taglauer and M.T. Robinson, *Nucl. Inst. Methods* 132 (1976) 655.

(64) O.B. Firsov, *Sov. Physics — JETP* 7 (1958) 308.

CHAPTER FIVE

COMPUTER SIMULATIONS

5.1 INTRODUCTION

The interaction of an energetic ion with a solid is a complex process which cannot be fully modelled by either analytical or simulation techniques. However, an understanding of the physical processes involved in such an interaction is only possible if the experimental observations can be related to physical parameters of the solid or to parameters of the interaction itself. For such a comparison to be made it is necessary to be able to predict the results of a model of the interaction with the solid as a physical parameter is varied. More complex models normally need to be simplified by assumptions about the nature of the interaction in order that they may be solved by analytical or numerical techniques. Care must be exercised to ensure that the assumptions made are realistic, otherwise predicted effects may only be artefacts of the unrealistic model.

Where possible the analytical approach is used as it is quicker than simulation techniques and it is easier to gauge the importance of a parameter from an algebraic expression. A major advantage of the analytical technique is that a variation of experimental conditions can be accounted for usually by a change of constants, but for the simulation technique it normally involves additional computing time. Unfortunately for low energy interactions, and to a lesser degree medium energy interactions, the analytical approach has very limited application. In these energy ranges the scattering integral (equation 5.1) has no general analytical solution which means that the determination of scattering angle and scattering cross section becomes a numerical problem which is not suited to simple analytical methods.

The scattering integral does have an analytical solution for the impulse approximation with some potentials.[1] For other potentials, which have restricted ranges of validity, exact analytical solutions exist. The limitations of these approximations restrict their general usage. The complexity of the low energy ion scattering model, incorporating discrete correlated collisions, compounds the problems associated with the analytical techniques to the extent that in general an intractable set of expressions is obtained and it becomes necessary to resort to numerical techniques.

A computer simulation has the advantage that it can solve the scattering integral numerically, as well as include a range of effects that would be difficult to incorporate in an analytical approach. However this advantage is achieved at the expense of program simplicity and speed of operation, normally resulting in increased cost for the use of computing facilities.

5.2 COMPUTER SIMULATION

The following description of important aspects of computer simulations is restricted to those of significance to the modelling of low energy ion scattering events. A more comprehensive description of the range of features associated with computer simulation of the ion-solid interaction process can be found in reviews[2-4] and program description papers.[5-9]

To compare a simulation to experimental observations it is necessary to produce a model of the solid and of the interaction of the ion with the solid, which is as near as possible to the real conditions. An ideal simulation would involve the following features:

(1) Large three-dimensional lattice with facilities for multi-element single crystals.

(2) Random relocation of the target atoms to account for thermal vibrations.

(3) Lattice Defects.

(4) Surface Relaxation.

(5) Surface Topography and defects.

(6) Charge exchange processes.

(7) Inelastic Energy loss.

(8) Ability to follow target atoms displaced from their lattice sites.

(9) Ability to change from binary collision to stepwise integration of trajectories if many-body effects become important.

Such a program, although versatile enough to satisfy most simulation requirements, would be too complex and too slow for individual applications. In addition, sufficient knowledge of most of the effects mentioned above is not yet available to allow satisfactory inclusion in a simulation. Most are still the subject of active research programs designed to determine the importance of these effects in ion-solid interaction. In most applications where only a few of these effects are important it is worthwhile using a specialized program to reduce computer processing time.

Most simulations have been developed for digital computers and they can be classified by the technique used to determine the path an energetic particle follows through the array of atoms. One technique is the stepwise integration of the path of the particle through the solid. In its simplest form it involves the evaluation of the forces experienced by a particle at a given time "t" and, knowing the position and velocity at that time, then determining the position of the particle at some later time "t + dt". This technique is slow but it does have the advantage of accurately describing the path of an ion when it is interacting with several atoms at any given time. This is especially the case for low energy particles where "effective mass" considerations are important. The speed and accuracy of this technique can be improved by the use of more advanced numerical techniques,[10] however it is still slower than the binary collision method described below.

The binary collision technique is usually used when the collisions can be treated as single discrete events. This method

involves calculating the scattering integral in order to determine the scattering angle from the impact parameter and ion energy, or else interpolating from a predetermined table of values of scattering angle. Details of these techniques can be found in the reviews and papers referred to previously. [2-9]

Another less common approach is through the use of a hybrid computer [6] which is the combination of an analogue and a digital computer. The advantage of the analogue computer is that it is faster because it can simultaneously solve a set of differential equations which on a digital computer would have to be solved separately by slower numerical techniques. In the hybrid system, the digital computer is used to facilitate the variation of starting conditions and to store intermediate results. It is claimed that the execution time on a hybrid or analogue computer is "typically seconds as contrasted to minutes of digital computation". [6] The savings in computer time are gained at the expense of accuracy and versatility. Hybrid computer facilities are not generally available so that further comparison to digital systems is not possible.

5.3 GENERAL DESCRIPTION OF SIMULATIONS USED IN THIS INVESTIGATION

A description follows of the computer simulations written to compare with the experimental observations which will be reported in the following chapter. There were three main simulation programs written to investigate different aspects of the scattering of low energy ions from crystal surfaces. One was a three-dimensional simulation written in FORTRAN IV code and was run on a UNIVAC 1100/42 computer. The other two programs, which were also in FORTRAN IV, were specialized atomic chain model simulations and were run on a HEWLETT-PACKARD 21MX computer. Before the programs are described individually, the common features of all three will be discussed.

All three simulations use the binary collision method described previously because it has been shown (see chapter two) that the binary collision model is valid down to several hundred eV or lower. In

addition, a test program using the stepwise integration technique was developed and it confirmed that neighbouring interactions were unimportant at the energies used in this study (i.e. > 1 keV). This test program was not developed further as it was found to be too slow for most applications.

The binary collision approach involves the numerical integration of the scattering integral at each collision or an interpolation from a predetermined table of values for the integral. The former technique is more time consuming and the latter requires more memory space.

In order to minimize memory requirements the numerical integration method was used and a relatively fast integration technique was developed for the evaluation of the scattering integral.

The scattering integral is difficult to evaluate in the form given by equation 5.1. The integrand is infinite at one limit of integration and the other limit is infinity:

$$\psi = \pi - 2s \int_{R_0}^{\infty} \frac{dr}{r^2 \sqrt{1 - \frac{s^2}{r^2} - \frac{V(r)}{E}}} , \qquad 5.1$$

where ψ is the scattering angle in the centre of mass system, s is the impact parameter, E is the reduced energy (equation 5.3) and R_0 is given by:

$$1 - \frac{s^2}{R_0^2} - \frac{V(R_0)}{E} = 0 , \qquad 5.2$$

where

$$E = \frac{M_2 E_0}{M_1 + M_2} . \qquad 5.3$$

Both of these problems can be eliminated by a change of variable[11] given by:

$$r = \frac{R_0}{1 - u^2} , \qquad 5.4$$

thus

$$\frac{dr}{r^2} = -\frac{2u\ du}{R_0}.$$
(5.5)

This change of variable results in the following expression:

$$\psi = \pi - 4 \int_0^1 \frac{du}{\sqrt{2 - u^2 + \dfrac{R_0^2}{Es^2 u^2}\ [V(R_0) - V(r)]}}.$$
(5.6)

By taking the limit of the expression in the denominator as "u" approaches zero, it can be shown that no singularities exist if the following condition is satisfied:

$$\frac{dV(R_0)}{dr} < \frac{2Es^2}{R_0^3}.$$
(5.7)

As this condition is always satisfied for repulsive potentials, this function is well behaved. The integrand in equation 5.6 is a slowly varying monotonic function of "u" which increases from:

$$\left(2 - \frac{R_0^3}{Es^2}\ \frac{dV(R_0)}{dr}\right)^{-\frac{1}{2}} \qquad \text{for } u = 0$$

to

$$\frac{s}{R_0} \qquad \text{for } u = 1\ .$$

This means that the integral can be accurately evaluated using one of the simple equal interval numerical integration techniques (e.g. Simpson's Rule).

To test the accuracy of this technique, the results of the numerical integration described above were compared to an adaptive quadrature integration technique.[12] It was found that the agreement was to within 0.1% or better for the determination of the laboratory angle θ using the Moliere potential. As a further test, the simplified technique was used to compute the scattering integral for the inverse square potential for which there is an analytical solution. Agreement was found to be within 0.1% or better for the determination of θ.

To uniquely determine the path of an ion after a collision both the scattering angle and a point on the exit asymptote must be

evaluated. The former we have already covered and the latter can be determined from the "time" integral[8,9] (see fig. 5.1):

$$dx = \frac{2M_1 \, \tau}{M_1 + M_2} + \frac{M_2 - M_1}{M_2 + M_1} \, s \, \tan \frac{\psi}{2},$$

5.8

where τ is given by:

$$\tau = (R_0^2 - s^2)^{\frac{1}{2}} - \int_{R_0}^{\infty} \left(\frac{1}{\sqrt{1 - \frac{s^2}{r^2} - \frac{V(r)}{E}}} - \frac{1}{\sqrt{1 - \frac{s^2}{r^2}}} \right) dr .$$

5.9

The "time" integral presents more problems than equation 5.1 because not only is the integrand infinite at one limit of integration and the other limit at infinity, but also no change of variable will satisfactorily remove these difficulties. The latter problem can be removed by a change of variable to $u = R_0/r$ but the integrand remains infinite at the other limit. This is therefore a more difficult integral which would be much more time consuming to evaluate than the scattering integral. The exit asymptote location is unimportant for single scattering events as neighbouring atoms are not involved, but it will be significant in the multiple collision sequences.

In the multiple collision events of interest in these simulations, the scattering angle for each event is smaller than for the single scattering event. For small angle scattering the exit asymptote can be determined by the hard sphere approximation of Begemann[13] (see fig. 5.2):

$$s' = s \cdot \frac{\cos\left(\frac{\psi}{2} - \theta\right)}{\cos\left(\frac{\psi}{2}\right)} .$$

5.10

Although not an exact method it is a good approximation for the small angle scattering events encountered in multiple scattering. As with any other computer simulation approximation, the effect of this approximation should be considered if major differences are found between the simulation results and the experimental observations.

As this expression will cause problems for large angle multiple
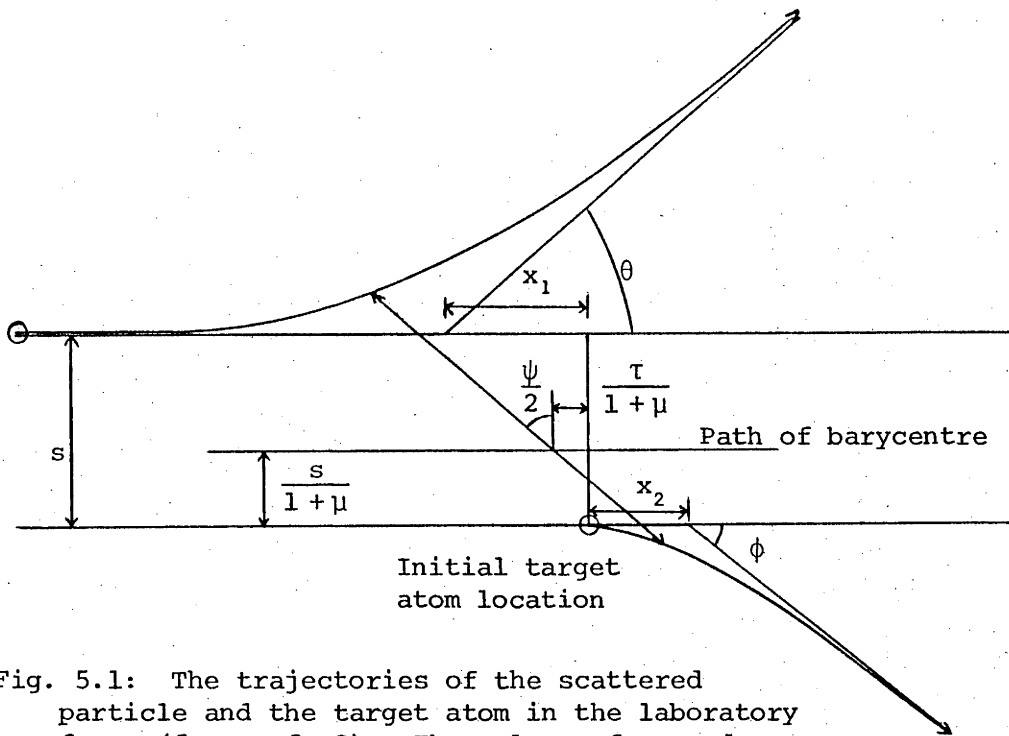
Fig. 5.1: The trajectories of the scattered particle and the target atom in the laboratory frame (from ref. 8). The values of x_1 and x_2 can be determined from the following equations:

$$x_1 = \left[2\tau + (\mu - 1) \; s \; \tan \frac{\psi}{2} \right] \Big/ (1 + \mu)$$

$$x_2 = s \; \tan \frac{\psi}{2} - x_1 \; .$$
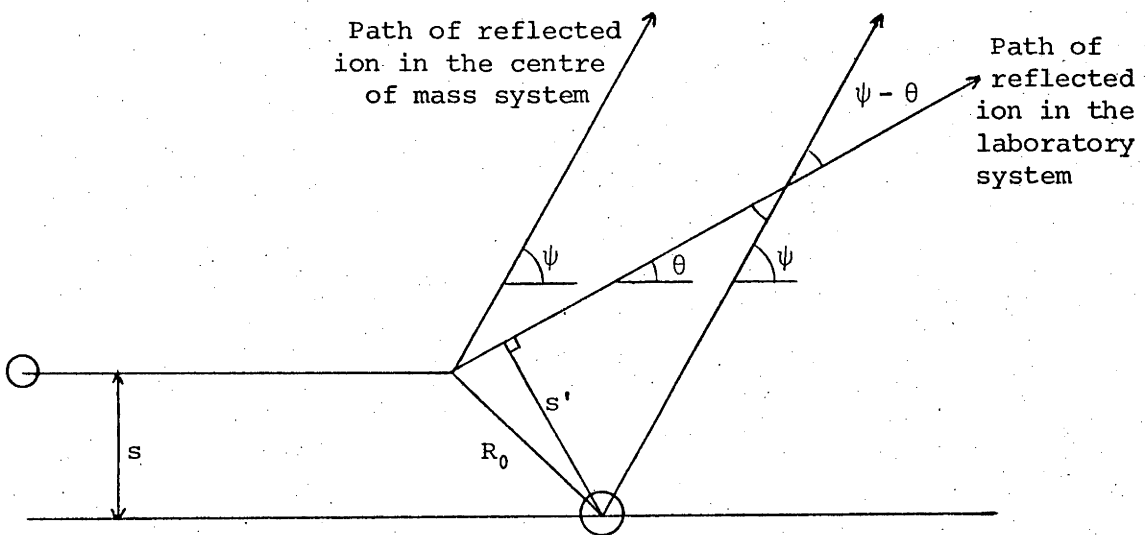
Fig. 5.2: Illustration of the relationship between the precollision impact parameter, s, and the post collision impact parameter, s'. (From reference 13.)

collision events, these simulations are restricted to forward scattering studies. This does not seriously limit its range of applications as most low energy ion scattering experiments involve forward scattering to achieve large scattering cross sections. The larger cross section offsets the high neutralization probability.

The two simulations which use the chain model, do not follow energetic target atoms ejected from their lattice sites. As only forward scattering is considered, the trajectory of the ion is unaffected by the vacancies it creates. Although the facility to follow recoil target atoms is available in the three-dimensional model, it is not normally used as it has little effect on the scattered particles. An ion which suffers a sufficiently hard collision to cause a vacancy and then one or more hard collisions which direct it past the same lattice site a second time, will have lost sufficient energy to ensure that it does not contribute to the high energy portion spectrum. It is also assumed that the additional time spent by this particle in the surface region will strongly increase the chances of neutralization.

In the simulations reported below, the inelastic energy losses were not included as sufficient information on these processes as when occurring at, or near the surface is not yet available. It is proposed to measure the inelastic loss by comparing the experimental observations with the results of the computer simulations.

5.4   THE THREE-DIMENSIONAL MODEL

The purpose of the three-dimensional model is to determine the features of low energy ion scattering which are not revealed by simpler models. In particular, it was necessary to determine the fate of the large percentage of incident ions which were disregarded by the chain model, i.e. those initially incident at points on the surface between atomic rows. As well, it was necessary to determine whether there were any major contributions to the energy spectrum other than from the single and double scattering predicted by the chain model. Finally, the three-dimensional model helped to evaluate the importance

of scattering from lower atomic planes and of ion penetration.

It was found that most of the scattered particles observed in the direction corresponding to the experimental arrangement were the result of scattering off the atomic chains (see fig. 5.3a). This is then a justification for comparison of the chain model with the experimental observations to be reported later. The results of the three-dimensional model were not used in direct comparison with experimental observations as the statistics were much poorer with this model than for the simpler and faster chain model simulations.

The three-dimensional model is a simplified version of the model described by Robinson and Torrens.[8] It works from a unit cell of the crystal and effectively creates the crystal structure in the direction that the ion is travelling in order to reduce memory requirements. This is achieved by relocating the ion with respect to the unit cell whenever it crosses the cell boundaries. The reduced number of target atoms helps speed up the collision partner search procedure. In collision sequences involving interactions with two or more target atoms simultaneously, the collisions are treated separately and the final direction is then taken as the vectorial sum of the individual directions.

The incident ions are evenly distributed over a representative area of the surface and the final fate of these ions falls into one of three classes. The first category consists of those ions which are singly or multiply scattered and escape the solid. This is the most important class as these ions have a better chance of remaining ionized and thus can be detected experimentally. The second category are those which pass below a preset depth (normally five atomic layers). These are regarded as "lost" in that if they were eventually scattered back out of the solid then sufficient energy would be lost by elastic and inelastic processes that they would not contribute to the single and multiple scattering yield. Also, by traversing such a large distance inside the solid there is a strong chance that they would emerge as neutrals and thereby escape detection. The third category incorporates all those ions which are still inside the surface region after a preset number of collisions (typically 200

Incident

beam direction
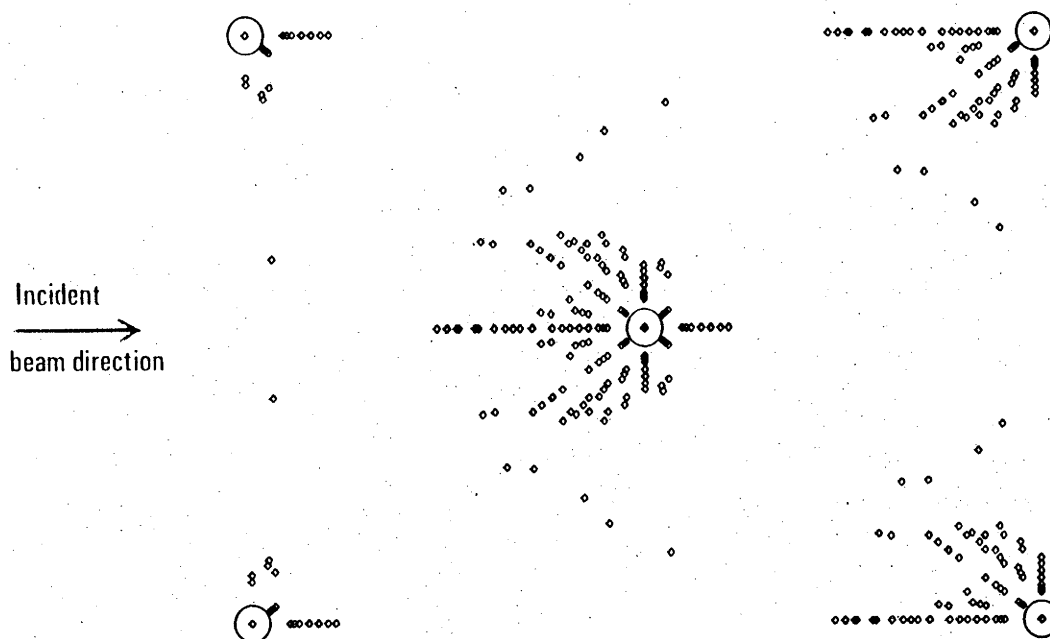
Fig. 5.3a: Results of the three-dimensional simulation for 6 keV Kr[+]
incident at 30° to the ⟨110⟩ surface chain of a W(110) crystal
face. The circles represent a surface unit cell, and the initial
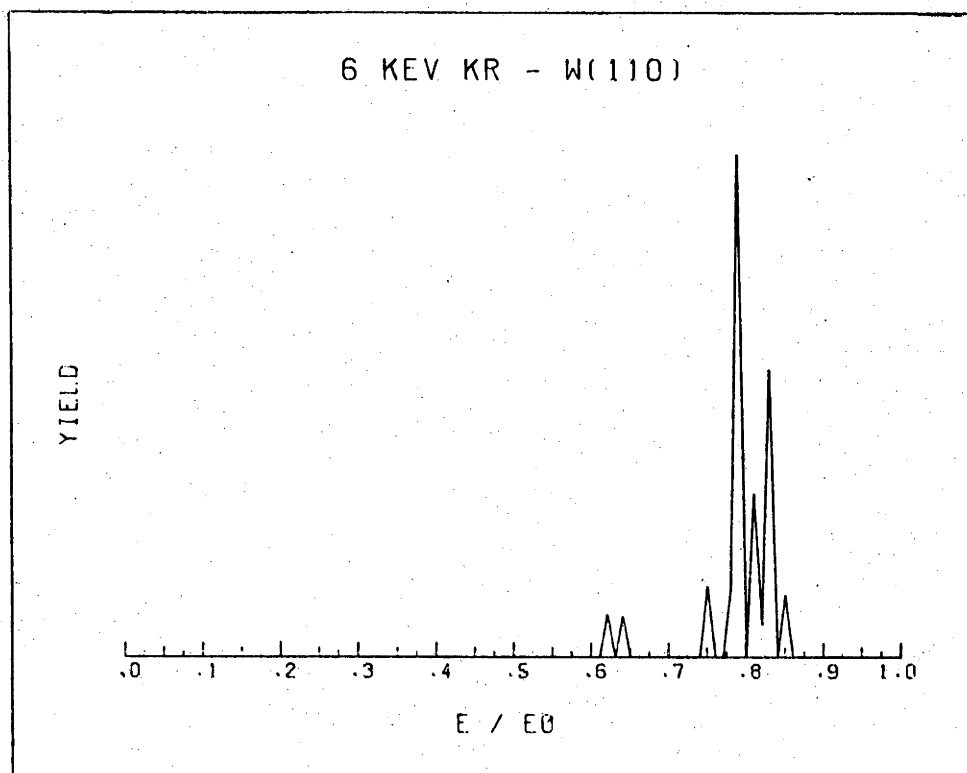impact sites which result in scattered ions are plotted.

6 KEV KR - W(110)

YIELD

.0   .1   .2   .3   .4   .5   .6   .7   .8   .9   1.0

E / E0

Fig. 5.3b: An energy spectrum of all the ions scattered into a solid
angle which includes all directions which are within 10° of the
total scattering angle of 50°. The simulation conditions are the
same as fig. 5.3a.

collisions). This group comprise those ions which are channelled into surface planar channels. They can be regarded as an intermediate group because on the plot of initial impact site mesh, the impact site of the ions belonging to category three forms a boundary zone between categories one and two.

The third category would be most susceptible to thermal vibrations as a broken chain would reduce the probability of channelling and as well increase the chance of dechannelling.[14] As this category typically includes 1-5% of the total incident ion yield, it was not considered sufficiently significant to warrant inclusion of thermal effects.

Thermal vibrations also have an effect on the angular distributions[15,17] of scattered particles but they were not studied with this model because the experimental apparatus is not capable of measuring this effect. For a proper comparison, an energy analyser with two degrees of freedom about the target is required. For thermal vibrations, additional run time is required for:

(1) Evaluation of the random displacements of the target atom,

(2) additional care in ensuring that an ion does not interact with the same lattice atom twice,[8]

(3) a greater number of trials to reduce statistical fluctuations.

There are three types of output from this simulation taking the form of a plot of the surface representative area (fig. 5.3a), an angular distribution plot (fig. 5.4) and energy spectra (fig. 5.3b). The angular distribution plot is a projection onto the vertical plane of the point on a unit hemisphere through which the ion passes. The energy spectrum can be taken in any desired direction, and the surface representative area plot identifies from which initial impact sites reflected ions originate. The results depicted in figures 5.3 and 5.4 are for the scattering of 6 keV Kr$^+$ off a W(110) face using the Moliere potential, and an angle of incidence of 30° (to the target surface). The ions initially incident in the region between surface atomic chains are scattered out of the plane defined by the incident

6 KEV KR — W(110)
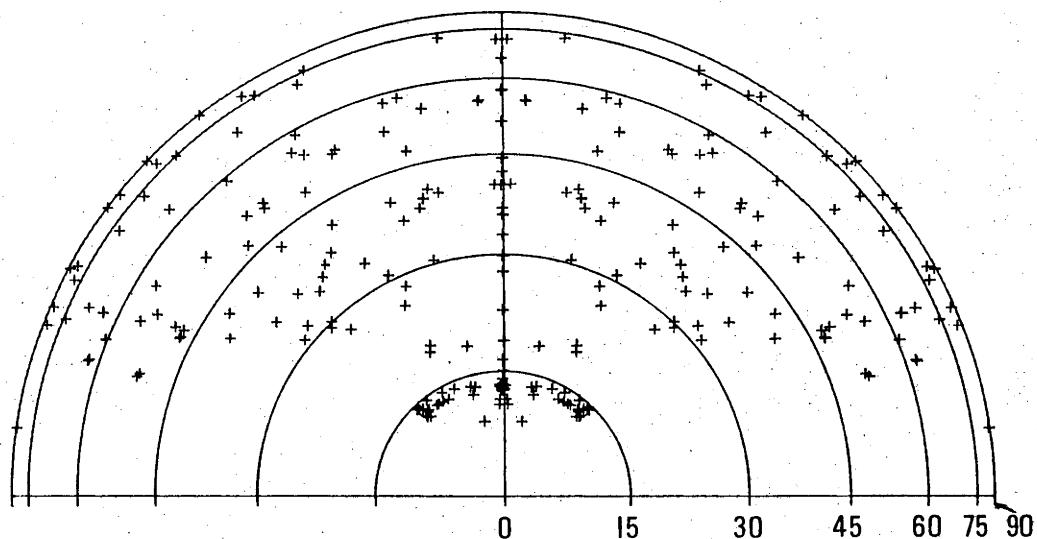
Fig. 5.4: A projection onto the vertical plane of all Kr$^+$ ions which
are forward scattered off a W(110) crystal face. These are the
results of a three-dimensional computer simulation of 6 keV Kr$^+$
ions initially incident at 30° to the W ⟨110⟩ surface direction.
The semicircles represent arcs of constant angular difference to
the surface ⟨110⟩ direction.

beam direction and the target normal. Some are focused by multiple collisions into preferred directions. Similar results have been obtained experimentally for medium and high energy[16] (20 keV - 2 MeV) low angle scattering but these results involve greater penetration of the solid.[18] Comparable results, including preferential scattering into non-specular directions have been obtained with other simulations.[17]

5.5   THE ENERGY ANGLE LOOP SIMULATION

This simulation was designed to study the importance of the interatomic potential in determining the relationship between the angle of incidence and the energy of the ions singly and multiply scattered from an atomic chain. It has been shown that the interatomic potential can be measured by comparing experimental observations to simulation results.[19-21] Objections have been raised concerning some aspects of these techniques,[22] but this point will be discussed in greater detail in the next section.

The evaluation of the inelastic energy loss by atoms scattered off the surface is only possible if the measured energy spectrum is compared to simulations using the chain model and a realistic interatomic potential. In this simulation the total scattering angle remained constant to conform with the experimental conditions ($\theta = 60°$). The interaction simulated is that of energetic ions scattered off a single chain of atoms. The atoms of the chain are assumed to be stationary and on their lattice sites (i.e. no thermal vibrations). The incident ions are distributed over a range of impact parameters from zero to d.sinα (see fig. 5.5), where d is the interatomic separation of the atoms of the chain and α is the angle of the incident ion beam to the chain direction. The impact parameters were distributed over a coarse mesh and when the exit angles of successive trials were either side of the observation angle, successively finer meshes were used until an ion with an exit angle within ±0.1° of the observation direction was located. The coarse mesh was chosen to be sufficiently fine that all significant forward scattering events were detected.
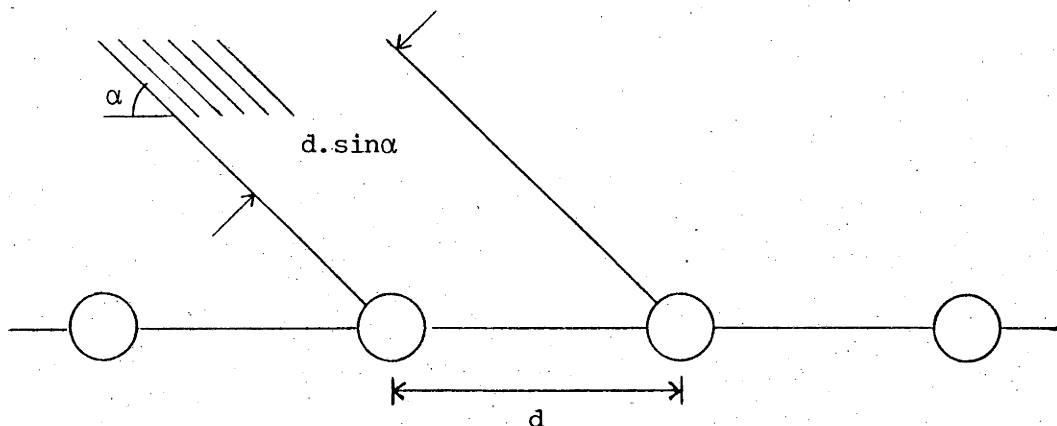
Fig. 5.5: Illustration of the definition of the atomic chain impact
parameter.

In this simulation the Thomas-Fermi screened Coulomb potentials
were used. These potentials take the form:

$$V(r) = \frac{Z_1 Z_2 e^2}{r} \Phi\left(\frac{r}{a}\right) ,$$

5.11

where a is the screening length and $\Phi(r/a)$ is a function to account
for the screening effect of the electron cloud. The interatomic
potentials chosen for this comparison are listed below:

(a) Moliere[23]

$$\Phi(x) = 0.35 \exp(-0.3 x) + 0.55 \exp(-1.2 x) + 0.10 \exp(-6.0 x) .$$ 5.12

This potential was used as it is widely accepted as the most accurate
at these energies.[8,16,20-22].

(b) Csavinsky[24]

$$\Phi(x) = (0.7111 \exp(-0.175 x) + 0.2889 \exp(-1.6625 x))^2 .$$

5.13

As this potential behaves similarly to the Moliere, it was chosen to
determine the sensitivity of this technique.

(c) Sommerfeld[25]

$$\Phi(x) = \left(1 + \left(\frac{x}{12^{2/3}}\right)^\lambda\right)^{-3/\lambda} ,$$

5.14

where [26] $\lambda = 0.8371$. The Sommerfeld potential is a long range interaction and as it is significantly different from the Moliere, it was used to determine the "insensitivity" of this technique.

(d)   Moliere with modified screening length

This potential is the same as the Moliere in form but a correction factor [27] (see chapter four) has been applied to the screening length. The correction factor was determined by a least squares fitting of experimental results to the Moliere potential.

The results of these simulations are shown in figure 5.6. This graph of the energy-angle relationship reveals that the interatomic potential used determines the critical angle of incidence for the closing of the energy-angle loop, and that the differences are large enough to be measurable.

It is important to note that the double scattering curves (i.e. the upper branch of the energy angle loop) for different potentials cross in one angular region. Thus, to a good approximation, a potential independent double scattering energy can be determined in this angular region. This feature will be used to correct the experimental observations for inelastic energy loss.

The critical angle of incidence is dependent on the atomic species used, (Z_1, Z_2), the energy of the incident ion, the interatomic spacing, the total scattering angle and the target temperature. The importance of target temperature is described in the following section. The importance of the first three factors is illustrated in figures 5.7-5.9. As the energy angle loops are almost symmetric about the specular conditions, only the low angle of incidence is included in these figures.

5.6   THE THERMAL VIBRATION MODEL

This simulation is an extension of the Energy Angle Loop simulation except that in this study the effects the thermal vibrations of the chain atoms have on the energy spectra of scattered
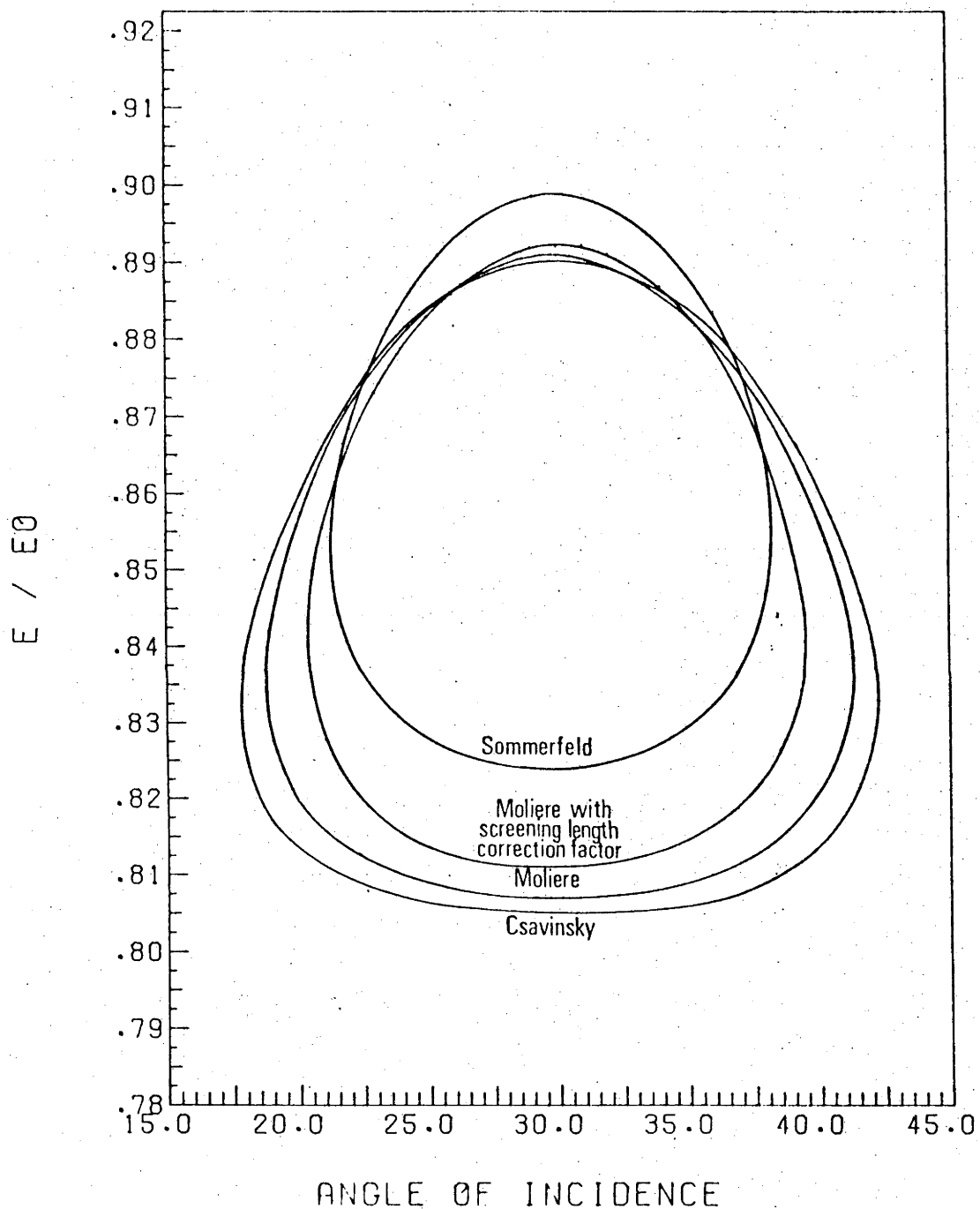
Fig. 5.6: Comparison of the results of the energy angle loop computer
simulation for different interatomic potentials. Note that the
double scattering energies for the Csavinsky potential and the
Moliere potential with and without a screening length correction
factor are equal at an angle of incidence of approximately 27°.
It is evident that the resultant critical angle of incidence for
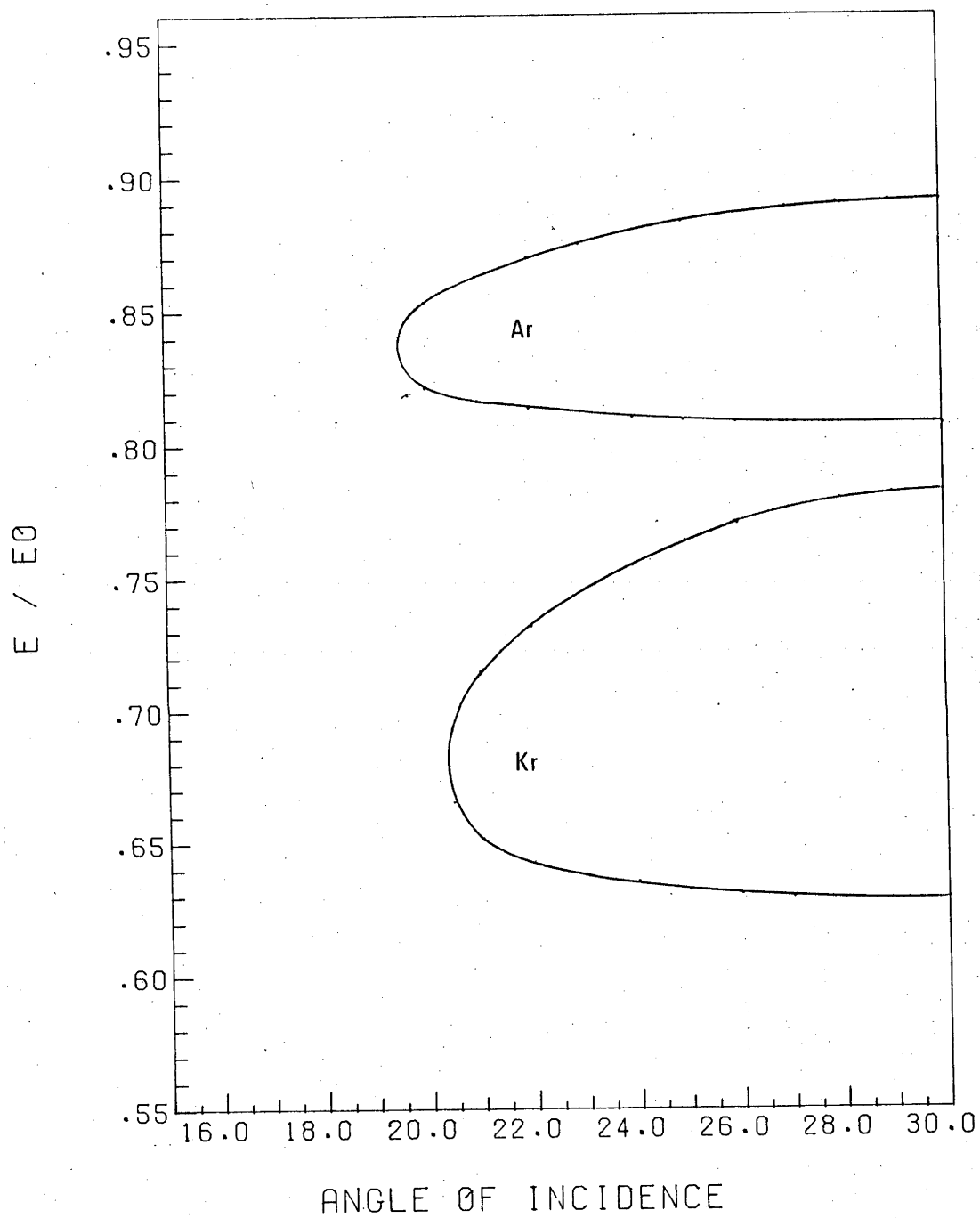each potential is measurably different from each of the other
critical angles.

5 KEV AR AND KR ONTO W <111>

Fig. 5.7: Comparison of the energy angle loops for 5 keV Ar^{+} and Kr[+]
off a W ⟨111⟩ chain. The total scattering angle is 60°.
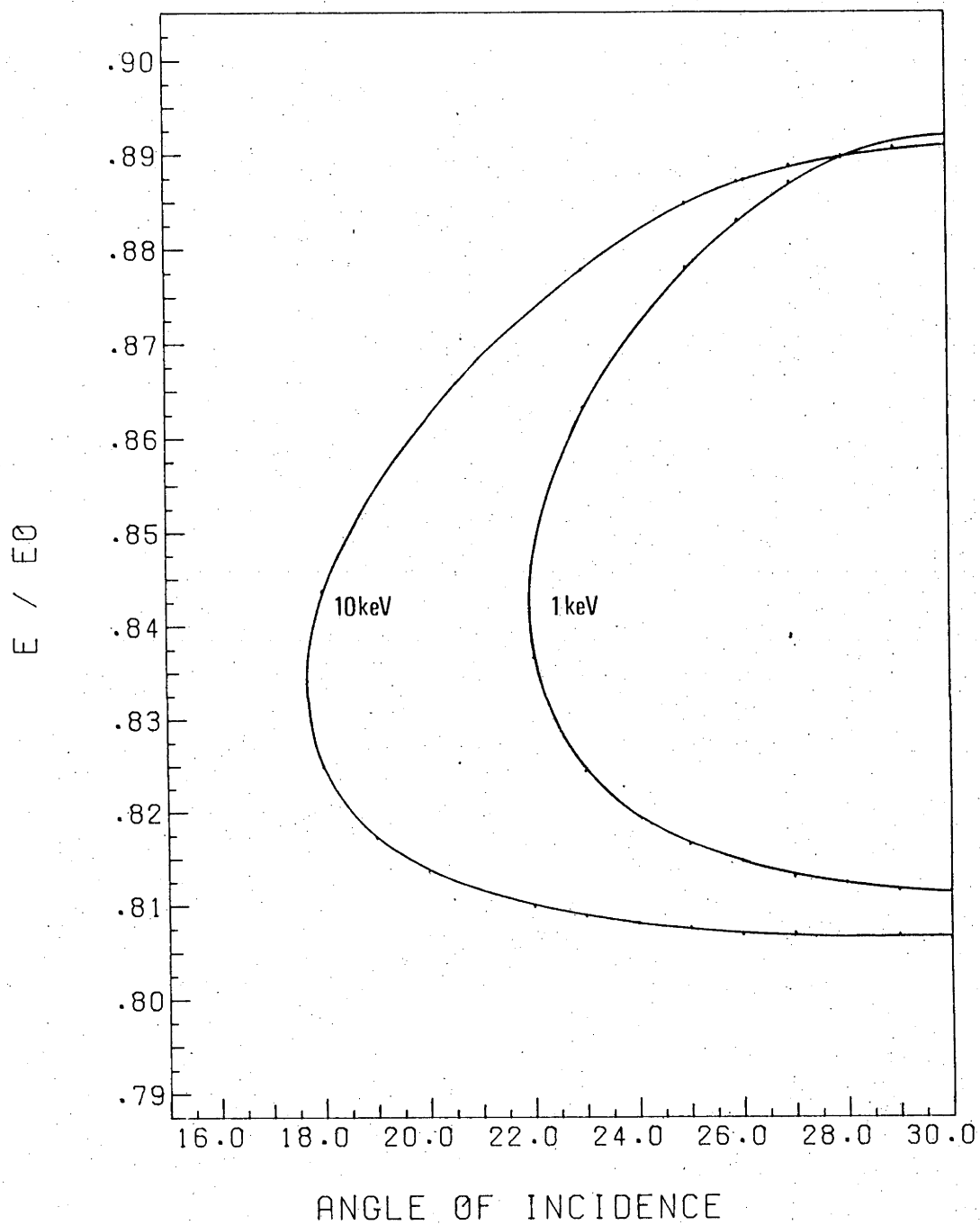
Fig. 5.8: Comparison of the energy angle loops for Ar$^+$ off a W ⟨111⟩ chain at different incident ion energies.

10 KEV AR – W
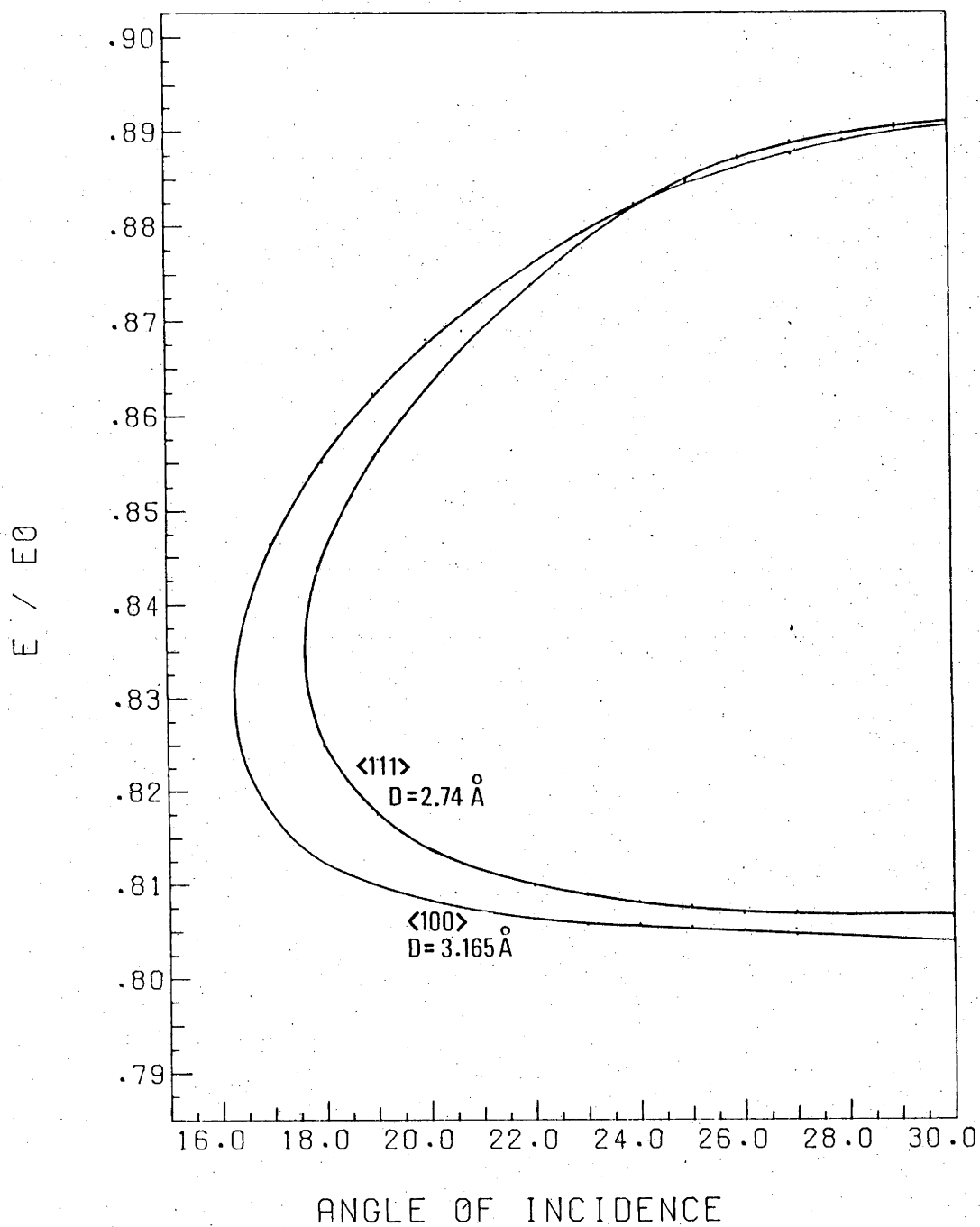
Fig. 5.9: Comparison of the energy angle loops for 10 keV Ar^{+} scattered off ⟨111⟩ and ⟨100⟩ W atomic chains.

ions is examined at different angles of incidence. It is necessary to include thermal vibrations in the chain model to allow the interatomic potential to be estimated from a comparison of simulation results and the experimental observations which were taken at room temperature. Previous attempts to estimate the interatomic potential using this technique[20,21] have been criticized[22] because proper account was not taken of the thermal vibrations.

The atoms of the chain are allowed to vibrate both parallel and perpendicular to the surface. The atoms are regarded as decoupled oscillators which means that the random displacement of an atom is independent of the displacement of its neighbours. The displacements are assumed to be Gaussian distributed with a standard deviation[28,29] given by:

$$\sigma_i = \frac{h}{2\pi\theta_D} \sqrt{\frac{T}{mk}} ,$$ 5.15

where θ_D is the Debye temperature, T is the temperature of the chain, h is Planck's constant, k is Boltzmann's constant and m is the mass of the chain atom.

The values for the Debye temperature were taken from calculations made by Jackson[30] who used the same decoupled oscillator model to determine the surface perpendicular and surface parallel Debye temperatures for the low index faces of a group of face centred cubic (FCC) and body centred cubic (BCC) crystals. The calculated values of the perpendicular Debye temperatures are in good agreement with Low Energy Electron Diffraction results. The Debye temperatures for a W(110) are listed below:

$$\theta_\perp = 186 \text{ °K} ,$$ 5.16

$$\theta_\parallel \langle 100 \rangle = 263 \text{ °K} ,$$ 5.17

$$\theta_\parallel \langle 111 \rangle = 308 \text{ °K} ,$$ 5.18

where $\theta_\parallel \langle 100 \rangle$ and $\theta_\parallel \langle 111 \rangle$ are the Debye temperatures for vibrations in the $\langle 100 \rangle$ and $\langle 111 \rangle$ directions. Two temperatures are given for the (110) faces of FCC and BCC crystals corresponding to the two
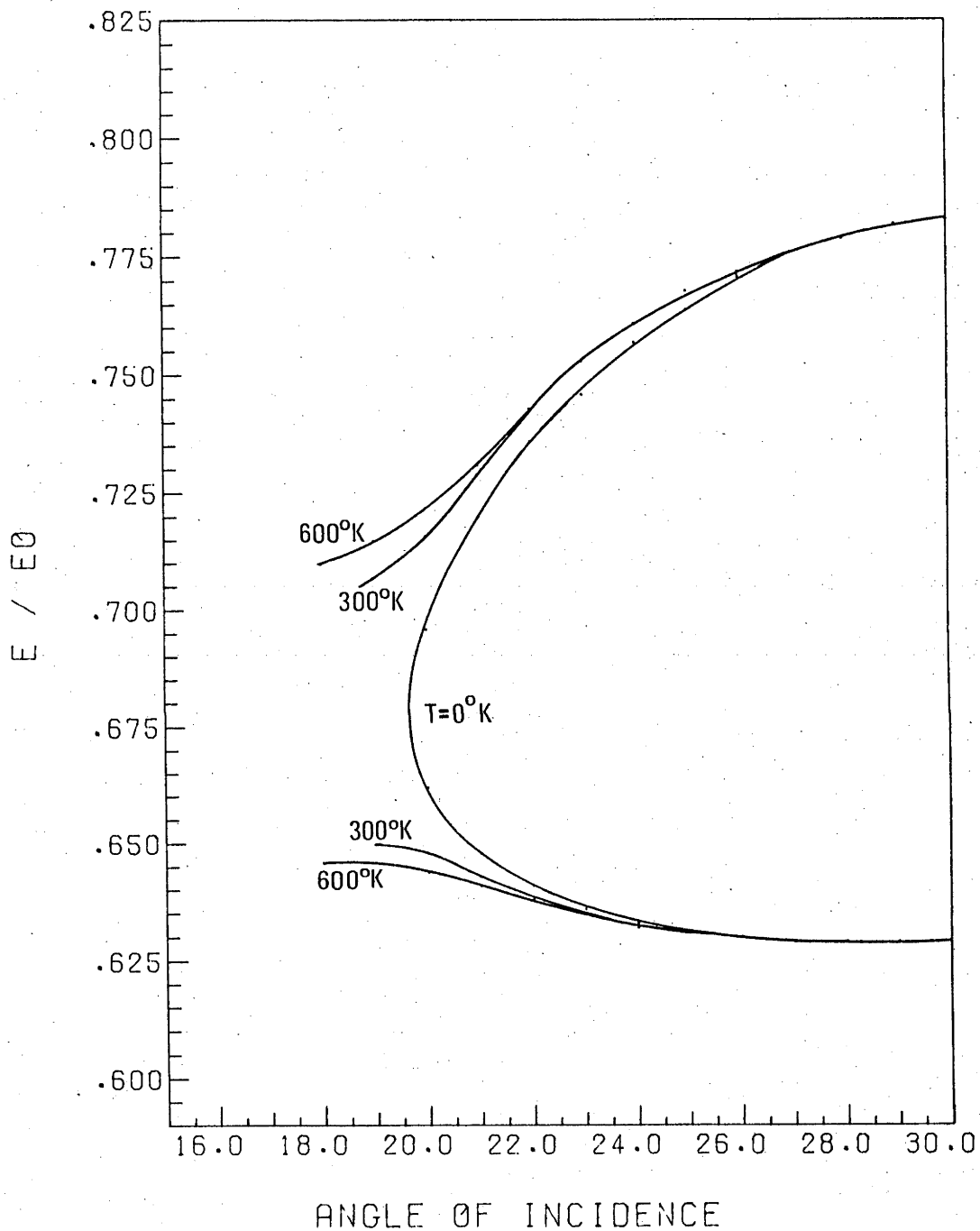
6 KEV KR-W(110)   <111>

Fig. 5.10: Comparison of the predicted energy angle relationship for different surface atomic chain temperatures. Note that the "loop" does not close when thermal vibrations are present.

"principal directions parallel to the surface". As these directions have not been identified, they have been assumed to be the close packed directions. The uncertainty in this assignment necessitates the investigation of the dependence of simulation results on the surface parallel Debye temperature. This was accomplished by simulating the scattering of 6 keV Ar off a W⟨111⟩ chain for different values of the parallel surface Debye temperature. The total scattering angle was 60° and the angle of incidence was 20°. The angle of incidence was chosen to be close to the critical angle predicted by the Energy Angle Loop simulation because under these conditions the results of the Thermal Vibration simulation are more sensitive to the atomic displacements (see fig. 5.10). To within statistical error, no difference was observed between simulations having surface parallel Debye temperatures of 300 °K and 10 000 °K, so that the assignments made above were assumed to be adequate. This test also illustrates the importance of the perpendicular vibrations of the chain atoms as it is these which are responsible for the difference between the perfect and the thermal chain model results.

In this simulation the random displacements of the chain atoms were evaluated, then the chain impact parameter varied from zero to $d.\sin\alpha$ to locate the singly and multiply scattered ions. To build up an energy spectrum, this procedure was repeated for up to 2000 trials, with new displacements for the atoms determined before each trial. In all other aspects, this simulation uses the same procedures outlined for the previous chain model simulation.

The results of the Thermal Vibration simulation have revealed that the energy retained by scattered ions is dependent on the magnitude of thermal displacements near the critical angle of incidence. The effect of the thermal displacements is to change the angle of incidence on an atomic scale (see fig. 2.7) which becomes important when the energy of scattered particles is strongly dependent on the angle of incidence. Near specular conditions, where $dE/d\alpha$ is nearly zero (see figures 5.6 - 5.9) the thermal chain results are similar to the cold chain results. When the critical angle of incidence is approached, when $dE/d\alpha$ is large, the single and multiple
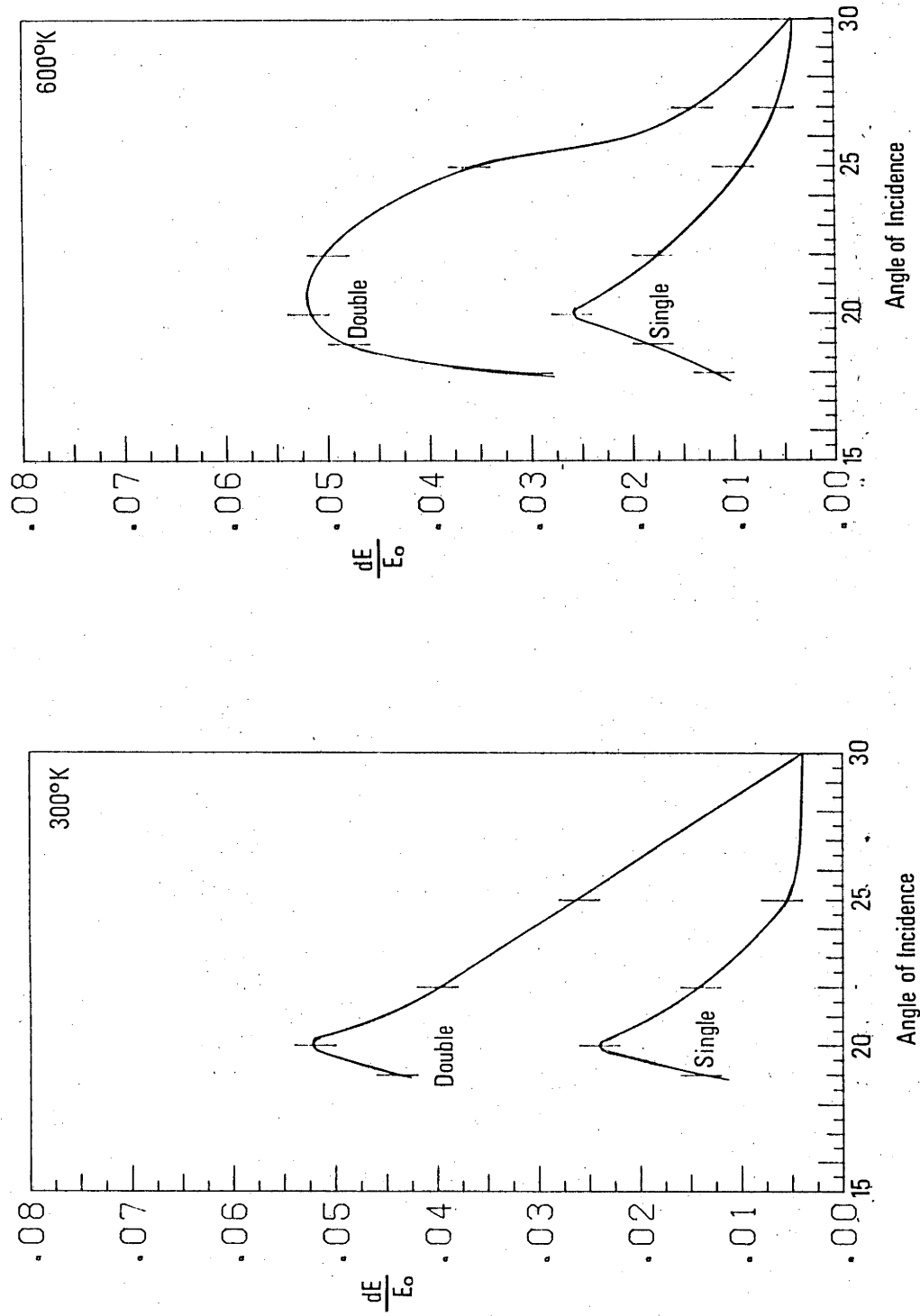
Fig. 5.11: Illustration of the dependence of the peak widths in the energy spectra on the angle of incidence and target temperature. These results were predicted by the computer simulation of 6 keV Kr^+ scattered off a $W \langle 111 \rangle$ chain.

peaks are strongly broadened (see figure 5.11) and the energy difference remains non-zero. It has also been found that as the angle of incidence decreases, the yield of singly and multiply scattered ions decrease which is in agreement with previously reported results.[21,22]

REFERENCES

(1) Chr. Lehmann and G. Leibfried, *Z. Phys.* <u>172</u> (1963) 465.

(2) D.P. Jackson, *Atomic Collisions in Solids*, Vol. 1, p.185, eds. S. Datz, B.R. Appleton and C.D. Moak (Plenum Press, 1975).

(3) D.P. Jackson and D.V. Morgan, *Contemp. Phys.* <u>14</u> (1974) 25.

(4) *Interatomic Potentials and Simulation of Lattice Defects*, eds. P.G. Gehlen, J.R. Beeler Jr. and R.I. Jaffee (Plenum Press, 1972).

(5) A. Van Veen and J. Haak, *Physics Letters* <u>40A</u> (1972) 378.

(6) J. Pearce, R.E. Crosbie, D.G. Armour and G. Carter, *Atomic Collisions in Solids*, Vol. 2, p.611, eds. S. Datz, B.R. Appleton and C.D. Moak (Plenum Press, 1975).

(7) M. Pryde, A.G. Smith and G. Carter, *Atomic Collision Phenomena in Solids*, p.573, eds. D.W. Palmer, M.W. Thompson and P.D. Townsend (North-Holland, 1970).

(8) M.T. Robinson and I.M. Torrens, *Phys. Rev.* <u>B9</u> (1974) 5008.

(9) B. Poelsema, L.K. Verhey and A.L. Boers, *Surface Science* <u>56</u> (1976) 445.

(10) Pp.735-751 of ref. 4.

(11) I.M. Torrens, *Interatomic Potentials*, p.151 (Academic Press, 1972).

(12) K.E. Hillstrom, Argonne National Laboratory Report #ANL-7511.

(13) S.H.A. Begemann, Thesis, chapter 3, Groningen (1972).

(14) D.V. Morgan and D. Van Vliet, *Atomic Collision Phenomena in Solids*, p.476, eds. D.W. Palmer, M.W. Thompson and P.D. Townsend (North-Holland, 1970).

(15) D.S. Karpuzov, *Surface Science* <u>45</u> (1974) 342.

(16) B.W. Farmery, A.D. Marwick and M.W. Thompson, *Atomic Collision Phenomena in Solids*, p.589, eds. D.W. Palmer, M.W. Thompson and P.D. Townsend (North-Holland, 1970).

(17) V.E. Yurasova, *Proc. VII Symposium and Summer School on the Physics of Ionised Gases*, p.427, Rovinj (1974).

(18) M.W. Thompson and J.H. Pabst, to be published in *Radiation Effects*.

(19) A.G.J. De Wit, G.A. Van der Schootbrugge and J.M. Flint, *Surface Science* 47 (1975) 258.

(20) W. Heiland, H.G. Schäffler and E. Taglauer, *Atomic Collisions in Solids*, Vol. 2, p.599, eds. S. Datz, B.H. Appleton and C.D. Moak (Plenum Press, 1975).

(21) W. Heiland, E. Taglauer and M.T. Robinson, *Nucl. Inst. Methods* 132 (1976) 655.

(22) B. Poelsema, L.K. Verhey and A.L. Boers, *Surface Science* 64 (1977) 554.

(23) G. Moliere, *Z. Naturforsch.* 2a (1947) 133.

(24) P. Csavinsky, *Phys. Rev.* 166 (1968) 53.

(25) A. Sommerfeld, *Z. Phys.* 78 (1932) 283.

(26) K. Umeda, *J. Phys. Soc. Japan* 9 (1954) 290.

(27) D.J. O'Connor and R.J. MacDonald, *Radiation Effects* 34 (1977) 247.

(28) C.B. Duke, *Electron Emission Spectroscopy*, p.51, eds. W. Dekeyser, L. Fiermans, G. Vanderkeler and J. Vennik (D. Reidel, 1973).

(29) B.T.M. Willis and A.W. Pryor, *Thermal Vibrations in Crystallography*, p.126 (Cambridge Univ. Press, 1975).

CHAPTER SIX

ION SCATTERING SPECTROSCOPY RESULTS

6.1 INTRODUCTION

The experiments described below involved the scattering of He^+, Ne^+, Ar^+ and Kr^+ off a W(110) crystal face to investigate the basic physical processes involved in low energy ion scattering and to determine the importance of wedge focusing, inelastic energy loss, interatomic potential and charge exchange. Results of the scattering of Ne^+ and Ar^+ off a Si(100) face are also reported and their importance to the determination of surface crystallography outlined.

Unless otherwise stated, the experiments reported here involve ions with an initial energy of 6 keV. This energy was chosen after due consideration of several important aspects of the scattering process. Lower energy ions are normally used to take advantage of the increased scattering cross section, the reduced chance of detecting particles scattered from the bulk, and to minimize radiation damage. Also to be considered are the higher neutralization probability of lower energy ions and the need to ensure that the binary collision conditions are valid. As insufficient quantitative information is available to allow predictions of the radiation damage to be made, it is not possible to include it directly in this discussion. It was found experimentally that for 6 keV ions, the reduced scattering cross section was offset by the enhanced ion fraction resulting in a greater yield of scattered ions per unit incident charge. The higher energy beam was expected to cause more radiation damage, but this was partly compensated by the shorter bombardment time resulting from the increased yield.

All energy spectra which illustrate the yield from zero energy to the incident ion energy in this chapter have been corrected for the

transmission function of the electrostatic energy analyser. As this
analyser has a constant resolution ($\Delta E/E \doteq 0.01$), the energy "window"
for transmitted particles is proportional to the analysis energy. The
correction factor is given by:

$$Y_c(E) = \frac{E_0}{E} \cdot Y(E) , \qquad 6.1$$

where $Y(E)$ is the measured yield at energy E,

   $Y_c(E)$ is the corrected yield, and

   E_0 is the incident ion energy.

This correction has not been applied to the energy spectra when
only segments are plotted. The angles used to describe the
experimental conditions are illustrated in fig. 6.1. The angle of
incidence, α, is measured to the target surface and the total
scattering, θ, is constant. For all W results, θ was 60°, and for the
Si results θ was 45°. When the term "specular reflection" is used, it
refers to the experimental condition where

$$\alpha = \frac{\theta}{2}. \qquad 6.2$$

The azimuthal angle, β, is defined as zero in the principal
surface direction, i.e. $\langle 100 \rangle$ for both W(110) and Si(100).

6.2   GENERAL COMMENTS ON INERT GAS
SCATTERING FROM A W SURFACE

The target was oriented and cleaned by the process outlined in
section 3.11. The surface and second layer atomic locations are
illustrated in figure 6.2, and the low index directions are shown.
The angles between these directions and the $\langle 100 \rangle$ direction, assuming
no surface relaxation, are listed in table 6.1.

Typical energy spectra obtained from the scattering of inert gas
ions off a W $\langle 100 \rangle$ surface chain are shown in figures 6.3 and 6.4. In
all cases a strong single scattering peak is observed at or just below
the predicted value (see table 6.2). The yield of charged particles

Fig. 6.1: Illustration of the definition of the angles used in
describing the experimental conditions.
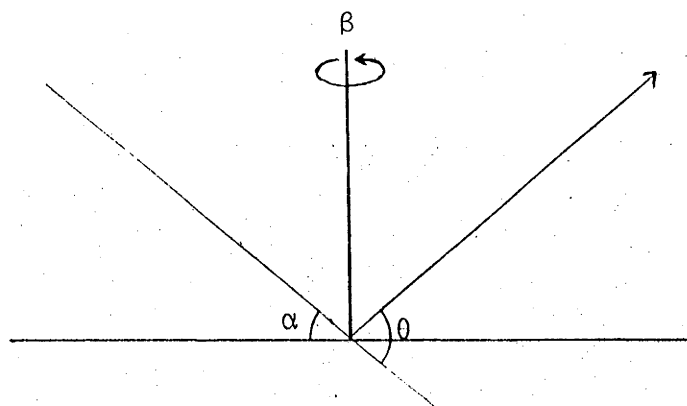
W (110) SURFACE STRUCTURE
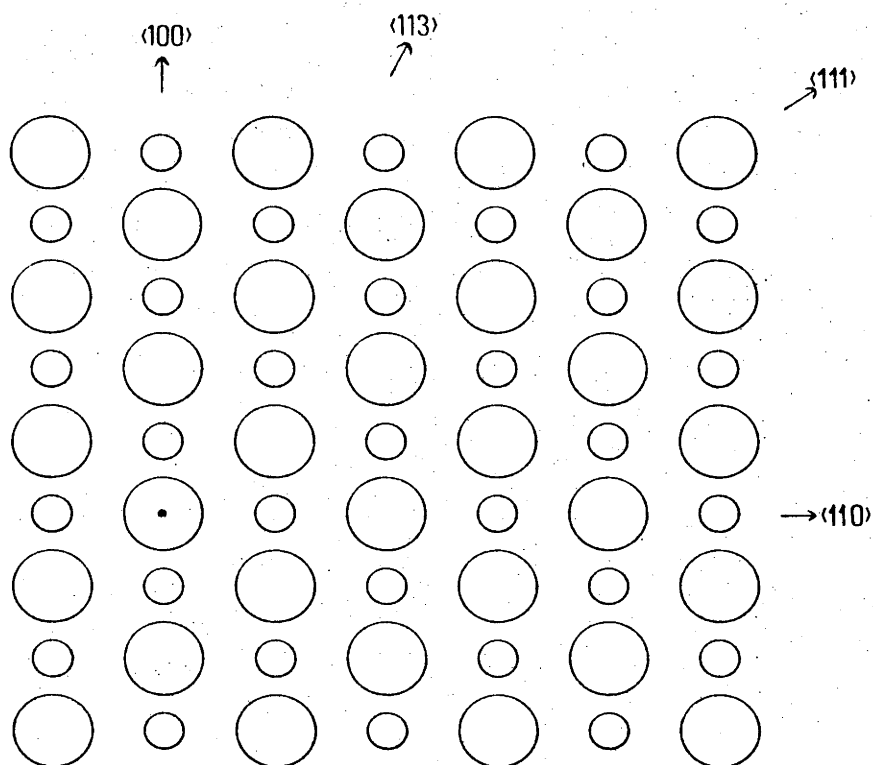
Fig. 6.2: The W(110) surface crystallography. The large circles
represent the surface atomic layer and the smaller represent the
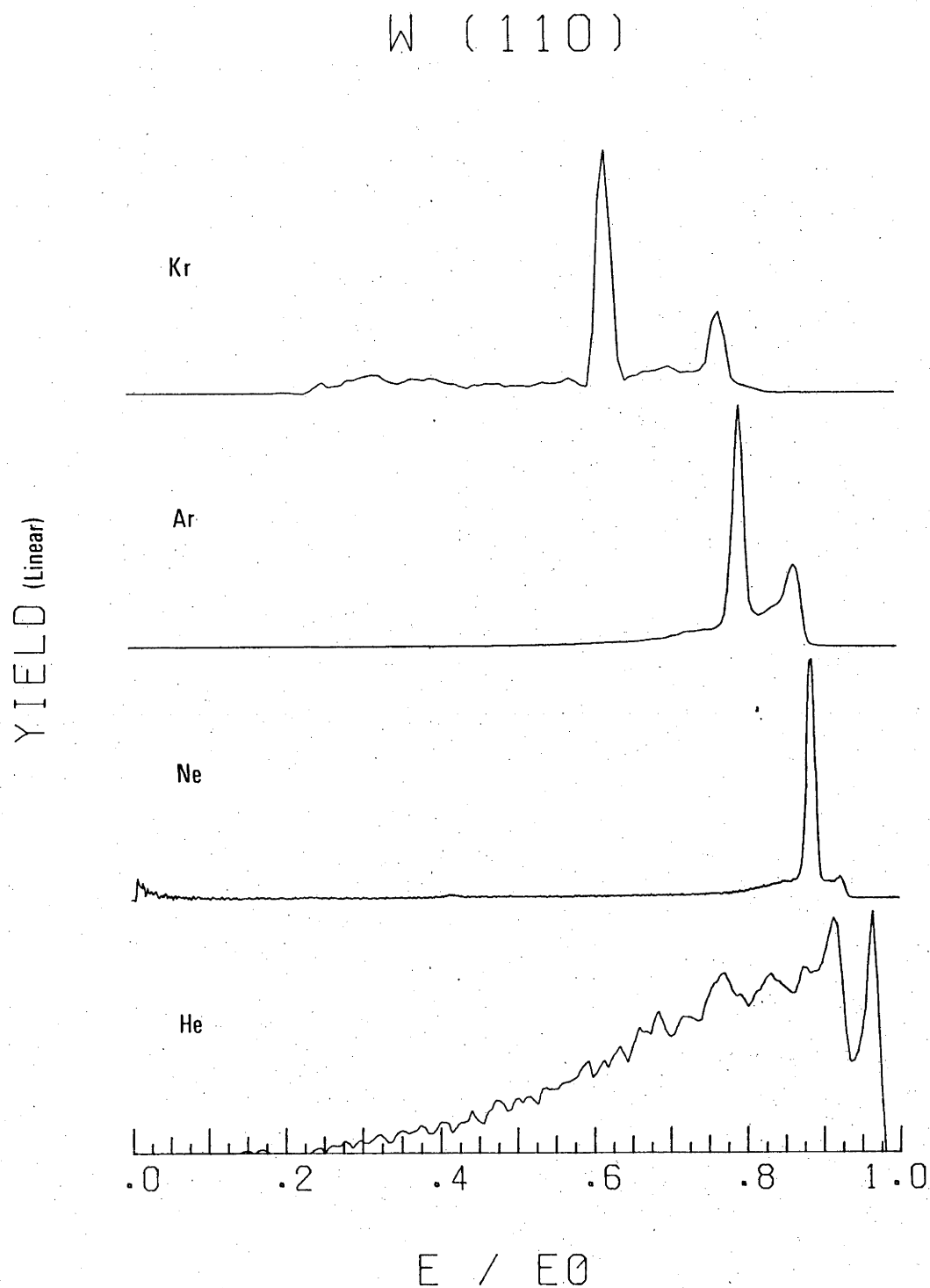second atomic layer.

W (110)

Fig. 6.3: Comparison of the measured energy spectra for 6 keV ions scattered off the ⟨100⟩ W surface atomic chains. The yield is in linear units.
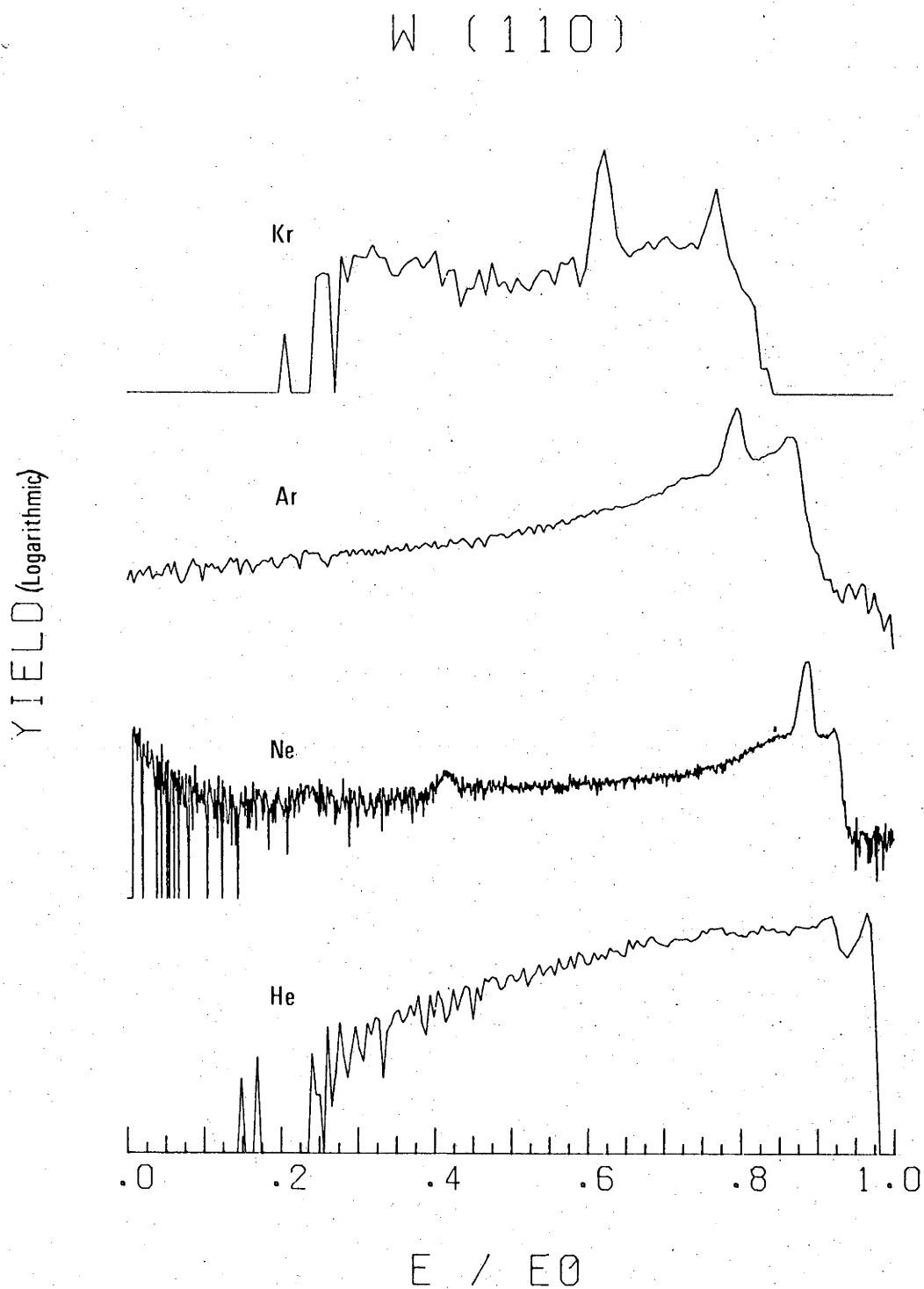
W (110)

Fig. 6.4: Comparison of the measured energy spectra for 6 keV ions scattered off the ⟨100⟩ W surface atomic chains. The yield is in logarithmic units.

Table 6.1

Angles between the Low Index Directions on a W(110) Face
and the ⟨100⟩ Direction

Direction	Angle
⟨100⟩	0°, 180°
⟨110⟩	±90°
⟨111⟩	±57.74°, ±122.26°
⟨113⟩	±25.24°

Table 6.2

Predicted Energies for Scattered and Recoil Particles
(from equations 2.1 and 2.3 for $\theta = 60°$)

Ion	Target	E_1/E_0	E_2/E_0
He^+	W	0.978	0.021
Ne^+	W	0.896	0.089
Ar^+	W	0.803	0.147
Kr^+	W	0.621	0.215

scattered from subsurface atomic layers is significant for He, but is
of less importance for the other ions. The double scattering peak is
most prominent for Kr and decreases in importance for decreasing
atomic number. This is in qualitative agreement with the dependence
predicted by Mashkova and Molchanov:[1]

$$\frac{I_2}{I_1} \propto \frac{Z_1 Z_2}{l^2 E_0 \theta^{5/2}} ,$$

6.2

where I_1 and I_2 are the single scattering and double scattering
intensities respectively, Z_1 and Z_2 are the atomic numbers of the
energetic particle and the target atom respectively. E_0 is the
initial projectile energy, θ is the total scattering angle and l is
the interatomic spacing in the target chain.

In the following sections the results obtained using the
different inert gas ions will be described individually and then the

results relating to the inelastic loss, interatomic potential and charge exchange will be combined in the respective sections.

6.3   Kr SCATTERING OFF W(110)

The analysis of Kr ions scattered off the W surface reveals an energy spectrum with strong single scattering ($0.625\ E_0$) and double scattering ($0.775\ E_0$) peaks (see fig. 6.3). There is also evidence of an intermediate peak at $0.695\ E_0$ but this will be discussed in greater detail later. Relative to the single scattering yield, there was a greater yield of Kr ions with energies ranging from $0.24\ E_0$ to $0.59\ E_0$ than there were of Ne or Ar ions at corresponding energies. This yield would normally be attributed to Kr ions scattered from the bulk of the target or from lower mass surface contaminants. If the yield was the result of scattering from the bulk, then it would be necessary to explain why there was a sharp cutoff at $0.24\ E_0$ and why the relative yield was much greater. Although this effect may be related to different electronic energy levels in Kr^+, it will be shown that there is a strong probability that it is the result of surface related processes involving W surface atoms and the incident ions.

If this yield were the result of scattering from lower mass contaminants, then the spectrum would be expected to consist of a series of peaks, with the masses of the contaminant atoms (from equation 4.3) ranging from 83 atomic mass units (a.m.u.) for $0.24\ E_0$ up to 168 a.m.u. ($0.59\ E_0$). As the integrated ion yield is sufficiently large to imply that the total concentration of these "contaminants" would exceed 1%, it is believed that this is not an adequate explanation of this feature.

As the recoil energy of W atoms at 60° is $0.215\ E_0$ (table 6.2) for Kr bombardment, this process cannot contribute directly to the yield observed over the range from $0.24\ E_0$ to $0.59\ E_0$.

There are three possible mechanisms which produce a yield at these energies. It may result from the scattering of Kr ions from subsurface atomic layers, however it will be shown that this is

unlikely as even particles scattered off the second atomic layer have an enhanced probability of neutralization. This yield may be the result of an indirect recoil process[2] which involves a W surface atom recoiling in a direction close to the surface (making an angle ϕ_1 to the incident ion direction), then being scattered by a neighbouring atom (through an angle ϕ_2) away from the surface (see fig. 6.5). The final energy of the indirect recoil is given by:

$$\frac{E'}{E_0} = \frac{4\mu}{(1+\mu)^2} \cos^2\phi_1 \cos^2\phi_2 \ , \qquad 6.3$$

where

$$\mu = \frac{M_2}{M_1} \ .$$

E' has a maximum value of 0.48 E_0 when:

$$\phi_1 = \phi_2 = 30° \ . \qquad 6.4$$
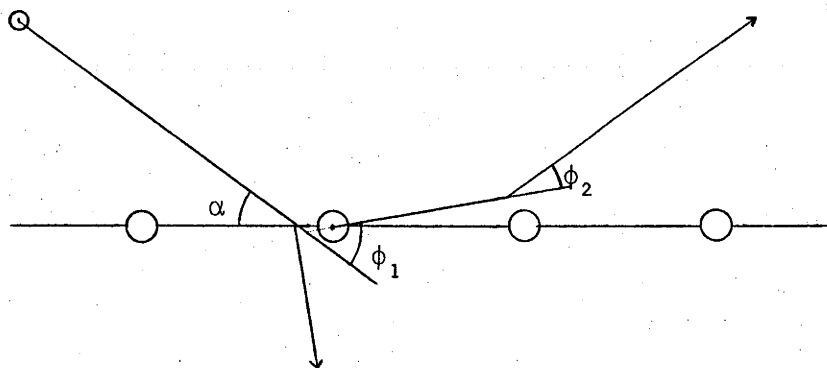
Fig. 6.5: Collision sequence for an indirect recoil scattering sequence.

This mechanism can result in a yield over the range from 0.215 E_0 to 0.48 E_0 but it is only possible to uniquely identify this component if a mass filter is included with the energy analyser.

The third mechanism, which is believed to contribute to the yield over this energy range, is called the "zig-zag" collision event. A zig-zag collision[3] involves the scattering of an ion to an adjacent atomic chain before being deflected away from the surface (in the direction of the analyser). This process is normally disregarded

because it is believed that the additional time the ion spends in the
surface region will ensure neutralization and thus will not be
detected. This however is not valid if the distance traversed during
a zig-zag event is comparable to that for a double collision event.
If between collisions the path of the zig-zag Kr ion makes an angle of
greater than 30° to the first atomic chain, then after scattering back
into the direction of the analyser its energy will be comparable to
that for a single collision event. In some cases it is possible to
identify this process from the energy spectra. If the angle to the
first atomic chain is less than 30° then the final energy of the
particle will fall between the single collision and double collision
energies. Evidence for this collision sequence can be found in the
energy spectra shown in fig. 6.6c. The peak between the single and
double scattering peaks in the ⟨110⟩ spectrum is the result of an ion,
initially incident along the ⟨110⟩ chain, being scattered towards the
surface atom in the ⟨111⟩ direction after the first collision. After
a collision with this atom it is scattered back towards the detector
direction (see fig. 6.7a). A more complex spectrum is obtained when
the azimuthal angle is 22.5° (spectrum for Kr denoted by NAD in fig.
6.6c). In this energy spectrum there are two peaks which can be
attributed to zig-zag collision processes. The lower energy peak of
these two is the results of scattering towards the atom in the ⟨111⟩
direction, while the higher energy peak is the result of scattering
towards the atom in the ⟨100⟩ direction (see fig. 6.7b).

The development of these peaks as a function of azimuthal angle
can be followed in fig. 6.8(b,c). These results consist of a series
of energy spectra taken at azimuthal increments of 1.75°. These
figures are a portion of a plot over an azimuthal scan of almost 180°
(see fig. 6.9). The increment of 1.75° was set by the necessity to
scan over 180° within the constraints of the digital counting system.
Monitoring the development of the additional peaks in the energy
spectra as the azimuthal angle is changed assists in identifying the
path of the particles involved in zig-zag collisions.

The identification of charged particles which have been involved
in zig-zag collisions supports the proposition that larger angle zig-
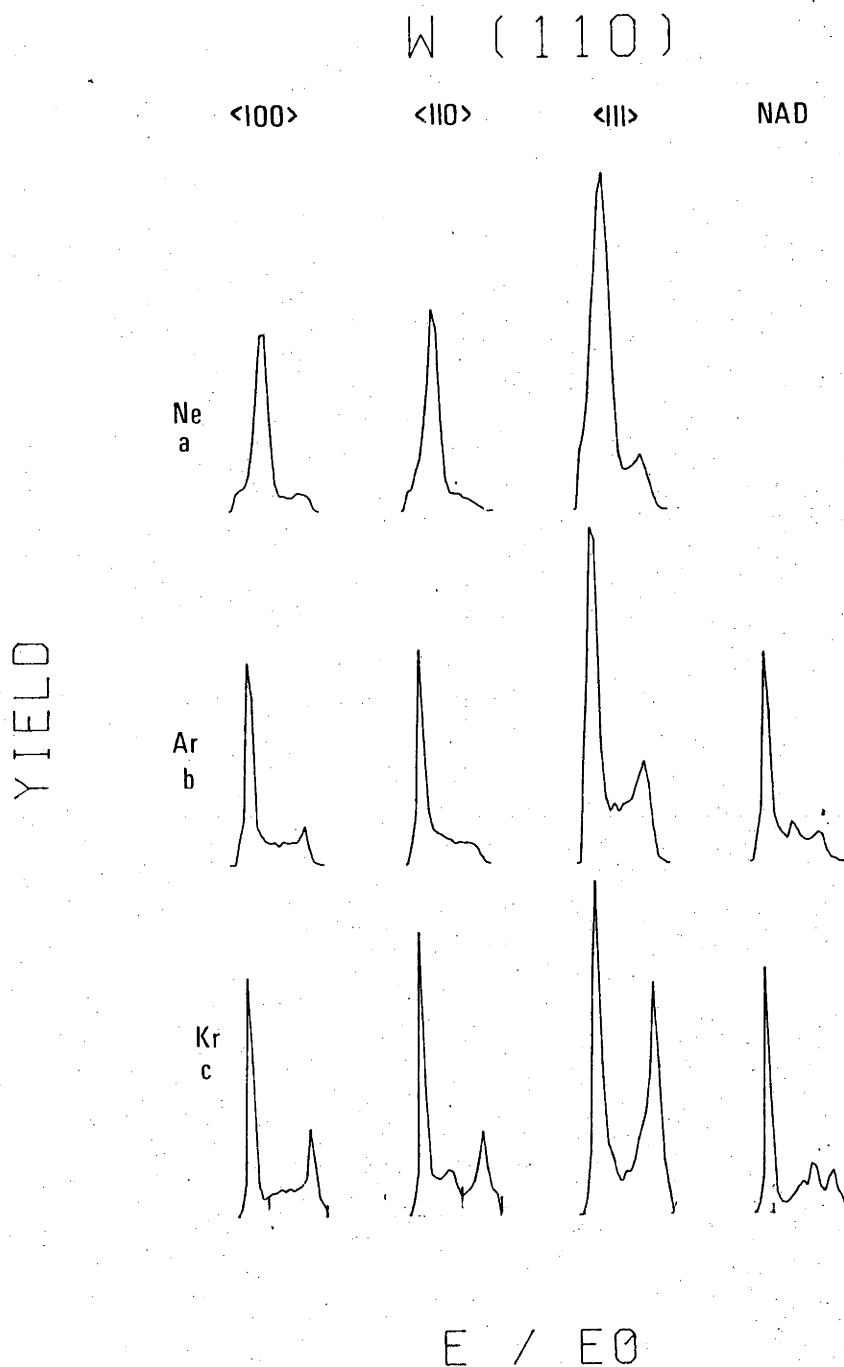
W (1 1 0)

Fig. 6.6: Comparison of regions of interest of energy spectra for different ions scattered off a W(110) surface. The region of interest incorporates the single and double scattering. The atomic chains from which the ions were scattered is shown above the spectra. The spectra which were taken in directions which do not correspond to simple crystallographic chains are denoted by NAD (non-aligned directions).
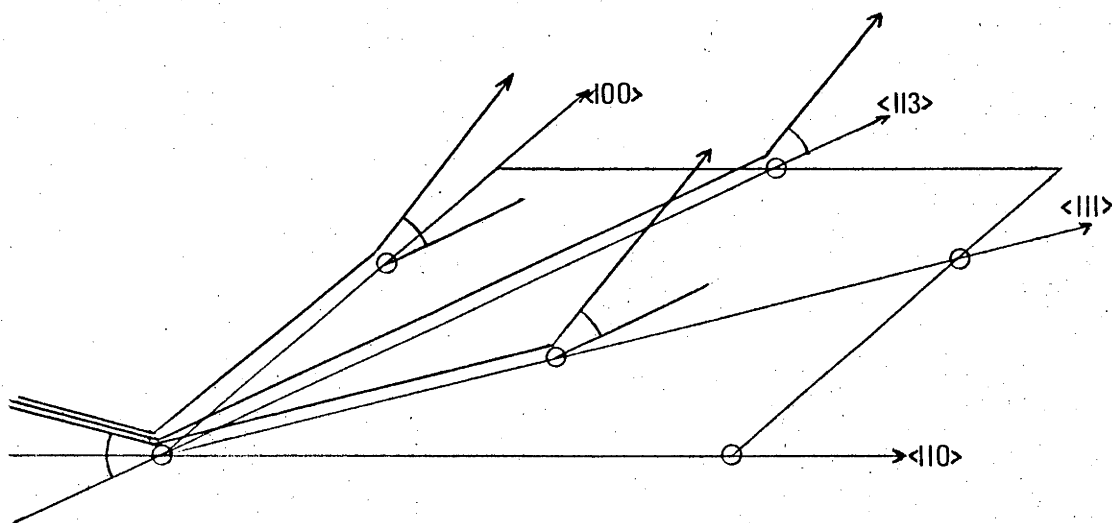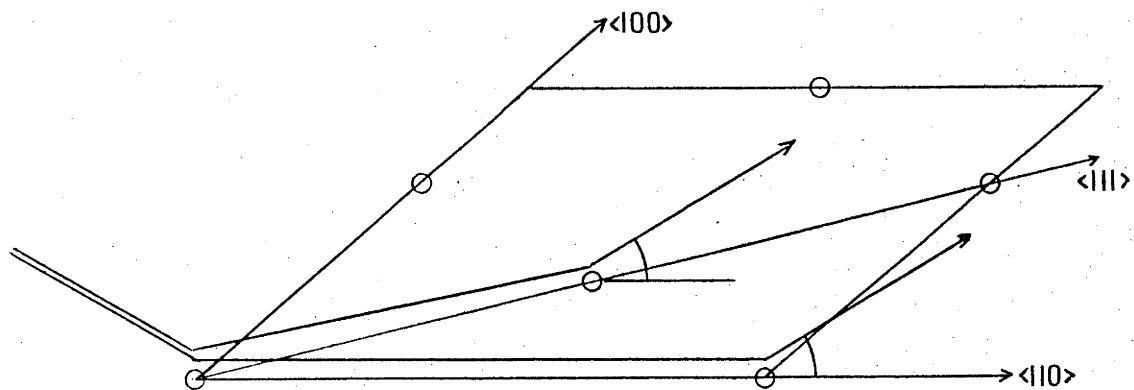
Fig. 6.7: Illustration of the zig-zag collision sequences which have been identified from the energy spectra.
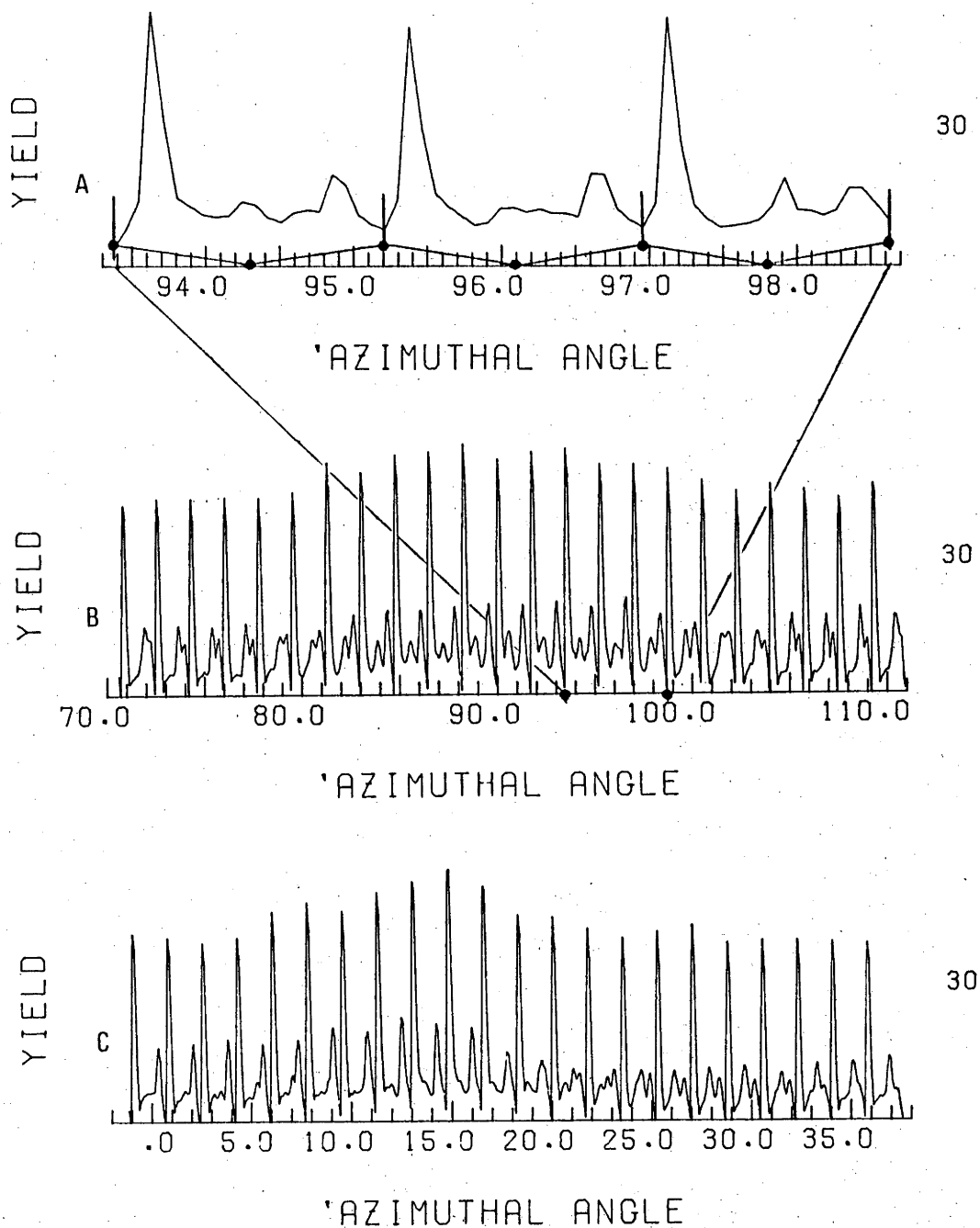
Fig. 6.8: Illustration of the change in a region of interest of the
energy spectra as the azimuthal angle is incremented. Figure 6.8a
is an expanded plot of the indicated portion of figure 6.8b. The
circles on the azimuthal angle of fig. 6.8a are the angles at
which the energy spectra contained in the space between the
delimiters are taken. The integer on the right hand side is the
angle of incidence at which these results were taken.
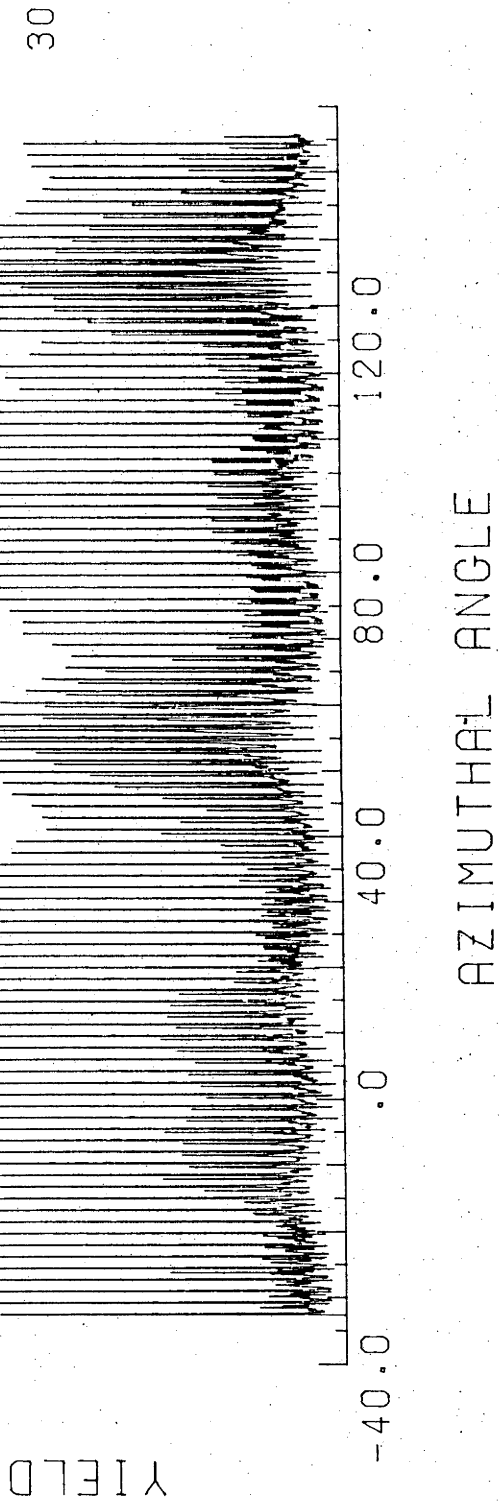
Fig. 6.9: The variation in the yield over a region of interest of the energy spectrum (incorporating both single and double scattering energies) for Kr$^+$ as a function of the azimuthal angle for a 30° angle of incidence.

zag collisions may contribute to the ion yield over the energy range from 0.24 E_0 to 0.59 E_0. As the intermediate angle to the atomic chain increases, the final energy decreases (i.e. 0.627 E_0 for 30° and 0.480 E_0 for 45°), as will the scattering cross section. This process will be more important at energies close to and above the single scattering energy.

Let us now return to the possibility that the yield over the range, 0.24 E_0 to 0.59 E_0 is the result of ions scattered from the bulk. Although direct conclusions cannot be drawn concerning the possibility of observing ions scattered from the bulk, it may be possible to generalize from single scattering results which involve scattering from the second atomic layer. The contribution of scattering from the second atomic layer to the single scattering yield can be observed in fig. 6.9 which is a similar plot to those in fig. 6.8, but it extends over 176.75° of the azimuthal range. The plot consists of a series of energy spectra taken at 1.75° azimuthal increments. The large peaks correspond to the single scattering yield while the lower intensity structure contains information on the yield from multiple scattering processes. In the five cases where there is increased yield in the single scattering peak ($\beta = \pm15°$, 55°, 90°, 125°), the enhanced yield can be explained by scattering from the second atomic layer. In four of these directions ($\beta = \pm15°$, 55°, 125°), a focusing mechanism exists which is expected to further enhance the yield from the second layer. For a W(110) crystal face the atoms of the second atomic layer do not occupy lattice sites below those of the first layer, but between them (see fig. 6.2).

The increased yield at the azimuthal angle of $\pm15°$ is the result of Kr^+ ions passing between four surface atoms which constitute a "surface lens" (when the ion beam is incident close to the $\langle 135 \rangle$ direction). These atoms focus the transmitted ions onto a second layer atom and again focus the ions which are scattered through another surface lens.

The increased yields at 55° and 125° result from the surface wedge in the $\langle 111 \rangle$ directions.[4,5,7] In these directions ions passing between the surface $\langle 111 \rangle$ chains of atoms will be focused onto

the $\langle 111 \rangle$ chains of the second layer. After scattering, the ions will again be focused and the expected single scattering yield should exceed double the yield from other surface scattering directions. It will be shown in the section on inelastic loss (fig. 6.18) that for Kr, the yield from the second layer does not exceed the surface component, and in fact is less than half that due to scattering off the surface atomic layer. This shows that there is significant neutralization of 3.7 - 6 keV Kr^+ when depths of typically 2.2 Å are involved in the scattering process. These results indicate that if the yield at energies below the single scattering energy are the result of scattering from the bulk then either there is an extremely high ion yield from this process initially (most of which is subsequently neutralized) or that these atoms experience a different neutralization process (or an ionization) when leaving the surface to that of the ions and atoms scattered off the second atomic row.

As these two possibilities are unlikely, preference must be given to the two previously explained mechanisms. Thus, the lower energy component (< 0.48 E_0 approximately) is believed to be the result of indirect recoil W atoms while the higher energy component is the yield from zig-zag collision sequences which have an intermediate angle (i.e. angle between path of the ion and the atomic chain direction between collisions) of greater than 30°.

6.4 W(110) SURFACE CRYSTALLOGRAPHY

Azimuthal angular scans can be used to further investigate the surface crystallography and obtain information about the scattering processes involved in low energy ion scattering. A series of azimuthal scans, which were taken at different angles of incidence of the Kr^+ beam to the crystal surface, are illustrated in figure 6.10. The integers on the right hand side are the angles of incidence in degrees. As the scan for 30° incidence is the same as figure 6.9, no additional comments will be made about it. For 25° incidence to the surface the yields at the azimuthal angles of ±15° have decreased as the focusing of ions onto the second layer by the "surface lens" is no longer possible.

6 KEV KR — W (110)

YIELD

30

25

20

15

10

-40   0   40   80   120
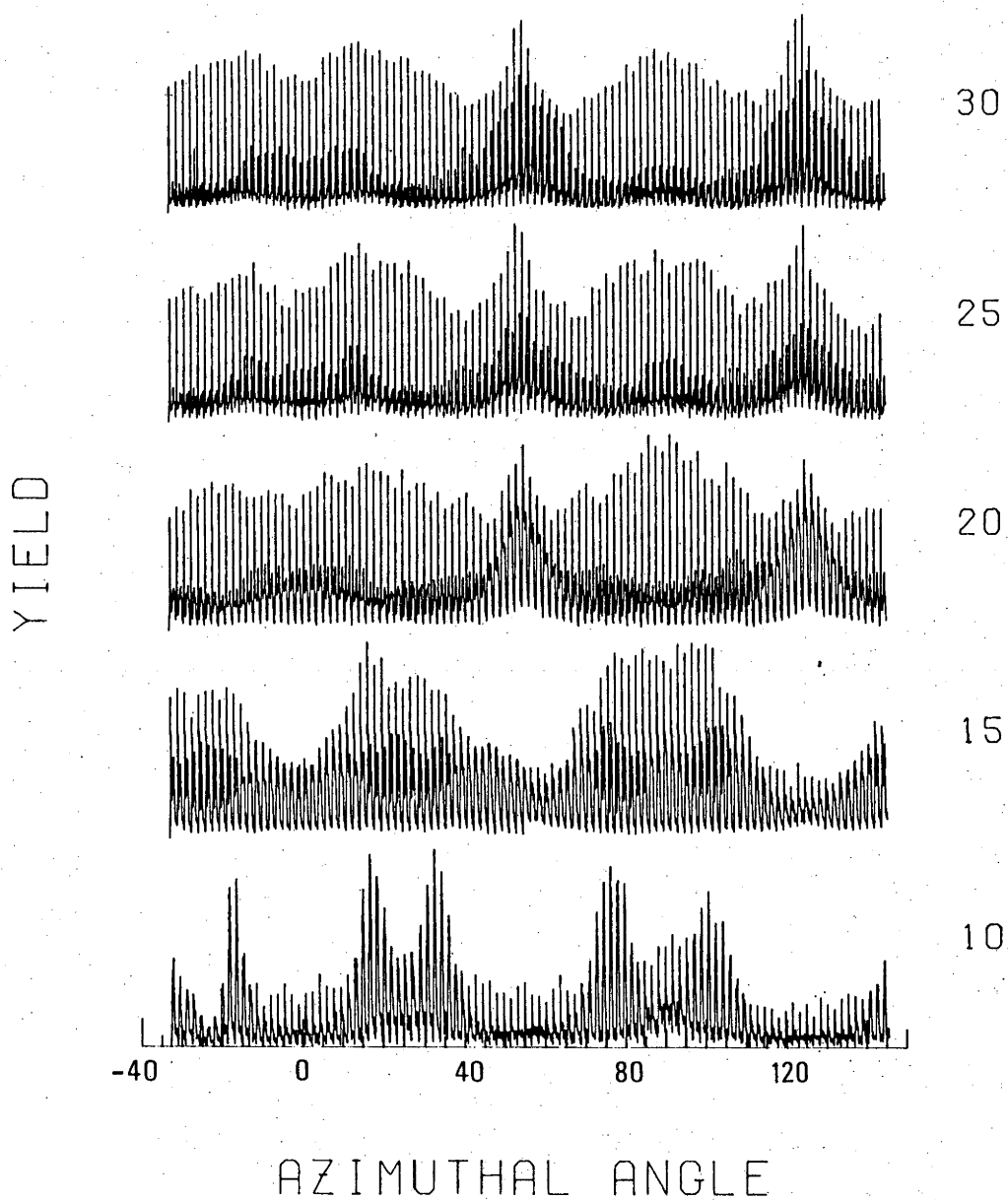
AZIMUTHAL ANGLE

Fig. 6.10: Comparison of the azimuthal scans for 6 keV Kr[+] scattered off a W(110) surface at different angles of incidence (indicated on the right hand side of each scan).

The energy-angle loop for Kr off a W ⟨111⟩ chain closes for angles of incidence between 15° and 20° (see chapter five). Thus the spectra at azimuthal angles 55° and 125° appear broadened for α = 20° as the double scattering peak merges with the single scattering peak. It can also be seen that the double scattering peak in the ⟨100⟩ direction (i.e. β = 0°) has decreased in energy.

The validity of the chain model is verified when the angle of incidence is reduced to 15°. This angle is less than the critical angle for the ⟨100⟩ and the ⟨111⟩ chains, and in theory the ion yield should be zero in these directions. The observed yield is the result of thermal vibrations of the chain atoms and surface defects. The broadened spectra at β = 90° indicates that 15° is close to the critical angle of incidence for the ⟨110⟩ atomic chain.

At 10° incidence the reduced yield at β = 90° confirms that the energy angle loop has closed. Also of interest are the reduced yields at β = ±25° which correspond to the ⟨113⟩ directions. These results confirm that the chain model can be valid for interatomic spacings of up to 5.25 Å. The additional reduction in yield between β = -20° and β = -25° (below that at β = 25°) is caused by a part of the target manipulator shadowing the target from the ion beam.

These results indicate that there is good qualitative agreement with the predictions of the chain model. The ability to identify surface atomic chains allows measurements to be made of the surface relaxation (parallel to the surface). The enhanced yields in the ⟨111⟩ directions allow more accurate measurements to be made of the angular separation between these chains. The measured angular separation is 70 ±1° which is in agreement with the bulk value of 70.53°. The angular separation between the ⟨100⟩ and the ⟨110⟩ chains has been measured to be 90 ±2°. It can be concluded from this that the surface relaxation (in the surface plane), if it exists, causes angular shifts between principal directions on the surface of less than 1°. It is not possible to make any estimates of the relaxation perpendicular to the surface from these results.

6.5   Ar SCATTERING OFF W(110)

The Ar^+ energy spectrum has similar characteristics to those
found for Kr ions, although there is less low energy yield relative to
the single and double scattering yield (see fig. 6.3). There is a low
energy tail evident on the single scattering peak and, from figure 6.4,
it is evident that there is a component of ion yield down to zero
energy. There is evidence for zig-zag collisions (see fig. 6.6) at
the azimuthal angle of 86.5° (i.e. close to the ⟨110⟩ direction), but
as the energy difference between the single scattering and double
scattering energies is only 0.087 E_0, it is not always possible to
resolve the separate processes. The zig-zag collision event may be
responsible for the low energy tail on the single scattering peak, but
there is no clear evidence to confirm this.

The azimuthal scans are shown in figure 6.11. These scans show
the same characteristics as those for Kr except that in the ⟨111⟩
direction at $\alpha = 15°$, there is a greater yield than for neighbouring
angles. This enhanced yield is due to the wedge focusing mechanism
mentioned previously.

The change in the single and double scattering peaks of an energy
spectrum as the angle of incidence is reduced in a low index direction
is shown in figure 6.12. As the angle of incidence decreases to the
critical angle, the two peaks in the energy spectra merge to become
one (at $\alpha = 18°$ approximately). Below the critical angle a narrow peak
at the single scattering energy is evident. This is believed to be
the result of scattering from surface defects. The yield at the low
angles of incidence is found to be as high as 35% of that measured for
$\alpha = 30°$. This is in agreement with similar results obtained by Heiland
and Taglauer.[6]

6.6   Ne SCATTERING OFF W(110)

The energy spectra of Ne is similar to those for Kr and Ar but
the energy separation between the single scattering and double
scattering peaks is even smaller (0.046 E_0 approximately); as
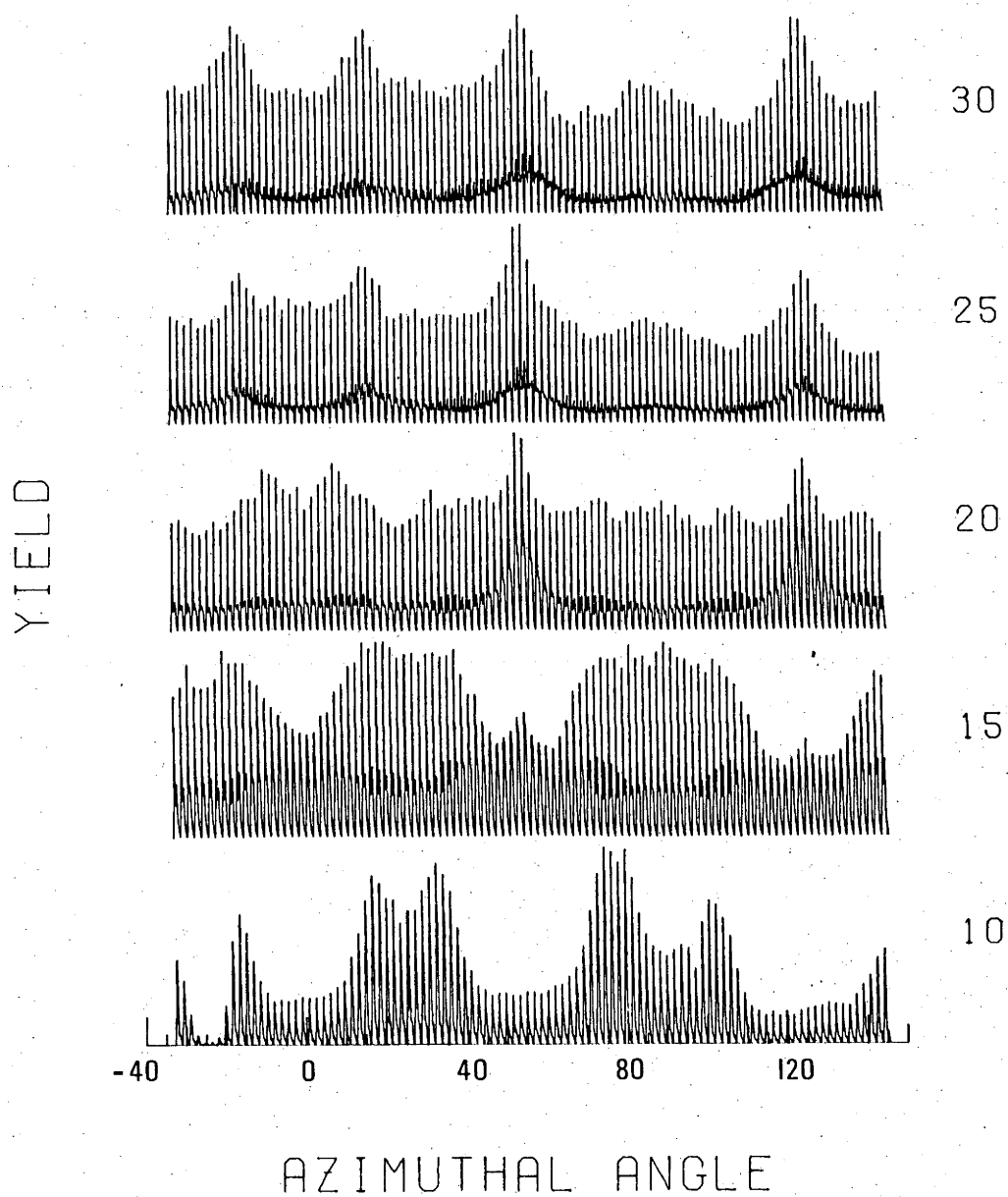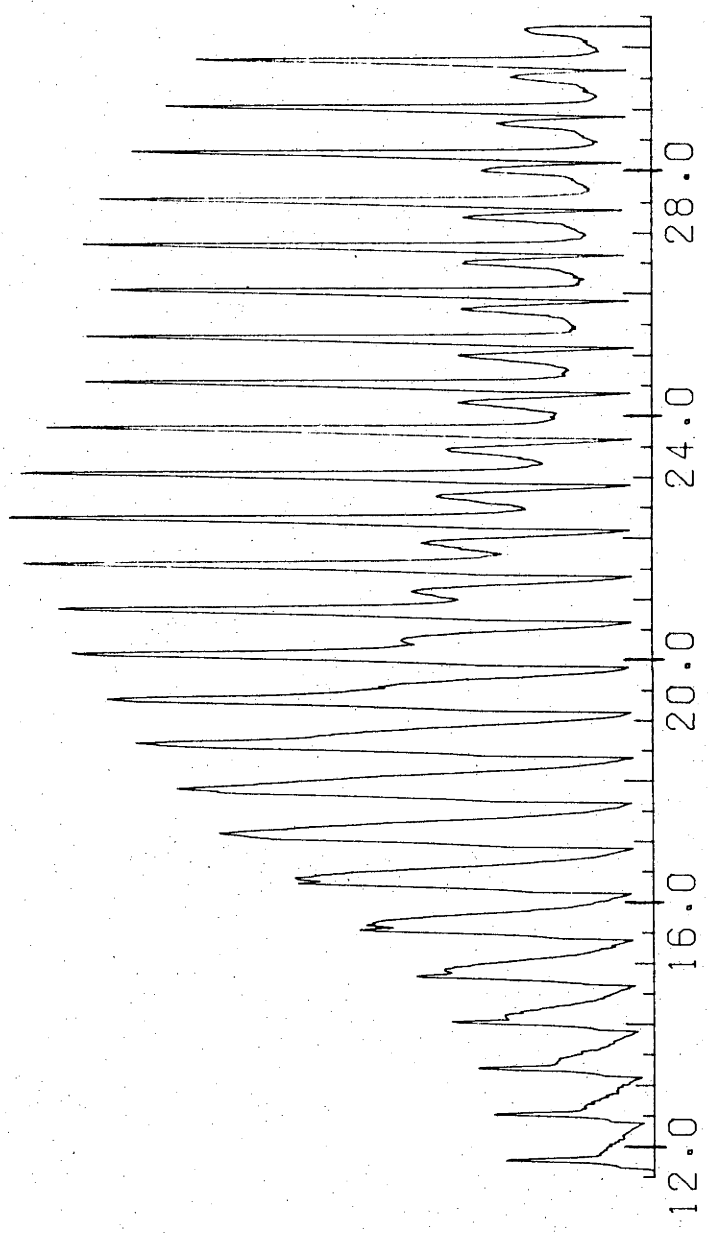
6 KEV AR — W (110)

Fig. 6.11: Comparison of the azimuthal scans for 6 keV Ar^{+} scattered off a W(110) surface at different angles of incidence (indicated on the right hand side of each scan).

6 KEV AR - W (110)

ANGLE OF INCIDENCE

YIELD

Fig. 6.12: Illustration of the change in yield and peak location of a region of interest of the energy spectrum of Ar^+ scattered off a $W\langle 111\rangle$ atomic chain. The spectra are taken at increments of 0.75° in the angle of incidence and reveal the merging of the single and double scattering peaks as the angle of incidence decreases.

illustrated in figures 6.3 and 6.4. As well, the intensity of the double scattering peak, relative to the single scattering peak, is reduced, which is in agreement with equation 6.2. The Ne^+ energy spectrum reveals a low energy tail on the single scattering peak as well as an ion yield extending down to zero energy. The small broad peak at 0.415 E_0 corresponds to Ne^+ scattering off an Al mask over the W target. This mask was removed after it was found that scattering could be detected from it. The azimuthal scans (figure 6.13) for Ne^+ reveal the increased yield in the $\langle 111 \rangle$ surface wedge directions ($\beta = 55°$ and $\beta = 125°$) and in the "surface lens" directions for $\alpha = 30°$ ($\beta = ^{\pm}15°$).

6 KEV NE — W (110)
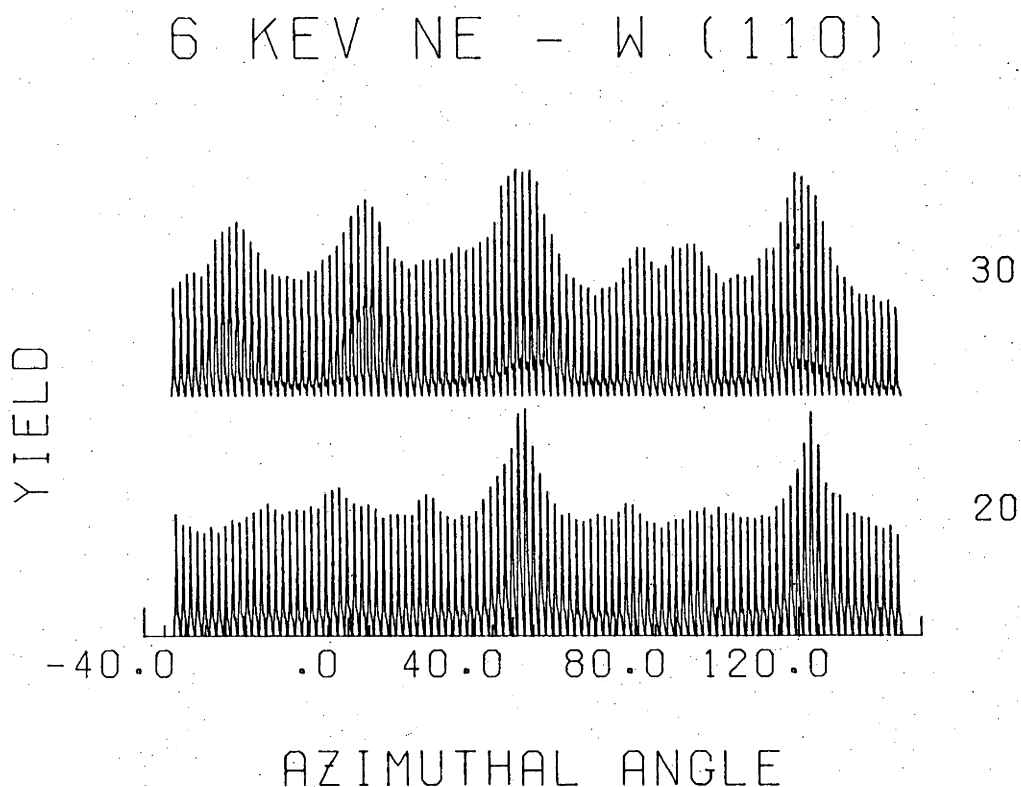
Fig. 6.13: Azimuthal scans for Ne onto W(110). The yield is in arbitrary units and the integer on the right of each scan is the angle of incidence.

6.7 He SCATTERING OFF W(110)

It is evident from figures 6.3 and 6.4 that there is a

significant yield of He ions which have been scattered from subsurface atomic layers. This is confirmed by the marked channelling structure observed in the angular scans (see figure 6.14). The full energy spectra in selected principal surface directions illustrates the difference the underlying atomic layers have on the yield (see figure 6.15). The only spectrum which consists of a single scattering peak and a relatively low yield from subsurface layers is that for $\beta = 35°$. At an angle of incidence of 30°, this azimuthal angle corresponds to a (110) planar channel. Although a similar spectrum would be expected in the ⟨100⟩ direction, the spectrum in fact consists of two peaks and a considerable low energy yield. The second peak is believed to correspond to scattering from the second layer atomic chains. The He ions pass between neighbouring atoms of the surface chain, are scattered off the second layer chain and again pass between neighbouring atoms of the surface chain when leaving the solid. The energy difference corresponds to the inelastic energy loss, and this energy difference will be used in the next section to determine the electronic stopping power.

The ion yield at energies below the single scattering energy are higher (relative to the single scattering peak intensity) than for similar experiments involving He^{+} scattering off Ni[8] and Cu.[7] Eckstein and Verbeek obtained a strong single scattering peak which was two orders of magnitude greater than the lower energy yield (down to 0.6 E_0) for 2 keV He[+] scattered off polycrystalline Ni through an angle of 135°. Feijen did not give a full energy spectrum for He^{+} scattered off Cu ($\theta = 30°$), however the yield for 4-10 keV ion scattering at 0.93 E_0 (below single scattering) was typically 10-20% of the single scattering yield for a range of different experimental conditions. Possible causes for the different neutralization efficiencies for low energy ions include:

(1) Different scattering geometries,

(2) Different ion energies,

(3) Different cyrstalline structures or orientations,

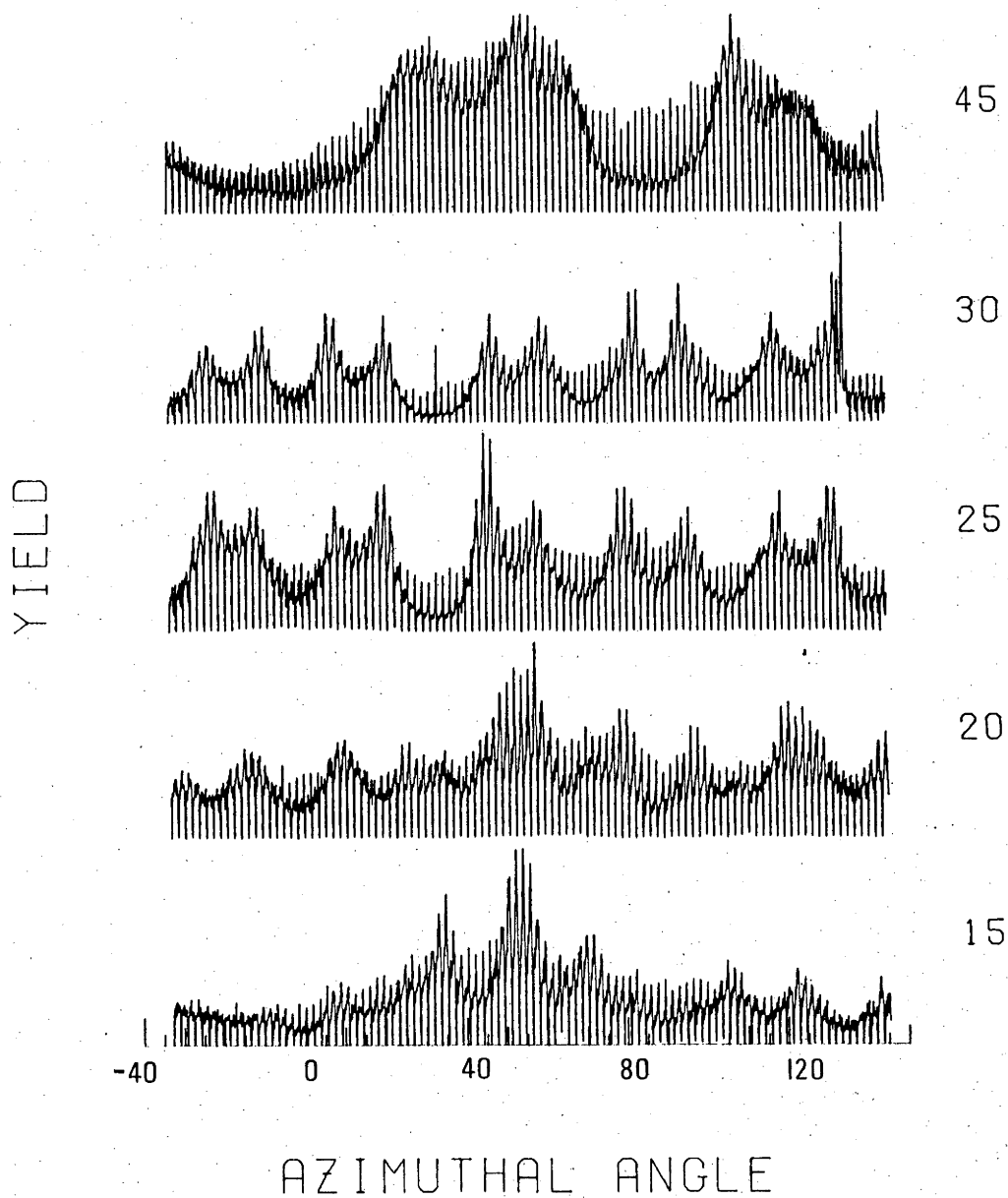(4) Different electronic energy levels.

6 KEV HE — W (110)

Fig. 6.14: Comparison of the angular scans for He scattering off a W(110) surface at different angles of incidence.
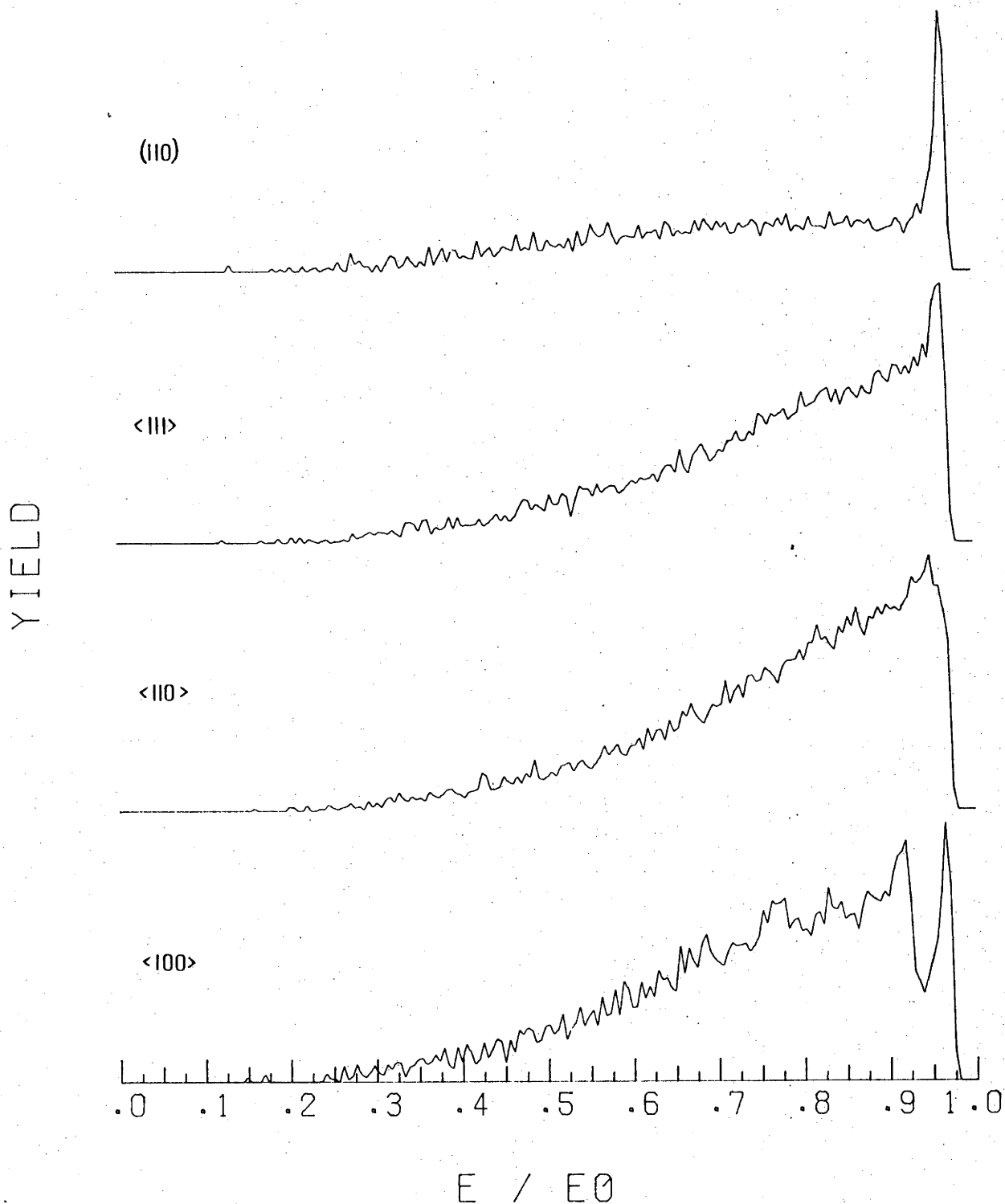
HE - W (110)

(110)

<111>

<110>

<100>

YIELD

.0   .1   .2   .3   .4   .5   .6   .7   .8   .9   1.0

E / E0

Fig. 6.15: Comparison of the energy spectra of He$^+$ scattered off a
   W(110) surface. The three lower spectra are from scattering along
   the indicated atomic rows, while the top spectrum corresponds to a
   (110) planar channel.

The scattering geometry for this investigation is intermediate between the low angle of incidence and small total scattering angle of Feijen and the high angle of incidence and large total scattering angle of Eckstein and Verbeek. As well the incident energy in this investigation is intermediate in that for He$^+$ onto Ni, 2 keV ions were used and for Cu bombardment 4-10 keV ions were employed. It is therefore unlikely that the first two possibilities can explain this difference. Also as the Cu study involved a single crystal and the Ni study a polycrystalline sample it is not simply a crystalline effect.

The possibility remains that the difference in the low energy yield is caused by a difference in the electron band structure of the solids, or some other, as yet unmentioned, characteristic of the solid. The work function[12] for W ($E_W = 4.50$ eV) is intermediate between those for Ni ($E_{Ni} = 4.84$ eV) and Cu ($E_{Cu} = 4.47$ eV). Thus if the electronic energy levels are responsible for the difference then the interaction must involve levels below the conduction band.

It is not evident from the available experimental information why there should be a greater low energy ion scattering yield for He$^+$ off W than for similar scattering of Ni or Cu. It may be that it results from not one of the previously mentioned possibilities, but two or more in conjunction which produces a complex interaction.

6.8 INELASTIC ENERGY LOSS

It has been shown in chapter two that it is possible to measure the inelastic energy loss by comparison of the single scattering peak in the surface wedge direction ($\langle 111 \rangle$) to the single scattering peak in any other direction. Assumptions involved in determining this parameter as well as experimental measurements will be discussed below.

In the $\langle 111 \rangle$ direction of the W(110) face the second layer atomic chains lie between the surface atomic chains. If the ion fraction of the particles scattered off the second layer is comparable to that of the surface scattered particles, then it is possible to compare the different scattering processes. As the ions scattered off the second

layer suffer the same single scattering process as those scattered off the surface layer, the final energy difference between these components is the result of inelastic losses experienced while traversing the wedge. The rate of inelastic energy loss (i.e. the electronic stopping power) is believed to be proportional to velocity[9,10] and can be expressed as:

$$\frac{dE}{dx} = - \lambda v .$$ 6.5

This expression can be reduced to the dimensionless form:

$$\frac{d\varepsilon}{d\rho} = - k \, \varepsilon^{\frac{1}{2}} ,$$ 6.6

where

$$\varepsilon = \frac{E \, a \, M_2}{Z_1 Z_2 \, e^2 \, (M_1 + M_2)} ,$$ 6.7

and

$$\rho = \frac{4\pi \, M_1 \, x \, N \, M_2 \, a^2}{(M_1 + M_2)^2} .$$ 6.8

The variables have the same meanings as those ascribed to them in chapter two. Lindhard, Scharff and Schiott[11] gave the following expression for k:

$$k = 0.0793 \, \xi_e \left(\frac{Z_1 Z_2 (M_1 + M_2)^3}{(Z_1^{2/3} + Z_2^{2/3})^{3/2} \, M_1^3 M_2} \right)^{\frac{1}{2}} .$$ 6.9

The Firsov theory, which evaluates the inelastic loss to bound electrons during a collision, yields an expression for loss which incorporates the distance of closest approach and is proportional to velocity:

$$dE = \frac{(Z_1 + Z_2)^{5/3} \times 4.3 \times 10^{-8}}{[1 + 3.1(Z_1 + Z_2)^{1/3} \cdot 10^7 \, R_0]^5} \cdot v ,$$ 6.10

where v is in cm/sec and R_0, the distance of closest approach, is in Ångstrøms.

It has also been shown[13,14] that the inelastic energy loss is

given by:

$$\frac{d\varepsilon}{d\rho} = - k \varepsilon^s ,$$ 6.11

where s is a variable.

Results have been reported[7,15-17] which reveal that the inelastic stopping power depends on the distance of closest approach to the atomic rows. This can be evaluated using Firsov's theory but for this application it would involve a computer simulation to sum all the interactions with neighbouring rows when the ion is in the channel. For simplicity, the results will be compared to the Lindhard, Scharff and Schiott theory.

It has been shown in chapter two that the additional energy loss suffered by an energetic particle, which is scattered off the second atomic layer, is given by:

$$\Delta\varepsilon = k \varepsilon_0^{\frac{1}{2}} d \left(\frac{1}{\sin\alpha} + \frac{\gamma^{\frac{1}{2}}}{\sin(\theta - \alpha)} \right) ,$$ 6.12

where α is the angle of incidence, θ is the total scattering angle, ε_0 is the initial energy and γ is given by:

$$\gamma = \left(\frac{\cos\theta + \sqrt{\mu^2 - \sin^2\theta}}{1 + \mu} \right) ,$$ 6.13

where

$$\mu = \frac{M_2}{M_1} .$$

d is the depth of the wedge, which is 2.24 Å if there is no relaxation of the crystal structure perpendicular to the surface. The value of 2.24 Å was used to determine the stopping power from experimental results, but any reduction in the interplanar spacing between the top atomic layer and the second will increase the values of stopping power derived from these measurements.

To determine the component of scattered particles from the second layer, the "single scattering" peak of an energy spectrum, taken when the ion beam was incident along a principal surface direction, was subtracted from the corresponding energy spectrum of the "single

scattering" peak in the ⟨111⟩ direction. The scattering from an
atomic chain involves scattering from neighbouring atoms as well as
the "single scattering" process. The additional scattering events
increase the final energy of the scattered particle by an amount which
depends on the atomic chain density (see fig. 5.9). For the following
analysis the reference peak, from the ⟨100⟩, ⟨110⟩ and ⟨113⟩
directions, was shifted by an amount predicted by the Energy Angle
Loop Simulation using the Moliere potential. The result of the
subtraction of the surface peak component can be seen in figures 6.16 –
6.18. From the energy difference between the reference peak and the
resultant peak, the inelastic stopping power can be evaluated. For Ne
and Ar, the yield at lower incident energies was sufficient to allow
energy dependent measurements to be made (Fig. 6.19). However the
resultant peak for Kr is small for 6 keV ions and its intensity,
relative to the reference peak, becomes too low at lower incident
energies to allow energy dependent measurements to be made. The
efficiency of the neutralization process for Kr inside the wedge
reinforces the conclusions arrived at in section 6.3.concerning the
possibility of Kr scattering from the bulk. The width of the
resultant peak as well as the low energy tail are believed to
originate from the yield of ions which are focused from close to one
of the surface rows. Such ions, having a smaller distance of closest
approach to the surface chain, will pass through a region of higher
electron density and will experience a higher stopping power. A
component of the width is also attributable to the straggling caused
by the random nature of the electronic collisions.

When the He ions were incident along the surface wedge direction,
the energy spectra of the scattered ions included a strong component
from ions scattered off subsurface atomic layers (see figure 6.15).
As the low energy yield was a strong function of the crystallographic
direction, it was not possible to simply subtract a spectrum from
another direction to obtain the second layer component. However the
two peak structure of the energy spectra taken in the ⟨100⟩ direction
(see figure 6.15) does present the possibility of allowing a
measurement of the inelastic loss. The cause of this double peak
structure has been described in section 6.7, so it is only necessary
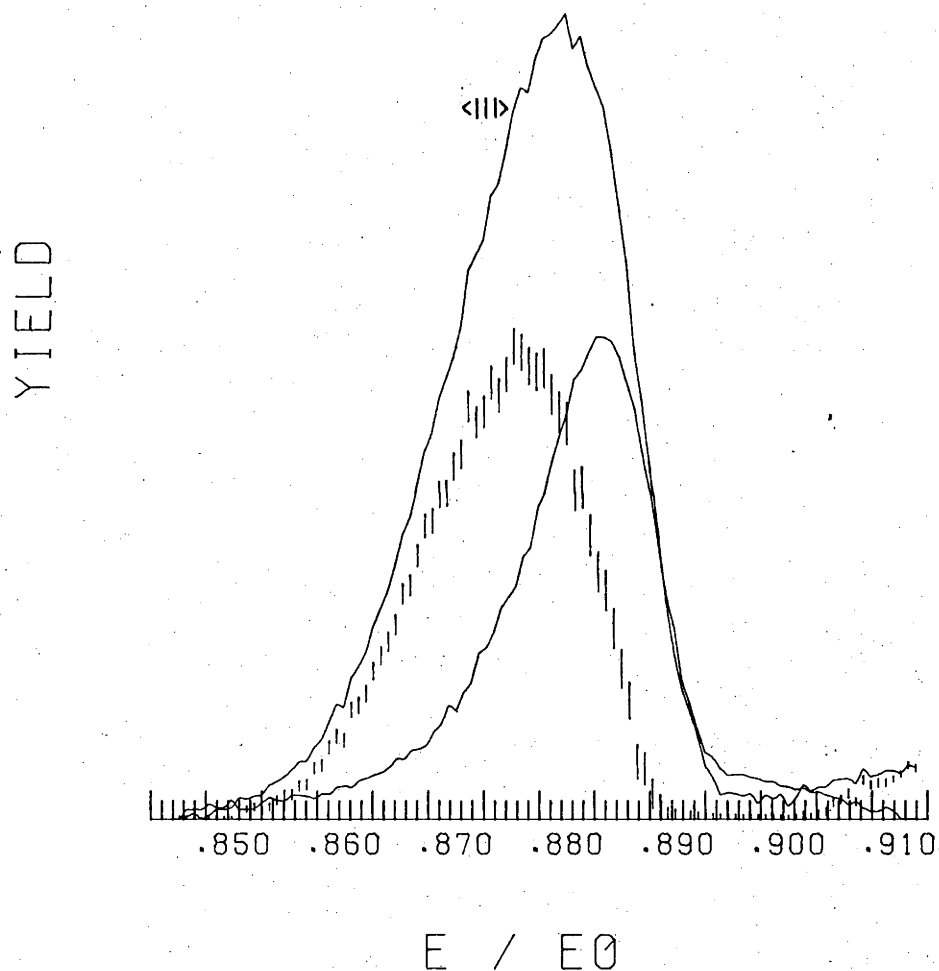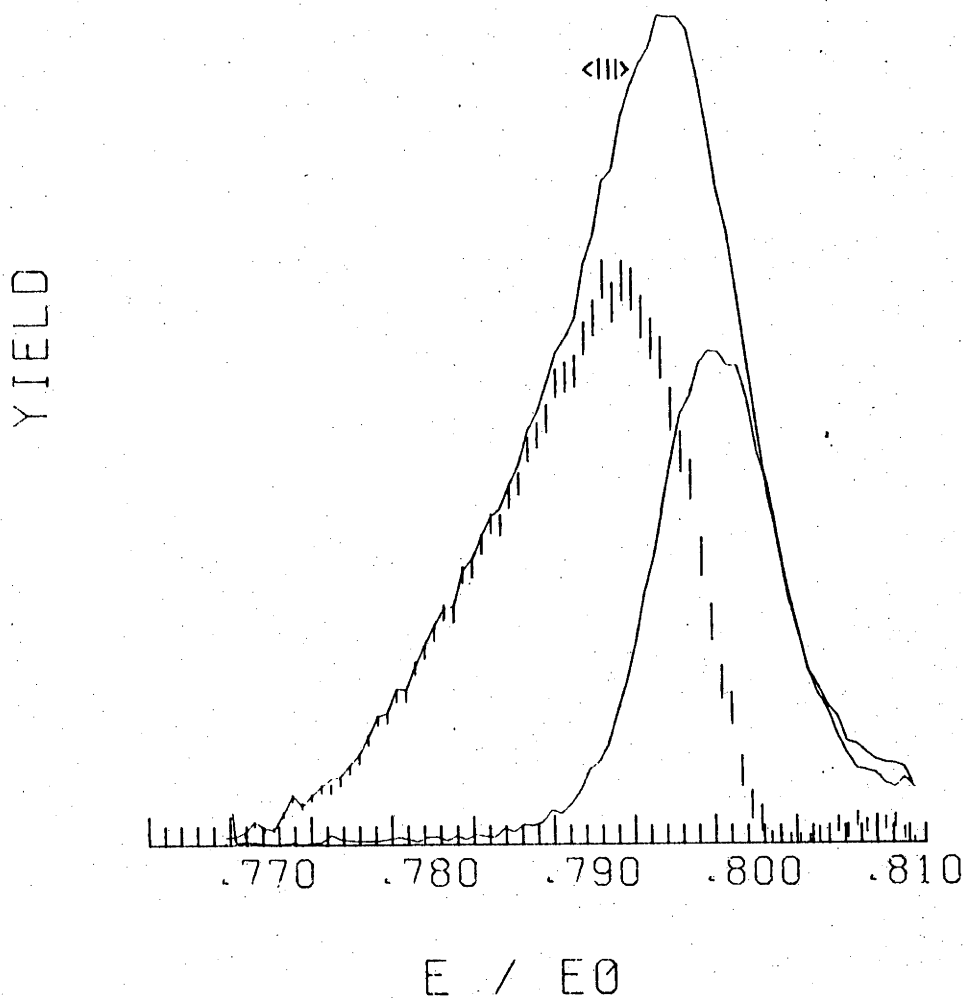
6 KEV NE — W (110)

Fig. 6.16: An illustration of the method used to determine the inelastic energy loss. The upper curve (solid) is the Ne[+] energy spectrum obtained in the ⟨111⟩ direction while the second solid curve corresponds to the spectrum in another surface direction. The difference between these two is represented by the results which include error bars. The indicated errors are those due to the statistical uncertainties in the experimental measurements.
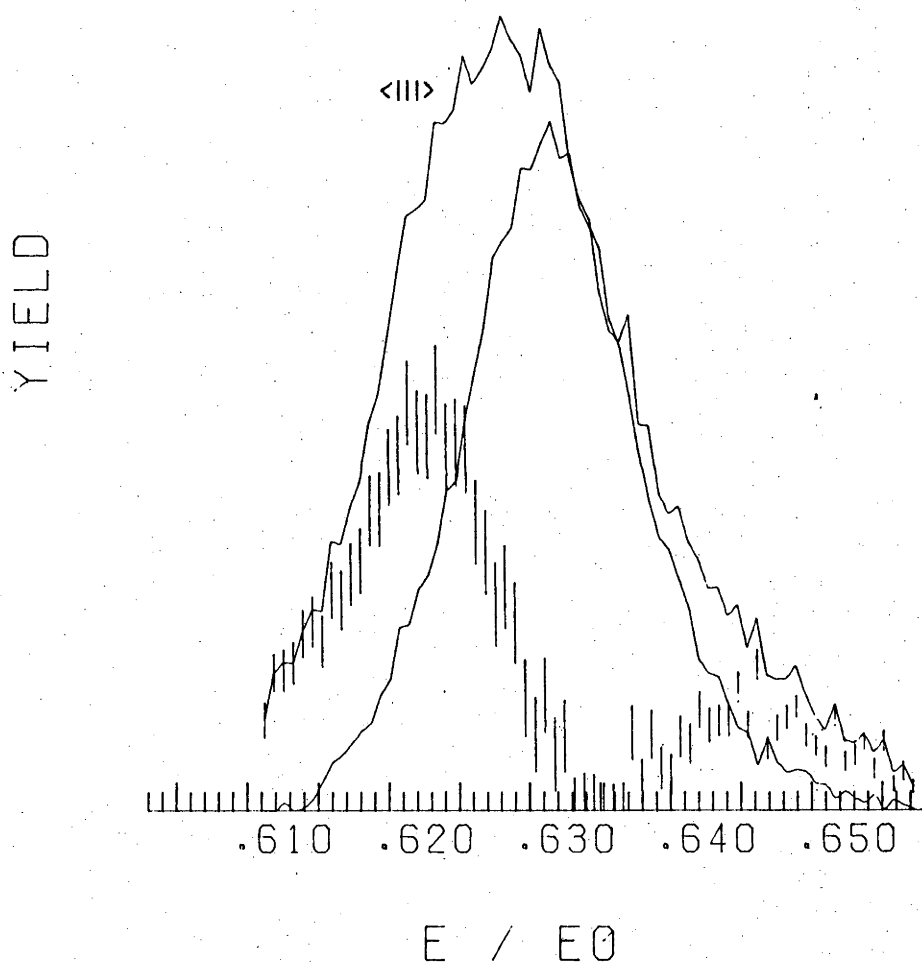
6 KEV AR – W (110)

Fig. 6.17: An illustration of the method used to determine the inelastic energy loss. The upper curve (solid) is the Ar^+ energy spectrum obtained in the $\langle 111 \rangle$ direction while the second solid curve corresponds to the spectrum in another surface direction. The difference between these two is represented by the results which include error bars. The indicated errors are those due to the statistical uncertainties in the experimental measurements.

6 KEV KR — W (110)

Fig. 6.18: An illustration of the method used to determine the inelastic energy loss. The upper curve (solid) is the Kr^+ energy spectrum obtained in the ⟨111⟩ direction while the second solid curve corresponds to the spectrum in another surface direction. The difference between these two is represented by the results which include error bars. The indicated errors are those due to the statistical uncertainties in the experimental measurements.
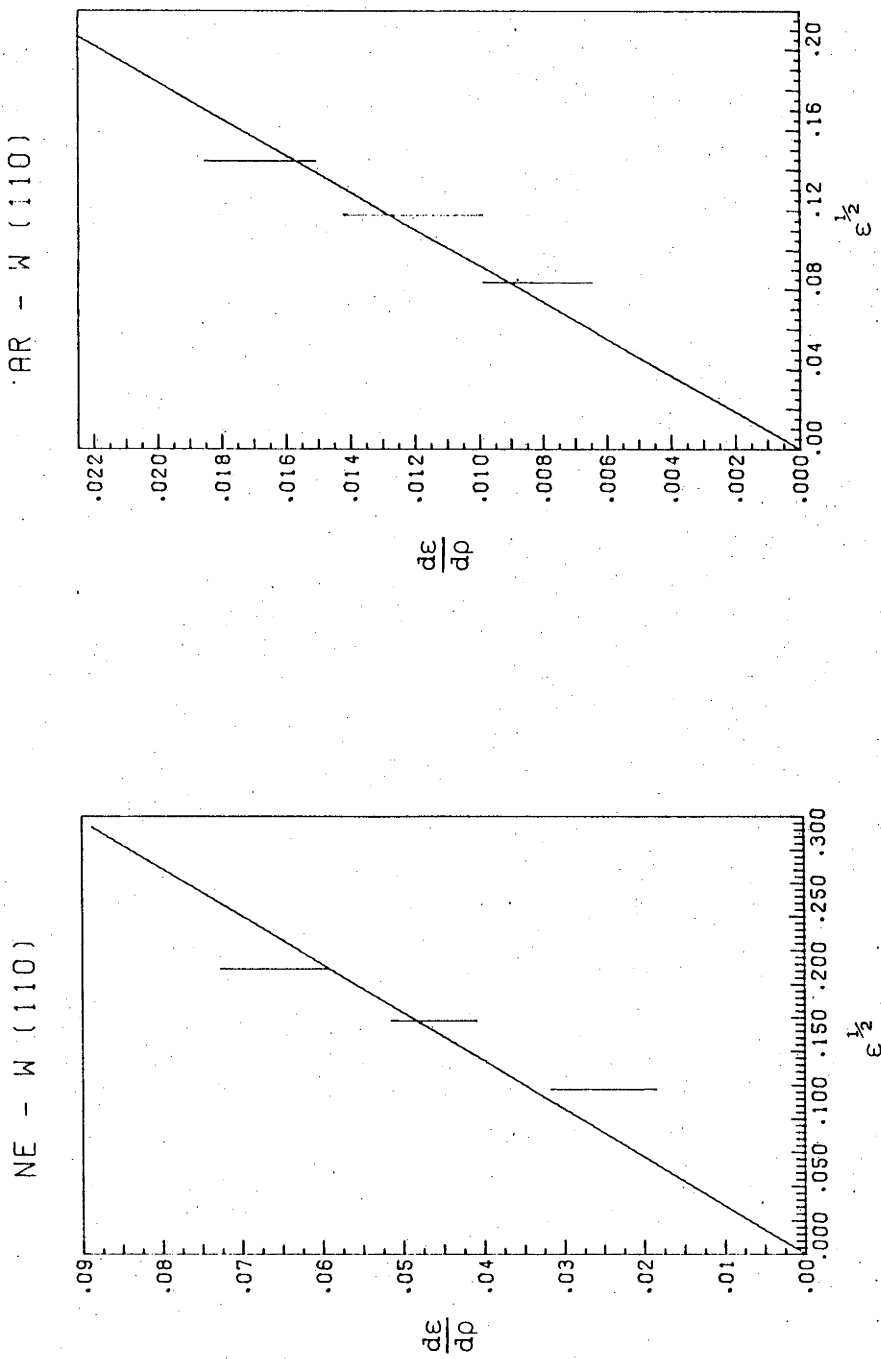
Fig. 6.19: The energy dependence of the measured inelastic energy loss for Ne and Ar scattering off W.

to add that in this scattering sequence the He passes close to the
atoms of the chain where the electron density is high. It is expected
therefore that the energy loss is greater for this scattering process
than for the other inert gas ion scattering described above.

The results of these measurements are presented in the following
table. Included for comparison are the values of k_L predicted by the
Lindhard, Scharff and Schiott model.

Table 6.3

Inelastic Energy Loss Measurements

Ion	Energy Loss (eV)	Loss Rate (eV/Å)	k	k_L
He	260 ± 30	30 ± 3	16 ± 2	2.80
Ne	45 ± 4	5.0 ± 0.4	0.28 ± 0.03	0.732
Ar	35 ± 3	3.9 ± 0.3	0.109 ± 0.006	0.416
Kr	50 ± 4	5.5 ± 0.4	0.083 ± 0.006	0.254

The values determined for k for Ne, Ar and Kr are between 0.25
and 0.4 of the value predicted by the Lindhard, Scharff and Schiott.
The relationship between these results and the theoretical estimates
for this model is in agreement with similar experiments conducted at
higher energies.[18]

The results for He cannot be compared to channelled ion losses,
but the results of Feijen[7] for 10 keV He[+] scattered off Cu reveal
that ions focused from regions close to the surface atomic rows
experience an inelastic stopping power of 16.3 eV/Å. As the distances
of closest approach to individual atoms is better defined in this
experiment, the Firsov model can be compared to the experimental
results. However the distance of closest approach will be a function
of surface relaxation. Using the Firsov model, the inelastic loss is
predicted to vary from 455 eV for no relaxation perpendicular to the
surface, to a minimum loss of 358 eV for a 10% contraction of the
surface layer and second layer separation. Therefore the measured
inelastic loss is between 0.6 and 0.7 of that predicted by the Firsov

expression.

It will be shown in the following section that ions scattered from the surface atomic layer also suffer inelastic losses. As the electron density varies quite significantly near the surface, the measurements made cannot be compared to these results.

6.9 MEASUREMENT OF THE INTERATOMIC POTENTIAL

In order to estimate the interatomic potential, the energy of the singly and multiply scattered ions, measured at various angles of incidence, were compared to simulation results described in chapter five.

In the following presentation of results, it should be noted that the total scattering angle was 60° and that measurements were only made for angles of incidence below 30°. It has been shown in the previous chapter that the limiting angles of incidence to the surface are approximately symmetric about the specular direction, so that no additional information is obtained by measuring the angle of incidence upper limit.

The lower angle of incidence was favoured as it both increased the yield and reduced radiation damage and implantation. At the higher angle of incidence there is a greater probability that the incident ions will penetrate the chain and cause radiation damage below the surface layer. The ions penetrating the chain will also become implanted and cause lattice distortion. This effect is reduced at lower angles of incidence where the reflection coefficient is higher.

The nature of the neutralization process is such that the ion yield at the lower angles of incidence is generally higher than that for the higher scattering angles (symmetric about the specular conditions). The increased ion yield reduces statistical fluctuations and allows more confident measurements to be made of peak separations. For low angles of incidence the velocity perpendicular to the surface is relatively large for the approach to the surface and the departure

from it. For high angles of incidence the perpendicular component is large on the approach to the surface, but significantly smaller on the departure, which will reduce the ion fraction. This can be proven for the general case where collisional ionization and neutralization are included, but in order to avoid such a complicated analysis, consider the simpler case which only involves an "Auger-like" neutralization process. For an ion with initial velocity v_0 and final velocity γv_0, where γ is given by equation 6.13, the ion fraction for an angle of incidence of $\theta/2 - \delta$, where θ is the total scattering angle and $\delta \geqslant 0$, is given by:

$$P^+\left(\frac{\theta}{2} - \delta\right) = \exp\left(- \frac{v_c}{v_0 \sin\left(\frac{\theta}{2} - \delta\right)}\right) \cdot \exp\left(- \frac{v_c}{\gamma v_0 \sin\left(\frac{\theta}{2} + \delta\right)}\right) , \quad 6.14a$$

where v_c is the characteristic velocity. To compare the yield for angle of incidence symmetric to this about the specular condition, replace $\theta/2 - \delta$ for $\theta/2 + \delta$ in the above equation:

$$P^+\left(\frac{\theta}{2} + \delta\right) = \exp\left(- \frac{v_c}{v_0 \sin\left(\frac{\theta}{2} + \delta\right)}\right) \cdot \exp\left(- \frac{v_c}{\gamma v_0 \sin\left(\frac{\theta}{2} - \delta\right)}\right) . \quad 6.14b$$

The ratio of these ion fractions reduces to give the following expression:

$$\frac{P^+\left(\frac{\theta}{2} - \delta\right)}{P^+\left(\frac{\theta}{2} + \delta\right)} = \exp\left(\frac{2v_c(1 - \beta) \sin\delta \cos\frac{\theta}{2}}{\sin\left(\frac{\theta}{2} - \delta\right) \sin\left(\frac{\theta}{2} + \delta\right)}\right) . \quad 6.15$$

As all the terms in the exponential are positive, the right hand side is greater than unity, i.e. $P^+(\theta/2 - \delta) > P^+(\theta/2 + \delta)$.

Measurements were made for Ar^+ and Kr^+ scattered off $\langle 100 \rangle$ and $\langle 111 \rangle$ surface chains, and comparison was initially made with the computer simulation results for atomic chains without thermal vibrations (i.e. "cold lattice"). The simulation results were determined using three interatomic potentials:

(1) Csavinsky potential,

(2) Moliere potential,

(3) Moliere potential with a screening length correction factor of 1.16 for Ar and 1.25 for Kr (see chapter four).

The results of this comparison can be seen in figures 6.20 - 6.23. While there is better agreement for Kr than for Ar to the simulation results and the energies of the ions exhibit a similar dependence on the angle of incidence as is expected, there is no general agreement with any one potential.

The most marked feature of the Ar^+ results is that both the single and double scattering energies fall below that predicted by the simulation. The single scattering energy for specular reflection is measured to be (0.796 ± 0.001) E_0 whereas the minimum energy predicted by the chain model for single scattering is 0.803 E_0 for a short range interatomic potential. The measured energy of the double scattering peak was 0.867 E_0 for the $\langle 111 \rangle$ chain and 0.871 E_0 for the $\langle 100 \rangle$ chain while the chain model predicts a minimum double scattering energy 0.890 E_0.

The energy difference is believed to be accounted for by inelastic energy losses experienced by the particle near the surface and during the collision. The greater energy deficit for doubly scattered particles is the result of inelastic losses between collisions and the additional collision event. As the distance of closest approach to the surface is smaller (hence a greater electron density) for Ar than for Kr, the inelastic losses are greater.

To allow a meaningful comparison between experimental results and simulation results it was necessary to make allowance for the inelastic processes. This was accomplished by determining correction factors for the single and multiple scattering peaks and applying that correction at all angles of incidence. This is based on the assumption that the same fraction of energy will be lost at different angles of incidence. This may not strictly be correct, but present knowledge of the electron density distribution near the surface and its effect on the inelastic loss process is not adequate enough to suggest an alternative.
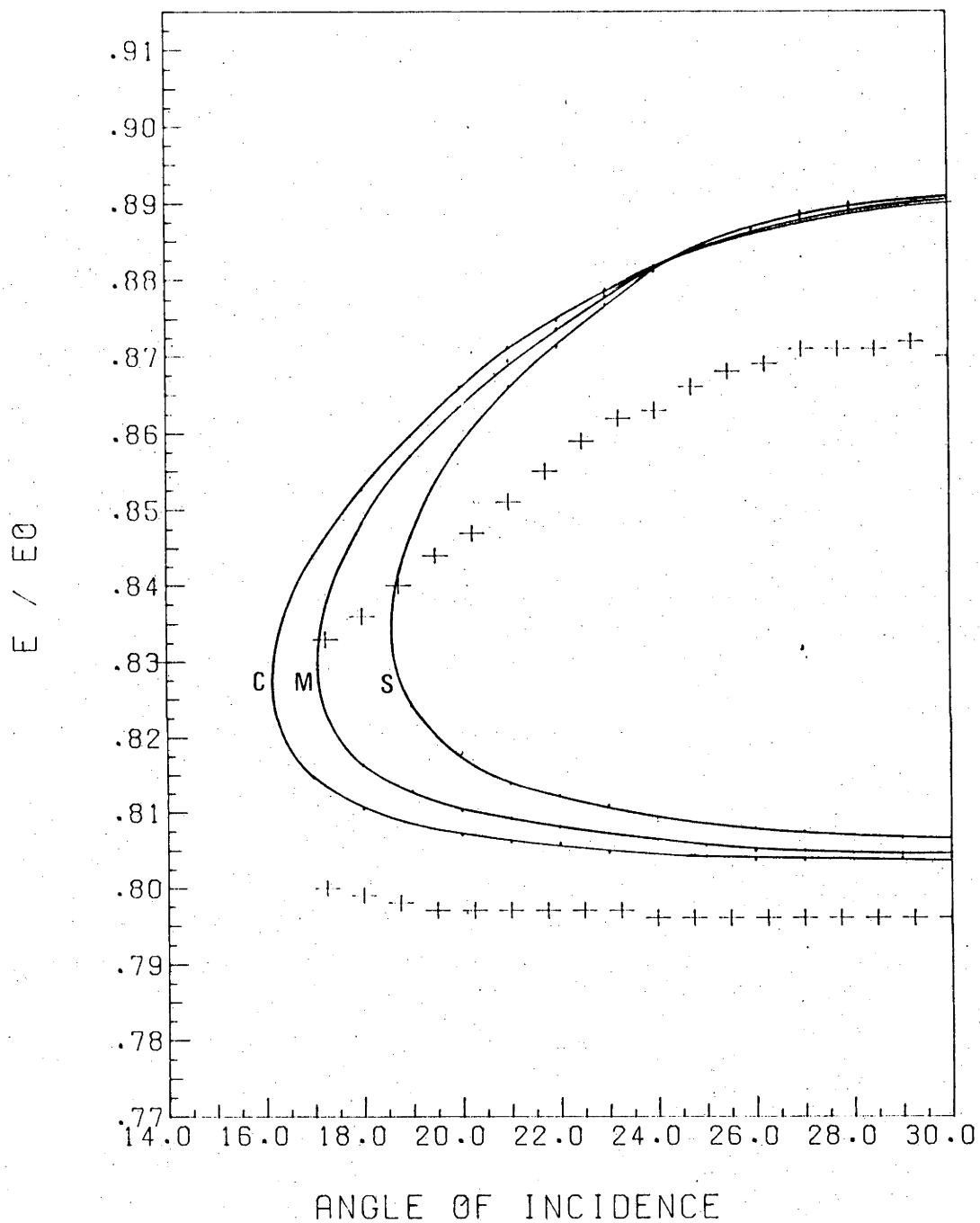
'6 KEV AR-W(110) <100>

Fig. 6.20: Comparison of the experimental measurements of the single
and double scattering energies of Ar$^+$ scatterred off a W(100)
surface chain. The results of the energy angle loop simulation
are denoted by C for the Csavinsky potential, M for the Moliere
potential and S for the Moliere potential with a screening length
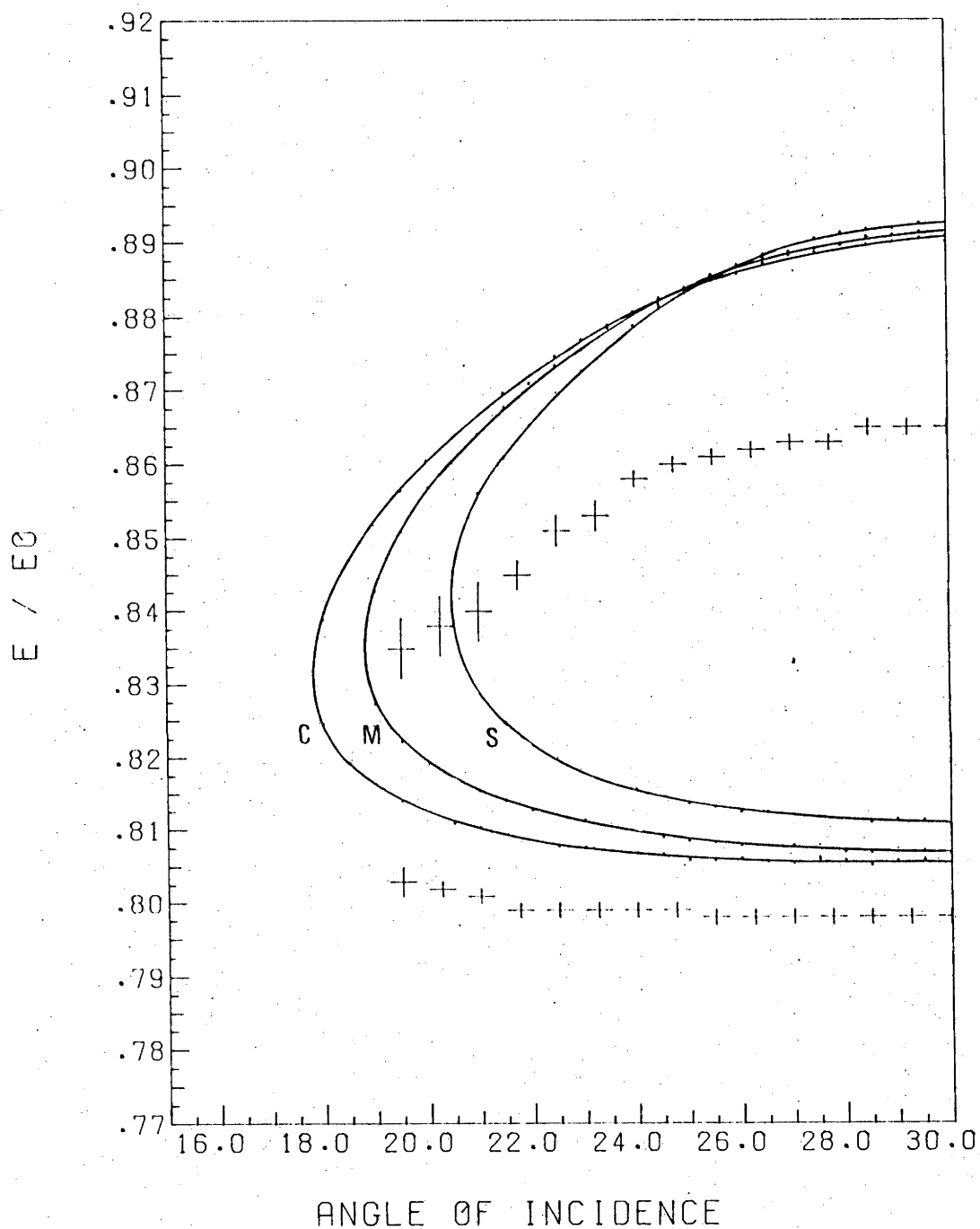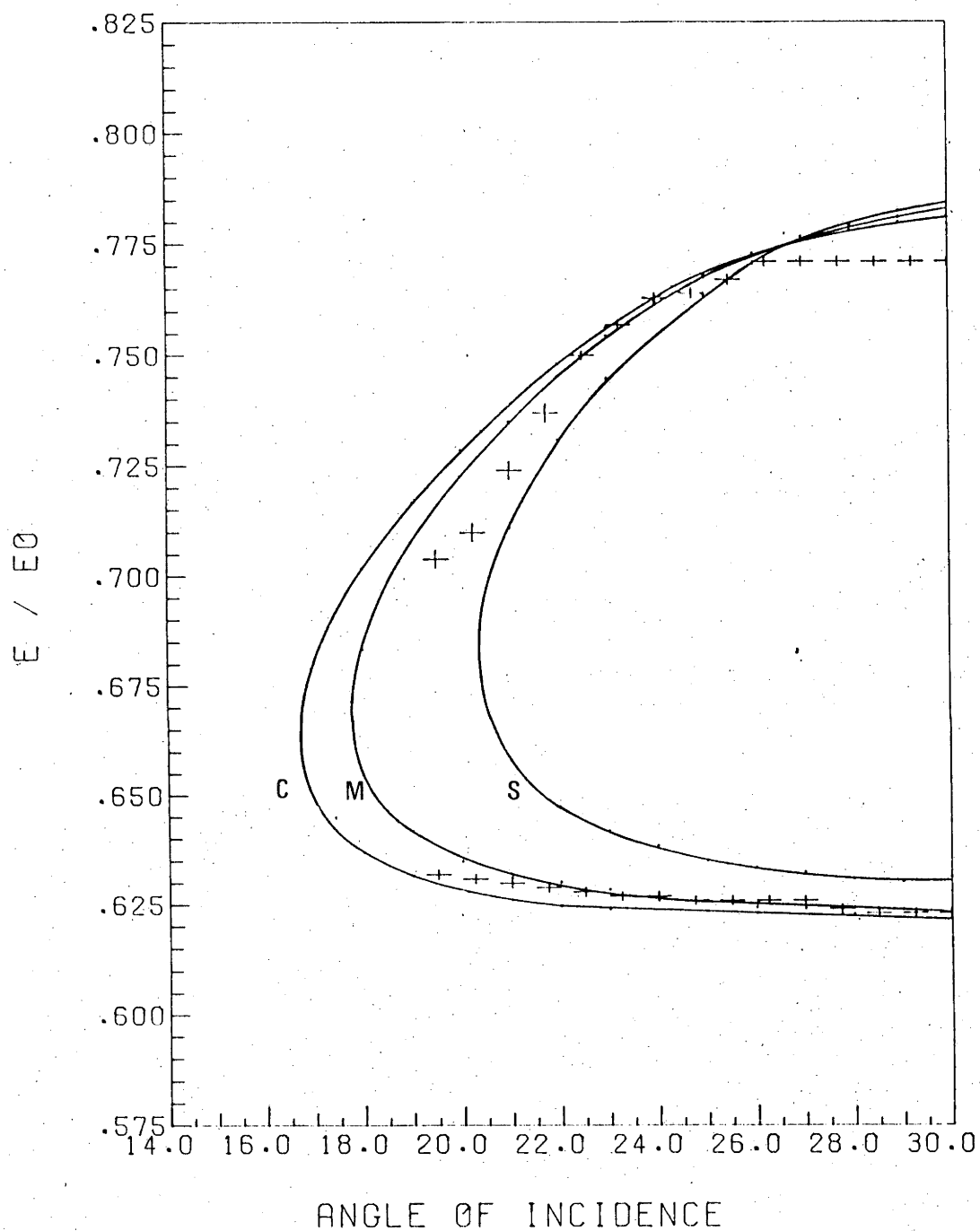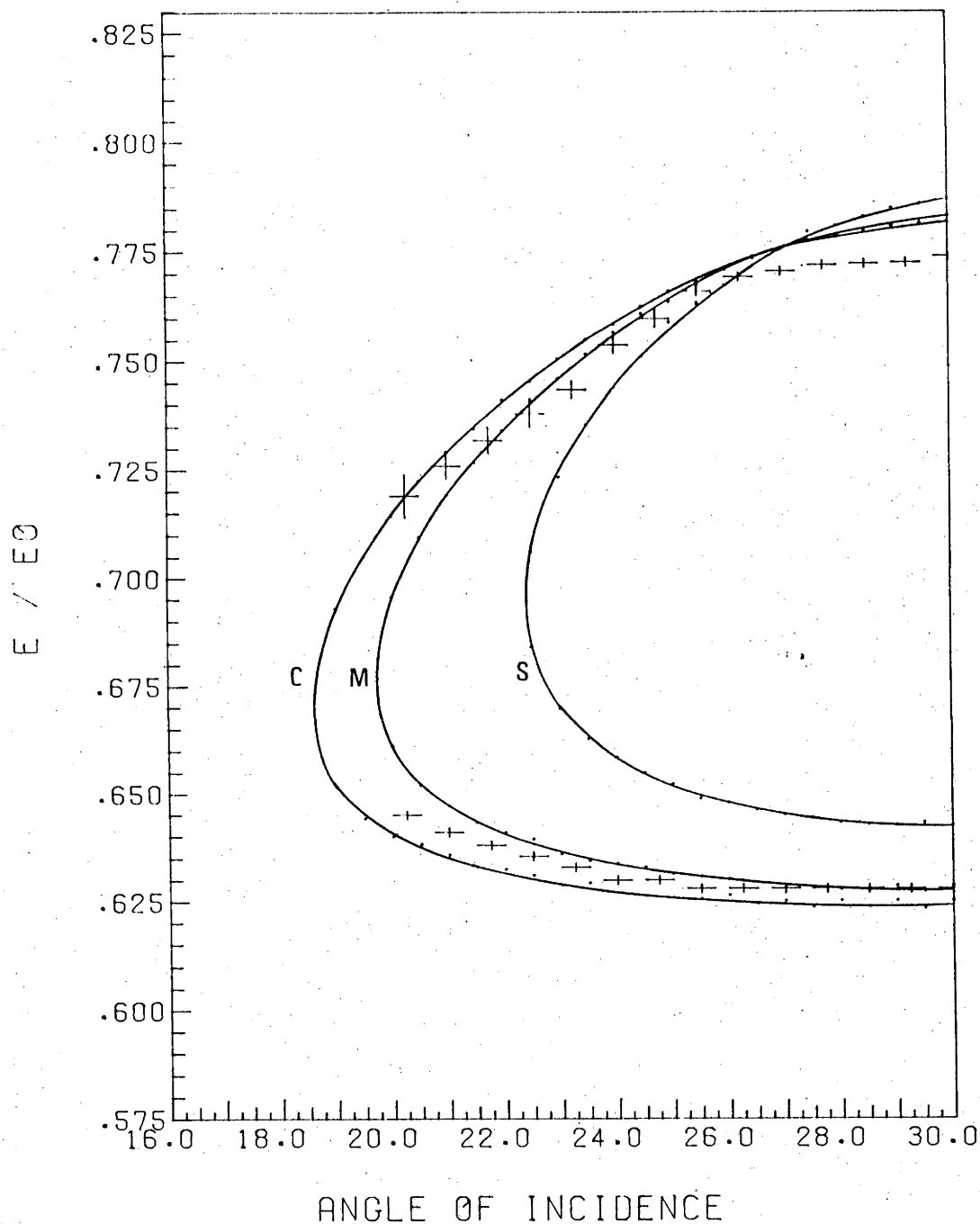correction factor of 1.16.

'6 KEV AR-W(110)   <111>

Fig. 6.21:   Comparison of the experimental measurements of the single
   and double scattering energies of Ar^{+} scattered off a W⟨111⟩
   surface chain.   The results of the energy angle loop simulation
   are denoted by C for the Csavinsky potential, M for the Moliere
   potential and S for the Moliere potential with a screening length
   correction factor of 1.16.

Fig. 6.22: Comparison of the experimental measurements of the single and double scattering energies of Kr$^+$ scattered off a W ⟨100⟩ surface chain. The results of the energy angle loop simulation are denoted by C for the Csavinsky potential, M for the Moliere potential and S for the Moliere potential with a screening length correction factor of 1.25.

'6 KEV KR-W(110) <111>

Fig. 6.23: Comparison of the experimental measurements of the single and double scattering energies of Kr^+ scattered off a W⟨111⟩ surface chain. The results of the energy angle loop simulation are denoted by C for the Csavinsky potential, M for the Moliere potential and S for the Moliere potential with a screening length correction factor of 1.25.

For the double scattering energy, the correction is made at the angle for which the computer simulations predict a nearly potential independent multiply scattering energy (i.e. at the double scattering curve crossing angle). No potential independent energy exists for single scattering so the correction is determined from the average predicted for the three potentials mentioned previously, at an angle for which the difference between the three is a minimum (i.e. specular conditions). The correction factors, η, and the corresponding energy loss, ΔE, for the four inert gas ions is given below.

Table 6.4

Measured Inelastic Loss for Surface Scattering of 6 keV Ions

Ion	$\langle 100 \rangle$				$\langle 111 \rangle$*			
	Single		Double		Single		Double	
	ΔE (eV)	η	ΔE (eV)	η	ΔE (eV)	η	ΔE (eV)	η
He	69	1.012	–	–	69	1.012	–	–
Ne	96	1.018	180	1.033	69	1.013	140	1.025
Ar	53	1.011	100	1.019	53	1.011	150	1.029
Kr	11	1.003	60	1.013	5	1.001	56	1.012

* $\langle 111 \rangle$ direction energy spectra peaks have not been corrected for the second layer component.

The typical error in these correction factors is ±0.001. The energy dependence of these results can be seen in figure 6.24 and it is evident that a velocity dependent loss is applicable for the loss suffered by surface scattered ions.

Using these correction factors the results were replotted as shown in figures 6.25 and 6.26. As the correction factors for Kr were small these are not replotted. It is evident that the "cold lattice" computer simulation does not adequately describe the interaction for angles of incidence close to the critical angle. The experimental results were therefore compared with the simulation results which incorporated thermal vibrations. As this simulation was more
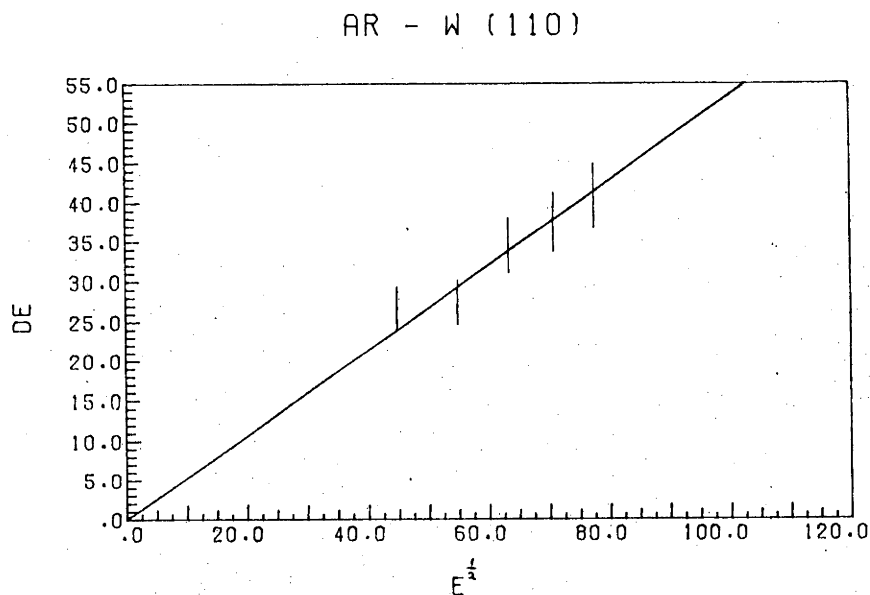
AR - W (110)

Fig. 6.24: For Ar onto W(110), the inelastic energy loss, DE, for singly scattered ions off the surface atomic layer is given by:

$$DE = (0.53 \pm 0.01) \cdot E^{\frac{1}{2}},$$

where DE and E are in eV, and E is the incident ion energy.

demanding of computational facilities, results have only been obtained for the Moliere potential with screening length correction factors of unity and either 1.16, for Ar, or 1.25, for Kr.

The comparison of experimental results to the Thermal Vibration model predictions in general reveal excellent agreement (see figs. 6.27 - 6.30). The experimental double scattering measurements are bracketed by the simulation results using the different screening length correction factors. The single scattering energy does not strictly follow the predicted trend in that it does not increase in energy as rapidly as expected as the angle of incidence is decreased. This could be the result of varying inelastic losses as the angle of incidence changes, or the increasing importance of single scattering off surface defects. It has already been shown (fig. 6.12) that scattering from defects is an important contribution to the yield
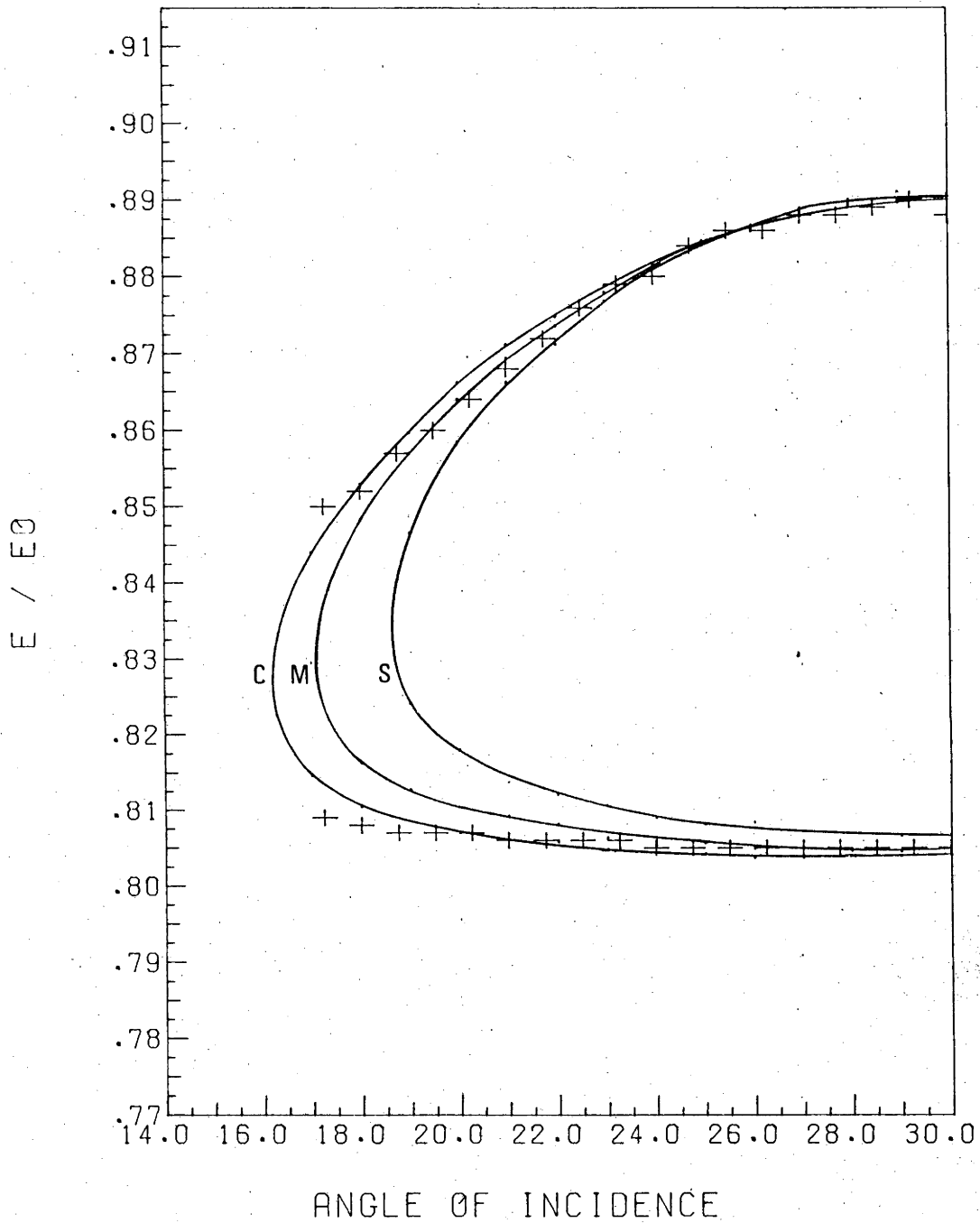
Fig. 6.25: Comparison of the results presented in fig. 6.20 to the simulation results for Ar$^+$ scattered off a W⟨100⟩ surface atomic chain. These results have been corrected for the inelastic energy loss.

Fig. 6.26: Comparison of the results presented in fig. 6.21 to the simulation results for Ar+ scattered off a W ⟨111⟩ surface atomic chain. These results have been corrected for the inelastic energy loss.
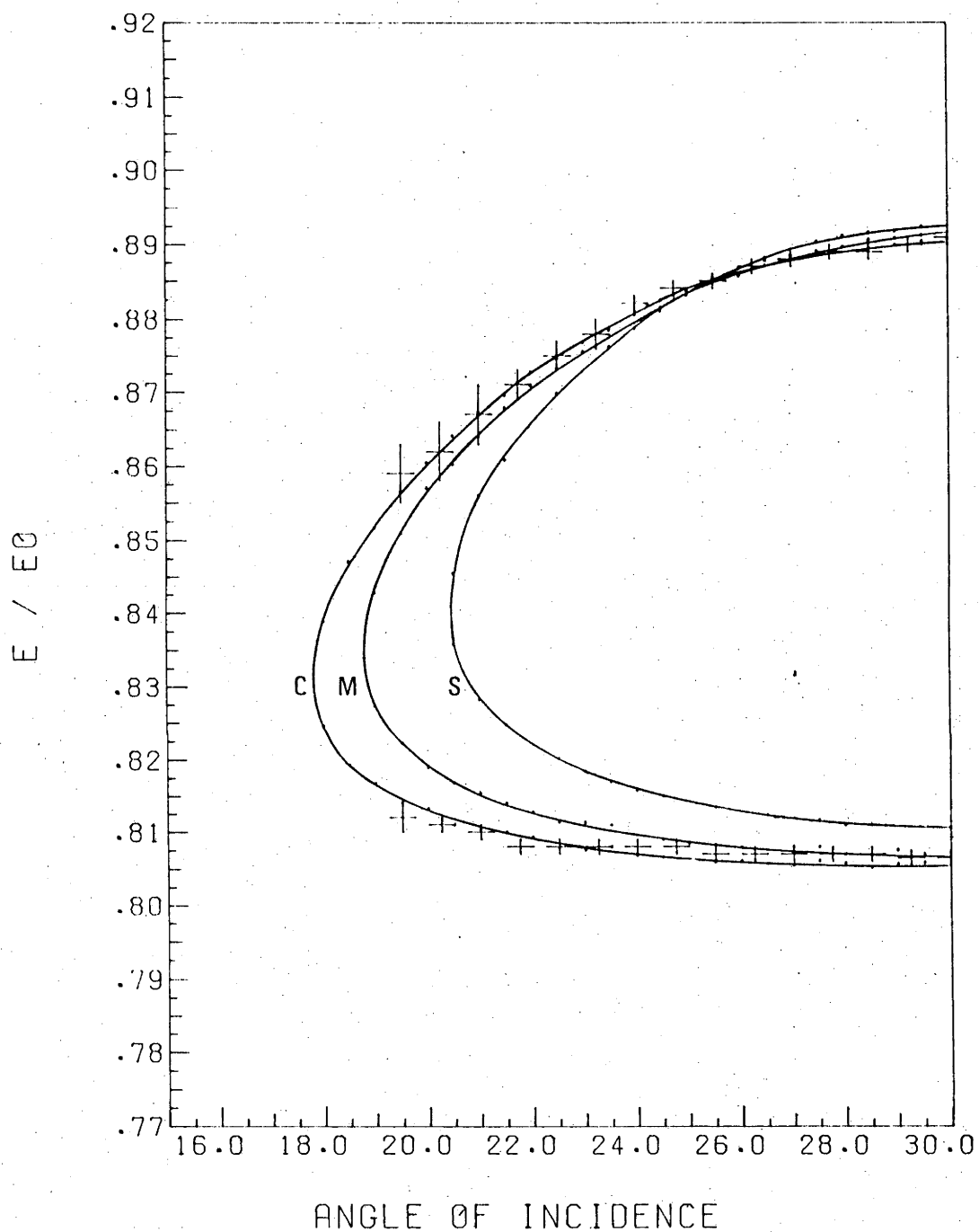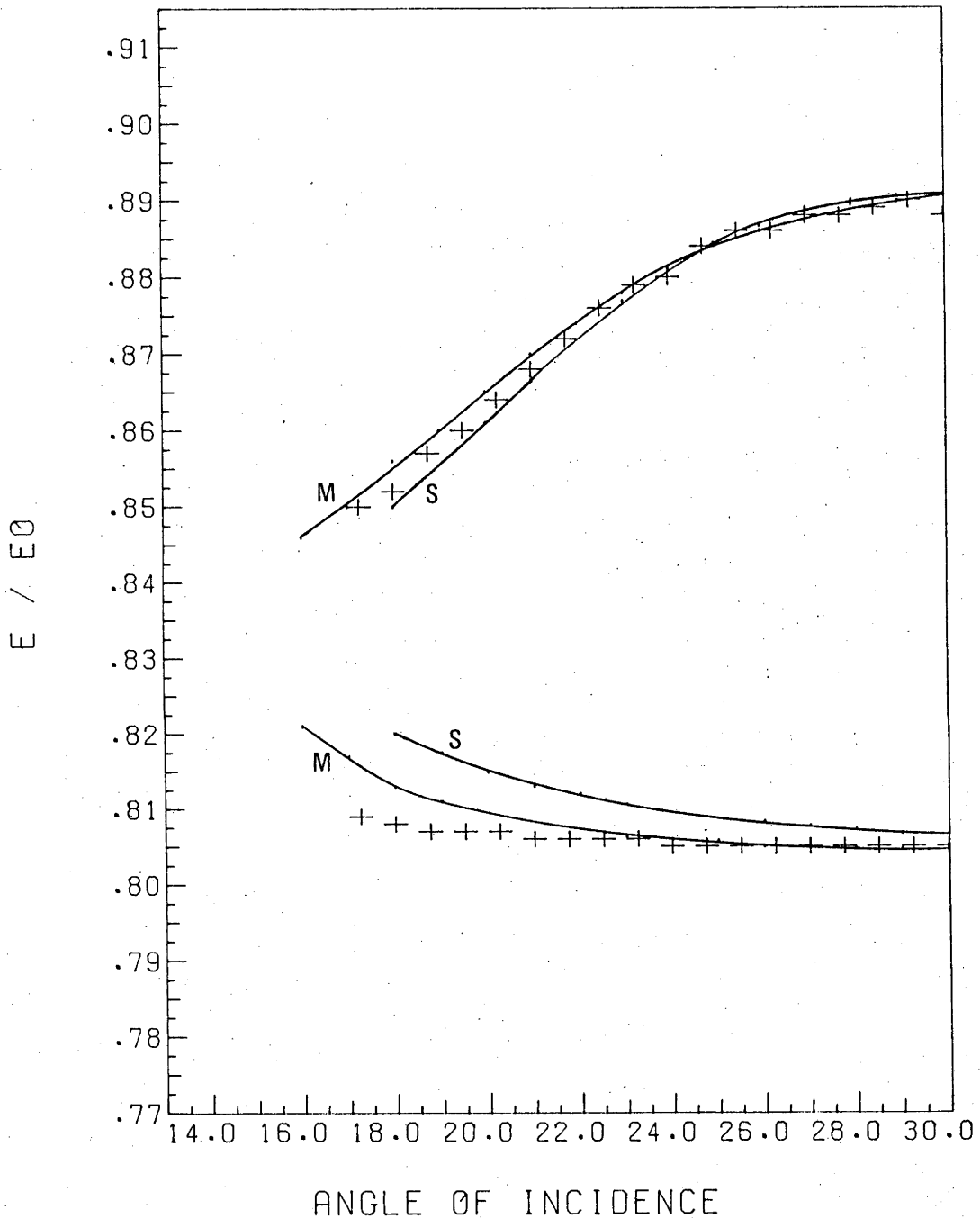
'6 KEV AR-W(110) <100>

ANGLE OF INCIDENCE

Fig. 6.27: Comparison of the experimental measurements of single and
double scattering energies (corrected for inelastic energy loss)
with the thermal vibration simulation for Ar^+ scattered off a W
⟨100⟩ chain. The simulation results are denoted by M for the
Moliere potential and S for the Moliere potential with a screening
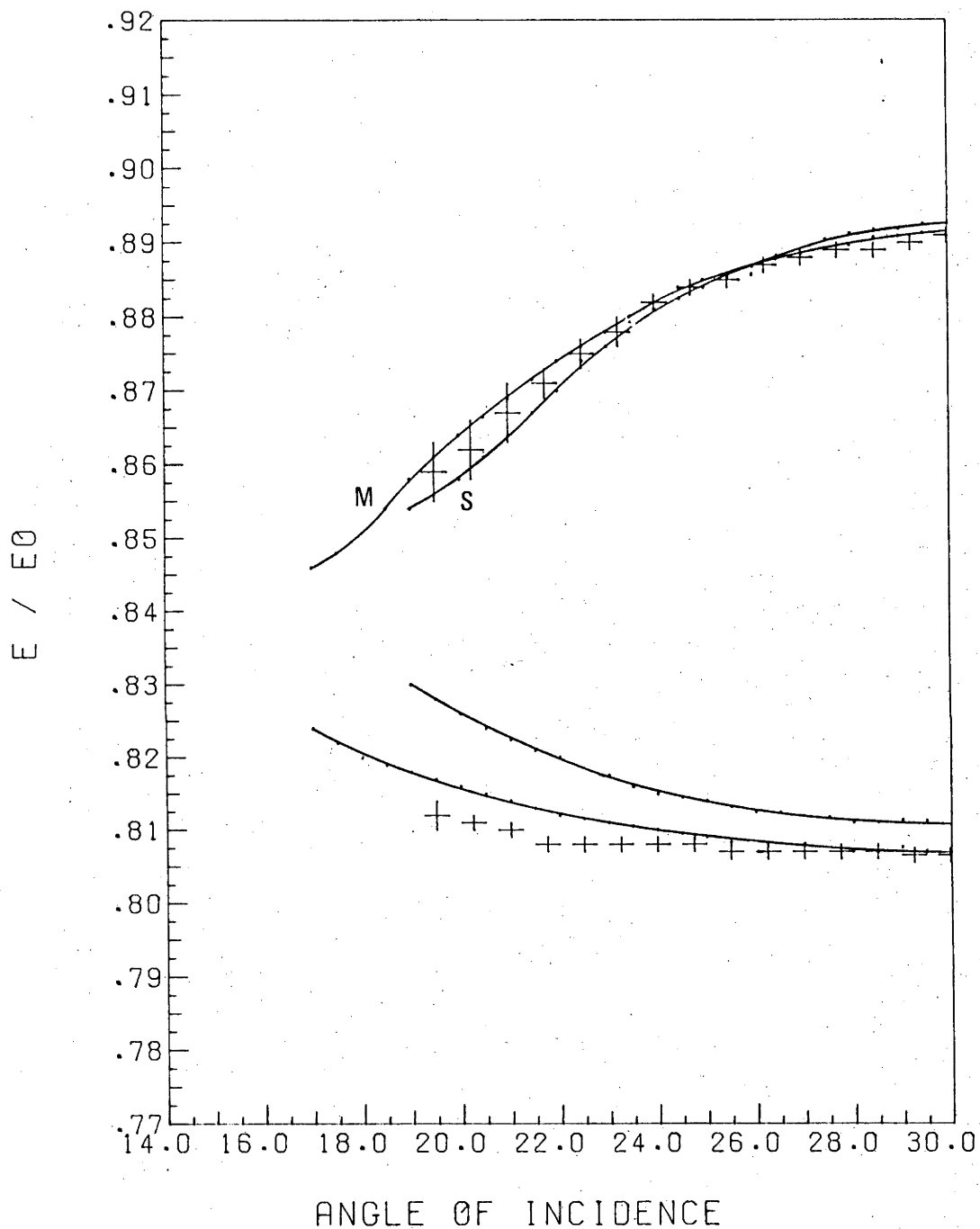correction factor of 1.16.

'6 KEV AR-W(110) <111>

Fig. 6.28: Comparison of the experimental measurements of single and double scattering energies (corrected for inelastic energy loss) with the thermal vibration simulation for Ar^+ scattered off a W ⟨100⟩ chain. The simulation results are denoted by M for the Moliere potential and S for the Moliere potential with a screening length correction factor of 1.16.
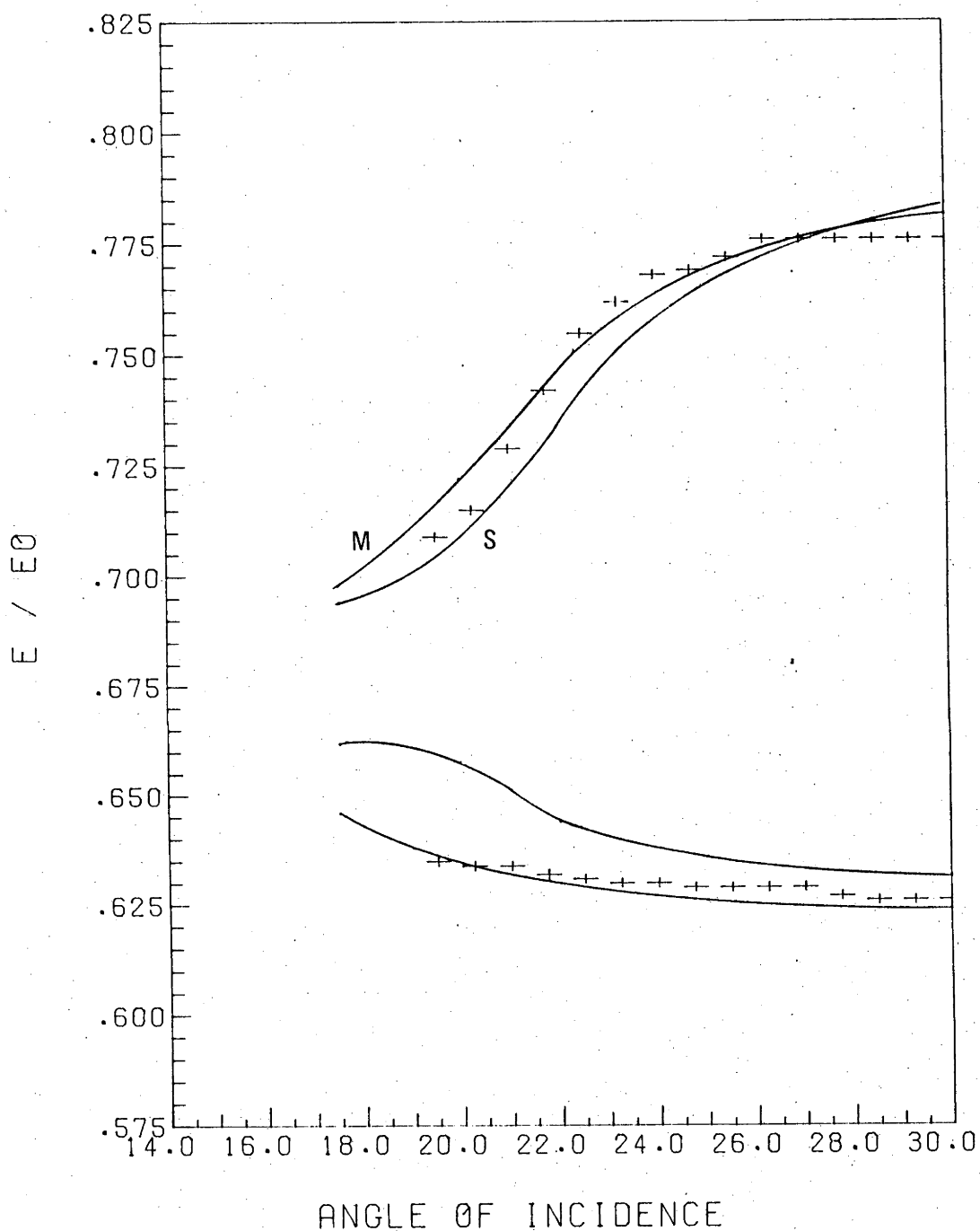
'6 KEV KR-W(110)   <100>

Fig. 6.29: Comparison of the experimental measurements of single and double scattering energies (corrected for inelastic energy loss) with the thermal vibration simulation for Kr$^+$ scattered off a W $\langle 100 \rangle$ chain. The simulation results are denoted by M for the Moliere potential and S for the Moliere potential with a screening length correction factor of 1.25.
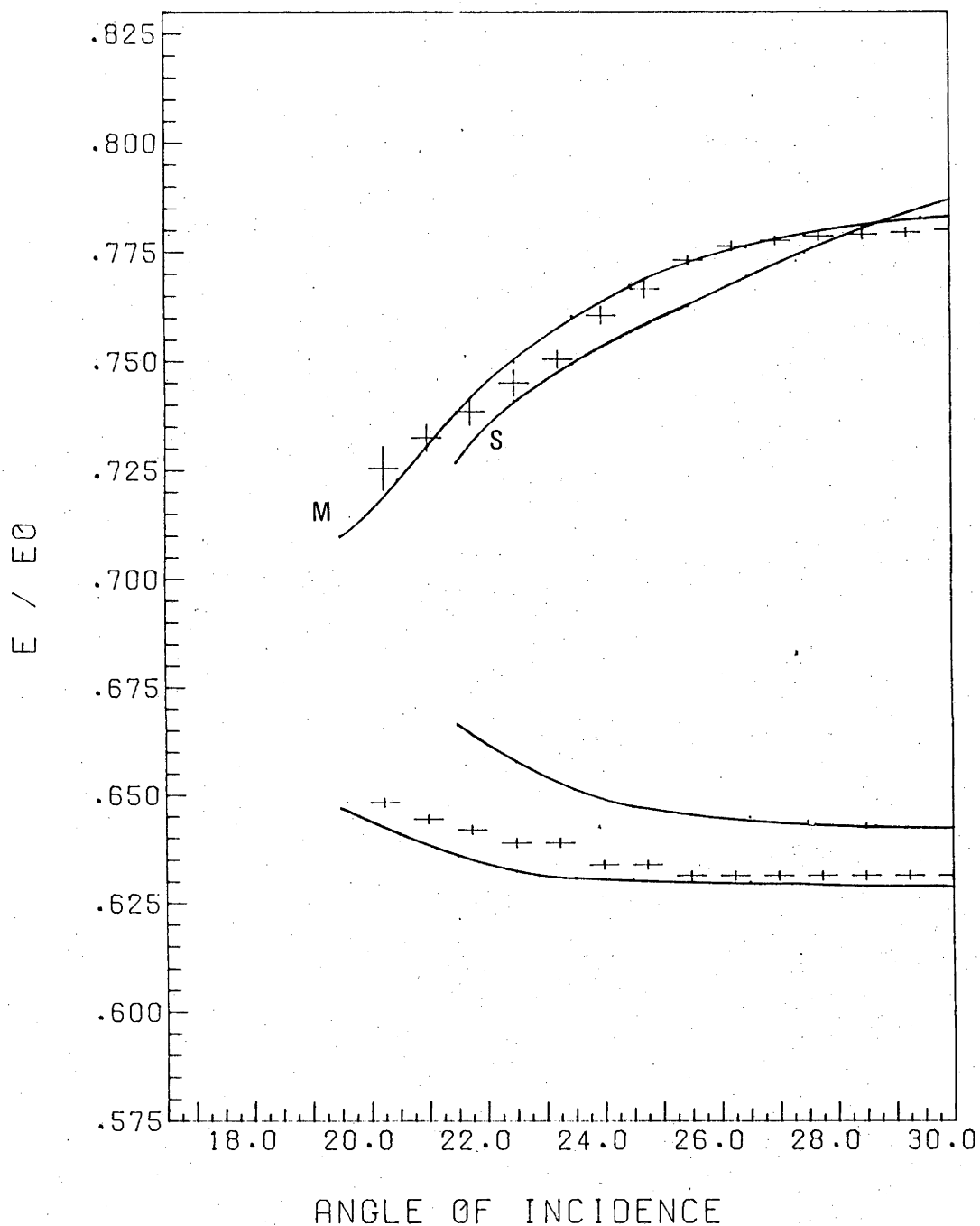
'6 KEV KR-W(110) <111>

Fig. 6.30: Comparison of the experimental measurements of single and double scattering energies (corrected for inelastic energy loss) with the thermal vibration simulation for Kr^+ scattered off a W ⟨111⟩ chain. The simulation results are denoted by M for the Moliere potential and S for the Moliere potential with a screening length correction factor of 1.25.

below the critical angle of incidence. No quantitative estimate of the yield from these defects is possible until more is known of the nature and density of surface defects.

In view of the uncertainty in determining single and double scattering energies which is caused by the thermal vibrations of the chain atoms, the inelastic energy loss and the effect of surface defects, the estimate for the screening length correction factor is accompanied by a considerable error. The best estimate from these results is that it lies in the range between unity and the value determined from the analysis presented in chapter four. The correction factors can therefore be given as:

$$\gamma_{Ar} = 1.08 \pm 0.08 , \qquad \qquad 6.16$$

and

$$\gamma_{Kr} = 1.13 \pm 0.12 . \qquad \qquad 6.17$$

The comparison of these results with the results presented in chapter four is illustrated in fig. 6.31.

6.10 CHARGE EXCHANGE

The charge exchange models have been described in chapter two where it was shown that the most comprehensive model is that of Verhey *et al.* This model incorporates "Auger-like" neutralization in the surface region as well as collisional ionization and neutralization. The predicted yield is given by:

$$Y(\alpha) = N_0 \, n \, \frac{d\sigma}{d\Omega} \, \Delta\Omega \cdot f_2 [f_1 (1 - P_N) + (1 - f_1) \, P_I] , \qquad 6.18$$

where α is the angle of incidence, N_0 is the number of incidence ions, n the number of target atoms and $d\sigma/d\Omega$ is the differential scattering cross section. $\Delta\Omega$ is the detector solid angle, P_I is the probability of collisional ionization and P_N is the probability of collisional neutralization. f_1 and f_2 are given by:
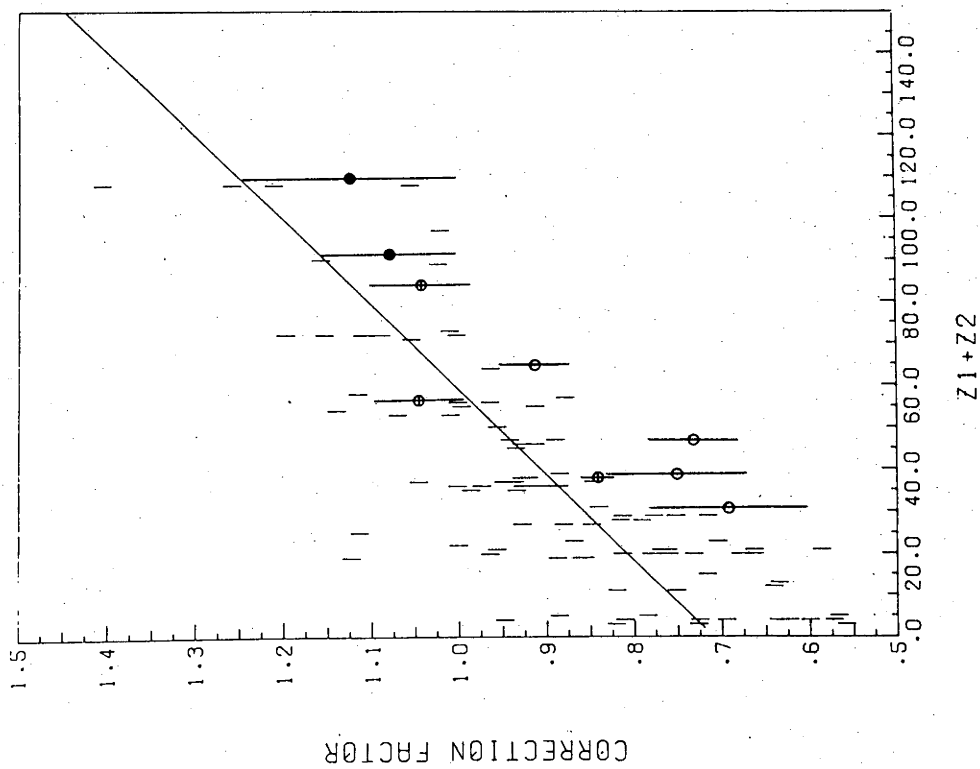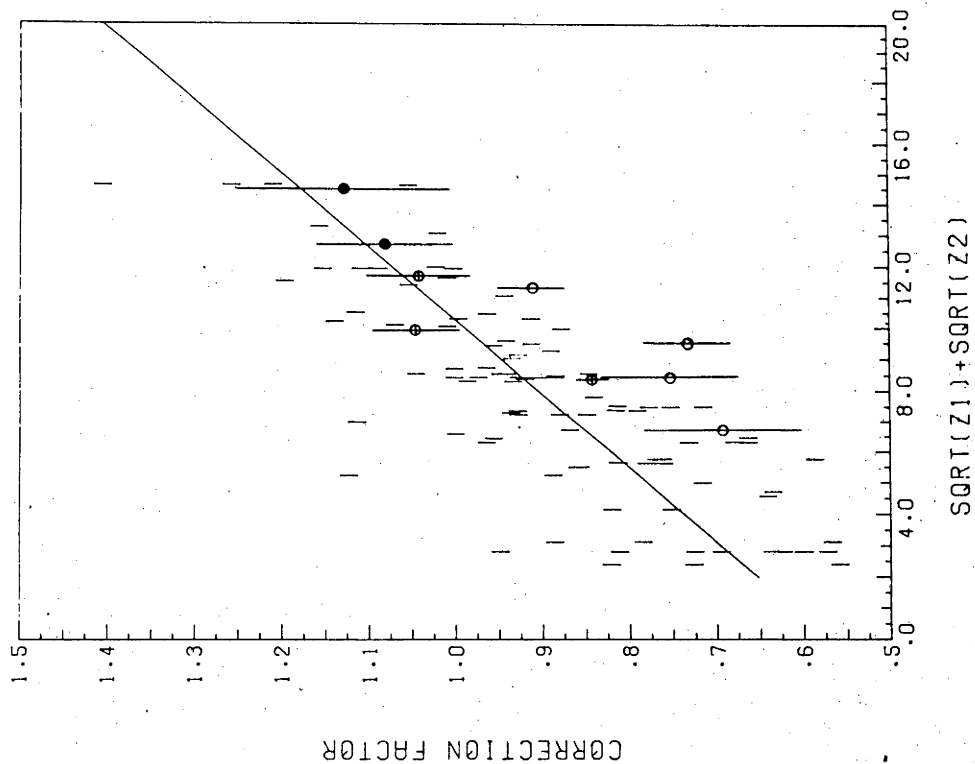
Fig. 6.31: Comparison of the screening length correction factors determined for Ar and Kr off W (denoted by ●) with the results presented in fig. 4.4.

$$f_1 = \exp\left(- \frac{v_c}{v_0 \sin\alpha}\right) , \qquad\qquad 6.19$$

and

$$f_2 = \exp\left(- \frac{v_c}{\gamma v_0 \sin(\theta - \alpha)}\right) . \qquad\qquad 6.20$$

The assumptions involved in this model are that the characteristic velocity, v_c, is independent of the perpendicular velocity, that the number of scattering centres, n, remains constant and that the scattering cross section is known. It has also been assumed that the same "Auger-like" neutralization is possible before and after the collision. This assumption cannot be expected to be valid. If it is possible to measure significant collisional ionization and neutralization, then collisional excitation is also possible. Collisional excitation has been shown to have a threshold energy of 200 eV for Na^+-Ne scattering.[20] As the value of v_c is a function of the transition rate, excitation can alter the value of v_c. The expression quoted above (equation 6.18) is only valid if the characteristic velocity for the excited particles is equal to that for the incident particles.

The fitting of three parameters to the experimental measurements results in a reduced confidence in each parameter and Verhey *et al.*[21] reported that for a simpler model which did not incorporate collisional neutralization, values of v_c between $(1.5 - 3.5) \times 10^5$ m/sec could be fitted to the results of scattering 4-10 keV He^+ off Cu(100).

In order to determine the applicability of this charge exchange model to the scattering of inert gas ions off W, a series of measurements were made of the ion yield about the specular scattering direction. In order to avoid problems with scattering cross section variations caused by interactions with neighbouring atoms of the chain, the angle of incidence was limited to between 25° and 35°. Computer simulation results using the "cold lattice" model revealed that there was no significant change in the scattering contributions of neighbouring chain atoms for these conditions. The results were fitted to the above equation by a least squares fitting program. The consistency of this fitting procedure was tested by comparing analysed

results for peak heights and for integrated peak yield. In all cases
where there was no shift in the peak position, the separate sets of
data resulted in the same fitting parameters to within the errors
associated with this procedure.

As mentioned previously, this model assumes that the number of
scattering centres remains constant, however it has been shown
previously that significant yields can be detected from scattering
events involving the second atomic layer. Results obtained under such
conditions will not give meaningful results.

The results of these experiments as well as the least squares
fitted curves are shown in figures 6.32 - 6.34 for the various inert
gas ions. These results have been corrected for the change in yield
caused by the change in the bombardment spot area as the angle of
incidence is varied. The results have been normalized to the yield at
specular scattering conditions to eliminate the unknowns in equation
6.18.

As the $\langle 110 \rangle$ is a planar channel the results for Kr (fig. 6.32)
are in agreement with the theoretical model. The atoms of the second
row are shielded at these angles and the probability of penetration is
smaller for Kr than for the other ions. The poor agreement in the
$\langle 111 \rangle$ direction is probably the result of a change in the focal length
associated with the surface rows as the angle of incidence is altered.
The change in focusing conditions effectively alters the number of
incident ions as the beam is focused onto the second layer. The
result in the $\langle 100 \rangle$ direction corresponds to a zero value of v_c and is
either the result of a "blocking" of the Auger transition process in
this direction, or an enhanced yield at larger angles of incidence
caused by changing scattering conditions. As there is no
corroborative evidence for a blocking of the neutralization process
from other studies, it must be assumed that the yield enhancement is
caused by a change in the number of scattering centres as the angle of
incidence is changed.

The Ar^+ results (fig. 6.33) agree with the model for the $\langle 111 \rangle$
direction, but not for the $\langle 110 \rangle$ direction which is the reverse of

'HE — W <100>

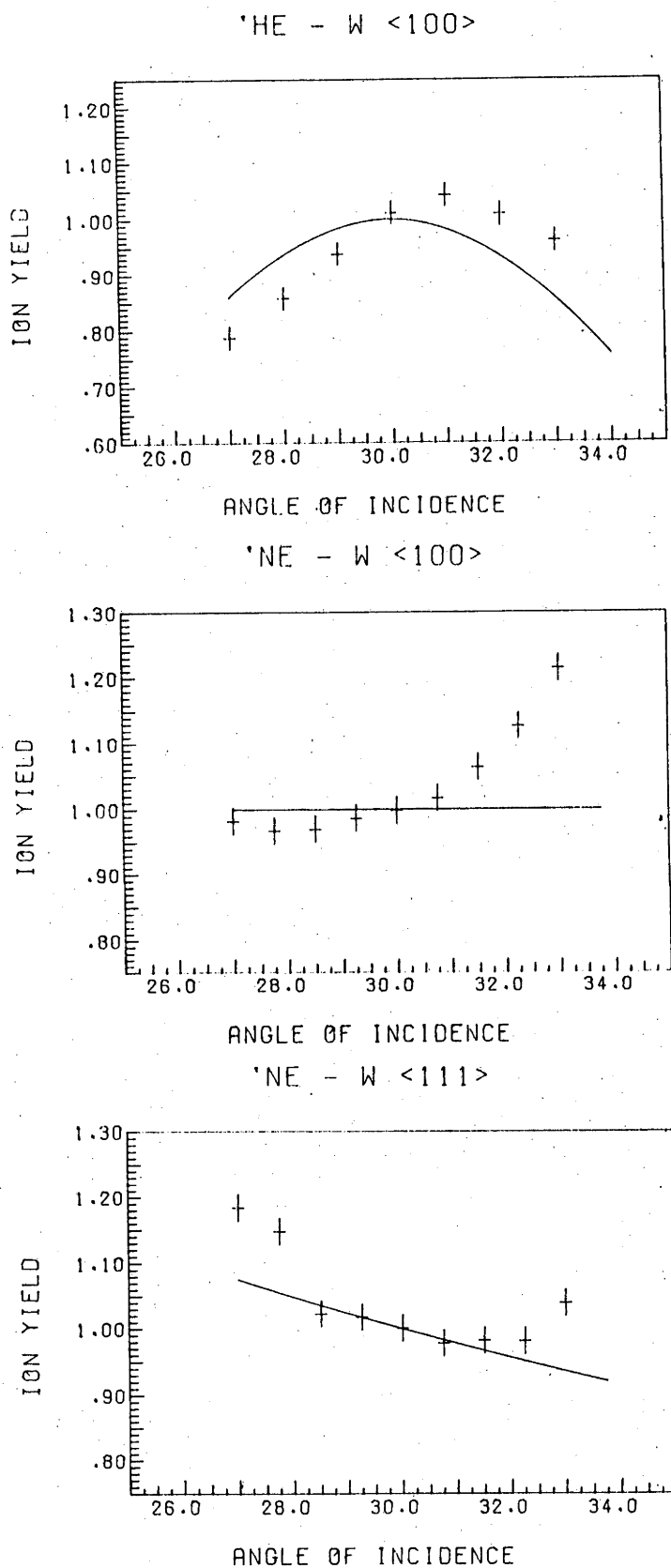'NE — W <100>

'NE — W <111>

Fig. 6.32: The comparison of the normalized ion yield to the least
squares fitted dependences predicted by the charge exchange model.
These results are for He$^+$ and Ne$^+$ scattered off the specified
atomic chain directions.

'AR - W <100>

'AR - W<110>

'AR - W <111>

Fig. 6.33: The comparison of the normalized ion yield to the least squares fitted dependences predicted by the charge exchange model. These results are for Ar^+ scattered off the specified atomic chain directions.

'KR - W <100>

ANGLE OF INCIDENCE

'KR - W <110>

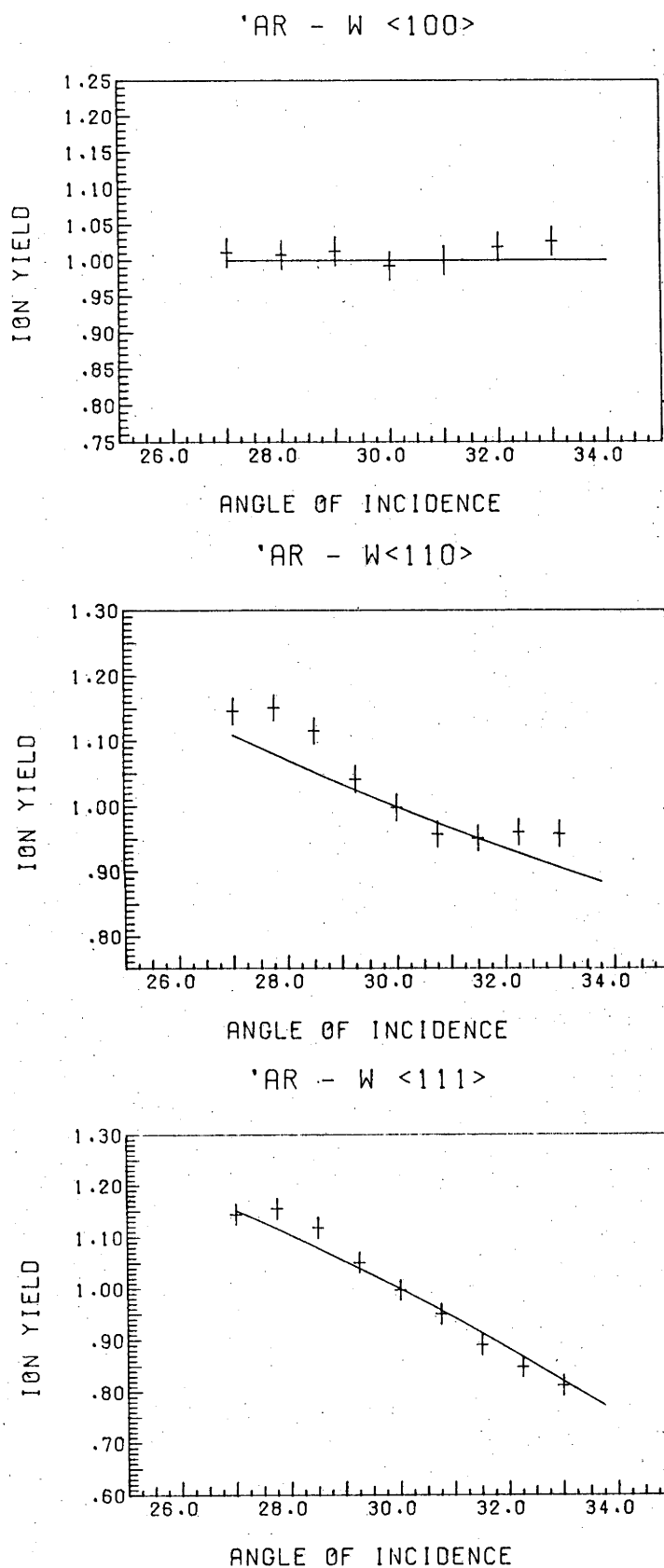ANGLE OF INCIDENCE

'KR - W <111>
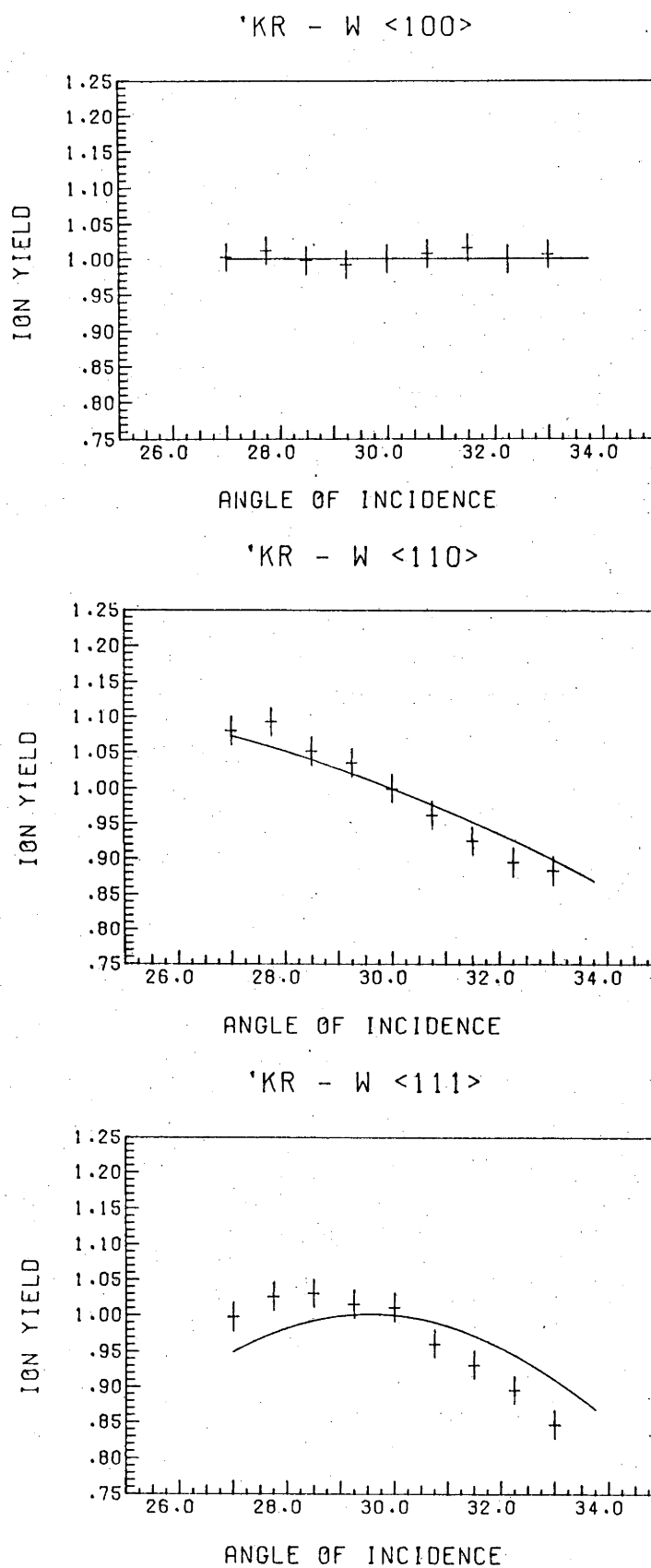

ANGLE OF INCIDENCE

Fig. 6.34: The comparison of the normalized ion yield to the least
squares fitted dependences predicted by the charge exchange model.
These results are for Kr$^+$ scattered off the specified atomic chain
direction.

that found with the Kr^+ results. Although this difference with the Kr results may be due to different focal lengths and surface chain penetration probabilities, insufficient evidence is available to allow a definite conclusion to be arrived at. The results in the $\langle 100 \rangle$ direction are similar to the Kr^+ results in the $\langle 100 \rangle$ direction which indicates that the effect which is causing the disagreement with the model is not necessarily dependent on the atomic species used. This disagreement with the theoretical charge exchange model is worse for Ne^+ in the $\langle 100 \rangle$ direction (see fig. 6.34) where the yield increases at high angles of incidence. The only explanation for this, apart from a yield due to scattering from the second layer, would be an ionizing transition when in the surface region, with transition characteristics similar to those for an Auger process. A resonance ionization process involving electron tunnelling to the conduction band of the solid is a possibility but it would be necessary to explain why this has not been observed for the other crystallographic direction. It seems that the most likely explanation is once again that the scattering off the subsurface atomic layers contributes to the single scattering yield at high angles of incidence. For Ne bombardment in the $\langle 111 \rangle$ direction there is agreement to the model over a limited range of angles.

For He scattering, the only direction for which the surface scattering component is separate from subsurface contributions over a range of angles of incidence is the $\langle 100 \rangle$. The results of measurements taken in this direction are illustrated in fig. 6.34.

The fitted parameters from these results are listed in table 6.5. In each case, the parameters are taken from the direction which yields results that best fit the theoretical model. The typical errors are $\pm 25\%$ for the value of v_c and ± 0.10 for P_I and P_N.

On the basis of the results obtained for 60° total scattering it would appear to be unwise to make measurements of the charge exchange process at large scattering angles as it is possible that scattering from subsurface layers will contribute to the measured yield.

It is hoped that experiments at lower total scattering angles

Table 6.5

Measured Charge Exchange Parameters

Ion	v_c (m/sec)	P_I	P_N
He	2.0×10^6	0.0	0.50
Ne	1.5×10^4	0.98	0.90
Ar	2.2×10^5	0.11	0.07
Kr	8.0×10^4	0.25	0.06

planned for the future will resolve the uncertainties raised by these results. It is important to obtain information under controlled conditions where subsurface scattering does not contribute to the ion yield.

The importance of the results of scattering from W will be summarized and conclusions drawn from them discussed in the following chapter.

6.11 SILICON SURFACE STRUCTURE

In view of the successful application of low energy ion scattering to the determination of the W(110) surface, preliminary studies were made to assess its application to the determination of the Si(100) surface.

The surfaces of Si and Ge have been known for some time, from low energy electron diffraction (LEED) studies, to have surface structures which are not characteristic of the bulk structure.[21,22] Schlier and Farnsworth[21] in 1959 reported the observation of "half order" spots in LEED studies with a clean Si(100) surface. This corresponds to a doubling of the conventional unit cell spacing. This structure is readily observed for samples cooled from 800 °C while annealing at temperatures of 700-900 °C for periods of an hour can produce "quarter-order" features.[22] Since the earliest discoveries of the surface reconstruction many LEED studies have been made of Si crystal surfaces and, from these, a number of models have been proposed to

explain the results.[21-25]   While not all the models can be
considered here, those which seem to have attracted most attention and
which have been compared to LEED experimental studies, will be
considered.   It should be noted that the reconstruction has been
observed for all the low index faces of Si and Ge, and that the models
differ for each face.   The LEED results have revealed different
diffraction patterns for each crystal face.   In the following
discussion only the (100) face of Si will be considered.

The proposed surface reconstruction models are compared to the
unreconstructed surface in fig. 6.35.   In these figures the ⟨100⟩
surface direction is at 45° to the horizontal axis.   The analysis of
the surface structure is complicated by the fact that the atomic
structure of alternate atomic layers is rotated by 90°.   Thus in any
experimental investigation, the results from two effectively different
surface structures will be measured simultaneously.

Care must be taken in the experimental investigation as it is
believed that low levels of contamination can destroy or modify the
reconstruction.[26,27]   The contamination may result from the
adsorption of residual gas, diffusion of contaminants from the bulk of
the sample or surface migration.   Modifications may result from the
implantation of the bombarding ion as well.

As the silicon surface is known to become amorphous under ion
bombardment, it was necessary to conduct these experiments with a
heated target.   The temperature chosen to obtain the most ordered
surface was that found by Molchanov and Snisar[28] in higher energy
studies of radiation damage annealing in Si.   Using 10-30 keV Ne, Ar
and Kr bombardment of various low index faces of Si, they found that
the surface damage was annealed for temperatures over the range from
300 °C to 700 °C and that the temperature for maximum order was
believed to be 450 °C.   All experiments described in this study
concerning structure investigation were conducted with the target at
450 °C.

As the results for W revealed that, at these energies (6 keV), He
could be scattered by subsurface atomic layers in a charged state, the
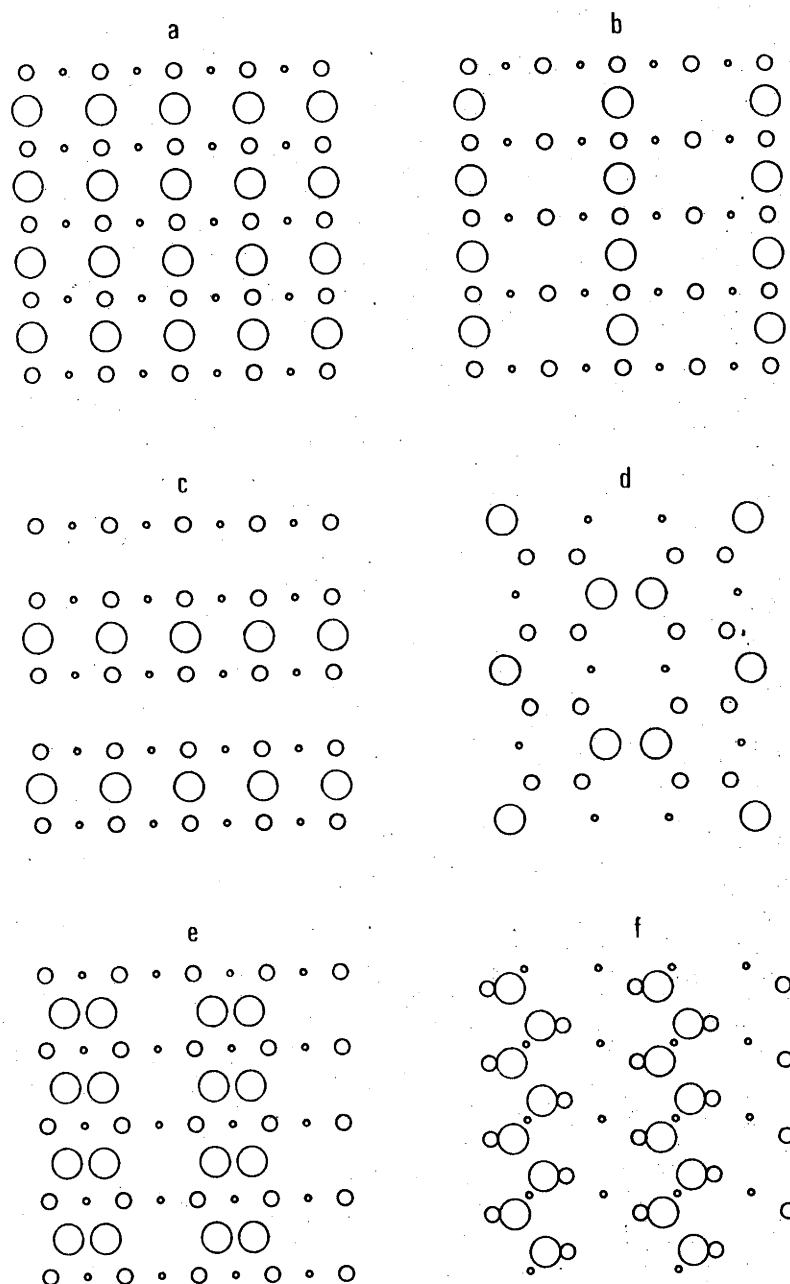
SI (100) SURFACE STRUCTURES

Fig. 6.35: The comparison of an ideal Si(100) surface structure (a) with models of the reconstructed surface which are referenced in the text. The largest circles represent the surface atomic layer, the smaller represent the second atomic layer and the smallest circles represent the third atomic layer.

ions used in this investigation were Ne^+ and Ar^+. Ar^+ scattering was studied as it promised to yield the greatest information on the surface structure. As the total scattering angle was 45° and the limiting scattering angle for Ar off Si is 44.7°, single scattering was not possible (see equation 2.4). However the double scattering for two smaller angles, which is more sensitive to surface structure, was possible.

6.12 EXPERIMENTAL DETERMINATION OF SILICON SURFACE CRYSTALLOGRAPHY

The energy spectra for Ne^+ and Ar^+ scattered off Si(100) are shown in figure 6.36. The Ne^+ spectrum consists of a single scattering peak at 0.643 E_0 and a broad high energy peak which has a maximum yield at 0.767 E_0. The energy spectrum for Ar^+ scattering consists of a broad Si^+ recoil peak over the energy range of 0.47 - 0.52 E_0 and a small double scattering Ar^+ peak at 0.59 E_0 on top of a broad high energy peak. The high energy component of the Ar^+ spectrum consists of multiple scattering Ar^+ and surface scattered Si recoils (see fig. 6.5).

To investigate the surface structure, a series of angular scans were obtained for Ne^+ and Ar^+ bombardment at different angles of incidence (see figures 6.37 and 6.38). In these figures the zero angle is aligned with the ⟨100⟩ direction of the bulk crystalline structure as determined by X-ray diffraction. The complications arising from the 90° surface structure rotation are evident from these scans which reveal a roughly regular structure with a period of 90°. The only deviation from this 90° periodicity is the high energy peaks at ±90° for the Ar^+ scans. As these are not observed at β = 0°, they must be the result of scattering off a portion of the target holder.

The predominant features to note in these figures are the enhanced yield at ±7° and in the region of β = 45°. As well, there is an apparent asymmetry about the β = ±45° directions. This asymmetry implies that the surface has only one axis of symmetry in its structure. To explain this point, consider a surface which has one
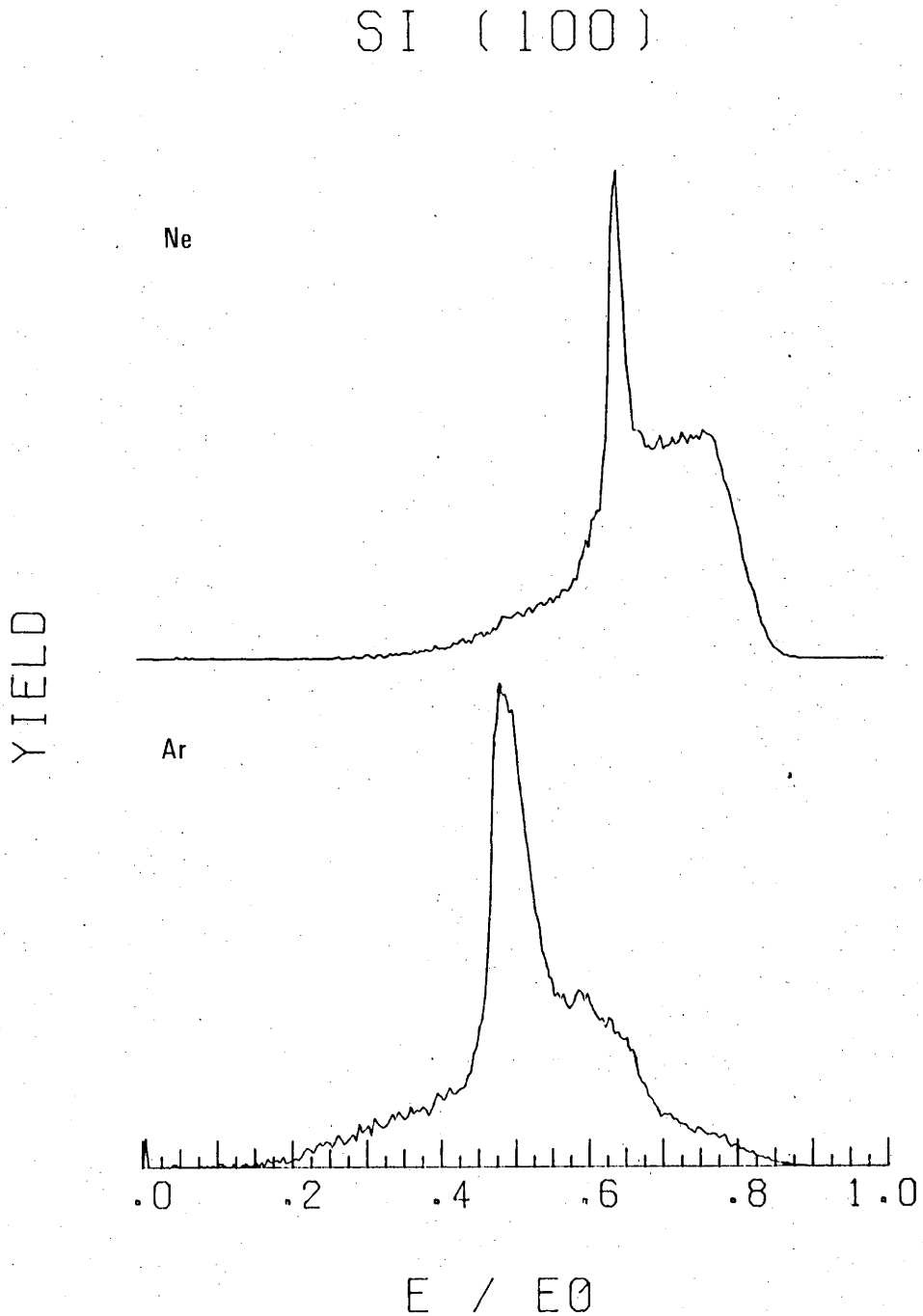
SI (100)

Fig. 6.36: Typical energy spectra obtained from Ne$^+$ and Ar$^+$ bombardment of a Si(100) surface. The principal peak for the Ne$^+$ bombardment is the result of single scattering while the principal peak for Ar$^+$ bombardment results from direct recoils of Si surface atoms.
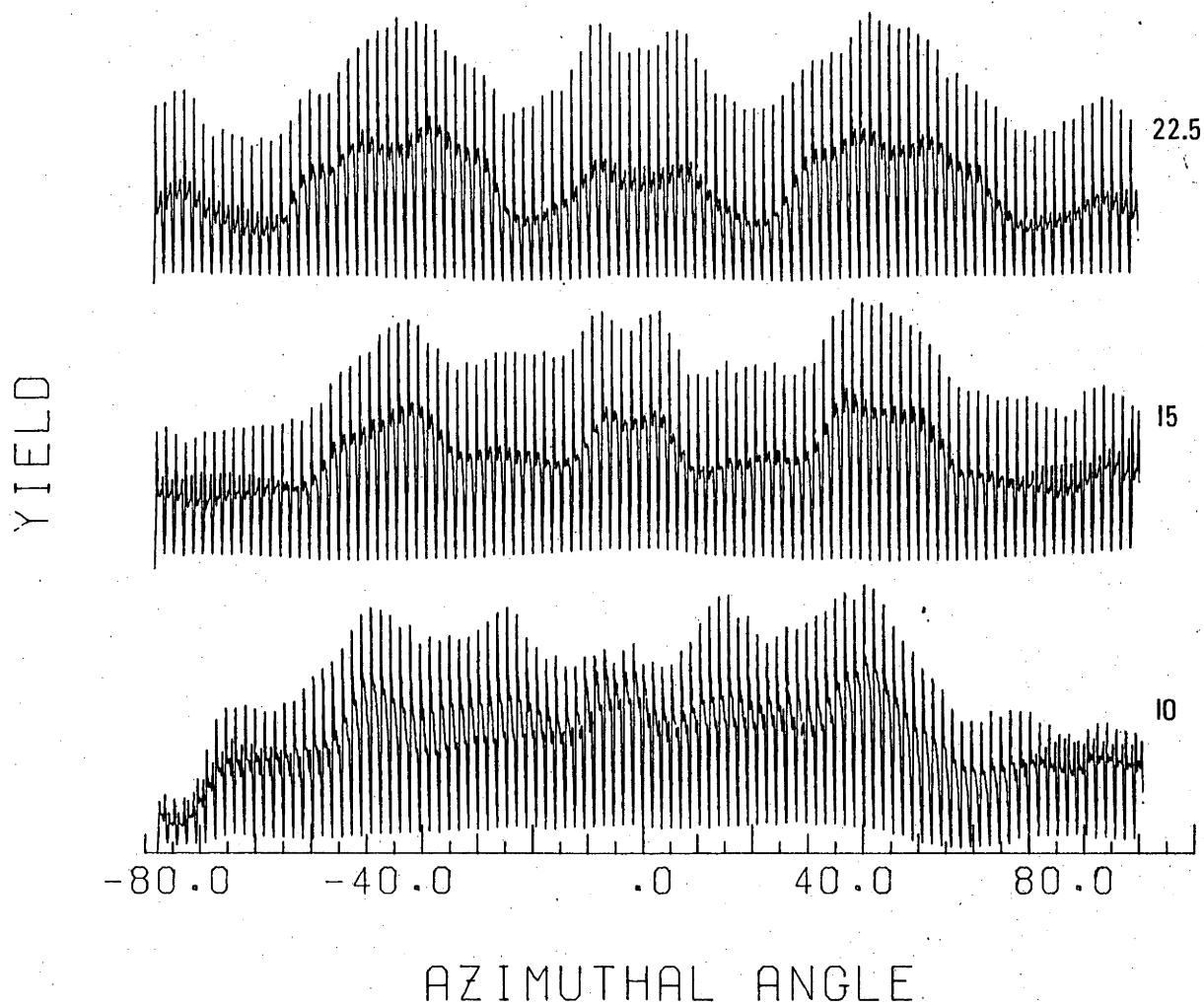
Fig. 6.37: Azimuthal scans for 6 keV Ne[+] bombardment of a Si(100) surface.
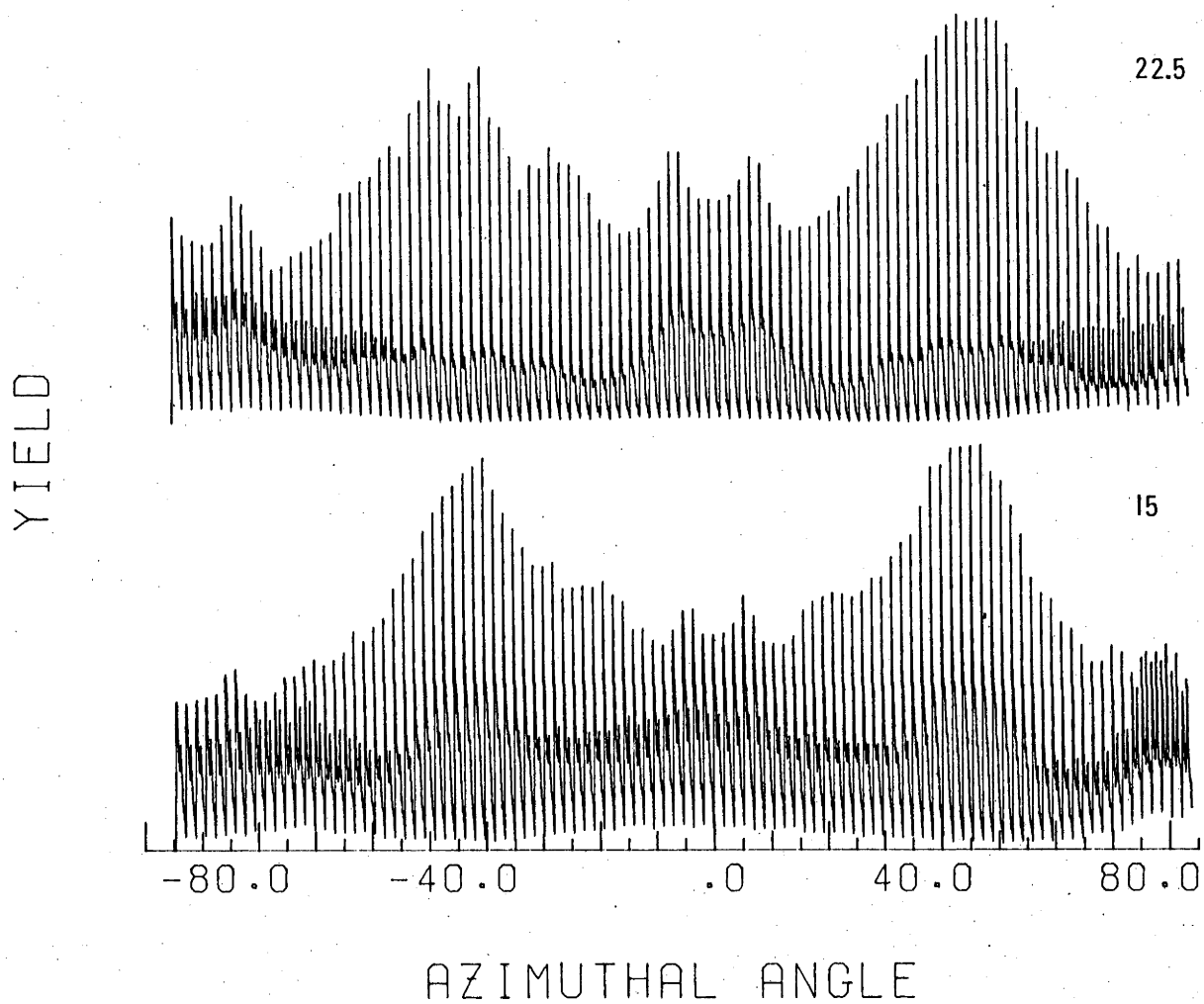
6 KEV AR — SI (100)

Fig. 6.38: Azimuthal scans for 6 keV Ar+ bombardment of a Si(100) surface.

are perpendicular to the beam direction and there is no chance for
shielding of target atoms by neighbours.

There appears to be qualitative agreement for the surface model
illustrated by fig. 6.39f, but a more definite decision on the surface
structure cannot be made until further experiments are conducted.
Although a crystallography has been determined, without accompanying
LEED analysis there is no way of determining whether it corresponds to
that which gives "half order" patterns, "quarter-order" patterns or
some other crystallography. To determine the cleanliness of the
surface, an Auger Electron Spectrometer is also necessary. With these
added facilities, not only could the surface structure be determined
but also the importance of contaminants to the "fixing" of different
structures could be ascertained. The determination of the surface
structure of Si, or any other element or compound, clearly needs a
hybrid analysis system incorporating ISS, LEED and Auger Electron
Spectroscopy as minimum requirements.

6.13 Si^+ CHARGE EXCHANGE

The strong recoil peak measured for Si^+ using Ar^+ bombardment
allowed measurements to be made of the characteristic velocity, v_c,
for the neutralization of Si^+ at a Si surface. The recoil ion yield
is given by:

$$Y^+(\alpha) = n\ N_0 \cdot \frac{d\sigma}{d\Omega} \cdot \Delta\Omega \cdot P_I(E_0)\ \exp\left(-\frac{v_c}{v_2\ \sin(\theta-\alpha)}\right), \qquad 6.21$$

where n is the target atomic density, N_0 the number of incident ions,
$d\sigma/d\Omega$ is the recoil cross section, and $\Delta\Omega$ is the detector solid angle.
$P_I(E_0)$ is the probability of collisional ionization of the Si atom, θ
is the total scattering angle, α is the angle of incidence and v_2 is
given by:

$$\frac{v_2}{v_0} = \frac{2\ \cos\theta}{1+\mu}, \qquad 6.22$$

where v_0 is the incident ion velocity. Assuming that the recoil cross
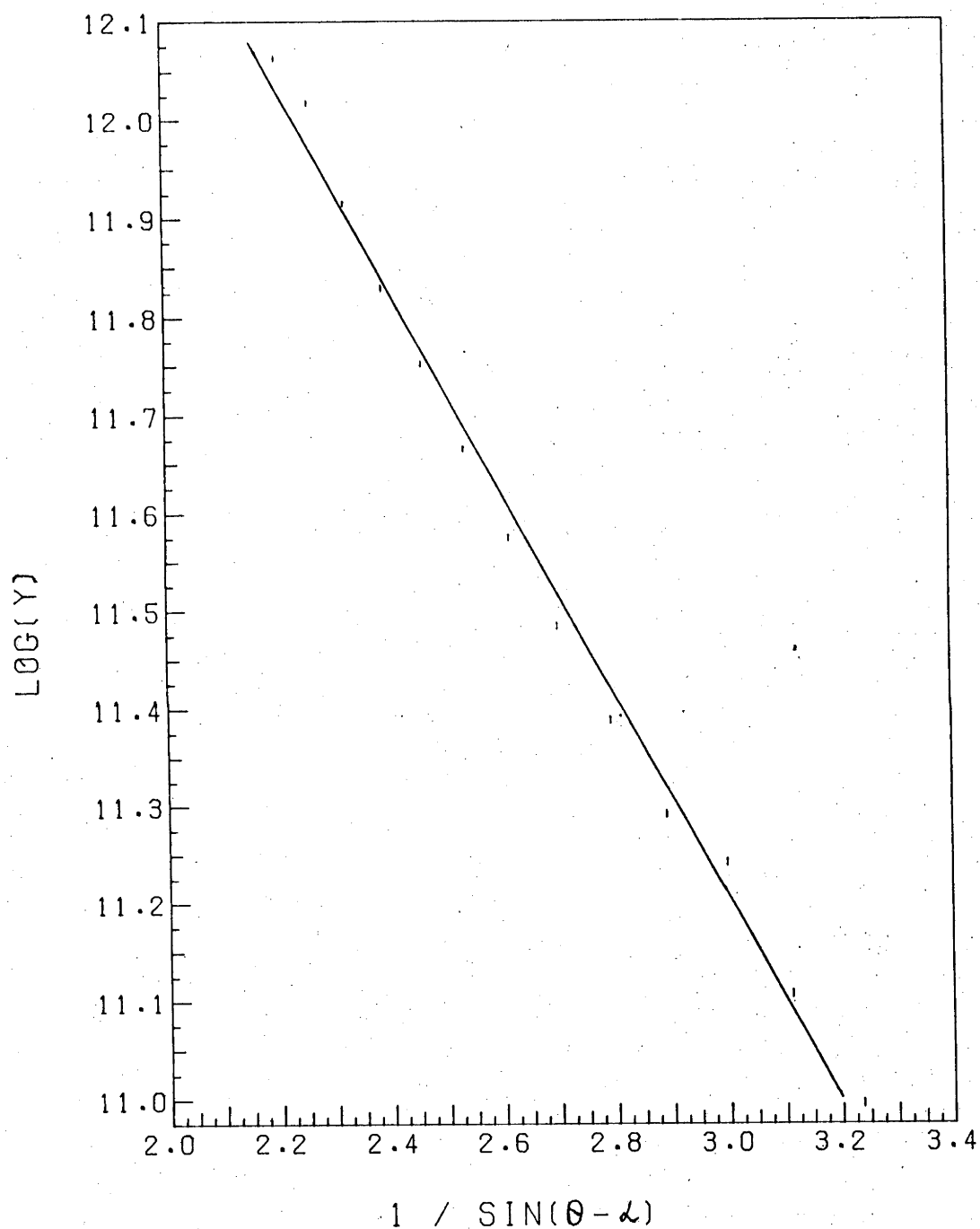section and the probability of collisional ionization are independent

SI CHARGE EXCHANGE

Fig. 6.40: Illustration of the linear relationship between the component of velocity perpendicular to the surface and the $\log_e$(yield) for recoiling Si surface atoms. From the gradient, the Auger characteristic velocity can be determined.
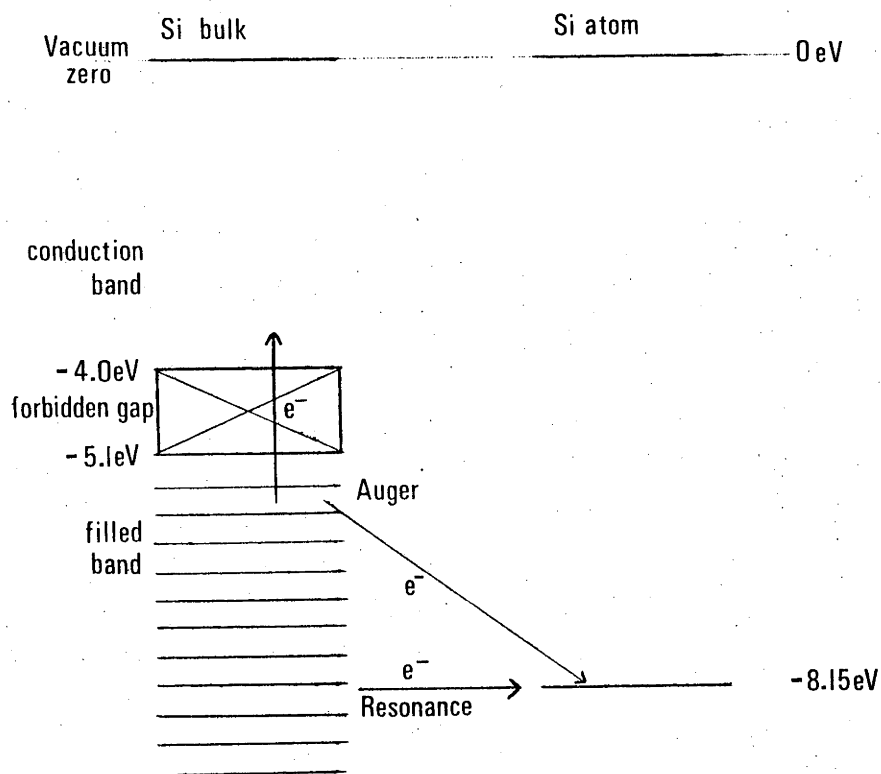
Fig. 6.41: Illustration of the charge exchange mechanisms proposed for the neutralization of Si^+ near a Si surface.

of the angle of incidence, the previous equation can be simplified to give:

$$\ln Y^+(\alpha) = -\frac{v_c}{v_2 \sin(\theta - \alpha)} + C .$$ 6.23

Therefore, a measurement of the ion yield as a function of the angle of incidence will allow the determination of the characteristic velocity v_c.

The recoil yield as a function of the angle of incidence was measured from an amorphous silicon target. The amorphous target was used to reduce the possibility of shadowing effects encountered in the single crystal studies. The results are illustrated in figure 6.40 and from the least squares fit to the measurements, the value of v_c was determined to be $(1.47 \pm 0.04) \times 10^5$ m/sec at 2.9 keV.

CHAPTER SEVEN

CONCLUSION

In the past Ion Scattering Spectroscopy (ISS) has been used to analyse solid surfaces and to investigate low energy ion scattering processes. In this study, the examination of these processes has been extended to give more detailed information concerning the basic physical and electronic interactions.

The comparison of ion scattering from surface wedge directions with that for other surface directions has allowed the inelastic energy loss of ions entering the surface region to be estimated. In the cases of Ne and Ar scattering, energy dependent measurements of this loss confirm the velocity dependent nature of the inelastic loss. The inelastic loss measurements for He^+ confirm earlier reports that the inelastic loss varies considerably with the distance of closest approach to an atomic row. Measurements have shown that the inelastic losses for single scattering and double scattering are different, but insufficient information is available to relate this to the types of collisions suffered, or to the electron density distributions through which the ions pass. It has been shown that the inelastic loss suffered by a singly scattered ion is velocity dependent, which is in agreement with the two major theoretical models. Experiments with a higher resolution energy analyser at different incident ion energies, when correlated with photon emission, may allow the identification of the type of electron excitation involved in energetic collisions.

Analysis of empirical interatomic potentials determined from gas scattering experiments revealed general agreement with the Moliere potential. Detailed analysis indicated that better agreement was possible if a correction factor was applied to the Firsov screening length. These two conclusions are in agreement with similar studies

using ISS.

The comparison of experimental investigations designed to empirically determine the correction factor were compared with computer simulations of ion scattering from atomic chains. This comparison allowed estimates to be made of the importance of thermal vibrations and the interatomic potential in computer simulation studies. The effect of inelastic energy loss on the interpretation of experimental results was also assessed. The ability to measure the interatomic potential using this method was found to be limited by the thermal broadening of the single and double scattering peaks in the energy spectrum, as well as the uncertainty related to the dependence of the inelastic energy loss on the angle of incidence. A more successful method of measuring the interatomic potential from a thermal atomic chain may be achieved by measuring the broadening of the peaks in the energy spectrum as a function of the angle of incidence. This requires an analyser with better resolution than the thermal energy spread, although this requirement could be relaxed if the instrument resolution could be deconvoluted from the measured energy spectrum. Regardless of which technique is used, there will be less uncertainty in the results of such an investigation if the target could be cooled significantly (e.g. below surface Debye temperature). The reduced target temperature will reduce the importance of thermal vibrations which means that the atomic chain will approach the cold lattice model. This simplifies the analysis of results and reduces the uncertainty in the computer simulation caused by the lack of a complete understanding of the thermal vibrations of surface atoms.

The charge exchange model of Verhey *et al.* has been applied to scattering of inert gas ions off W. The success of this model has been unpredictable for scattering along different crystallographic directions. The deviations are believed to result from the scattering of charged particles off subsurface atomic layers. This effect raises doubts about the use of changing total scattering angle to determine the characteristic velocity for the neutralization process. If the angle of incidence or the angle of detection to the surface is charged considerably then the subsurface component of the ion yield may become

significant. Results from such experiments must be critically
examined before the values obtained can be regarded as accurate. The
possibility also exists that the neutralization rate after a collision
is different to that before due to electronic excitation. Although
the facilities are not yet available to determine the accuracy of this
proposal, it should be kept in mind when interpreting the results of
charge exchange measurements.

Although the results of the Silicon experiments do not identify
the surface structure which corresponds to a particular Low Energy
Electron Diffraction (LEED) pattern, it has been shown that such
analysis is possible. A combined study with *in situ* LEED and Auger
analysis should give more conclusive results. Although not essential,
the use of a fast computer simulation to predict the azimuthal
dependence of the ISS yield and energy spectrum may help to determine
the surface structure as well as assist in measuring physical
parameters of the surface (e.g. Debye temperature, inelastic energy
loss, surface relaxation). These are but a few of the advantages
which can be associated with the simultaneous use of several analysis
techniques and comparison with a fast computer simulation.

One of the problems associated with fast computer simulations is
that often accuracy is sacrificed for speed. Further studies are at
present under way to simplify the accurate estimation of the
scattering integral for the Moliere potential to save computer
processing time.

The measurement of an "Auger-like" characteristic velocity for
Si^+ recoiling from a Si surface identifies the existence of complex
electron transition processes. The existence of Si^+ reveals that
either the ionization event occurred at some distance from the surface
instead of during the collision or that the neutralization by
resonance processes were blocked till the particle escaped the
vicinity of its neighbours. Otherwise the resonance process would be
expected to dominate the charge exchange process and no ions would be
observed. Attention has been drawn to the existence of two possible
neutralization processes and further analysis may be able to
differentiate between them. This involves altering the band structure

of the solid which may become an important technique in the analysis of charge exchange mechanisms. However, this technique requires that facilities to analyse the nature of the band structure exist if a meaningful result is to be obtained.

From these comments it is clear that although some advance has been made to the further understanding of the complex interaction of an energetic ion with a solid surface, there are still more questions than there are models or theories, let alone answers.